THE 22nd INTERNATIONAL WORKSHOP ON ECR ION SOURCES

ECRIS2016
The 22nd International Workshop on ECR Ion Sources

28 AUGUST ~ 1 SEPTEMBER, 2016

BUSAN, KOREA Hanwha Resorts HAEUNDAE TIVOLI

KBSI KOREA BASIC SCIENCE INSTITUTE | Chair **Mi-Sook Won**

Workshop Topics

- Status reports and new development
- RF generation and transport
- Plasma investigations
- Beam extraction & optics
- Charge breeding
- Theory
- Applications
- Miscellaneous

Co-Hosted by RISP Rare Isotope Science Project | NFRI National Fusion Research Institute


The 22nd International
Workshop on ECR Ion Sources Busan, Korea
28 August ~ 1 September 2016
ECRIS2016
www.ecris2016.org
THE 22nd INTERNATIONAL WORKSHOP ON ECR ION SOURCES
28 AUGUST ~ 1 SEPTEMBER, 2016 | Hanwha Resorts HAEUNDAE TIVOLI, BUSAN, KOREA
KBSI KOREA BASIC SCIENCE INSTITUTE
NFRI

The 22nd International Workshop on ECR Ion Sources (ECRIS2016), which is the first ECR workshop in Busan, Korea, was held from 28th August to 1st September 2016.

Due to the effort on the development of 28 GHz superconducting ECR ion source, the IAC of ECRIS2014 decided Korea Basic Science Institute as a host institute of the ECRIS2016. Following that the ignition of the first ECR plasma was generated in 2014; we have successfully extracted the various ion beams from KBSI-ECRIS. For further performance improvement of our system, it is now on beam optimization after almost one year overhaul. For the optimization of the system, some modification of plasma chamber and so on are ongoing that will be provided better performance of the system.

ECRIS Workshop is a well-known event being excellent for on-going new result presentation. Under comprehensive discussions with IAC, the sessions were prepared to deal with the topics: Status Reports and New Development, RF Generation and Transport, Plasma Investigations, Beam Extraction & Optics, Charge Breeding, Theory, and Applications. Technologies as well as brand-new results related on ECRIS were presented and discussed during the workshop with 82 presentations including 38 oral contributions, including special talk by Dr. Claud Lyneis on the history of ECRIS development.

The selection committee of the Geller prize was chaired by Dr. Vadim to encourage young scientist at the research field of ECR ion source. The fifth “Richard Geller Prize” sponsored by the PANTECHNIK company was awarded to Dr. Alessio Galata, INFN-LNL, Italy.

I wish that all participants will keep good memories of the BULGUK temple, Museum of fine Arts, and the impressive Banquet in the Chosun Beach Hotel.

During the workshop, the International Advisory Committee agreed on holding the 23nd workshop in INFN-LNS, Italy in 2018.

The ECRIS2016 was a great success thanks to the active participation and enthusiastic support of all attendants. We are looking forward to the next workshop in beautiful city of Sicily.

Thank you very much

Mi-Sook Won

Chair, ECRIS2016

International Advisory Committee

Yong-Seok Hwang	SNU
Ivan Izotov	IAP, RAS
Andrey Efremov	JINR
Vadim Skalyga	IAP, RAS
Santo Gammino	INFN-LNS
Hannu Koivisto	JYFL
Thomas Thuillier	LPSC
Sandor Biri	Atomki
Peter Spädtke	GSI
Takahide Nakagawa	RIKEN
Hongwei Zhao	IMP
Michael Hotchikis	ANSTO
Daniel Xie	LBNL

Organizing Committee

Mi-Sook Won (Chair)	KBSI
Byoung Seob Lee	KBSI
In Seok Hong	IBS (RISP)
Hyun-Jong You	NFRI
Jang-Hee Yoon	KBSI
Hyun Gyu Kim	KBSI
Se Yong Choi	KBSI
Jung Woo Ok	KBSI

Contents

SCALING LAWS IN ELECTRON CYCLOTRON RESONANCE ION SOURCES *

C. M. Lyneis, Lawrence Berkeley National Laboratory, CA 94720, USA

Abstract

In the last 36 years, the performance of high charge state ECRIS has improved dramatically as a result of improvements to the magnetic field confinement, increases in the microwave heating frequency and techniques to stabilize the plasma at high densities. For example, in 1980 15 eμA of O^{6+} was produced in an ECRIS[1] and now it is possible to produce as much as 4700 eμA. [2] In this paper the parameters and performance of ECRIS are reviewed and compared to empirical scaling laws to see what can be expected when fourth generation ECRIS begin to operate.

INTRODUCTION

Electron Cyclotron Resonance Ion Sources, ECRIS, are widely used to produce intense high charge state ions for accelerators used for nuclear physics and for hadron cancer therapy facilities. In nuclear physics, new heavy-ion driver accelerators are under construction and these machines require ion source production beyond the present day performance both in terms of ion charge states and ion intensities. In some ways, this parallels the efforts in the much larger field of magnetic fusion where the goal is to improve the performance beyond that of existing machines and demonstrate net power production. For many years the fusion community has used various scaling laws to both study the complex behavior of these plasma devices and to guide the design of future devices. For ECR ion sources, the search for and testing of scaling laws began with experiments in Grenoble in the 1970's, when the first high charge state ECRIS was built under Richard Geller's direction. During the last 40 years, the performance of ECRIS has progressed a great deal as illustrated with the 300 fold increase in O^{6+} currents going from 15 eμA to 4700 eμA. We now have a large number of ECRIS operating between 6.4 GHz and 28 GHz, built with a variety of shapes, sizes and operating parameters and these can be used to test existing scaling laws and perhaps uncover new ones.

Scaling laws for plasma devices can take several forms. In some cases they are used to describe the parameters of a single machine as a function of some external variable such as ECRH frequency, magnetic field confinement or RF power level. In other cases a scaling law could be used to summarize a general performance characteristic than can be applied across a wide variety of ECRIS sources. When this latter approach is applied to ECRIS, the result is often more qualitative than quantitative because there are a wide variety of source designs and only the very strong dependences will be clearly demonstrated.

Many aspects of the physics of ECR ion sources are well understood, such as the atomic physics of electron impact ionization and the magnetic confinement of plasmas and these processes can be simulated with computer codes. [3] However, the picture is not complete since these codes typically require that certain internal parameters be specified; such as the plasma density, electron energy distribution function, electron and ion confinement times and even the microwave electric field strength. Typically these parameters cannot be experimentally measured in an ECRIS plasma and so we have to rely on other methods to extrapolate ECRIS performance.

In this paper, we will review some of the scaling laws, which have been proposed over the years, and test them against to the data generated by the ECRIS now in operation. In addition we will look for new scaling laws or even rules of thumb that can help predict the performance of future ECRIS.

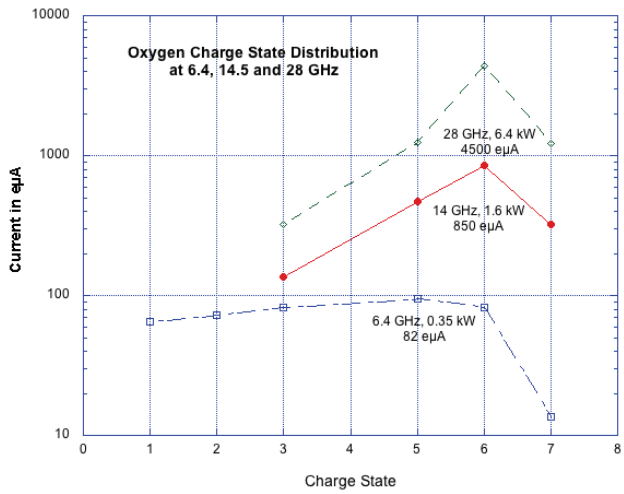

Figure 1: Oxygen charge state distributions produced on the 6.4 GHz LBL ECR, the 14 GHz AECR-U and VENUS at 28 GHz.

PHYSICS AND SCALING LAWS IN ECRIS

The physics and operation of ECRIS has been reviewed a number of times in depth. [4-6] This paper focuses on certain aspects of high charge state ECRIS, which could help in understanding the performance and scaling without an exhaustive review of the physics behind them. For the discussion that follows, it is still useful to briefly discuss the key plasma and physics mechanism in the production of high charge state ions in an ECRIS. For electrons in a magnetic field their cyclotron resonance frequency is given by

$$B_{ecr} = F_{rf}/28$$

where B_{ecr} is in Tesla and F_{rf} is in GHz.

ISBN 978-3-95450-186-1

The plasma frequency, which arises from the oscillations between the electron and plasma densities, increases as the square root of the plasma density, ne, and the critical density defined by the density at which the plasma frequency is equal to the microwave frequency, F_{rf}, or

$$n_{crit} = 1.26 \times 10^{10} \ (F_{rf})^2 \text{ electrons/cm}^3,$$

where n_{crit} is in units of electrons/cm^3 and F_{rf} is in GHz. At the critical density, the propagation of microwaves becomes problematic. While over dense plasmas can be produced in ECR ion sources designed for 1^+ ion production, the electron temperature are only on the order 10 eV and the neutral densities are also very high and under these conditions no high charge state ions are produced. While direct measurements of the plasma density in high charge state ECRIS have not been done, modeling of ion charge state production indicate they operate at a fraction of the critical density.

Another important parameter of the a magnetically confined plasma is the ratio of the kinetic plasma pressure to the magnetic field confinement pressure, which is expressed by the dimensionless factor

$$\beta = P_{plasma}/[B^2/2\ \mu o]$$

where plasma pressure, $P_{plasma} \sim n_e k T_e$, depends on the electron temperature T_e and the plasma density n_e. For stability $\beta < 1$, and while the large fusion devices can achieve values of have $\beta \sim 1$, in high charge ECRIS β values are much lower, perhaps ~ 0.01, although the values are not well quantified because of the lack of direct measurement. [7]

One of the key aspects of high charge state ECR ion sources is the use of a minimum B magnetic field configuration consisting of a two solenoid mirrors to provide axial confinement and a superimposed multipole field, typically a sextupole, to provide radial confinement. The minimum B configuration stabilizes the outward plasma pressure described above and also reduces the electron losses. The combination of these effects results in ion and electron life times in the millisecond range compared to microsecond confinement times in simple mirror traps.

Much of the progress in the performance of ECRIS has come from increasing the magnetic confinement. Largely based on experimental results, the optimum fields have the following characteristics. The minimum B field generates closed surfaces of constant magnetic field and ideally there should be a closed surface inside the chamber with $B \geq 2\ B_{ecr}$. The injection field should be 3 B_{ecr} or more, the extraction field ~ 2 B_{ecr} and the radial field ~ 2 B_{ecr}. The large value of B_{inj} reduces the ends losses at injection and the lower value of B_{ext} increases end loss and extracted current. The optimum magnetic field strengths are summarized in Table I. [8]

While the injection, extraction and wall fields should be scaled directly with B_{ecr} or equivalently with F_{rf}, practical considerations may require limiting Bmin values below 0.75 T. Recent experiments on the 28 GHz VENUS ECRIS show that the spectral temperature of axial bremsstrahlung is depends linearly on B_{min} and that it is independent of B_{ecr} and F_{rf}.[9]. The increase in the spectral temperature with B_{min} indicates that the hot tail of the electron energy distribution function above 50 keV increases linearly with Bmin. The hot tail carries a significant proportion of the plasma energy and as it increases this causes two practical problems in superconducting ECRIS. First, bremsstrahlung generated by collisions of the hot electrons with the plasma chamber walls can penetrate into the cold mass and add an unwanted cryogenic heat load.[10] Second, the x-ray shielding requirements grow rapidly and the x-rays can also damage the high voltage insulation between the plasma chamber and magnet system. Additionally, excess energy in the hot tail may lead to turbulence, which reduces the global lifetime of the plasma and limits the production of high charge states.[11]

Table 1: Optimum Magnetic Field for ECRIS

Last Closed Bsurface	$\geq 2 * B_{ecr}$
B_{inj}	$\geq$ 3 to 4 times B_{ecr}
B_{ext}	~ 2 B_{ecr}
B_{rad} at wall	~ B_{ext}~2 B_{ecr}
B_{min}	~ 0.4 to 0.8 B_{ecr}

Frequency Scaling

The most important scaling law, which was proposed by Geller[12] is that the current for a charge state q should scale as frequency squared,

$$I_q \propto F_{rf}^2.$$

This was based in part on the Grenoble measurements of the miniMafios sources at 10, 16 and 18 GHz and the Caprice sources at 10 and 14 GHz. Also, Geller pointed out that the since the critical density scales as frequency squared, that provides upper limit on plasma density, which scales with F_{rf}^2. [12] This simple relationship may be somewhat akin to Moore's Law in semiconductors, which was initially based on the observation that the number of transistors in an integrated circuit double approximately every two years. The semi-conductor industry was able to innovate fast enough to follow the law for a couple of decades. Similarly in the ECR community Geller's frequency scaling ideas have spurred the effort to build higher frequency, higher magnetic field ECRIS. In Fig. 1, the oxygen charge state distributions are shown for the LBL ECR at 6.4 GHz, the AECR-U at 14 GHz, and VENUS at 28 GHZ and these demonstrate how ion currents has grown with high microwave frequency sources.

Experimentally, this relationship only holds if the magnetic fields are scaled appropriately with frequency as described above in Table 1. An alternative explanation is that since B is scaled with frequency, then the scaling is actually due to the increase in magnetic field and that

$$I_q \propto B^2.$$

ISBN 978-3-95450-186-1

With the requirement that frequency and magnetic field be scaled together, it is difficult to determine experimentally whether I_q goes as F_{rf}^2or B^2. From an ion source design point of view, it is not critical to decide, which is correct, as long as both B and F_{rf} are scaled as shown in Table 1.

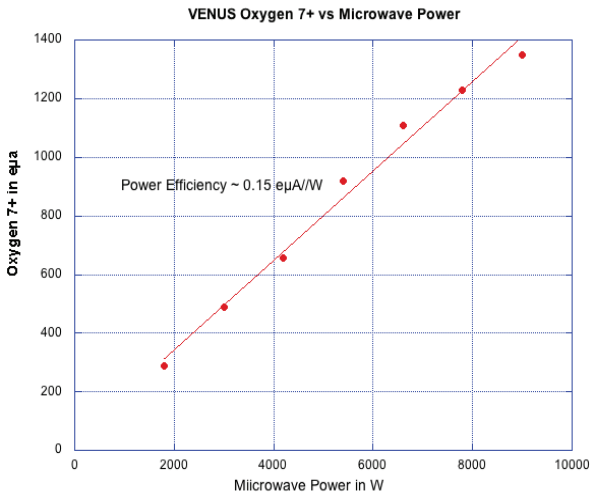

Figure 2: The linear dependence of O^{7+} current vs input microwave power measured on VENUS.

The output of a particular ion charge state depends on a number of variables including, the microwave power injected, the background pressure in the ion source or neutral pressure, presence of impurity ions in the plasma, which can improve the production of high charge states in the case of gas mixing [13] or depress the production when impurities higher mass than the desired ion. The charge state distributions have been successfully simulated when the plasma density, neutral density, electron energy distribution function and ion confinement time constant are considered variables[3]. These provide useful guidelines for understanding some aspects of ECR performance. For example the peak of the distribution depends primarily on the plasma density n_e, the ion confinement time τ_i and the electron energy distribution function, which usually approximated by a Maxwellian distribution for the electrons with a temperature T_e.

Scaling RF Power and Frequency

While the maximum ion currents produced in ECRIS roughly scale as frequency squared, the microwave power needed to produce those beams has also increased rapidly. Recent experiments with superconducting sources show that under certain conditions, the ion currents of a single ion charge state depend linearly on microwave power over a significant range of powers. [14] For example in Fig. 2, the O^{7+} ion current scales as 0.15 eμA per watt of microwave power between 1800 W and 8000 W as measured in VENUS. In this measurement, the neutral pressure was maintained at a constant value by increasing the input gas flow to adjust for the plasma pumping due to beam extraction. The charge state distribution stayed constant as did the spectral temperature. The linear behavior indicates the efficiency in converting microwave power into current remains unchanged while the power is increased a factor of 5. Other measurements on VENUS and SECRAL have shown a similar linear dependence with the power to current efficiencies for O^{6+} production between 0.7 and 1.2 eμA/watt. Since the maximum currents scale roughly as frequency squared and the current per W is linear, the power requirements for higher frequency sources should also scale as frequency squared. Scaling the VENUS source power at 10 kW and 28 GHz to a 45 GHz source would predict at least 26 kW would be needed and 40 kW would be needed at 56 GHz .[15]

As we have shown, the extracted current scales roughly as F_{rf}^2 or B^2 and this means that operation at higher frequencies and magnetic fields operation will increase the total extracted currents. This in turn will require higher source extraction voltages in order to control space charge effects. Although the beam current in an ECRIS typically does not increase as $V_{ext}^{3/2}$ when the Child-Langmuir law dominates extraction, the space charge of the beam after extraction does contribute to the transverse size of the beam and to maintain the same transverse dimensions V_{ext} should be scaled as $I_{tot}^{2/3}$. Assuming the total extracted current scales with the F_{rf}^2 , then V_{ext} should be scaled as

$$V_{ext} \propto F_{rf}^{4/3}.$$

The VENUS source needs 30 kV to properly transport a total extracted current of 20 mA in high power operation and then V_{ext} should be at least 56 kV at for 45 GHz operation and 75 kV at 56 GHz. If an ECRIS at these frequencies were designed only for the production of very high charge state ions well above q_{opt}, then the total extracted currents would be somewhat less and it would require somewhat lower extraction voltage.

For the measurements shown in Fig. 2, the charge state distribution and the spectral temperature remained constant as the power was increased from 1.8 to 9 kW. This indicates that $n_e\tau$ and T_e were approximately constant. The ion current, which depends on n_e/τ, scaled linearly with power. These two conditions can only be met if n_e is proportional to $P^{1/2}$ and τ is proportional to $P^{-1/2}$. While further work is needed to understand the full implications of this, the linear nature of the process indicates that even at 10 kW of 28 GHz power, the plasma density is well below the critical density, where many nonlinearities would be evident.

ISBN 978-3-95450-186-1

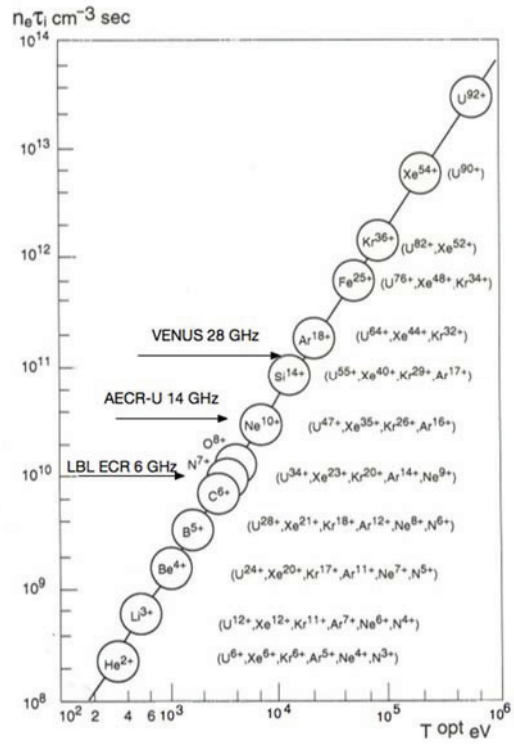

Figure 3: This illustrates the required values of $n_e\tau_i$ and optimum electron temperature to produce various ions.

The analysis of power scaling above was done for oxygen, which is a relatively light element and has relatively low ionization potentials. For example the ionization potential in oxygen going from 5 to 6^+ is only 146 eV and even 7 to 8^+ is only 836 eV. For much heavier elements such as xenon, the situation is more complex and a wide range of charge state distributions can be produced by varying the parameters of an ECRIS. Often useful intensities of ions can be utilized from the tail of the charge state distribution, well above the charge state, q_{opt}, which is defined as the ion charge state with the maximum electrical current. For example, q_{opt} for xenon in VENUS is Xe^{27+}, but Xe^{43+}, while produced at much lower intensities, is often used at the 88-Inch Cyclotron for radiation effects testing. For these ions with charge state far above q_{opt}, the scaling of intensity with frequency is stronger than F_{rf}^2 because q_{opt} increases with frequency. Figure 3 illustrates the requirements for high charge state production in terms of $(n_e\tau_i)$ and electron temperature T_e. The ionization potential for going from Xe^{42+} to Xe^{43+} is 3 keV and the maximum electron impact ionization cross section K.S. Golovanivsky criterion[4] in Fig. 3 indicates that $n_e\tau_i$ in VENUS at 28 is about 10 times that for the 6.4 GHz source and this is reflected in the maximum current for very high charge states such as Ar^{16+} scaling much faster than frequency squared between the LBL ECR at 6.4 GHz and VENUS at 28 GHz.

REFERENCES

[1] V. Bechtold, N Chan-Tung, S. Dousson, R. Geller, B. Jacquot, and Y. Jongen, Nucl. Instruments and Methods, 178 (1980) pp. 305-308.

[2] D. Z. Xie, W. Lu, J. Y. Benitez, C. M. Lyneis and D. S. Todd, "Recent Production of Intense High Charge Ion beams with VENUS", Presented at ECRIS 2016 Busan, Korea, Aug. 2016, paper THA001.

[3] G. D. Shirkov, Plasma Sources Sci. Technol 2(1993) pp. 250-257.

[4] R. Geller, 1996. *Electron cyclotron resonance ion sources and ECR plasmas*. CRC Press.

[5] A. Girard, D. Hitz, G. Melin, and K. Serebrennikov, 2004. "Electron cyclotron resonance plasmas and electron cyclotron resonance ion sources", Physics and technology. *Review of scientific instruments*, *75*(5), pp.1381-1388.

[6] D. Hitz, 2006. "Recent progress in high frequency electron cyclotron resonance ion sources", *Advances in imaging and electron physics*, *144*, pp.2-164.

[7] G. Melin, F. Bourg, P. Briand, P., M. Delaunay, G. Gaudart, A. Girard, D. Hitz, J.P. Klein, P. Ludwig, T.K. Nguyen, T.K. and M. Pontonnier, 1994. "Status of development of ECR ion sources at Grenoble." *Review of scientific instruments*, *65*(4), pp.1051-1056.

[8] D. Hitz, A. Girard, G. Melin, S. Gammino, G. Ciavola, and L. Celona, 2002. "Results and interpretation of high frequency experiments at 28 GHz in ECR ion sources, future prospects." *Review of scientific instruments*, *73*(2), pp.509-512.

[9] J. Y. Benitez†, C. M. Lyneis, L. W. Phair, D. S. Todd, D. Z. Xie, "Recent Bremsstrahlung Measurements from the Superconducting Electron Cyclotron Resonance Ion Source VENUS", Presented at ECRIS 2016, Busan, Korea, August 2016, paper MOA004.

[10] D. Leitner, J.Y. Benitez, C.M. Lyneis, D.S. Todd, T., Ropponen, J., Koivisto, H. and Gammino, S., 2008. "Measurement of the high energy component of the x-ray spectra in the VENUS electron cyclotron resonance ion source." *Review of Scientific Instruments*, *79*(3), p.033302.

[11] G. Melin, F. Bourg, P. Briand, M. Delaunay, G. Gaudart, A. Girard, D. Hitz, J.P. Klein, P. Ludwig, T.K. Nguyen, and M. Pontonnier, M., 1994. "Status of development of ECR ion sources at Grenoble." *Review of scientific instruments*, *65*(4), pp.1051-1056.

[12] R. Geller, 1996. *Electron cyclotron resonance ion sources and ECR plasmas*. CRC Press, p395.

[13] G. Melin, A.G. Drentje, A. Girard, and D. Hitz, 1999. "Ion behavior and gas mixing in electron cyclotron resonance plasmas as sources of highly charged ions." Journal of applied physics, 86(9), pp.4772-4779.

[14] L. Sun, J.W. Guo, W., Lu, W.H. Zhang, Y.C., Feng, Y. Yang, C. Qian, X., Fang, H.Y. Ma, X.Z.Zhang, and H.W. Zhao, 2016. "Advancement of highly charged ion beam production by superconducting ECR ion source SECRAL" Review of Scientific Instruments, 87(2), p.02A707.

[15] C. Lyneis, P. Ferracin, S. Caspi, A. Hodgkinson and G. L. Sabbi, Rev. Sci. Instrum. 83, 02A301 (2012).

ISBN 978-3-95450-186-1

POSSIBLE OPTIMIZATIONS OF EXISTING MAGNET STRUCTURES FOR THE NEXT GENERATION OF ECRIS

D. Z. Xie†, W. Lu[1], G. Sabbi, D. S. Todd
Lawrence Berkeley National Laboratory, Berkeley, CA 94720, USA
[1]also at Institute of Modern Physics, Lanzhou 730000, China

Abstract

The next generation of Electron Cyclotron Resonance Ion Sources (ECRISs) will operate with higher magnetic fields and higher heating frequencies than those currently in use. Constructing a min-B configuration with higher confining fields is the prerequisite for this next generation of sources. There are three leading candidates for superconducting magnet structures in future ECRISs: a Mixed Axial and Radial field System (MARS) that merges the sextupole racetrack coils and segmented end-solenoids into an exotic closed-loop-coil; a classical structure of Sextupole-In-Solenoids; and a non-classical structure of Solenoids-In-Sextupole. Focusing on efficient magnetic field generation, this article briefly reviews the advantages and disadvantages of each of these magnet structures. Though Sext-In-Sol and Sol-In-Sext magnetic structures using NbTi conductor have been proven in current ECRISs, there are still rooms for improvements of these magnet structures. Potential optimizations to these existing magnet structures, such as using a non-conventional sextupole magnet consisting of either V-bend or skew coils, are discussed. The development status of a MARS NbTi magnet for a new ECRIS at LBNL will be also presented.

INTRODUCTION

Geller's scaling laws [1] predict that ECRIS performance will improve with magnetic fields and heating frequencies. This is the most effective path as demonstrated by the successful ECRIS developments in the past decades, especially the great achievements of the 3rd generation NbTi-magnet-based ECRISs [2-7]. Future operations with even higher magnetic fields require superconducting magnet systems capable of generating higher strength min-B fields (B > 4 T) for operations at frequency f > 28 GHz. Presently there is a novel magnet system under development at LBNL, MARS (Mixed Axial and Radial field System), which merges a sextupole and two segmented end solenoids into a closed-loop-coil to efficiently generate a high strength min-B configuration. This structure is unique in that its closed-loop-coil generates not only the high radial field but also contributes substantially to the axial field. Once the MARS magnet structure has been successfully developed, it will play an important role in constructing future high-field ECRISs utilizing either NbTi or Nb_3Sn magnets [8, 9]. This new magnet structure, along with the existing classical Sextupole-In-Solenoids (Sext-In-Sol) and the non-classical structure of Solenoids-In-Sextupole (Sol-In-Sext), shown in Fig. 1, will provide three base magnet systems for constructing future ECRISs. Table 1 lists the advantages and disadvantages of each of these structures. MARS' closed-loop-coil with its minimized forces on coils stands out as the magnet choice that harnesses the advantages but avoids the disadvantages of the two existing magnet structures. However, a price is paid in increased complexity in coil winding and the magnet cryostat, in which hexagonally-shaped warm bore and inner thermal shield are required to match the MARS cold mass [9].

Table 1: Comparison of the Three Potential Magnet Systems for Future ECRISs

System	Advantages	Disadvantages
a) Sext-In-Sol	Better utilization of the radial field **(~ 50%)***	Bulkier magnet and cryostat, higher and complex interaction forces
b) Sext-In-Sol	Lower and simpler interaction forces, smaller magnet and cryostat, simpler fabrication, lower cost.	Inefficient utilization of the radial field **(~ 34%)***
c) MARS	Least and simplest interaction forces, uses substantially less conductor, smallest magnet and cryostat, Best utilization of the radial field **(~ 67%)***	Complex fabrication of the closed-loop coil, slightly complex cryostat.

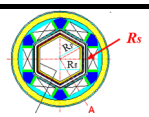

**: Defined as square of the ratio of the plasma chamber inner radius Rc over the smallest inner radius Rs of the sextupole coil: $(Rc/Rs)^2$.*

The shortcoming of existing designs comes when looking toward the future with ECRIS operation at or above 45 GHz. For conventional operation of these sources at 45 GHz frequency, the required axial fields (6.5 and 3.3 T for injection and extraction) and radial fields (3.3 T at the wall) are shown in Figs. 2(a) and 2(b), respectively. The question arises as to whether there is any room to increase the magnetic field generation efficiency, where better efficiency would mean achieving the required fields with the lower total coil excitations CE = LI (wire length x current). A reduced coil excitation should lead to lower magnetic forces, system stored energy, conductor loading and smaller superconductor volume resulting in reduction of overall magnet size. Field calculations with TOSCA indicate that there are optimizations that can be made to the current structures, and they are presented below.

†email address: zqxie@lbl.gov

ISBN 978-3-95450-186-1

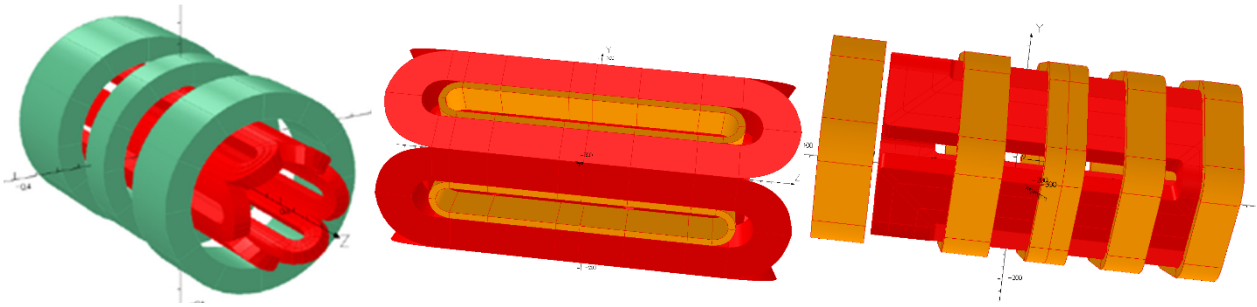

a) Sext-In-Sol b) Sol-In-Sext c) MARS

Figure 1: Schematic layout of the three possible magnet systems for future higher-field ECRISs.

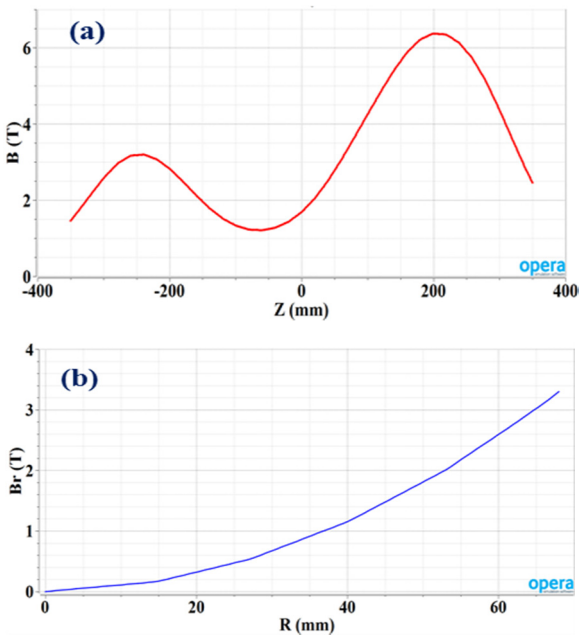

Figure 2: The axial (a) and radial (b) field profiles needed for an ECRIS to operate up to 45 GHz.

A SOL-IN-SEXT MAGNET WITH A SKEWED SEXTUPOLE

SECRAL, the first ECR ion source built with a Sol-In-Sext NbTi magnet, operates up to 24 GHz and has produced a number of CW beam records, validating the Sol-In-Sext magnet structure [10]. In order to generate the magnetic fields needed for operations up to 45 GHz, a straightforward path would be to simply replace the NbTi conductors by Nb_3Sn. Calculations show that this simple replacement would lead to maximum fields of 12.4 T on both the symmetric sextupole and the injection coils. Such high fields on the conductors are acceptable with the use of the very high J_c Nb_3Sn conductors, such as the Oxford Instruments Rod Restack Process (RRP) and the Brucker Powder in Tube (PIT). However the magnet performance can be significantly improved with a number of modifications to this magnet structure.

As schematically shown in Fig. 3, a magnetic structure here-to-fore referred to as a Skewed Sol-In-Sext design, would reduce magnetic fields on coils through the following modifications relative to the SECRAL parameters:

- Center section of the sextuple magnet skewed to lower the maximum field on the solenoids;
- Length of the magnet increased from 725 to 750 mm;
- Thickness of the sextupole reduced from 72 to 52 mm;
- Inner radii of the injection and extraction solenoids ir creased 3 mm, from 90 to 93 mm;
- Injection solenoid divided into two coils (1 and 2) to lower the loading;
- Plasma chamber radius R increased from 63 to 68 mm by slightly optimizing the cryostat to gain a 2 mm radial extra spacing;
- Sextupole, injection and extraction coils operate at higher current densities.

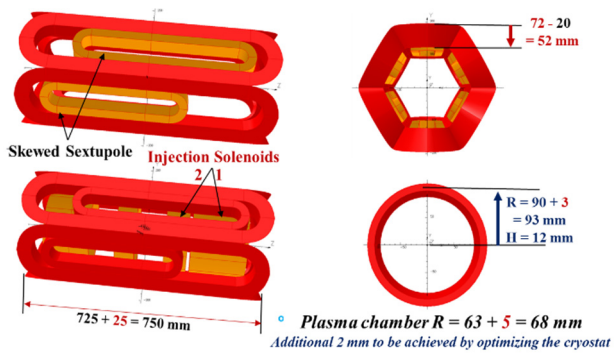

Figure 3: Layout of a Skewed Sol-In-Sext magnet constructed with an asymmetric sextupole and injection solenoid mechanically split (1 and 2) for reducing the maximum fields on the coil conductors.

Table 2 summarizes and compares the main parameters of the two magnet structures for generating the same min-B field for 45 GHz operations. The advantages of the Skewed Sol-In-Sext magnet can be easily seen and are listed below:

- Lower maximum fields on the coil conductors lead to thinner/smaller coils operating at higher currents for about the same and lower loading;
- Substantially lower system stored energy could help mitigating the quench heating somewhat in the cold mass with less LHe consumption;

ISBN 978-3-95450-186-1

- Greatly reduced the superconducting wire cost. If built with the same conductor wire the Skewed Sol-In-Sext uses only about ~ 60% of that would be needed for a conventional Sol-In-Sext magnet.

The primary drawback of the Skewed Sol-In-Sext is the requirement of two set of winding fixtures for the asymmetric sextupole coils instead of one set for the symmetric sextupole coils. Nevertheless, such an optimization to the Sol-In-Sext magnet would provide an option to a next generation ECRIS to be built with the Sol-In-Sext magnet structure.

Table 2: Sole-In-Sext Magnet System Variations

	Skewed Sol-In-Sext	SECRAL Sol-In-Sext
Magnet Length (mm)	750	725
Thickness (mm) of the sextupole coil	52	72
Designed plasma chamber ID R (mm)	136	126
ID/OD (mm) of the Injection Solenoid	186/210	180/210
Designed engineer current density $\mathbf{j_e}$ (A/mm^2) in Sext & Injection 1/2 coils	285/600/500	250/450
Peak fields on conductor: Sext & Injection 1/2 coils (T)	11.8/9.2/10.0	12.4/12.4
Loading Factor (%) on OST M grade conductor Sext & Injection 1/2 coils*	75/75/75	76/85
System Stored E (MJ)	1.0	1.7

*: 70% of bare wire packing assumed.

A SEXT-IN-SOL MAGNET WITH A V-BEND SEXTUPOLE

The Sext-In-Sol magnet structure was the first superconducting magnet structure used in an ECRIS and remains the most commonly used in the most recent (3rd) generation sources. It is built with a sextupole consisting of six coils assembled into an arched circle which, in conjunction with a circular plasma chamber, leads to ~ 50% utilization of the generated radial field in most of the sources. The disadvantage of this well-proven structure is the very complex and strong interaction forces require a fairly bulky magnet footprint and cryostat. Like the Sol-In-Sext structure there is room for further improvement.

A Sext-In-Sol structure using Nb_3Sn coils along with an arched sextupole to generate a min-B field for operations up to 45 GHz, named FECRAL, is under a joint engineering study at LBNL and IMP/CAS, China. The magnet structure of FECRAL is a slight variation of that designed for a 4th generation ECRIS for operations up to 56 GHz [11]. A possible optimization to this classical magnet system is to replace the arched sextupole with a hexagonally-shaped sextupole consisting of six "V-bend" coils. Figure 4 shows a V-bend Sext-In-Sol magnet constructed with a sextupole consists of six azimuthally V-shaped track coils and a mechanically split injection solenoid for slightly reduced maximum fields on the coil conductors. Using a hexagonal plasma chamber to match the sextupole shape, radial field utilization could equal that of MARS (~ 65%) with its hexagonal chamber. However, a distinct difference between this structure and MARS is the V-bend sextupole contributes nothing to the axial field which requires more of the solenoids for this structure.

Table 3 summarizes and compares the main parameters of the V-bend and the preliminarily designed (FECRAL) arched Sext-In-Sol magnets. With generation of the needed maximum radial field ≥ 3.2 T at the chamber inner surface, the major radius of 82 mm of the hexagonal plasma chamber is about 10% larger than the designed 75 mm for the arched sextupole, though the excitation of the V-bend sextupole is only ~ 85% of the arched sextupole. The overall footprints of the V-bend and arched magnets are essentially the same, but the V-bend sextupole operates at substantial lower current leading to lower maximum fields on the sextupole coils and greatly reduced conductor loading: a very preferable merit for magnetic field generation. The relatively low coil loading factors when using bronze (< 80%) given in Table 3 for both the sextupole and injection solenoid coils indicate that a V-bend magnet could be built with this wire, while the arched magnet would need to be built with Oxford Instruments' M-grade or higher grades of wires.

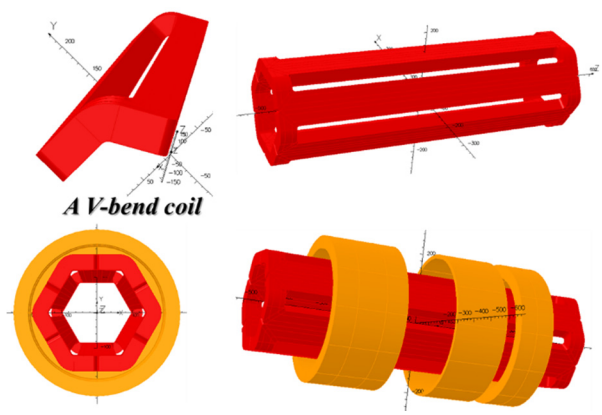

Figure 4: Schematic assembly of a V-Bend Sext-In-Sol magnet in which the sextupole constructed with six azimuthally V-shaped coils reduce the maximum fields on the coils. A hexagonal plasma chamber is to be used to match the shape of sextupole for better radial field utilization efficiency.

The fabrication complexity of a V-bend and an arched sextupole coil may vary slightly, but the coil clamping will differ substantially due to the geometric variation of the sextupoles. The issues of different coil clamping schemes

ISBN 978-3-95450-186-1

need be addressed by stress analyses to come up better solutions in the actual developments.

Table 3: Sext-In-Sol Magnet Variations

	V-bend	Arched* (FECRAL)
Total Magnet Length (mm)	940	947
Thickness (mm) of the sextupole coil	35	26
Designed max. plasma chamber radius R (mm)	82	75
ID/OD (mm) of the Injection Solenoid	340/410	310/372
Designed engineer current density $\mathbf{j_e}$ (A/mm^2) in Sext/Injection coils	230/290	440/320
Peak fields on conductor Sext/Injection coils (T)	9.4/9.5	10.8/9.5
Loading Factor (%) Sext/Injection coils** on Bronze conductor or OST M-grade conductor	72/77 60/63	98/80 78/65
System Stored Energy (MJ)	1.17	1.15

*: Based on its preliminary design layout.
**: 70% of bare wire packing assumed.

STATUS OF MARS COIL PROTOTYPING

To develop the winding techniques and fixtures for fabricating the MARS closed-loop coil, a test winding is underway at LBNL using copper wire of about the same size as the intended Oxford Instruments NbTi wire for the MARS-D's magnet [9]. The dimensions of the prototyped copper coil are about the same except the thickness is ~ 1/3 of the designed coil. Figure 5 shows the completed prototype copper coil with 396 turns wound while 420 turns were expected for a perfect winding. To get a feel of the agreement of the field strength and profile of the fabricated coil to the designed, a field mapping was conducted by energizing the copper coil with current of 1.00 A. Figure 6a and 6b show the measured axial and radial field profiles in comparison to the TOSCA calculations. Because of the complexity to completely simulate the coil-end winding layers that alternatively spread over a 112 mm width compared to the 92 mm width of the straight bars, the simulated coil end is simplified to three sections with two air gaps of 1.0 cm each in between. It is convincible that this simplified simulation has under estimated ~ 2% of the axial peak fields and overestimated ~ 3-4% of the center field, respectively as shown in Fig. 6a. In the radial field profile the discrepancy of the average measured Br peak field is merely $\leqslant$ 1.0 % to the calculation. It is reasonable to say that the overall measurement agrees very well with the calculation and has demonstrated the field tomography of the MARS closed-loop-coil.

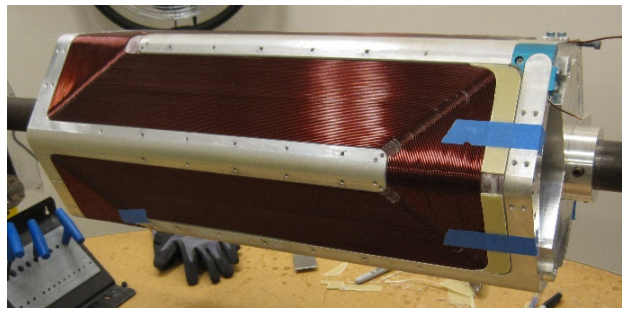

Figure 5: The wound prototype closed-loop copper coil in its winding fixture prior to field mapping.

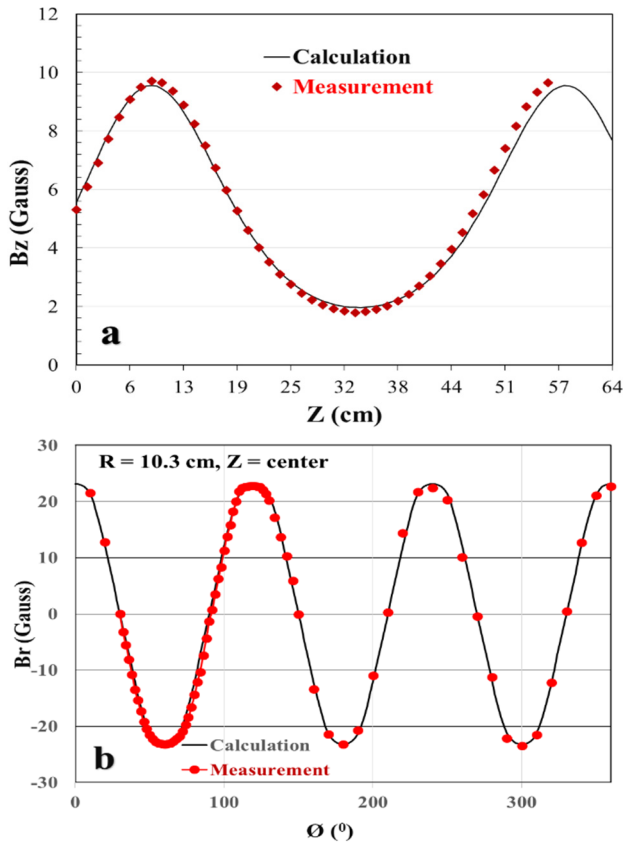

Figure 6: **a**. The measured axial field profile (red diamonds) of the prototype copper coil in comparison to the TOSCA calculation; **b**. The measured central radial field profile (red dots) at R = 10.3 cm in comparison to the calculation.

SUMMARY

The possible optimizations of magnet coil layout presented above, which can be further refined, have shown that there is still room for further improving the magnet design for ECRISs. The key enhancement comes essentially from converting the generated radial fields into the effective fields inside the ECRIS plasma chamber, i.e. increasing the utilization efficiency of the generated magnetic fields. For a given min-B configuration, the enhanced utilization of the generated fields leads to lower the maxi-

ISBN 978-3-95450-186-1

mum fields on the superconductors and loading, very preferable features for constructing a high field superconducting magnet system.

The field mapping of the prototype copper coil has demonstrated excellent agreement with the designed field profiles and the completion of the coil winding has demonstrated the techniques needed for fabricating an exotic-shape coil for a MARS magnet system. These accomplishments have further demonstrated the feasibility of a NbTi MARS-magnet-based 3rd generation ECRIS: MARS-D [9].

REFERENCES

[1] R. Geller *et al.*, "The Grenoble ECRIS Status 1987 and Proposals for ECRIS Scalings," in *Proc. of the 8th ECR Workshop*, NSCL Report: MSUCP-47 (unpublished), E. Lansing, MI, USA, 1987, p1.

[2] S. Gammino, G. Ciavola, L. Celona, D. Hitz, A. Girard, and G. Melin, *Rev. Sci. Instrum*. **72**, 4090 (2001).

[3] C. M. Lyneis and Z. Q. Xie, "Concept for a third generation ECR source at LBL," in *Proc of the 12th International Workshop on ECR Ion Sources*, RIKEN, Japan, 1995, p. 119, (unpublished).

[4] H. W. Zhao *et al*., *Rev. Sci. Instrum*. **77**, 03A333 (2006).

[5] P. A. Zavodszky *et al*., *AIP Conf. Proc*. 749, 131 (2005).

[6] T. Nakagawa *et al*., *Rev. Sci. Instrum*. **81**, 02A320 (2010).

[7] B. S. Lee, S. Choi, J. H. Yoon, J. Y. Park, and M. S. Won, *Rev. Sci. Instrum*. **83**, 02A347 (2012).

[8] D. Z. Xie, *Rev. Sci. Instrum*. **83** 02A302 (2012).

[9] D. Z. Xie, J. Y. Benitez, A. Hodgkinson, T. Loew, C. M. Lyneis, L. Phair, P. Pipersky, B. Reynolds, D. S. Todd, *Rev. Sci. Instrum*. **87**, 02A702 (2016).

[10] L. Sun *et al.*, *Rev. Sci. Instrum*. **87**, 02A707 (2016)

[11] C. Lyneis, P. Ferracin, S. Caspi, A. Hodgkison and G.L. Sabbi, *Rev. Sci. Instrum*. **83** 02A301 (2012).

ISBN 978-3-95450-186-1

RECENT DEVELOPMENTS OF RIKEN 28 GHz SC-ECRIS

Y. Higurashi†, J. Ohnishi ,H. Haba, M. Kidera, K. Ozeki and T. Nakagawa
RIKEN Nishina Center, Wako, Japan

Abstract

In the past two years, we have attempted to improve the performance of RIKEN 28GHz SC-ECRIS for the production of an intense U ion beam. Last year, we produced ~200 eμA of U^{35+} at an injected Radio frequency (RF) power of ~2.6 kW. For the RIKEN RIBF experiment, we produced ~110 eμA of U^{35+} ions with the sputtering method for longer than one month without a break. In this case, we surely require a very stable beam to increase the transmission efficiency in the accelerators and avoid any damage to the components of the accelerator due to the high-power beam. Very recently, we tested the production of a highly charged Zn ion beam to meet the requirements of the RIBF project and to produce an intense beam with a very low consumption rate.

INTRODUCTION

To increase the beam intensity of a highly charged U ion beam for the RIKEN RIBF project [1], we attempted to improve the performance of RIKEN 28 GHz SC-ECRIS for the past several years [2, 3]. Further, to increase the output beam from the accelerator, we need to increase the U beam intensity and stabilize it because we need to avoid any damage to the components of the accelerator due to the high-power beam. To produce U vapor, we chose the sputtering method, which has two advantages:

1. We can install a large amount of material in the chamber.
2. We only need to supply a negative voltage (several kilovolts) to obtain neutral U atoms, which is simpler than the use of a high-temperature oven.

On the other hand, in general, the beam intensity with the sputtering method is weaker than that with the oven method. Furthermore, the beam intensity is not very stable, which may be due to the sputtering process. To solve these problems, we experimentally searched for the optimum conditions of the ion source. In these experiments, we obtained an intense beam with a low material consumption rate and supplied an intense beam of U^{35+} ions to the accelerators over a long period of time without serious issues. To obtain a more stable beam, we are developing a high-temperature oven. This summer, we modified the crucible to increase the volume and carried out a test experiment to produce a U^{35+} ion beam for a long period of time.

Very recently, there has been strong demand for the production of an intense beam of medium-mass heavy ions such as ^{78}Kr and ^{70}Zn ions. To meet this requirement, we tested the Zn ion beam production with RIKEN 28 GHz SC-ECRIS and successfully obtained a highly charged Zn ion beam with a low consumption rate for the first time experimentally.

In this paper, we present the recent experimental results and the experiences of the long-term operation of the ion source for the production of a U ion beam. In the next section, the experimental results related to the increase in the beam intensity of the highly charged U ion beam are presented. Then, the performance of the ion source for long-term operation is described. Next, we describe the preliminary results of a test experiment for the production of a Zn ion beam. In last section, the conclusions and the plans for future work toward improving the performance are presented.

URANIUM ION PRODUCTION

The structure of the ion source and the method for producing neutral U atoms with the sputtering method are described in Refs. [2] and [3] in detail. The main feature of the ion source is that it has six solenoid coils for producing a mirror magnetic field. Using this configuration, one can produce the so-called "flat B_{min}" [4] and "classical B_{min}."

Figure 1a) shows the beam intensity of U^{35+} as a function of the injected RF power, which was calculated using the increase in the cooling water temperature of the plasma chamber. For the production of neutral U atoms, we used the sputtering method [3]. The extracted voltage was maintained at 22 kV in this experiment. Closed circles are the results with the magnetic field strength of RF injection side (B_{inj}) ~ 3.1 T, the minimum magnetic field of mirror magnetic field (B_{min}) ~ 0.66 T, magnetic field strength of the beam extraction side (B_{ext}) ~ 1.79 T, and the radial magnetic field strength on the inner wall of the plasma chamber (B_r) ~ 1.88 T, whereas open circles are the results with B_{inj} ~ 3.1 T, B_{min} ~ 0.56 T, B_{ext} ~ 1.76 T, and B_r ~ 1.88 T. In this case, we added 18 GHz microwaves (400–450 W, double frequency injection). The typical gas pressure with B_{min} ~ 0.66 T was ~7.6×10^{-5} Pa, and the optimum gas pressure for maximizing the beam intensity slightly increased as the injected RF power increased. Additionally, we observed that the beam stability improved with the use of double frequency injection, which is the same as the result in Ref. [5]. The beam intensity linearly increased as the injected RF power increased for both cases. The beam intensity with a lower B_{min} (~0.56 T) is slightly lower than that with a higher B_{min} (~0.66 T).

† higurasi@riken.jp

ISBN 978-3-95450-186-1

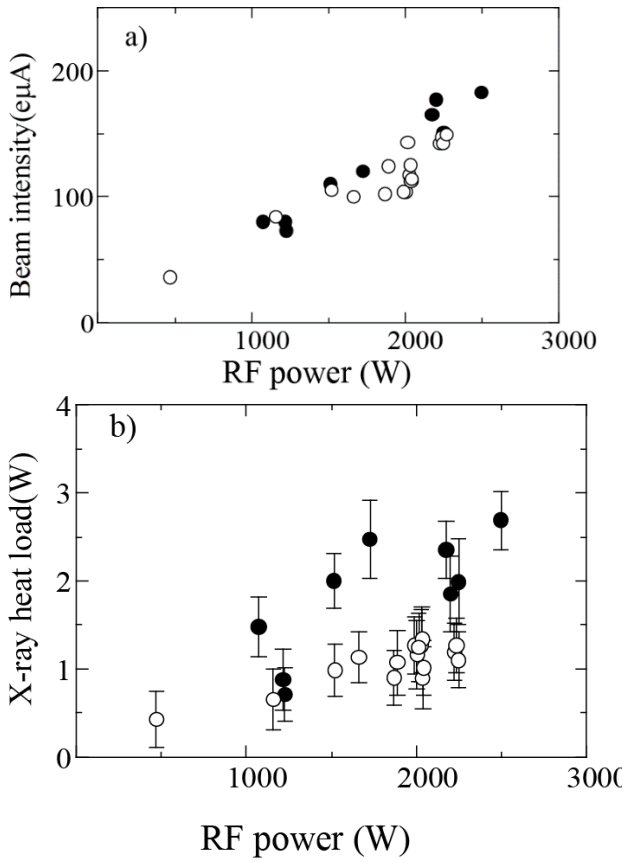

Figure 1: a) Beam intensity of U^{35+} ions as a function of the injected RF power. Open and closed circles are the results with B_{min} ~ 0.66 and 0.56 T, respectively. b) X-ray heat load as a function of the injected RF power. Open and closed circles are the results with B_{min} ~ 0.66 and 0.56 T, respectively.

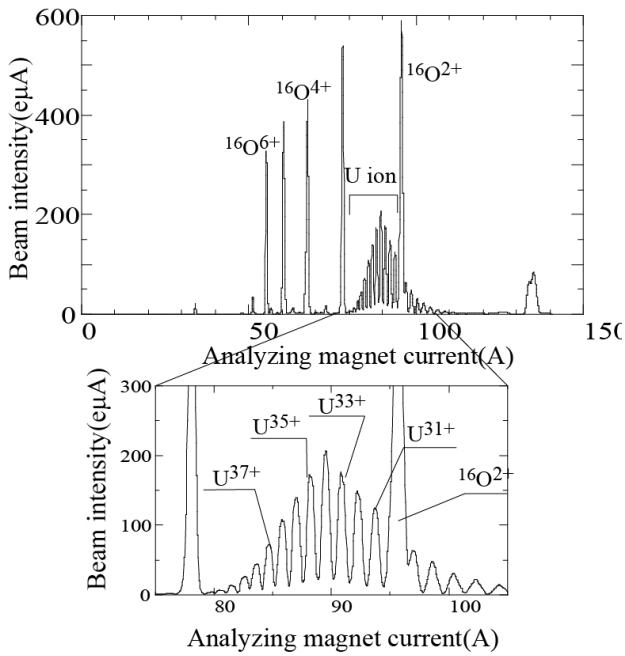

Figure 2: Charge state distribution of the highly charged U ion beam at an RF power of ~2.6 kW.

Figure 1b) shows the X-ray heat load as a function of the injected RF power under the same conditions in Fig. 1a). The closed and open circles are the results with B_{min} ~ 0.66 T and 0.56 T, respectively. The heat load for B_{min} ~ 0.56 T is significantly lower than that for B_{min} ~ 0.66 T, which is mainly due to the magnetic field gradient in the ECR zone. The average field gradient with B_{min} ~ 0.66 T is estimated to be ~2000 G/cm, which is less than that (~2400 G/cm) with B_{min} ~ 0.56 T. Generally, the energy transfer from the microwaves to the electrons in the ECR zone is inversely proportional to the magnetic field gradient. Therefore, high-energy electrons are easily produced with the lower field gradient. In this case, high-energy X rays were produced and easily penetrate the chamber walls and the wall of the cryostat. Consequently, there is an additional heat load on the cryostat of the SC-magnet owing to these X-rays emitted from the plasma.

Figure 2 shows the typical charge distribution of the highly charged U ion beam. B_{inj}, B_{min}, B_{ext}, and B_r were 3.1, 0.62, 1.78, and 1.87 T, respectively, and the RF power was ~2.6 kW.

Figure 3 shows the normalized rms emittance as a function of the focusing solenoid coil current. The beam intensity was fixed to approximately 100 eμA. In this experiment, only the focusing solenoid coil current was varied without any changes in the other parameters. The normalized X emittance dramatically decreased from 0.25 to 0.1 π mm mrad1 as the solenoid coil current increased. On the other hand, the Y emittance was almost constant. It is thought that the aberration of the analyzing magnet in the X direction (horizontal) is greater than that in the Y direction (perpendicular). Further, the beam size in the analyzing magnet becomes smaller as the magnetic convergence increases. For this reason, it may be concluded that the large X emittance with a lower focusing solenoid coil current is mainly due to the aberration of the analyzing magnet. As described in Ref. [6], the aberration of the analyzing magnet strongly affects the emittance size; that is, a larger aberration results in a larger emittance. To reduce the emittance size, we have to reduce the size of the beam using the focusing solenoid coil.

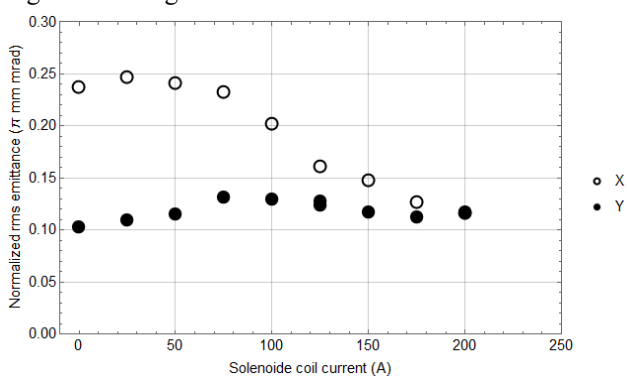

Figure 3: Normalized rms emittances as a function of the focusing solenoid coil current.

ISBN 978-3-95450-186-1

LONG-TERM OPERATION

Figures 4a) and b) show the extraction current of the ion source and the beam intensity of U^{35+} ions, respectively. The extracted current is quite stable, as shown in Fig. 5a), and the average beam intensity of U^{35+} was ~102 eμA over a long period of time. Under this condition, a maximum beam intensity of ~49 pnA was successfully extracted from the superconducting ring cyclotron for the RIBF experiment conducted last autumn [7].

For long-term operation, it is important to minimize the material consumption rate. To obtain the consumption rate, we operated the ion source with the same sputtering voltage for approximately one month. In 2012, we produced an intense beam of U^{35+} with a sputtering voltage of approximately –5 kV. In this experiment, we observed that the consumption rate of the material is higher than that in the oven method [6]. To minimize the consumption rate while maintaining the beam intensity, we systematically studied the consumption rate for several sputtering voltages. At a sputtering voltage of –1 kV, the consumption rate was ~2.1 mg/h for the production of approximately 100 eμA of U^{35+} ions, which is a significantly lower consumption rate than that at approximately –5 kV [3].

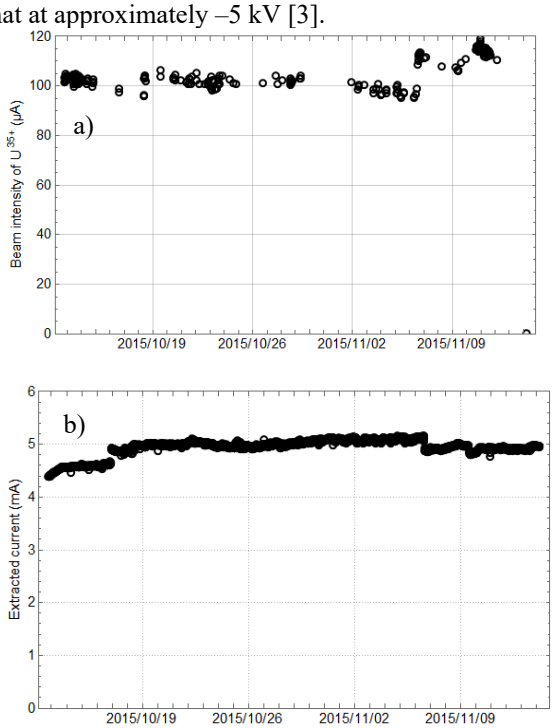

Figure 4: (a) Beam intensity of U^{35+} ions and(b) the extracted current as a function of time.

OVEN DEVELOPMENTS

When comparing the oven and sputtering methods, the oven method has several advantages, including the following:

1. We do not need to supply a high voltage to produce neutral atoms. Generally, the application of a high voltage between the plasma and metallic U increases the disturbance in the plasma. Consequently, the beam intensity may become unstable.
2. We can control the U vapor independently.

However, the oven method also has disadvantages, as described previously. In particular, we can only supply a small amount of the sample (UO_2) using the crucible (~1 g) [7]. Therefore, in this case, we have to minimize the consumption rate. In the last several years, we have attempted to maximize the beam intensity and minimize the consumption rate. In 2013, we successfully produced ~100 eμA of U^{35+} ions with a low consumption rate (~3 mg/h). However, the RIKEN RIBF experiments require the production of a beam for longer than one month without any breaks. To meet this requirement, we fabricated a crucible with a larger volume that can contain ~3 g of UO_2 and tested it this summer. Figure 5 shows the typical charge state distribution of the highly charged U ions. For the two-week experiment, we did not have any troubles and obtained a very stable beam. The consumption rate was ~2.5 mg/h for producing ~120 eμA of U^{35+} ions. Using it, we may produce a beam for longer than 1000 h, which meets the requirement.

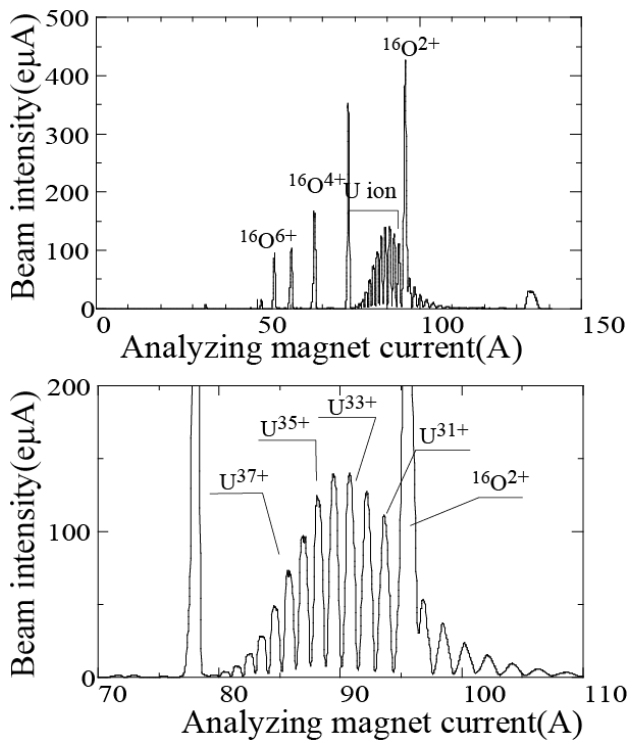

Figure 5: Charge distribution of the highly charged U ion beam.

ZINC ION BEAM PRODUCTION

For the production of Zn vapor, we used a low-temperature oven [8], which is same type as that used for 18 GHz ECRIS in RIKEN. In the test experiment, we used He gas as a support gas and ^{nat}ZnO as a sample. Figure 6 shows the typical charge distribution of the highly charged Zn ions. The injected RF power was ~1.6 kW (28 GHz + 18 GHz). B_{inj}, B_{min}, B_{ext}, and B_r were 3.1, 0.62, 1.78, and 1.94 T, respectively, and the typical gas pressure was $6.5–7.5\times10^{-5}$ Pa. The average beam intensity was ~26 eμA of $^{64}Zn^{19+}$

ISBN 978-3-95450-186-1

ions, which is the required charge state of the Zn ions for RIBF experiments. The consumption rate of Zn was ~0.20 mg/h. If we assume the use of enriched ^{70}Zn, the beam intensity will be ~60 eμA, which is the required beam intensity. Furthermore, the consumption rate for 28 GHz SC-ECRIS was almost same as that for 18 GHz ECRIS.

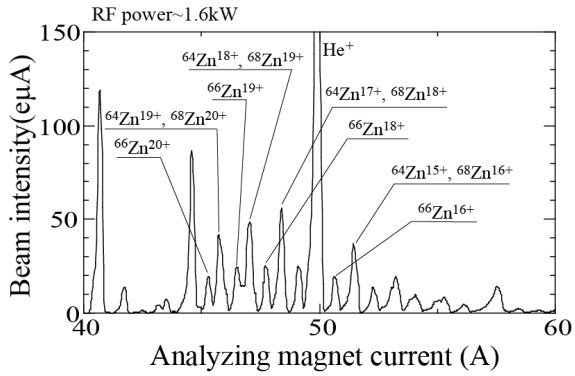

Figure 6: Charge distribution of the highly charged Zn ion beam.

CONCLUSIONS AND PLANS FOR FUTURE WORK

We produced 200 eμA of U^{35+} ions at an RF power of ~2.6 kW. We observed that the beam intensity becomes stable using double frequency injection (28 and 18 GHz). For long-term operation (approximately one month), we successfully produced a stable beam of over 100 eμA without any breaks using the sputtering method and did not observe any serious damage to the components of the accelerator. This summer, we attempted to produce a Zn ion beam with a low-temperature oven and produced ~30 eμA of $^{64}Zn^{19+}$ ions using ^{nat}ZnO in the first trial, which is the required charge state for RIBF experiments. It is estimated that the beam intensity is ~60 eμA for the ^{70}Zn ion beam when using 100% enriched ^{70}Zn. This is the required beam intensity for the ^{70}Zn ion beam from the ion source. The consumption rate was ~0.20 mg/h, which is sufficiently low for long-term operation. This autumn, we plan to produce a stable beam of U^{35+} higher than 100 eμA for long-term operation using the oven. For the production of the ^{70}Zn beam, optimization of the magnetic field, RF power, etc. will be carried out to maximize the beam intensity with a low consumption rate.

REFERENCES

[1] Y. Yano, *Nucl. Instrum. Methods Phys. Res. Sec*. B 261, 1009 (2007).
[2] T. Nakagawa *et al.*, *Rev. Sci. Instrum.* 81, 02A320 (2010).
[3] Y. Higurashi, J. Ohnishi, K. Ozeki, M. Kidera, and T. Nakagawa, *Rev. Sci. Instrum*. 85, 02A953 (2014).
[4] G. D. Alton and D. N. Smithe, *Rev. Sci. Instrum*. 65, 775 (1994).
[5] Z. Q. Xie, *Rev. Sci. Instrum*. 69, 625 (1998).
[6] O. Kamigaito *et al.*, in *Proc. IPAC2016*, paper TUPMR022 (2016).
[7] J. Ohnishi, Y. Higurashi, and T. Nakagawa, *Rev. Sci. Instrum*. 87, 02A709 (2016).
[8] K. Ozeki, Y. Higurashi, M. Kidera, and T. Nakagawa, in *Proc. HIAT2015*, paper WEPB22 (2015).

ISBN 978-3-95450-186-1

INNOVATIVE SCHEMES OF PLASMA HEATING FOR FUTURE MULTIPLY-CHARGED IONS SOURCES: MODELING AND EXPERIMENTAL INVESTIGATION

G. Castro*[1], D. Mascali[1], G. Torrisi[1], L. Celona[1], O. Leonardi[1], M. Mazzaglia[1,2], D. Nicolosi[1], R. Reitano[1,2], G. Sorbello[1,3], C. Altana[1,2], F. P. Romano[1,4], and S. Gammino[1]
[1]LNS-INFN, Catania, Italy
[2]Università degli studi di Catania, dipartimento di Fisica, Catania, Italy
[3]Università degli studi di Catania, DIEEI, Catania, Italy
[4]CNR, Istituto per i Beni Archeologici e Monumentali, Via Biblioteca 4, 95124 Catania, Italy

Abstract

The application of plasma heating methods alternative to the direct Electron Cyclotron Resonance coupling, such as the Electron Bernstein Waves heating, is already a reality in large-size thermonuclear reactors. The heating driven by these plasma waves gives the unique opportunity to largely overcome the cut-off density. The downsizing of tools and methods needed to trigger EBW in compact traps such as ECRIS devices is still a challenge, requiring advanced modeling and innovative diagnostics. At Istituto Nazionale di Fisica Nucleare-Laboratori Nazionali del Sud (INFN-LNS), the off-ECR heating (driven by Bernstein waves) has produced a highly overdense plasma. Interferometric measurements say the electron density has overcome by a factor ten the cut-off density at 3.76 GHz. More advanced schemes of wave launching have been then designed and implemented on the new test-bench called Flexible Plasma Trap, operating up to 7 GHz – 0.5 T, in flat/simple mirror/beach magnetic configuration. The paper will give an overview about modal-conversion investigation by a theoretical and experimental point of view, including the state of the art of the diagnostics developed to detect plasma emitted radiation in the RF, optical, soft-X and hard-X-ray domains.

INTRODUCTION

The Electron Cyclotron Resonance Ion Sources (ECRIS) and the Microwave Discharge Ion Sources (MDIS) are currently the best devices worldwide to feed effectively high-energy accelerators [1]. Plasma is produced by microwaves typically in the range 2.45-28 GHz by means of the so-called "Electron Cyclotron Resonance (ECR)". Most of the parameters of the extracted beam, such as the intensity, the emittance and the shape in the real space depend on the characteristics of the plasma from which the beam is extracted [2]. Any further development of ECR-type ion sources is thus intrinsically limited by physical properties of the plasmas. In microwaves-sustained plasmas, the density increases with RF power and stabilizes around a value below the critical density $n_{cut-off}$. An option to overcome this limitation consists in the use of ElectroStatic (ES) waves, showing no cut-offs within the plasma. An ES wave is a rarefaction-compression wave whose electric field is parallel to the wave propagation direction. Most of ES waves do not suffer any resonance within a plasma; however, Electron Bernstein Waves (EBW) [3] can be strongly absorbed by the plasma at cyclotron harmonics [4] . Due to their electrostatic nature, EBWs must be generated within the plasma from electromagnetic waves. EBWs are excited at UHR via the decay of a large-amplitude electromagnetic wave, propagating perpendicular to ambient magnetic field in the X-mode, into a short-wavelength electron Bernstein. Three main mechanisms of EM to EBW coupling have been studied and characterized in plasma fusion devices, as schematically depicted in Fig. 1:

- **High field side launch:** X waves are launched by regions where $B/B_{ECR} > 1$. X waves are here not screened by the R cut-off, reach the UHR crossing the ECR from the high field side, then being converted into EBWs.
- **Directed FX-B conversion:** The fast X-mode (FX) tunnels through the evanescent region between the R-wave cut-off and the UHR and couples to the slow X-mode (SX) that, in turn, mode converts to EBWs at Upper Hybrid Resonance (UHR).
  If the UHR layer is enclosed by R and L cut-offs, the X wave can be reflected back and forth passing through the UHR, then leading to the establishment of the Budden-type conversion scenario. The module of the conversion efficiency of a FX wave into a B-mode in these conditions is [5]:

$$|C_{XB}| = 4e^{-\pi\eta}\left(1 - e^{-\pi\eta}\right) \quad (1)$$

  η is the Budden parameter, obtained by expanding the wave potential around the UHR. If the length scale of magnetic field variation $L_B = B/(\partial B/\partial x)$ is larger than electron density variation length-scale $L_n = n_e/(\partial n_e/\partial x)$, η can be written as:

$$\eta = 294\,|BL_n|^{UHR} \quad (2)$$

  Direct FX-B conversion heating is used in experiments with relatively low magnetic field, where the normalized gradient length $k_0 L_n$ is ~ 0.3 (k_0 being the wave number of the incident wave in vacuum) and $\eta \sim 0.22$ [6, 7].

* Castrog@lns.infn.i

ISBN 978-3-95450-186-1

- **O-SX-B conversion:** in such a case, the R cut-off is crossed by the O wave that, if the conditions for O-SX conversion are valid at the O cut-off, is converted into SX waves which are, in turn, converted into Bernstein waves at UHR. The efficiency of O-SX transition process is maximized for $k_0 L_n \sim 1 - 20$, i.e. for flattened density profiles.

EBWs have been already generated in large devices for fusion, and the studies have shown that EBW heating could be a valid alternative to the ECR heating. At WEGA stellarator of Greifswald, for example, EBW heating allowed to reach densities up to 10 $n_{cut-off}$ [8].

In the experiments here described, EBWs are generated and absorbed in a small plasma reactor characterized by an axis-symmetric magnetic field, aimed to the generation of beams for accelerators.

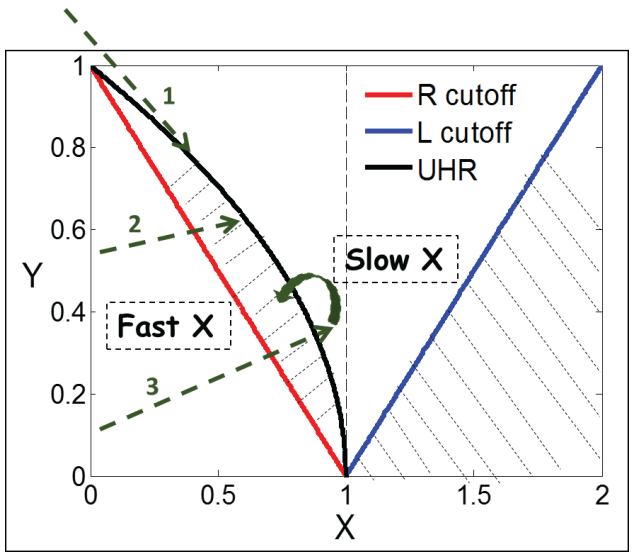

Figure 1: Main mechanism of conversion from the X wave to the EB waves: 1) High field side launch; 2) FX-B conversion; 3) O-SX-B conversion; X and Y are the dimensionless density and magnetic field respectively.

DIAGNOSTICS FOR HIGH DENSITY PLASMAS

High density plasmas require the development of "ad hoc" diagnostics (see Fig. 2) able to investigate the electron energy distribution function of the different electron populations and their distribution in the plasma chamber [9].

- **Langmuir Probe (LP) diagnostics** still represent the easiest way to perform plasma density measurements of bulk electrons (10-100 eV). However it features some limitations: i) the density measurement is "model-dependent"; ii) the probe undergoes to plasma damage, especially when density overcomes 10^{12}cm^{-3}; iii) the probes perturb the plasma chamber especially by an electromagnetic point of view.
  The development of a multimodel software to cross-check the Langmuir probe (LP) data by means of several "self-consistent" models validated for high density ($1 \cdot 10^8$ to $1 \cdot 10^{12}$ cm^{-3}), strongly magnetized plasma (see Ref. [10] for more details) allowed to obtain more and more reliable information from the resistivity curve.
- **Microwave interferometry** is a non-invasive method for plasma diagnostics for the whole plasma density measurements. Interferometry in ECR Ion Sources is a challenging task due to the very small λ/L ratio (with λ microwaves' wavelength and L typical size of the plasma chamber).
  At INFN-LNS a new interferometer, based on the so-called "frequency sweep" method has been developed for small size ion sources [11]. The measurements shown in [11] demonstrate the absolute plasma density can be measured in a non-intrusive way.
- **X-ray based systems**: X-ray volumetric measurements can be a powerful method for measuring the plasma density at medium-high energy ranges. the techniques developed in past years [12] allow to know the temperature and density of the electron population emitting X rays.
- **Plasma imaging and space-resolved analysis** is performed by using the Photon Counting (PhC) technique, provided by the X-ray pinhole. This technique allows to investigate both dimensions and geometry of the plasma source as well as the spatial distribution of X-ray energies in the plasma, allowing to distinguish hot regions from the cold ones .
- **Optical Emission Spectroscopy** may represents a powerful diagnostics for the low energy (1-10 eV) plasma electron population. It permits to distinguish different ion populations and identify them directly within the plasma.

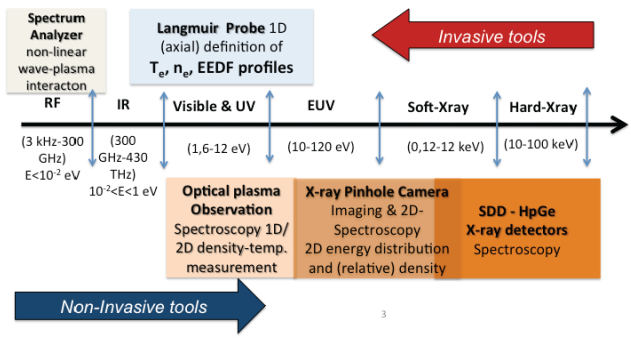

Figure 2: Diagnostics used and related electromagnetic spectrum.

EXPERIMENTAL EVIDENCES

The experimental apparatus has been already already shown in details in reference [10, 11]: A plasma reactor surrounded by permanent magnets generating a (maximum magnetics field ~ 0.1 T) is fed by microwaves at 3.76 GHz, generated by a Traveller Wave Tube (TWT). This frequency has been chosen after a fine tuning of the machine. The magnetic field strength is too low to permit ECR resonance,

ISBN 978-3-95450-186-1

but it is able to sustain the UHR. A plasma has been excited at $1.5 \cdot 10^{-4}$ mbar with increasing microwaves' power from 20 to 200 W. Experimental results, detailed in [10, 11], show that a largely overdense plasma has been obtained when microwaves' power overcomes 80 W. These results have been confirmed by measurement performed with both interferometry and LP diagnostics. In particular, interferometry gives an averaged plasma density value equal to: $n_e = 2.1 \pm 1 \cdot 10^{12}$ cm^{-3}. This value is four times larger than the average value measured - in exactly the same operative conditions - by means of the Langmuir probe, that resulted $n_e = 5.5 \pm 1.5 \cdot 10^{11}$ cm^{-3} (averaged value along the same line of sight). The discrepancy is probably due to the electromagnetic perturbation that the Langmuir probe (a metallic rod introduced in a compact resonator) generates within the plasma chamber, modifying the plasma features. Anyway, the values measured by interferometry and LP diagnostics are respectively ~ 10 times and~ 5 times larger than $n_{cut-off}$ at 3.7576 GHz, equal to $1.275 \cdot 10^{11}$ cm^{-3}. Table 1 summarizes the results of plasma density measurements.

Table 1: Results of Electron Density Measurements

	Electron density (cm^{-3})
Interferometry	$(2.1 \pm 1) \cdot 10^{12}$
LP diagnostics	$(5.5 \pm 1.5) \cdot 10^{11}$
$n_{cut-off}$ (at 3.76 GHz)	$1.75 \cdot 10^{11}$

Measurements of microwave power within the chamber [10] have shown EM waves do not propagate within the plasma bulk accordingly to measurements of plasma density (in overdense plasmas EM waves are reflected). However, selfconsistent simulations shown that plasma can be fed by EM waves propagating from the chamber walls towards the center, and thus orthogonal to the magnetic field lines (i.e. X and O waves). The plasma 2D imaging technique permitted to describe the radial plasma profile, by calculating the number of detected x-rays versus the chamber radius. This information enables us to calculate the η coefficient, in the hypothesis of wave propagating from the walls towards the plasma bulk.

Figure 3 shows the η coefficient, calculated by means of Eq. (2) and the normalized radial density, versus the plasma chamber radius. At the radial position of 35 – 50 mm, the η coefficient is in the range 0.20-0.25 (dark strip in the figure), a value which maximize the Budden conversion coefficient (Eq. (1)). These results lead to the conclusion that plasma is generated by the directed FX-B conversion, in Budden type scenario.

The fine tuning of the microwave frequency permit to find the best configuration in term of modal configuration within the chamber, favoring the conversion of larger amount of RF power, in the form of X waves, to Bernstein waves (modal dependent conversion). From a self-tuning point of view, also the density gradient assumes the value which maximizes FX-B conversion.

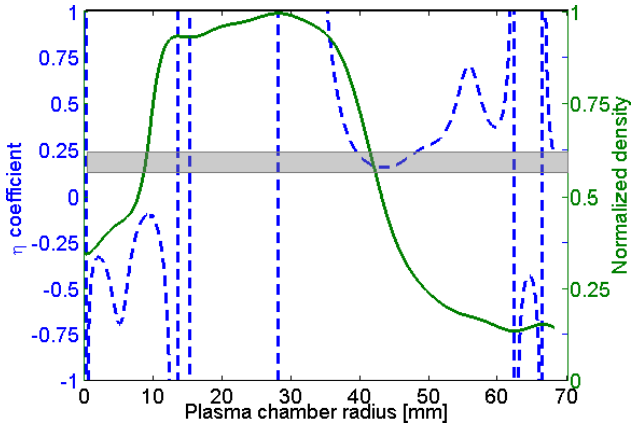

Figure 3: η coefficient and normalized density vs chamber radius.

The next goal of our research group is to force the conversion from EM to Bernstein waves without any influence of the plasma chamber modal behavior (modal independent conversion). The Flexible Plasma Trap (in commissioning at INFN-LNS) has been thought, developed and constructed with the aim to generate high density plasmas by means of novel plasma heating schemes. It is constituted by three coils generating different magnetic field profiles (maximum magnetic field is ~ 0.5 T). It is fed with microwaves in the range 3 – 7 GHz. A microwave launcher has been developed for a controllable (directional) launching of the pumping wave inside the plasma chamber, having specific angles with respect to the external magnetostating field. The launcher is placed orthogonally to the chamber axis, so it allows feeding O/X waves within FPT. The goal is to launch high frequency (14 GHz) microwaves inside a pre-formed plasma at 7 GHz or so, attempting to establish a high efficiency conversion scenario such as the OXB one. The first results of the new experimental campaign are expected in the next autumn.

ACKNOWLEDGEMENTS

The research leading to these results has received funding from the European Union Seventh Framework Program FP7/2007-2013 under Grant Agreement No. 262010 – ENSAR, and by INFN – 5th Nat. Comm. under the RDH and VESPRI experiments.

REFERENCES

[1] R. Geller, *Electron Cyclotron Resonance Ion Sources and ECR plasmas*, Taylor and Francis book, 1996.

[2] S. Gammino *et al.*, *Plasma Sources Sci. Technol.*, vol. 18, p. 045016, 2009.

[3] I. B. Bernstein, *Phys. Rev. Lett.*, vol. 10, p. 109, 1958.

[4] K. S. Golovanivsky, V. D. Dougar-Jabon, and D. V. Reznikov *Phys. Rev. E.*, vol. 52, p. 2969, 1995.

[5] K. Budden, *The Propagation of Radio Waves*, Cambridge: Cambridge University Press, 596-602, 1996.

[6] H. P. Laqua, *Plasma Phys. Control. Fusion*, C49, R1–R42, 2007.

ISBN 978-3-95450-186-1

[7] A. K. Ram, A. Bers, and C. N. Lashmore-Davies, *Phys. Plasmas*, 7, 4084–9, 2000.

[8] Y. Y. Podoba *et al.*, *Physical Review Letters* 98, 255003, 2007.

[9] L. Celona *et al.*, *Rev. Sci. Instrum.*, 87, 02A742, 2016.

[10] G. Castro *et al.*, "Overdense plasma generation in a compact ion source", submitted for publication.

[11] D. Mascali *et al.*, "The first measurement of plasma density in an ECRIS-like device by means of a frequenecy-sweep microwave interferometera", paper accepted for publication by *Rev. Sci. Instrum.*

[12] D. Mascali *et al.*, *Rev. Scie. Instrum.*, 85, 02A956, 2014.

ISBN 978-3-95450-186-1

CAVITY TUNING EXPERIMENTS WITH THE JYFL 14 GHz ECRIS *

O. Tarvainen†, T. Kalvas, H. Koivisto, R. Kronholm, J. Laulainen, J. Orpana
University of Jyväskylä, Jyväskylä, Finland
V. Toivanen
European Organization for Nuclear Research (CERN), 1211 Geneva 23, Switzerland
I. Izotov[1], V. Skalyga[1]
Institute of Applied Physics, RAS, 46 Ul'yanova St., 603950, Nizhny Novgorod, Russian Federation
[1]also at Lobachevsky State University of Nizhny Novgorod (UNN), 23 Gagarina St., 603950
Nizhny Novgorod, Russian Federation

Abstract

Experimental results showing the effect of cavity tuning on oxygen beam currents extracted from the AECR-type JYFL 14 GHz ECRIS are reported. The microwave-plasma coupling properties of the ion source were adjusted by inserting a conducting tuner stub through the injection plug, thus changing the dimensions of the plasma chamber and affecting the cavity properties of the system. The beam currents of high charge state ions were observed to vary up to some tens of percent depending on the tuner position and the microwave frequency. In this paper we focus on reporting results obtained in the frequency range of 10.75–12.75 GHz.

INTRODUCTION

Experiments with 2nd generation ECR ion sources have demonstrated that the beam currents of high charge state ions are sometimes sensitive to microwave frequency variations on the order of 10 MHz [1, 2]. The effect has been ascribed to frequency dependent electromagnetic field pattern over the resonance surface [3,4], i.e. excitation of cavity modes, and named frequency tuning effect (FTE). This explanation, however, has two significant shortcomings: (1) the electromagnetic properties of the cavity are strongly affected by the plasma [5], thus obscuring the mode structure, and (2) only Caprice-type ion sources [6] exhibit strong frequency dependence while the performances of A-ECR type sources [7] are less sensitive to FTE. The most significant difference between the two source types is the microwave coupling scheme. In Caprice-type sources the microwave power is launched into the plasma chamber through an external waveguide-to-coaxial transition component equipped with a stub tuner for impedance matching. In the AECR-type sources the microwave-plasma coupling is realized through a waveguide port inserted directly into the plasma chamber, hence making the A-ECR design less complex. These microwave coupling structures are presented in Fig. 1 [8].

It can be argued that the observed differences between the source types could be explained solely by the sensitivity of the microwave-plasma coupling system on the frequency variations, not by the excitation of cavity modes. Thus, probing the source performance by varying the frequency of the microwave radiation is not the optimal technique to detect the existence of possible cavity modes and to study their effect on the high charge state ion beams. This is because both, the microwave launching system and the (possible) cavity modes are sensitive to frequency variations. The cavity modes and their Q-values are determined by the dimensions and surface properties of the plasma chamber. Thus, a preferred technique to probe the existence of the cavity modes and their influence on the source performance is to change the dimensions of the plasma chamber while keeping the microwave frequency constant. Such experiments probing the *cavity tuning effect* (CTE) of an A-ECR-type ion source operating in the frequency range of 14.00–14.15 GHz have been reported recently [9]. It was shown that the extracted currents of the high charge state ions can be increased only moderately (<10 % for O^{6+}) by tuning the cavity properties of the plasma chamber. Since the frquency range probed in Ref. [9] is rather narrow, the CTE was studied further in a wider range of frequencies as described in the following sections.

EXPERIMENTAL SETUP

The experimental data discussed hereafter were taken with the JYFL 14 GHz ECRIS [10] (see Fig. 2), which is a typical A-ECR-type room-temperature ion source. The plasma chamber of the JYFL 14 GHz ECRIS has an inner diameter of 76.2 mm and length of 278 mm and is made of aluminum. The cylindrical symmetry of the chamber is broken by two waveguide ports (WR62 and WR75) and radial pumping holes between each magnetic pole of the sextupole. Furthermore, the cavity properties are affected by ϕ =21 mm biased disc and ϕ =8 mm plasma electrode aperture. In the present study the cavity dimensions were modified by inserting a cylindrical (ϕ =15 mm) water-cooled copper rod shown in Fig. 2 into the plasma chamber through the opening in the injection plug, normally used as a port for a miniature oven. The rod was connected electrically to the plasma chamber and its position was adjusted online by using a linear feedthrough without compromising the vacuum or switching off the microwave power or the high voltage while monitoring the extracted beam currents. The rod position was varied from 0 mm, corresponding to the

* Work supported by the EU 7th framework programme 'Integrating Activities — Transnational Access', project number: 262010 (ENSAR), the Academy of Finland under the Finnish Centre of Excellence Programme 2012–2017 (Nuclear and Accelerator Based Physics Research at JYFL).
† olli.tarvainen@jyu.fi

ISBN 978-3-95450-186-1

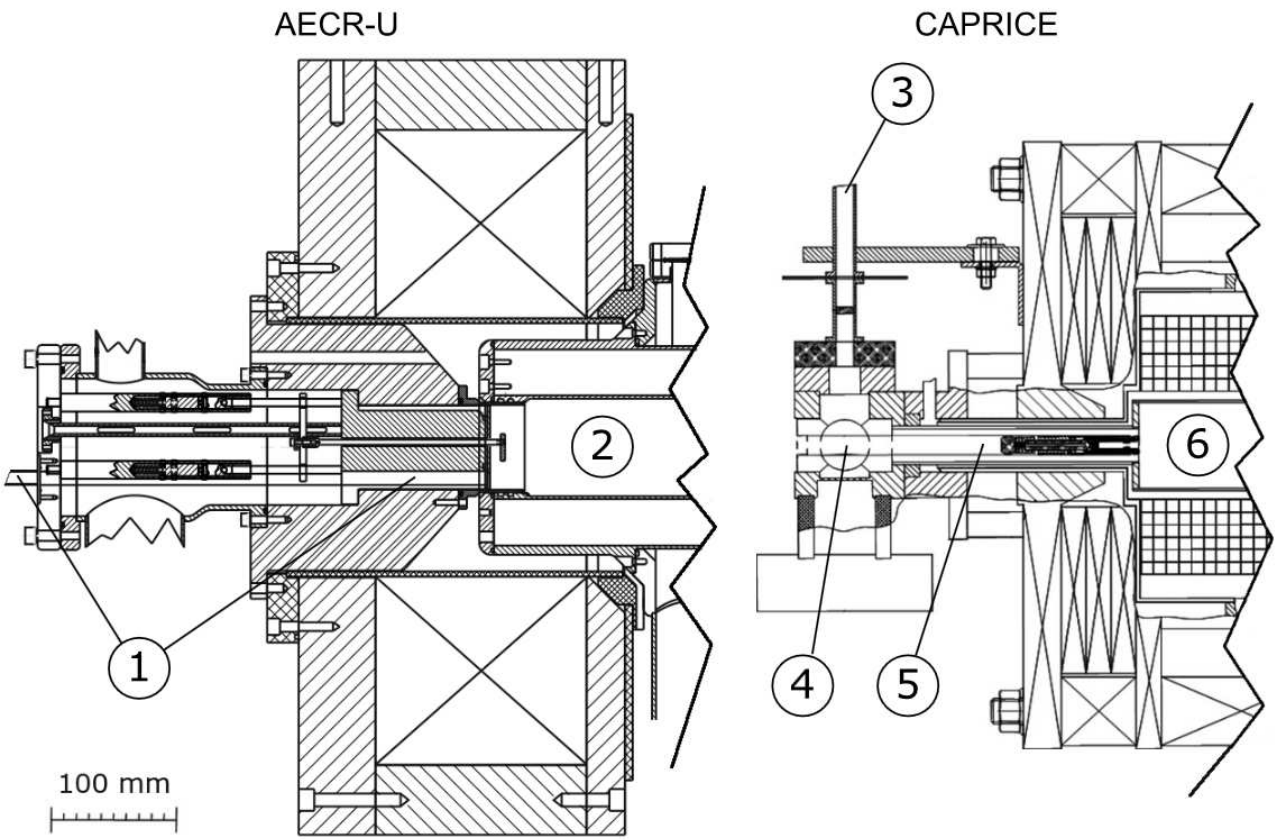

Figure 1: Comparison of the microwave coupling schemes of JYFL 14 GHz AECR-U and GSI Caprice ECR ion sources. AECR-U: (1) rectangular waveguide (WR62 / WR75), (2) plasma chamber. Caprice: (3) rectangular waveguide, (4) tunable matching cavity, (5) coaxial transmission line, (6) plasma chamber. The figure is borrowed from Ref. [8].

tip of the rod being aligned with the plane defined by the plasma facing surface of the biased disc, to 50 mm corresponding to the rod being inserted further into the plasma chamber. It was observed that the tip of the tuner rod was in contact with one of the plasma flutes at a distance of 60 mm and, therefore, the linear motion of the rod was restricted to 50 mm where no outgassing from the rod surface was observed. The arrangement allows tuning the cavity properties without affecting plasma losses or the magnetic mirror ratios.

The cavity properties were initially studied experimentally with a Rohde&Schwarz 9 kHz–15 GHz vector network analyzer that was used for measuring the output return loss, hereafter referred as the S11-parameter, of the waveguide system in the frequency range of 10.75–12.75 GHz corresponding to the bandwidth of the TWT amplifier connected to the WR75 port. The effect of the tuner position on the S11-parameter was first studied with an empty cavity. The experiment was then repeated with the ECR plasma being sustained by microwave radiation (at 14.053 GHz) provided by the klystron amplifier connected to the WR62 waveguide port. In this experiment the network analyzer connected to the TWTA waveguide (WR75 port) was protected from transmitted power with a low-pass filter. The power applied for sustaining the plasma was varied and the effect of the tuner position on the S11-parameter within the TWTA bandwidth was studied at different microwave powers presumably corresponding to different plasma densities. Measurement of the S11-parameter allowed distinguishing certain frequencies of interest, which were then used in the experiments studying the effect of the tuner position on the extracted beam currents of oxygen charge states O^{3+} – O^{7+} in single frequency heating mode with the TWTA. The beam currents were measured from a Faraday cup located downstream from a 90 degree m/q-analyzing magnet. The source potential was set to 10 kV, which is a typical value for the operation of the JYFL 14 GHz ECRIS. The currents of O^{+} and O^{2+} were not measured because their magnetic rigidity, resulting from the 10 kV source potential, is too high for these charge states to be transported through the bending magnet. On the other hand decreasing the source potential is not desired as the transport efficiency of the low energy beamline would become rather poor at values $\leq$ 7.5 kV potentially skewing the results. Since the parameter space of ECRIS optimization is extensive, the microwave power, oxygen feed rate and biased disc voltage were kept constant throughout the experiment. The (solenoid) magnetic field strength was optimized for each microwave frequency with the tuner fully retracted (at 0 mm) and then kept constant while moving the tuner inwards.

ISBN 978-3-95450-186-1

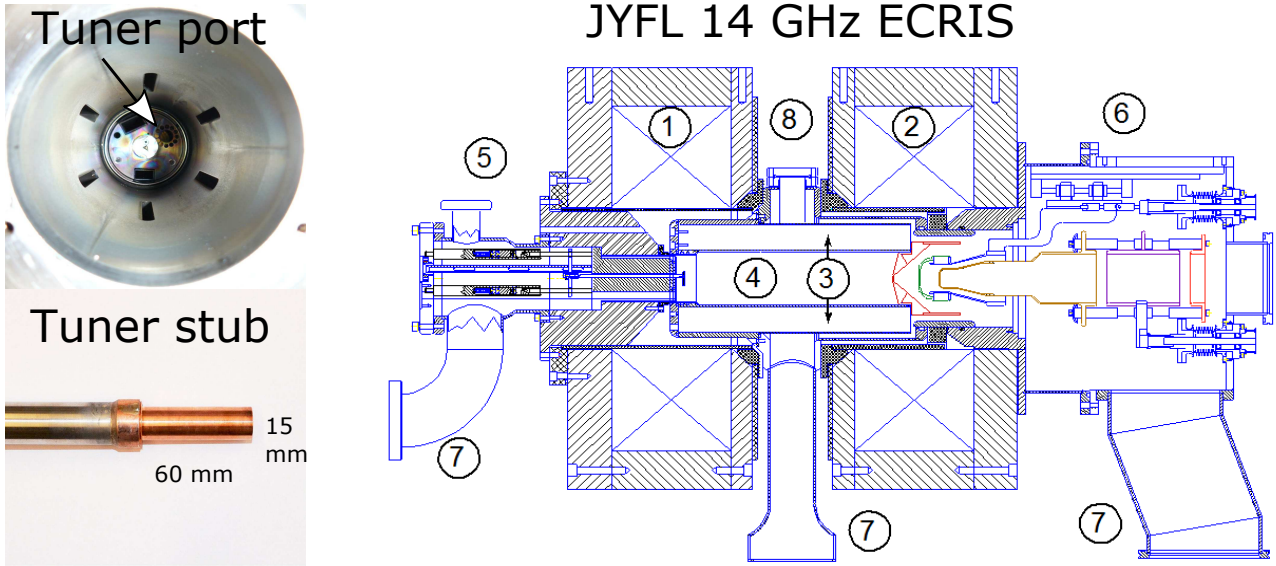

Figure 2: The JYFL 14 GHz ECRIS and the tuner used in the cavity tuning experiments: (1) injection coil (2) extraction coil (3) permanent magnet sextupole (4) plasma chamber (5) iron plug, biased disc, waveguide ports and oven (tuner) port, (6) extraction system, (7) vacuum pumping and (8) radial port (vacuum gauge). The location of the tuner port is shown in the upper left subfigure where the injection plug of the ECRIS is viewed from the extraction.

EXPERIMENTAL RESULTS

The Effect of Cavity Tuning on the S11-Parameter

Figure 3 is an example showing the empty cavity S11-parameter measured from the WR75 port (including the plasma chamber, vacuum window, high voltage break and short section of the waveguide) as a function of the tuner position in a narrow microwave frequency range of 11.70–11.85 GHz. The periodic ripple that is practically immune to the tuner position and dominates the frequency response of the S11-parameter is due to excitation of waveguide modes. The tuner effect is responsible for the seemingly random variation superimposed on the periodic structure, best observed at approximately 11.76 and 11.83 GHz. The implication of Fig. 3 is that studying the excitation of cavity modes and the subsequent effect on the electron heating by varying only the frequency is virtually impossible due to the dominance of the waveguide system.

The presence of the plasma affects the cavity behavior significantly as demonstrated in Fig. 4 showing the S11-parameter as a function of the tuner position at 11.70–11.85 GHz with the plasma sustained by 100 W power at 14.053 GHz. It was observed that already at 2 W of power from the klystron was sufficient to suppress the effect of the tuner position on the S11-parameter. The value of the S11-parameter at each frequency is defined by the combined effect of the short waveguide section, vacuum window, high voltage break and the plasma chamber. However, it is clearly seen that the presence of the plasma obscures the S11-behavior observed with the empty cavity. In the presence of the plasma the number of the S11-parameter minima in the given frequency range is determined by the length of the remaining waveguide i.e. the influence of the cavity is

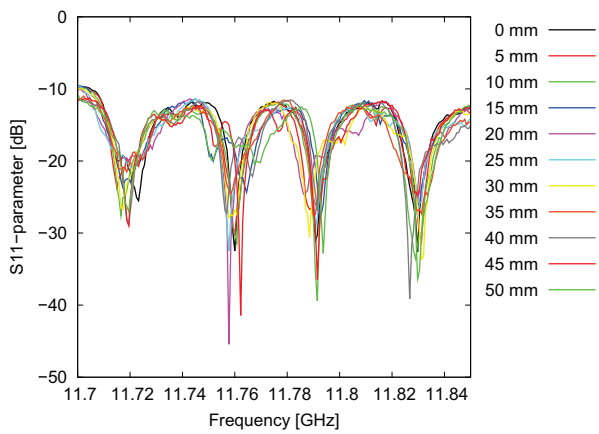

Figure 3: The empty cavity S11-parameter as a function of the microwave frequency at several tuner positions.

effectively suppressed. Although Figs. 3 and 4 only demonstrate the effect of the plasma in a narrow frequency range, similar observation was made for the complete frequency range of the TWTA.

The Effect of Cavity Tuning on Oxygen Beam Currents

The effect of the tuner position on the extracted currents of different charge states of oxygen was studied at several frequencies within the range of 10.75–12.75 GHz. The frequencies were chosen based on the measurement of the S11-parameter i.e. the m/q-spectra were recorded at those frequencies where the empty cavity S11-parameter was observed to be sensitive to the tuner position throughout the adjustment range of the tuner.

ISBN 978-3-95450-186-1

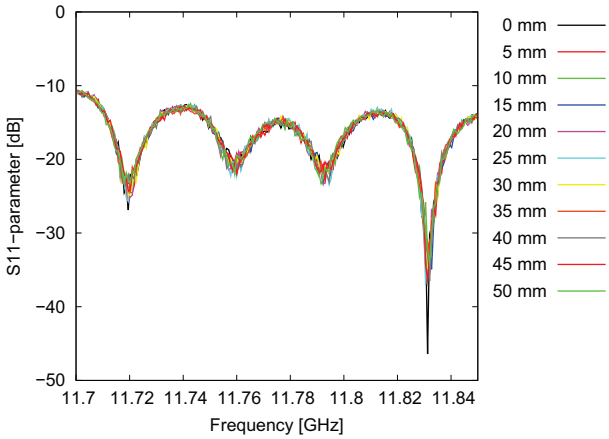

Figure 4: The S11-parameter in the presence of the plasma, sustained by 100 W power at 14.053 GHz, as a a function of the microwave frequency at several tuner positions.

Figure 5 shows the recorded m/q-spectra at 11.56 GHz. The microwave power was kept constant at 150 W (typical for the TWTA operation of the JYFL 14 GHz ECRIS) while all the other source parameters, i.e. magnetic field, gas pressure, bias disc voltage and extraction optics were first optimized for the charge state O^{6+} with the tuner at 0 mm. The data were chosen for display because they represent the frequency at which the source performance was found to be most sensitive to the tuner position within the studied range. Three different m/q-spectra are shown - the tuner fully retracted (0 mm), and at tuner positions corresponding to minimum and maximum O^{6+} current obtained at the given frequency. It is clear from the figure that the tuner position affects the charge state distirbution.

The (temporally averaged) O^{6+} currents obtained at each studied frequency and tuner position are displayed in Fig. 6. It can be seen that the O^{6+} current is affected at all frequencies by several tens of percent depending on the tuner position. At 11.56 GHz the current was observed to vary +15 / –40 % in comparison to the baseline (tuner at 0 mm). This is partially explained by the fact that varying the tuner position makes the plasma prone seemingly arbitrary hopping between two modes at irregular intervals, which can suppress the average currents of the high charge states by several tens of percent. It was observed that the susceptibility of the plasma to the 'mode-hopping' depends on the frequency. For example, at 10.91 GHz there were no signs of the phenomenon while at 11.56 GHz mode transitions were observed consistently with the tuner positions of 25–35 mm and 45–50 mm, which explains the large (up to 40,%) variation of the high charge state currents in the latter case.

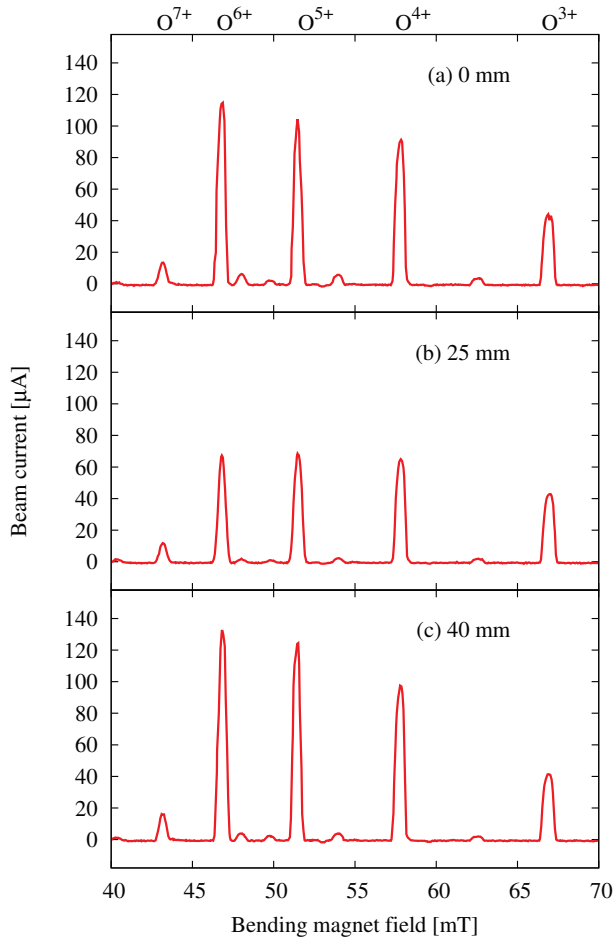

Figure 5: The m/q-spectrum of oxygen recorded with 150 W at 11.56 GHz at the tuner positions of (a) 0 mm with 115 μA of O^{6+}, (b) 25 mm with 69 μA of O^{6+} (minimum) and (c) 40 mm with 132 μA of O^{6+} (maximum).

DISCUSSION

The experimental results and conclusions can be summarized as follows:

- The charge state distribution of extracted oxygen beam can be affected by the tuner position.
- The optimum tuner position depends on the microwave frequency.
- The extracted currents of the high charge state ions can be increased moderately (≥20 % for O^{6+}) in comparison to the baseline, i.e. tuner at 0 mm, by optimizing the tuner position when operating in the frequency range of 10.75 – 12.75 GHz.
- Varying the tuner position makes the plasma prone to being unstable, which explains the shift of the charge state distibution in some cases.
- The S11-parameter can not be considered as a good indicator of the source performance as a function of the tuner position. The presence of the plasma even at low density makes the S11-parameter insensitive to the tuner position although the tuner clearly affects the charge state distribution.

The experimental results and conclusions are largely similar to those reported in Ref. [9] for the (klystron) frequency

ISBN 978-3-95450-186-1

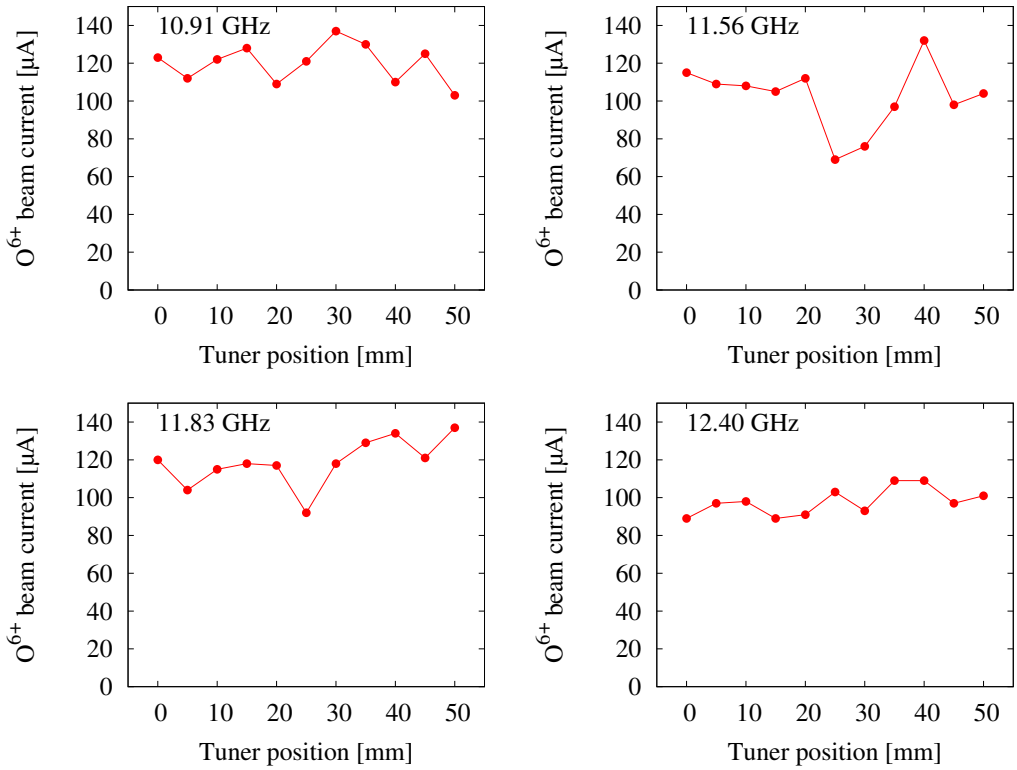

Figure 6: Temporally averaged O^{6+} beam currents as a function of the tuner position at different microwave frequencies with 150 W power.

range of 14.00–14.15 GHz. The variation of the high charge state beam currents (e.g. O^{6+}) was found to be more significant in operation with the TWTA at 10.75–12.75 GHz. This is probably be due to lower power (plasma density) operation with the TWTA with approximately 150 W maximum power across the frequency band. At lower power even a small change in the microwave-plasma coupling efficiency could drastically change the source performance whereas at high power the extracted beam currents of the JYFL 14 GHz ECRIS tend to saturate and, therefore, variations of the coupling efficiency are not as pronounced. It is, nevertheless, concluded that cavity tuning affects the plasma properties of the ECRIS. This is most likely due to modified electric field structure.

It must be emphasized that the ECRIS plasma is a dynamic load, i.e. the electric field configuration is affected by the plasma properties, which are driven by the electron heating (electric field) and ionization (neutral gas density and species). Thus, it could be expected that attempts to optimize the source performance by optimizing the electric field configuration (cavity mode) would inevitably result to unstable operation due to strong feedback loop. As already described, such mode-hopping effect was observed for certain frequency / tuner position combinations. Furthermore, it was demonstarted that the S11-parameter is not a good measure for the source performance and should not be used for probing the frequency response of the microwave-plasma coupling.

REFERENCES

[1] L. Celona *et al.*, *Rev. Sci. Instrum.* 79, 023305 (2008).

[2] F. Maimone, L. Celona, R. Lang, J. Mäder, J. Roßbach, P. Spädtke, and K. Tinschert, *Rev. Sci. Instrum.* 82, 123302 (2011).

[3] F. Consoli, L. Celona, G. Ciavola, S. Gammino, F. Maimone, S. Barbarino, R.S. Catalano, and D. Mascali, *Rev. Sci. Instrum.* 79, 02A308 (2008).

[4] L. Celona, S. Gammino, G. Ciavola, F. Maimone, and D. Mascali, *Rev. Sci. Instrum.* 81, 02A333, (2010).

[5] V. Toivanen, O. Tarvainen, C. Lyneis, J. Kauppinen, J. Komppula, and H. Koivisto, *Rev. Sci. Instrum.* 83, 02A306 (2012).

[6] B. Jacquot, F. Bourg, and R. Geller, *Nucl. Instr. and Meth.* A 254 (1987) 13.

[7] D. J. Clark, C.M. Lyneis, and Z.Q. Xie, 14th Particle Accelerator Conference (PAC), IEEE Conference 91 CH3038-7 (1991), unpublished.

[8] V. Toivanen, "Studies of Electron Cyclotron Resonance Ion Source Beam Formation, Transport and Quality", Doctoral thesis, University of Jyväskylä, ISBN 978-951-39-5286-0, (2013).

[9] O. Tarvainen, J. Orpana, R. Kronholm, T. Kalvas, J. Laulainen, H. Koivisto, I. Izotov, V. Skalyga, and V. Toivanen, accepted for publication in *Rev. Sci. Instrum.*, (2016).

[10] H. Koivisto, P. Heikkinen, V. Hänninen, A. Lassila, H. Leinonen, V. Nieminen, J. Pakarinen, K. Ranttila, J. Ärje, and E. Liukkonen, *Nucl. Instrum. Methods* B 174, (2001), p. 379.

ISBN 978-3-95450-186-1

RECENT BREMSSTRAHLUNG MEASUREMENTS FROM THE SUPERCONDUCTING ELECTRON CYCLOTRON RESONANCE ION SOURCE VENUS

J. Y. Benitez#, C. M. Lyneis, L. W. Phair, D. S. Todd, D. Z. Xie
LBNL, Berkeley, CA 94720, USA

Abstract

Axial bremsstrahlung from the superconducting Electron Cyclotron Resonance ion source VENUS have been systematically measured as a function of RF heating frequency, and the axial and radial field strengths. The work focuses on bremsstrahlung with energies greater than 10 keV to extract the spectral temperature T_s. The three axial coils and the radial coils in the superconducting VENUS can all be set independently and have a large dynamic range, which makes it possible to decouple B_{min} and ∇B_{ECR} and study their effects on the bremsstrahlung independently. With typical pressure and RF power levels, the measurements show that T_s depends approximately linearly on B_{min} and is not correlated with the ∇B_{ECR}, the magnetic field mirror ratios, or the RF frequency. These results are important for the next generation of ECR ion sources, which are designed to operate at frequencies above 40 GHz and significantly higher magnetic fields where bremsstrahlung is expected to cause a significant cryogenic heat load and increase the radiation shielding requirements.

INTRODUCTION

Electron Cyclotron Resonance Heating (ECRH) is an efficient method to couple microwave energy into the plasma electrons. Use of ECRH to generate plasma began with the early mirror machines developed by the plasma fusion community and later as a spin-off in the high charge state ECR ion sources, ECRIS, initially developed by R. Geller in the 1970's [1]. VENUS is the first 3rd generation ECR ion source using both 18 and 28 GHz microwave power to produce a plasma with electrons of sufficient energy to produce high charge states such as Ar^{18+} [2], Xe^{43+}, and U^{50+} [3]. The ionization potential for these highly-charged ions is in the range of 2 to 5 keV and the maximum cross section for electron impact ionization occurs at three to five times those energies or approximately 6 to 25 keV. VENUS produces plasma with electrons of maximum energy up to several hundred keV as is evidenced in the hot tail of the emitted bremsstrahlung. The existence of the electron hot tail has been observed in both simple mirror machines for fusion research in the 60's [4] and in the minimum B magnetic field structures used in modern high charge state ECR ion sources [5].

The performance of high charge state ECR ion sources scales roughly with the square of RF heating frequency, as predicted by R. Geller [6]. The third generation ECRIS operating at either 24 or 28 GHz [2, 7-9] are presently the best performers. These sources operate at higher magnetic fields than earlier generation sources operating at frequencies of 18 GHz or lower. The third generation ECRIS also produce significantly more intense and more energetic bremsstrahlung. The high energy bremsstrahlung adds a thermal load to the cryogenic system for superconducting ECRIS because the high energy x-rays (~ E > 300 keV) easily pass through the plasma chamber and outer wall of the cryostat and then are absorbed in the cold mass [5]. The fourth generation sources currently being developed will operate at higher magnetic fields with heating frequencies above 40 GHz [10]. It is anticipated that the next generation source will produce even more intense and energetic hot electrons and therefore methods to understand, control, or reduce the bremsstrahlung production are needed. This research explores which ECRIS parameters including magnetic field geometry and microwave frequency affect the production of bremsstrahlung and the spectral temperature T_s obtained from it.

#jybenitez@lbl.gov

EXPERIMENTAL SETUP

VENUS uses three superconducting solenoids and one superconducting sextupole to generate the minimum-B magnetic field configuration to confine the plasma, as shown in Figure 1. Each coil is independently powered and the axial fields can produce up to 4 T at injection, 3T at extraction and a center coil that can produce a B_{min} value from 0 to 2 T. The sextupole coils can produce up to 2.2 T on the plasma wall at a radius of 72 mm and the radial field generated by the sextupole is typically set to values close to the peak axial field at extraction. This produces a closed resonance field at 2T or twice B_{ECR} at 28 GHz [11].

The central field can be lowered sufficiently so there are simultaneous resonance fields for 14, 18 and 28 GHz. The VENUS microwave system consists of a 2 kW 18 GHz klystron and a 10 kW 28 GHz gyrotron. A 2 kW 14 GHz klystron was also used briefly to test the frequency dependence of the spectral temperature.

The axially emitted bremsstrahlung spectra from VENUS were recorded using an Amptek XR-100-CdTe X-Ray and Gamma Ray diode detector [12]. It consist of a 1 mm thick, 25 mm^2 detector that sits behind a 4 mil Be window. Its resolution at 122 keV is < 1.5 keV FWHM, which is not as good as Si diode detectors. However, the CdTe detectors are much more sensitive at energies above 20 keV as they have a higher stopping power with shorter attenuation lengths [13]. In addition, the XR-100-CdTe detector has the advantage that it can be operated in vacuum, without attenuation caused by windows.

ISBN 978-3-95450-186-1

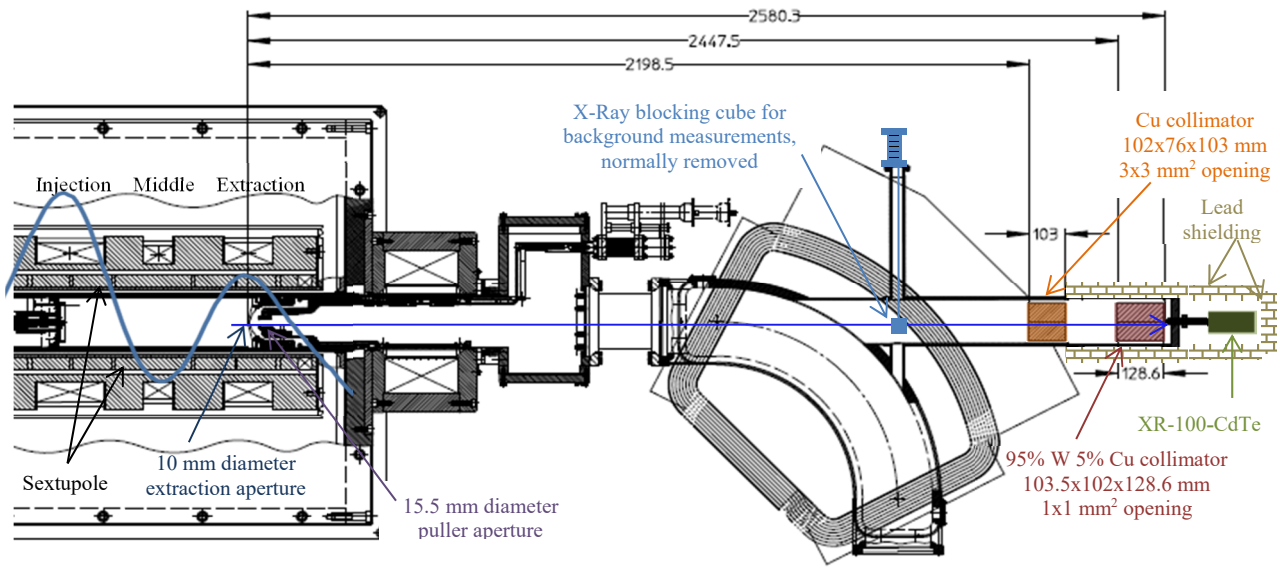

Figure 1: Schematic of the experimental setup of the XR-100-CdTe detector at the VENUS ion source. All units in mm.

From 4 keV to 80 keV the intrinsic efficiency, a ratio of the number of pulses recorded by the detector to the number of gamma rays hitting the detector, with the window taken into account, is above 80%. However, this paper includes x-rays measured between 10 keV to 300 keV. Between 80 keV and 300 keV the efficiency drops gradually to 10%. All spectra shown have been corrected for detector intrinsic efficiency which includes the correction for the 4 mil beryllium window on the detector. The detector's intrinsic efficiency was verified using various radioactive sources with known activities and compared well to that quoted by the manufacturer and this was used to make the corrections. The detector sits on the optical axis, in line with the extraction electrode center, and inside the vacuum chamber, as shown in Figure 1. Therefore, no corrections due to attenuation in air or through a window are necessary. The spectra are not corrected for the detector's photopeak efficiency, the probability of producing a full-energy peak. The detector's energy was calibrated used standard radioactive sources with known gamma lines.

Between the detector and the extraction aperture is a set of two collimators. The first sits directly up against the detector face and is a heavy metal (95% W and 5% Cu) block. It is 128.6 mm long and has a 1 mm square groove. The second collimator is 146 mm upstream of the first collimator and is solid Cu. It is 102 mm long with a 3 mm square groove. This corresponds to a square with 20 mm sides at the extraction electrode that is visible to the detector. The VENUS ion source has an aluminium extraction electrode. It is important to note that midway through the measurements, which spanned several months, the 10 mm diameter extraction aperture was replaced with a slightly thicker aluminium electrode at the aperture opening to improve heat transfer and prevent melting it. Analysis of spectra recorded before and after show that this only affected their shapes at the low energy end that is not considered in this paper. Although the new electrode decreases the total counts by up to 50%, the slope of the spectra in the energy range between 80 and 300 keV did not change.

The spectral temperature, T_s, is obtained from the recorded bremsstrahlung by fitting a straight line to the semi-logarithmic representation of the spectra over a selected energy. For this paper the energy range was approximately 80-120 keV. The T_s, taken as the reciprocal of the line's slope, is an indirect measure of the energy distribution of the plasma electrons and is used to characterize the temperature distribution and relative hot electron density in high charge state ECR plasma. This spectral temperature is not a direct measure of the electron energy distribution of the hot electrons in the plasma.

An x-ray blocking cube, shown in Figure 1 was installed to measure the background reaching the detector from outside the collimator apertures. When the 22 mm side cube, made from a tantalum-niobium alloy, is inserted, it blocks the x-rays from entering the collimators and reaching the detector. The remaining x-rays detected are indirectly scattered bremsstrahlung and can be subtracted as a background. The background spectrum below 100 keV is negligible but it does contribute a large percentage of the counts at higher energies and this affects the spectral temperature extracted from the data. When the background is subtracted from the original spectra, the spectral temperature is reduced by 2% to 20%.

EXPERIMENTAL RESULTS

Experiment Design

Aside from the magnetic field configuration and heating frequency the measurements were made with similar parameters through all data sets. All data was recorded at

ISBN 978-3-95450-186-1

a power level of 1000W, measured at the transmitter, for 14, 18, or 28 GHz heating frequency, and at similar oxygen gas pressure and bias disk voltage. The power was limited to 1000W to avoid unstable plasmas that can generate large fluctuations in the bremsstrahlung output. However, it was verified that T_s remained relatively constant up to a power level of 9000W as shown in Figure 2.

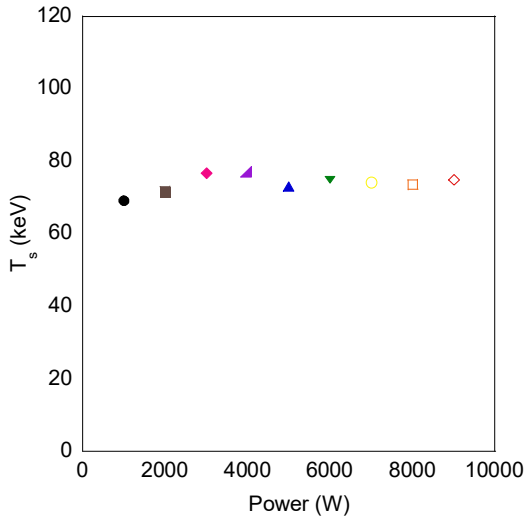

Figure 2: T_s obtained show essentially no change with increasing power from 1000 to 9000W at a fixed magnetic field configuration.

We focused on how the magnetic configuration and microwave heating frequencies affect the axial bremsstrahlung and resulting spectral temperature. The investigation was divided into three main sections. First, B_{min} was varied while the gradient at the resonance zone B_{ECR} was held approximately constant. Second, the gradient at the resonance zone B_{ECR} was varied while B_{min} was held constant. Third, we also compared spectra recorded at a fixed magnetic field configuration for three different heating frequencies.

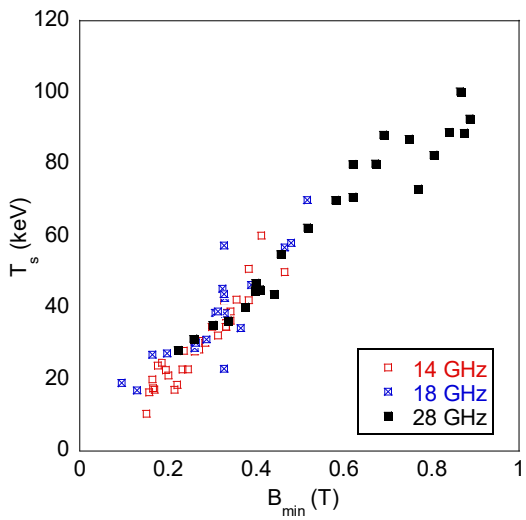

Figure 3: All data collected for VENUS is summarized in this table where T_s is plotted versus B_{min}.

The gradient at the resonance zone B_{ECR}, henceforth written as ∇B_{ECR}, is calculated on axis. Figure 3 shows graphically a summary of the measurements in which the T_s for all collected data is plotted versus the minimum center field B_{min} for three different independently used heating frequencies of 14, 18 and 28 GHz, at various field configurations and gradients. This summary plot clearly shows that the hot electron T_s depends linearly on B_{min} and does not depend on the RF heating frequency.

Constant Gradient at B_{ECR} while Varying B_{min}

In the first part of the investigation we held ∇B_{ECR} approximately constant and varied B_{min} for the three heating frequencies. For the case of 18 GHz heating, ∇B_{ECR} was varied by 9.1% while B_{min} was varied by 59.4%. The parameters used for 18 GHz heating are listed in Table 1. Also listed are the field parameters for the case of 28 GHz heating, in which ∇B_{ECR} was varied by 12.9% while B_{min} was varied by 81.8%. It is seen when ∇B_{ECR} is held approximately constant and B_{min} is varied this changes T_s significantly. The experiment was also done with 14 GHz heating frequency and similar results were seen. Figure 4 show the magnetic field configuration and T_s versus B_{min} for the 28 GHz settings.

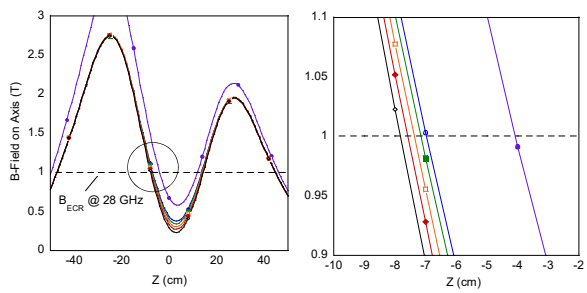

a.)

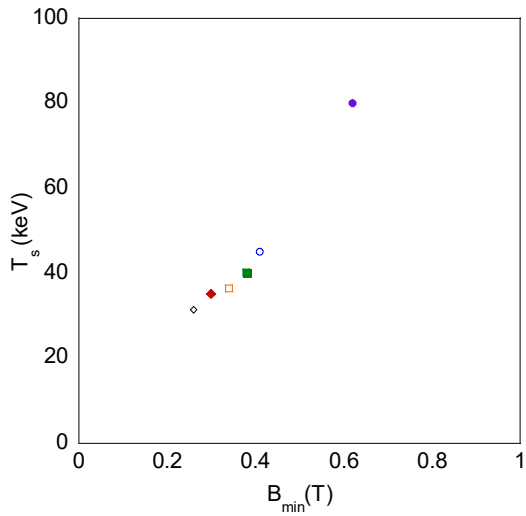

b.)

Figure 4: Using 28 GHz heating frequency a.) axial magnetic fields on axis for quasi-constant gradient at the resonance zone and b.) spectral temperatures.

ISBN 978-3-95450-186-1

Table 1: Magnetic Field Settings with Approximately Constant Gradient at the Resonance Zone and Variable B_{min} for 18 and 28 GHz Heating

f (GHz)	B_{min} on axis (T)	Inj. ∇B_{ECR} (T/m)	Ext. ∇B_{ECR} (T/m)	Ts (keV)
18	0.26	-7.5	6.77	30.2
	0.31	-8.16	6.44	38.9
	0.33	-7.64	7.03	38.5
	0.36	-7.54	6.44	46.6
	0.38	-7.45	6.32	55.0
	0.48	-7.71	6.54	58.0
28	0.26	-12.66	10.98	31.3
	0.30	-12.44	10.75	35.2
	0.34	-12.29	10.62	36.4
	0.38	-12.05	10.09	40.2
	0.41	-11.15	9.88	45.1
	0.62	-11.13	8.74	80.0

Constant B_{min} while Varying Gradient at B_{ECR}

In the second part of the investigation we held B_{min} constant and varied ∇B_{ECR} for 14 and 18 GHz. Figure 5a illustrates how ∇B_{ECR} was varied while maintaining a constant B_{min} for the 14 GHz tests. For 14 GHz heating, in order to vary ∇B_{ECR} the injection and extraction fields were varied from 1.64 T to 2.14 T and 1.07 T to 1.45 T, respectively. The minimum field and radial field were held constant and were 0.26 T and 1.0 T, respectively.

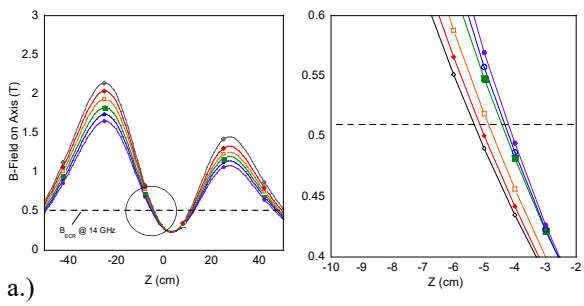

a.)

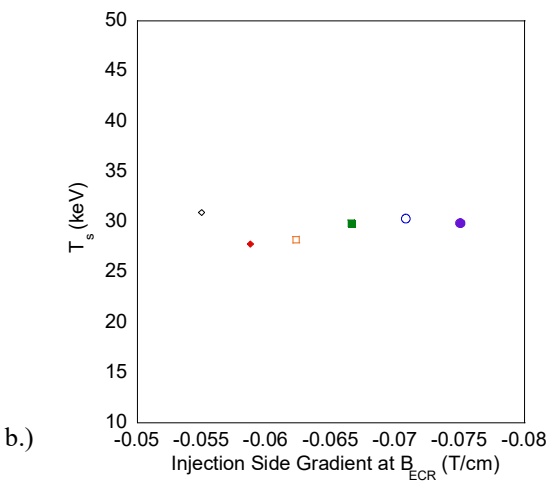

b.)

Figure 5: Using 14 GHz heating frequency a.) axial magnetic fields on axis when varying the gradient at the resonance zone and b.) spectral temperatures.

Column 5 of Table 2 shows that there is little variation in the spectral temperature while the gradient at injection is varied by 24% and at extraction by 20.6%. Figure 5b shows the resulting T_s versus B_{min} for the 14 GHz settings. For 18 GHz the injection and extraction fields were varied respectively from 1.67 T to 2.90 T and 1.14 T to 1.93 T, while minimum axial field and radial field were held constant at 0.33 T and 1.29 T, respectively. The spectral temperatures obtained using 18 GHz heating do not vary by more than 17% while the gradient at the injection was varied by 36%. The experiment was also done with 28 GHz heating frequency and similar results were seen.

Table 2: Magnetic Field Settings for Constant B_{min} While Varying Field Gradients at the Resonance Zone for 14 and 18 GHz Heating

f (GHz)	B_{min} on axis (T)	Inj.∇B_{ECR} (T/m)	Ext.∇B_{ECR} (T/m)	Ts (keV)
14	0.26	-6.3	5.09	30.9
	0.26	-5.94	5.40	27.8
	0.26	-6.30	5.40	28.2
	0.26	-6.69	5.66	29.9
	0.26	-7.15	6.14	30.3
	0.26	-7.58	6.26	29.9
18	0.33	-7.24	6.16	42.8
	0.33	-7.64	7.03	43.8
	0.33	-8.91	7.65	38.4
	0.33	-9.25	8.41	45.3

Comparison of Different Frequencies with Fixed Magnetic Field Values

Spectra were recorded at the same magnetic field configuration with each heating frequency 14, 18, and 28 GHz. Figure 6b shows spectra for a fixed magnetic field configuration. The shape of the spectra do not depend on the heating frequency used, although the count rate differs. For all spectra the RF power was set to 1 kW at the exit of the klystron or gyrotron. There was a mismatch in between the 14 GHz klystron and VENUS plasma chamber resulting in about 10% reflected power. However, our tests show that the spectral temperature was insensitive to small differences in RF power levels. While the magnetic field configuration was kept constant, for different heating frequencies this results in significantly different gradients at each resonance zone as shown in Table 3. For example in this test ∇B_{ECR} at injection changes from -4.67 T/m at 14 GHz to -12.75 T/m and the spectral temperature remain approximately constant. This supports the idea that the spectral temperature is not correlated with the value of the magnetic field gradient at resonance. Although only one set of measurements is presented, it was shown true for several configurations.

ISBN 978-3-95450-186-1

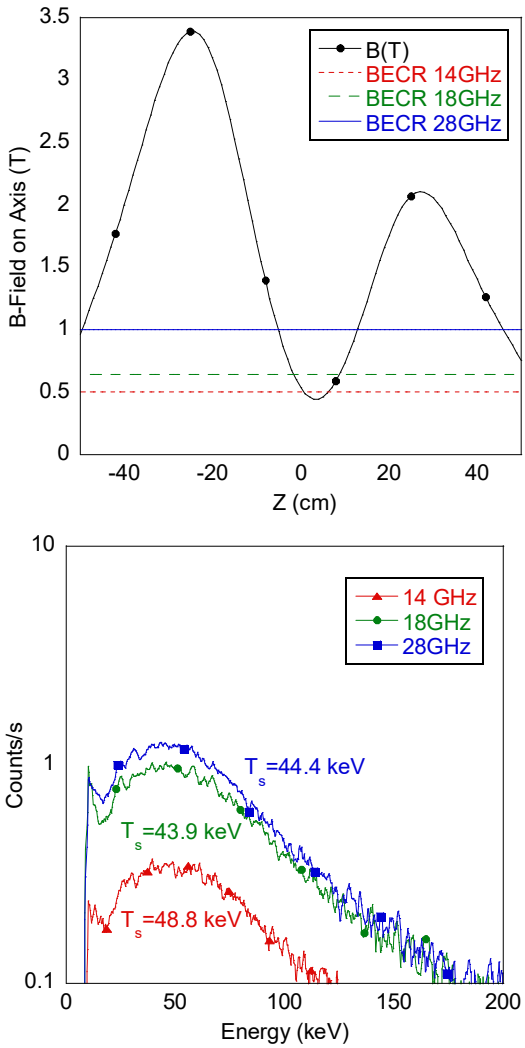

Figure 6: a.) Axial magnetic field on axis used for spectra recorded at 14, 18, and 28 GHz heating frequency. b.) Resulting spectra.

Variation of the Radial Magnetic Field

The radial field was also varied to see its effect on the spectral temperature. VENUS is typically operated with the radial field at the wall slightly less than the axial magnetic field at extraction and this was the magnetic field configuration used for most of the measurements reported.

Table 3: Results for Spectra Recorded with Each Heating Frequency at Identical Magnetic Field Configuration of Injection, Extraction, and Middle Axial Fields 3.39 T, 2.10 T and 0.48 T, respectively

Frequency (GHz)	**Injection** ∇B_{ECR} (T/m)	**Extraction** ∇B_{ECR} (T/m)	**Ts** (keV)
14	-4.67	4.22	48.8
18	-7.71	6.54	43.8
28	-12.75	10.00	44.4

Figure 7 shows the spectra and calculated values of the spectral temperature at 18 GHz with the injection, extraction, and middle fields set to 3.39 T, 2.1 T and 0.48 T, respectively while the radial field was varied while the radial field was varied from 1.29 T to 2.15 T. There was no significant shift in the spectral temperature or in the shape of the spectra and this indicates T_s remains unaffected as long as the radial field at the wall is lower than the maximum field at extraction. For these measurements, the value of the radial field quoted is that produced by the sextupole alone at the plasma wall. The magnitude of B at the wall is also influenced by the fields from the solenoids and varies across the plasma wall depending on both z and phi.

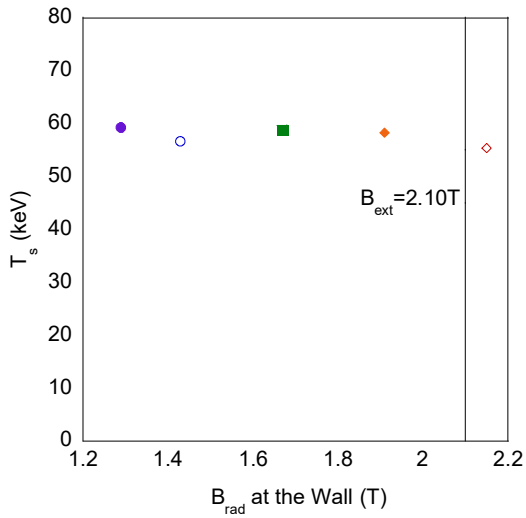

Figure 7: T_s for the 18 GHz operations with injection, extraction and middle field values of 3.39 T, 2.1 T and 0.48 T, respectively, while the radial field was varied from 1.29 T to 2.15 T.

In a second set of data the extraction field was lowered to 1.47 Tesla, the injection and middle field were held at 2.23 T and .33 T while the radial field was varied from 1.29 T to 2.15 T. With the extraction field set at 1.47 T, Figure 8 shows that both the intensity and shape of the spectra begin to increase and change when the radial field is increased to values well above the extraction field, which reduces the loss of electrons radially and enhances the loss in the extraction region.

In Figure 9 we investigated the dependence of T_s on B_{min} when the extraction field was set to values well below the field on the radial wall of the chamber. The data obtained when varying the radial field demonstrates that T_s still depends strongly B_{min} remains even when the weak point in confinement is shifted toward the extraction end. However the slope of T_s is different. These results can be related to the simulations discussed by Thuillier et al who present a simple model where the hot electrons are fully magnetized and follow the magnetic field lines [14]. The reference shows that a geometrical model studying where the field lines pass through the ECR zone and land on the chamber walls can be used to show how electrons escape

ISBN 978-3-95450-186-1

confinement at the regions where the magnetic field is weakest. Experimentally we have shown that by raising the radial field above the extraction field, the weak point in the magnetic confinement is shifted towards the extraction plate, thereby causing electrons to preferentially escape axially and collide at the extraction plate. This creates higher count rates with our axial detector and in one case at high microwave power excessive heat was dumped on the extraction plate damaging it.

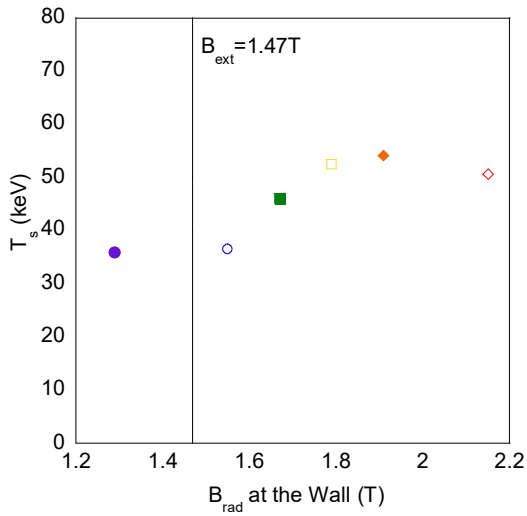

Figure 8: T_s for the 18 GHz operations with injection, extraction and middle field values of 2.23 T, 1.47 T and 0.33 T, respectively, while the radial field was varied from 1.29 T to 2.15 T.

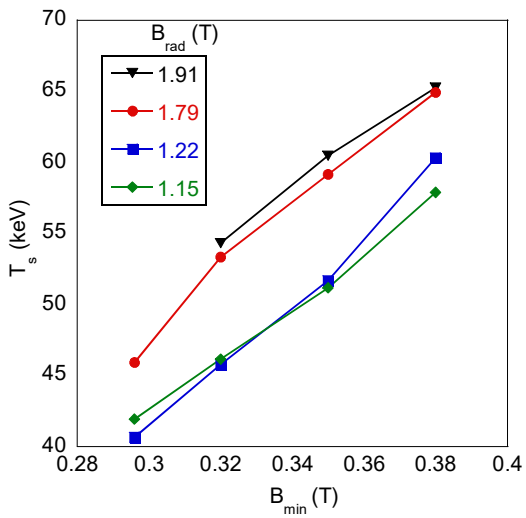

Figure 9: B_{min} is varied at each value of B_{rad}. When B_{rad} is raised above B_{ext} of 1.49 T the slope of the spectra changes with an increase in T_s but remains the proportional dependence on B_{min}.

DISCUSSION

There are two key results from the experimental measurements. First, the spectral temperature of the axial bremsstrahlung depends on the value of B_{min} and is not correlated with the value of ∇B_{ECR}. In a number of previous measurements, there appeared to be a correlation between ∇B_{ECR} and T_s, and this was thought to be evidence that at lower ∇B_{ECR} electron heating is more efficient. However, in these earlier studies both ∇B_{ECR} and B_{min} were changed at the same time [15-16].

The key difference in the measurements presented here is that the presence of a center coil in addition to the injection and extraction coils used in most other sources allows us to vary ∇B_{ECR} and B_{min} either together or with one held approximately fixed. It has often been observed that as an ECRIS is operated at higher frequencies the spectral temperature increases. Furthermore, it was typically thought that it was the ratio of B_{min}/B_{ECR} that was the important factor in determining T_s. These results show that T_s depends not on the ratio of B_{min} to B_{ECR}, but simply on the magnitude of B_{min}. This means that as new, higher frequency sources come into operation the generation of hot electrons can be controlled if B_{min} is not scaled up with frequency. In the case of the VENUS operation with B_{min} at about .4 T can produce excellent results without generating large amounts of high energy bremsstrahlung which can penetrate into the cold mass and generate an unwanted cryogenic heat load. Additionally, for fixed magnetic field geometry, T_s is independent of whether the RF frequency is 14, 18 or 28 GHz. This result strengthens the case that T_s is not correlated with ∇B_{ECR}, since with a fixed magnetic geometry, the value of ∇B_{ECR} is different for each frequency.

Further experimental measurements are planned to measure the axial bremsstrahlung at energies between 100 eV and 10 keV using a X-123 SDD detector from Amptek [17].

REFERENCES

[1] R. Geller, "Electron Cyclotron Resonance (E.C.R.) Multiply Charged Ion Sources," in *IEEE Transactions on Nuclear Science*, vol. 26, no. 2, pp. 2119-2127, April 1979.

[2] D. Xie *et al.*, "Recent production of intense high charge ion beams with VENUS," presented at ECRIS'16, Busan, Korea, August 2016, THAO01, these proceedings.

[3] J. Benitez *et al.*, "Production of high intensity ^{48}Ca for the 88-Inch Cyclotron and other updates," *Rev. Sci. Instrum.*, vol. 85, 02A961, 2014.

[4] T. Rognlien *et al.*, "Electron cyclotron resonance heating in tandem-mirror end cells," *Phys. Fluids B*, vol. 2, p. 338, 1990.

[5] D. Leitner *et al.*, "Measurement of the high energy component of the x-ray spectra in the VENUS electron cyclotron resonance ion source," *Rev. Sci. Instrum.*, vol. 79, 033302, 2008.

[6] R. Geller, *Electron Cyclotron Resonance Ion Sources and ECR Plasmas*. London, England, UK: Institute of Physics Publishing, 1996.

[7] L. Sun *et al.*, "Advancement of highly charged ion beam production by superconducting ECR ion source SECRAL (invited)," *Rev. Sci. Instrum.*, vol. 87, 02A707, 2016.

ISBN 978-3-95450-186-1

[8] G. Machicoane *et al.*, "First results at 24 GHz with the superconducting source for ions (SUSI)," in *Proc. of ECRIS'14*, Nizhny Novgorod, Russia, May 2014, paper MOOMMH03.
[9] Y. Higurashi *et al.*, "Recent development of RIKEN 28 GHz superconducting electron cyclotron resonance ion source," *Rev. Sci. Instrum.*, vol. 85, 02A953, 2014.
[10] C. Lyneis *et al.*, "Concept for a fourth generation electron cyclotron resonance ion source," *Rev. Sci. Instrum.*, vol. 83, 02A301, 2012.
[11] D. Hitz *et al.*, "Results and interpretation of high frequency experiments at 28 GHz in ECR ion sources, future prospects," *Rev. Sci. Instrum.*, vol. 73, 509, 2002.
[12] Amptek, http://amptek.com/products/xr-100t-cdte-x-ray-and-gamma-ray-detector/
[13] R. Redus *et al.*, "Combining CdTe and Si detectors for energy-dispersive x-ray fluorescence," *X-Ray Spectrom.*, vol. 41, p. 393, 2012.
[14] T. Thuillier *et al.*, "Investigation on the electron flux to the wall in the VENUS ion source," *Rev. Sci. Instrum.*, vol. 87, 02A736, 2016.
[15] H. Zhao *et al.*, "Effects of magnetic configuration on hot electrons in highly charged ECR plasma," *Plasma Sources Sci. Technol.*, vol. 18, 025021, 2009.
[16] C. Lyneis *et al.*, "Measurement of bremsstrahlung production and x-ray cryostat heating in VENUS," *Rev. Sci. Instrum.*, vol. 77, 03A342, 2006.
[17] Amptek, http://amptek.com/products/x-123sdd-complete-x-ray-spectrometer-with-silicon-drift-detector-sdd/

ISBN 978-3-95450-186-1

STRUCTURAL INFORMATION ON THE ECR PLASMA BY X-RAY IMAGING

R. Rácz†, S. Biri, J. Pálinkás, Institute for Nuclear Research, Hungarian Academy of Sciences (Atomki), Debrecen, Hungary
D. Mascali, G. Castro, C. Caliri, L. Neri, F. P.Romano[1], S. Gammino
Instituto Nazionale di Fisica Nucleare – Laboratori Nazionali del Sud, Catania, Italy
[1]also at CNR-Istituto per i Beni Archeologici e Monumentali

Abstract

Precise knowledge on the density distribution of the Electron Cyclotron Resonance Ion Source plasma is needed by several reasons: i) in order to possibly improve the quality parameters of the extracted ion beam (emittance, brightness) strongly linked to the plasma structure, ii) to correctly investigate the recently observed plasma instabilities and/or the implementation of alternative heating methods (e.g. modal conversion) iii) in order to improve the general microwave-to-plasma coupling efficiency, in view of a microwave-absorption oriented design of future ECRIS. The non-destructive spectroscopic diagnostic methods give information always corresponding to integration over the whole plasma volume. X-ray imaging by pin-hole camera can partly overcome this limitation. We performed volumetric and space resolved X-ray measurements at the ATOMKI ECRIS operated at lower frequencies than usual. The experimental setup in detail and the methods how the working parameters were selected will be shown. The integrated and photon-counting analyses of the collected plasma images show a strong effect of the frequency and magnetic field on the plasma structure and local energy content.

INTRODUCTION

Imaging of the electron cyclotron resonance (ECR) plasmas by using CCD camera in combination with a pinhole is a non-destructive diagnostics method to record the strongly inhomogeneous spatial density distribution of the X-ray emitted by the plasma and by the chamber walls. This method can provide information on the location of the collisions between warm electrons and multiple charged ions/atoms, opening the possibility to investigate plasma structure in more details. Precise knowledge on the density distribution of the Electron Cyclotron Resonance Ion Source (ECRIS) plasma is needed by several reasons: 1) ECRISs provide worldwide highly charged ion beams for high energy accelerators and also the low energy ion beam of the source can be used in various fields of science (e.g. in atomic physics research, material science). In both application cases the parameters of the extracted ion beam are essentially and strongly determined by the shape, structure and quality of the ECR plasma. 2) Development path of the ECRISs is mainly traced by the trend to apply stronger magnetic confinement with higher RF frequency. However the coupling efficiency may also improves by a microwave-absorption oriented design. The next generation of ECRISs may take into account the optimisation of the spatial density distribution of the plasma. 3) The correct investigation of the recently observed plasma instabilities [1] and/or the implementation of alternative heating methods (e.g. modal conversion [2]) are inconceivable with the few existing experimental data on the precise plasma density profiles.

In 2002 the Atomki ECR group carried out and published for the first time space-resolved plasma diagnostics measurements by a pinhole X-ray camera [3]. In 2014 a new series of volumetric and space resolved X-ray measurements have been carried out at the Atomki ECR ion source. The measurement was done in close collaboration between the Atomki ECRIS team (Debrecen, Hungary) and the ion source group of INFN-LNS (Catania, Italy). The aim was to study mainly the effect of the microwave frequency but also the effect of some setting parameters like microwave power and strength of the axial magnetic field on the plasma structure. The result of the volumetric measurements and the comparison of the two (2002 and 2014) experimental setups were published already in recent articles [4, 5].

Two different type of exposing methods were applied. In case of the spectrally integrated mode the photos are taken with several ten seconds exposure time. The only limitation for the exposure time was to avoid the blooming of the CCD (when a pixel in a CCD image sensor is overloaded). Individual pixels can be loaded by many X-ray photons, therefore the energy information of a given photon are lost. Photos were also taken in photon counting mode. In that case thousands of images are exposed with experimentally adjusted short (milliseconds) exposure time. Each pixel registered either 0 or 1 X-ray events. Therefore any individual pixel can be used as a single photon detector to spectrally resolve the plasma image. Because of the strong inhomogenity of the plasma, region of interests (ROIs) were selected and the exposure time was settled by the intensity of the given region. The intensity of the other parts of the images was left out of consideration.

The huge amount of obtained experimental and then analysed data require the publication of the results in several papers. The present paper will show the methods how the working parameters for the pinhole camera measurements were selected. The presented preliminary

†rracz@atomki.hu

ISBN 978-3-95450-186-1

results will demonstrate the strong effect of the frequency and magnetic field on the spectrally integrated X-ray plasma images. Further detailed analysis of the integrated photos and the analysis of the more sophisticated photon counted images will be published elsewhere soon.

EXPERIMENTAL SETUP

The experiment was performed at the Atomki ECR ion source [6].The experimental setup presented in Figure 1. allows to take X-ray images and m/q spectra simultaneously, providing charge state distribution (CSD) and spectral, structural information on exactly the same plasma. Two detectors were applied at the injection side, alternatively. First the Silicon Drift Detector (SDD) (for volumetric measurements) was placed beyond a kapton foil ensuring vacuum break, and collimated by a lead cylinder with a drilled hole. Then the CCD X-ray camera (for spatially resolved measurements) made by 256x1024 pixels operational in the range of 500 eV – 10 keV was coupled to a lead pinhole (100 μm in diameter) and placed along the axis, facing the chamber. The area of the circle shape injection plate was divided into two regions in the ratio 3:2. The smaller area was used for microwave and gas injection, while the larger part was closed by stainless steel mesh to keep a closed resonant cavity and to provide transparency for imaging. In addition, aluminum windows of variable thickness (range 1–6 μm) were used to screen the CCD from the visible and UV light emitted also by the plasma.

A High Purity Germanium (HPGe) detector was also placed on the axes, but at the other (extraction) side of the source beyond the 90-degree analysing magnet, after a quartz window. It was used for monitoring the X-rays emitted by the high energy electrons and it was collimated by lead blocks. The HPGe detected the radiation passing through the extraction hole of the plasma chamber.

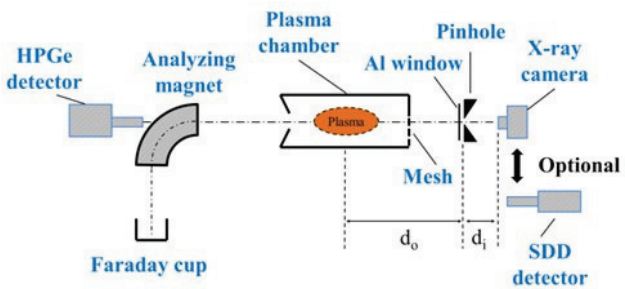

Figure 1: Schematic drawing of the X-ray diagnostic setup.

For microwave coupling low power (40 W) TWTA was used and the microwave frequency was varied between 12.8 and 13.4 GHz. The microwave signal was provided by HP 8350B sweep oscillator with HP 83590A plug-in (2 - 20 GHz). The injected power was measured at the closest possible point (at a distance of 130 cm from the plasma chamber entrance) by an RF probe after a directional coupler. The low power level (varied between 20 and 40 W) was decided in order to prevent high dead-times in the SDD detector and pixels-saturation in the CCD camera. The ECR ion source was optimized for Ar^{4+} ions production. The gas pressure measured at the injection side of the ion source was $P_{inj}=3.3*10^{-6}$ mbar.

SELECTION OF WORKING PONTS

During the measurements a wide range of external ion source setting parameters and technical solutions were tried and tested. Volumetric measurements (by SDD and by HPGe detectors) were done at different pumping microwave frequencies between 12.80-13.40 GHz, with 40 MHz steps (16 frequencies). Some of these frequencies proved to be better or worth than others, in terms of resulting higher or lower Ar^{4+} current.

In the preceding paper [4] several good agreements were found between the external beam features (analysed and total beam intensity, average charge, SDD counts) and the calculated plasma electron parameters (density, temperature, number of modes) vs microwave frequency. In Figure 2 the electron density, temperature and the extracted and analysed Ar beam current is drawn as a function of the frequency.

Frequency

For the integrated plasma images eight frequencies from 12.84 to 13.16 GHz with 80 MHz steps were selected while a limited number from them (so-called "representatives") had to be selected for the time-consuming spectrally-resolved recordings. The 12.84 and 12.92 GHz frequencies were selected for this studies as being the two frequencies producing broad fluctuation in both X-ray flux and output current, while 13.24 GHz represents a significant frequency since the increase of output current does not correspond – as occurs for the other data – to a comparable increase of X-ray flux.

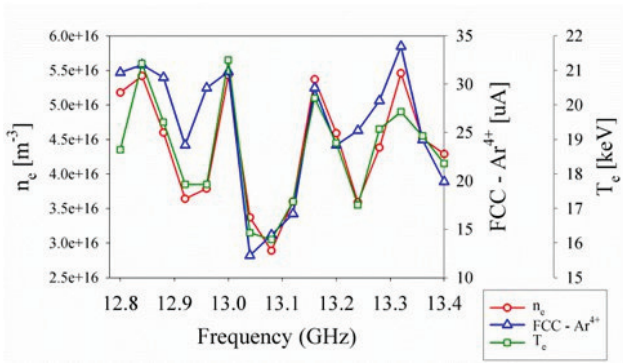

Figure 2: Trend of the electron density, temperature and Ar^{4+} current vs pumping frequency.

Magnification and the Thickness of the Al Window

The position of the pinhole respect to the plasma and to the CCD chip develops the magnification of the pinhole system. By varying the thickness of the Al-window the flux of the visible and UV part of the obtained spectra respect to the X-ray part can be justified. Both parameters were optimized.

ISBN 978-3-95450-186-1

Mounting D = 6 micrometres Al-window (Figure 3 (a)) the window filtered strongly the X-ray radiation. In contrary, D = 1 micrometres proved to be too thin (Figure 3 (b)), the picture is too noisy. D = 3 micrometres (Figure 3 (c)) is a good compromise; this window was selected and used for the energy-resolved measurements.

The magnification (M) is the quotient of d_i and d_o (image and object distances) as shown in Figure 1. Three average M values were set and tried: 0.082, 0.124 and 0.158. Also three different Al-windows were tested with thicknesses of 6, 1 and 3 micrometres (D). These are altogether 9 combinations but among them only 3 were tested, as seen in Figure 3 (a) - (c). From the figures it is obvious that the largest magnification (M = 0.158) can be and has to be applied, because it is still cover the important parts of the plasma. It is true however that the lowest middle plasma branch (as it is seen in the (d) picture) is not shown (outside) in the right picture. That is why for photon counting analysis this magnification and alignment were applied at the beginning (Fig. 3. (c)).

After that the pinhole camera was vertically tilted by a few degrees to "move back" that branch of the plasma into the picture. Then the camera was not moved anymore and the integrated images investigating the power dependence and the effect of the strength of the axial magnetic field were recorded using the alignment represented by Fig. 3 (d).

M = 0.158 magnification and D = 3 micrometres thick aluminium window was used all the images cases presented in this paper. The only exception is the frequency dependence series because it was recorded at the earlier stage of the experiment. At that time the magnification and the window thickness were M = 0.082 and D = 6, respectively.

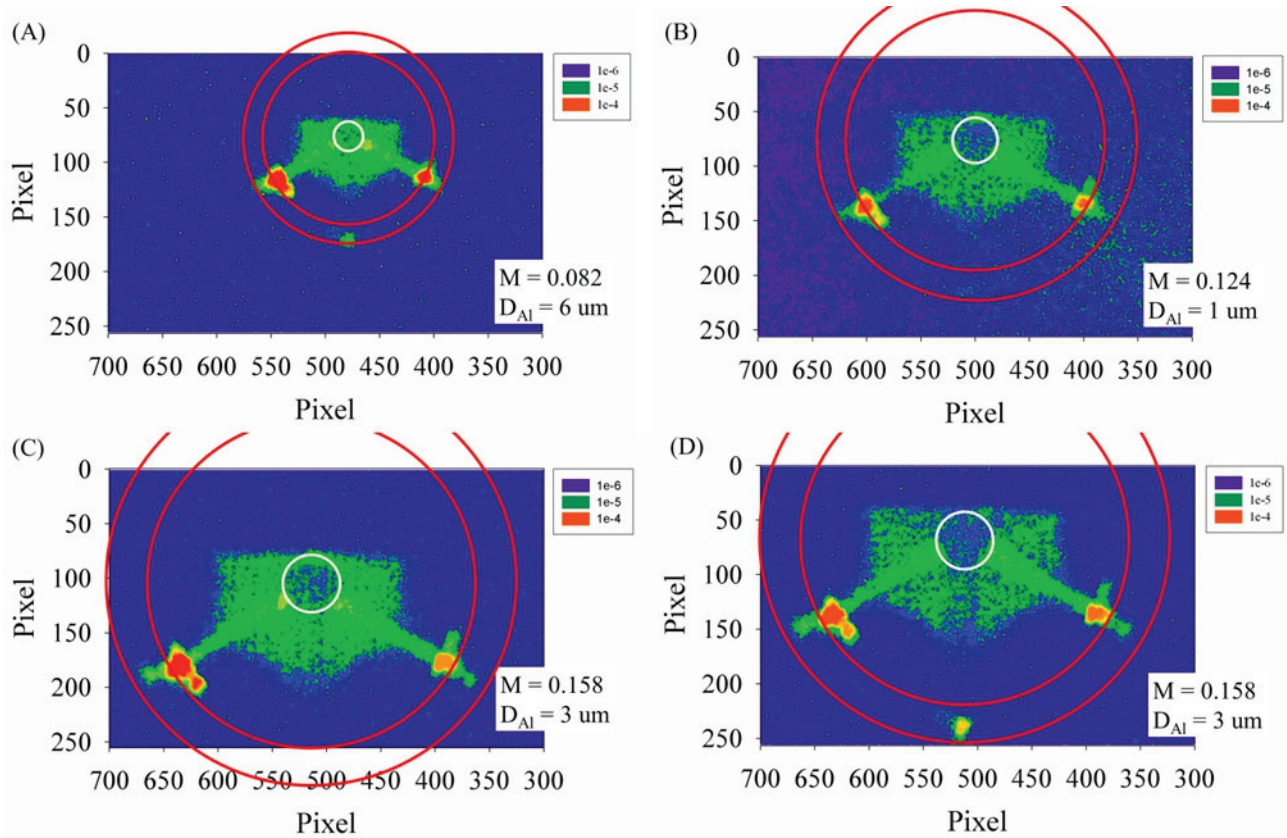

Figure 3: Integrated plasma images for the selection of the optimal magnification (M) and Al-window thickness (D). From (a) to (c) (M/D): 0.082/6, 0.124/1, 0.158/3. For (d) only the alignment was changed respect to (c). All the images were normalised to 1 (total number of counts in each picture = 1) and mirrored by two axes to see exactly the original arrangement. The red circles roughly represent the contours of the farther (extraction side, small circle) and the closer (injection side, large circle) end-plates of the plasma chamber, respectively. The white circle shows the contour of the extraction hole.

ISBN 978-3-95450-186-1

DEPENDENCE ON THE ECR SETTING PARAMETERS

The effect of some external setting parameters of the ion source (microwave frequency, axial magnetic field, microwave power) on the spectrally integrated images were recorded and studied. Due to the long exposure time (15 – 40 seconds) the spectral information in a given pixel is superposed and lost, however the changes in the shape, structure and local energy contents of the plasma is clearly visible in the images presented by this chapter.

Frequency Dependence

The injected RF frequency was varied between 12.84 GHz and 13.16 GHz with 80 MHz steps. The microwave power coupled to the plasma chamber was 30 W. The strength of the magnetic trap was maximal (100 % coils currents). Because this wide set of frequencies were applied only at the first series of the measurement the magnification and the window thickness are M = 0.082 and D = 6, respectively. The acquisition time was 15 seconds for each frame. Figure 4 shows the spectrally integrated plasma images taken at different frequencies.

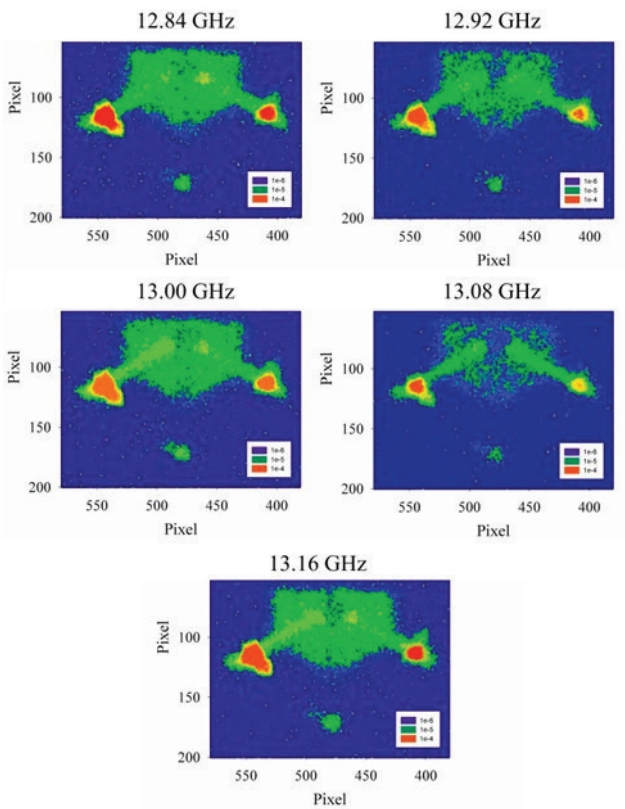

Figure 4: Spectrally integrated plasma images as function of the RF frequency. The images were normalised to 1 (total number of counts in each picture = 1) and mirrored by two axes to see exactly the original arrangement.

It is clear from the volumetric measurements that the intensity of X-ray photons emitted by the plasma strongly depends on the RF frequency and it is in strong correlation with the mean charge state (<Q>) of the extracted ion beam [4]. Figure 4 clearly shows that the total counts obtained at the near axis regions (extraction hole) are also fluctuating. One can conclude that the emptier the near axis region the lower the <Q>. This highlights the effect of the density distribution of the plasma to the ionization efficiency.

Power Dependence

Effect of the microwave power to the integrated images was recorded. The frequency was fixed at 12.84 GHz. Spectrally integrated X-ray images were exposed when the microwave power coupled to the plasma chamber was 20 W, 30 W and 40W. The strength of the magnetic trap was maximal (100 % coils currents). The average magnification and the window thickness were M = 0.158 and D = 3, respectively. The acquisition time was 40 seconds for each frame. The spectrally integrated plasma images as function of the injected microwave power can be seen in Figure 5. While the total count of the X-ray photos are increased with the microwave power the structure of the plasma was not changed remarkably.

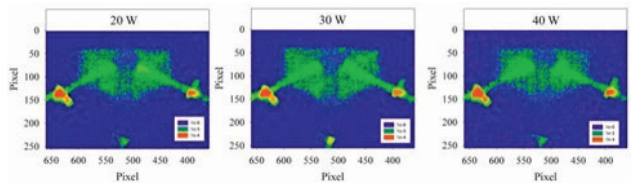

Figure 5: Spectrally integrated plasma images as function of the injected microwave power. The images were normalised to 1 and mirrored by two axes.

Axial Magnetic Field Dependence

Effects of the decrease of the axial confinement on the integrated images were recorded. The frequency was fixed at 12.84 GHz. X-ray images were exposed when the axial magnetic field provided by the coils were decreased while the injected microwave power was fixed at 30 W. Images were taken when the coils current was set to 100%, 80% and 60% of the maximum output current of the power supply (Figure 6.).

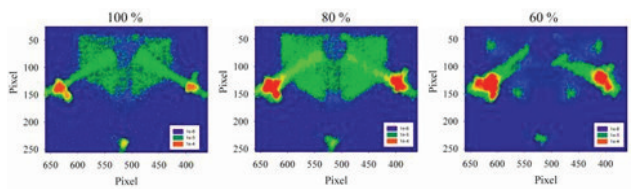

Figure 6: Spectrally integrated plasma images as function of the strength of the axial magnetic confinement. The average magnification and the window thickness are M = 0.158 and D = 3, respectively. The acquisition time was 40 seconds for each frame. The images were normalised to 1 and mirrored by two axes.

Similarly to the effect of the microwave power the total counts of the images are increasing with the applied coils

ISBN 978-3-95450-186-1

current, meanwhile strong structural effect appear; the near axis region becomes emptier at each reduction step, the plasma is expanding and is shifting toward the plasma chamber wall. This shift can be explained by the radial expand of the resonant surface.

SUMMARY

Experimental campaign with wide instrumentation was carried out to measure the volumetric and spatially resolved X-ray emission of the ECR plasma. Methods were shown how the working parameters for the pinhole camera measurements were selected. As preliminary results correlation between the global setting parameters of the plasma (axial magnetic field, RF frequency, microwave power) and the spatial distribution of the pinhole X-ray images were demonstrated: (1) strong effect of the RF frequency on the plasma images especially in the near axis region, (2) strong effect of the axial magnetic confinement on the radial dimensions of the plasma; the plasma is expanding and is shifting toward the plasma chamber wall meanwhile the plasma images in the near axis region becomes emptier at each reduction step, (3) no remarkably effect on the plasma structure as function of the externally coupled microwave power.

Further detailed analysis of the integrated photos and the analysis of the large amount and more sophisticated photon counted images are needed and will be published in a subsequent paper soon.

ACKNOWLEDGEMENT

“This project has received funding from the European Union’s Horizon 2020 research and innovation program under grant agreement No 654002 (ENSAR2-MIDAS)”.

REFERENCES

[1] O. Tarvainen, T. Kalvas, H. Koivisto, J. Komppula, R. Kronholm, J. Laulainen, I. Izotov, D. Mansfeld and V. Skalyga, Kinetic instabilities in pulsed operation mode of a 14 GHz electron cyclotron resonance ion source, Review of Scientific Instruments 87 (2016) 02A701

[2] G. Castro, D. Mascali, F. P. Romano, L. Celona, S. Gammino, D. Lanaia, R. Di Giugno, R. Miracoli, T. Serafino, F. Di Bartolo, N. Gambino and G. Ciavola, Comparison between off-resonance and electron Bernstein waves heating regime in a microwave discharge ion source, Review of Scientific Instruments 83 (2012) 02B501

[3] S. Biri, A. Valek, T. Suta, E. Takács, Cs. Szabó, L. T. Hudson, B. Radics, J. Imrek, B. Juhász and J. Pálinkás, Imaging of ECR plasmas with a pinhole x-ray camera, Review of Scientific Instruments 75 (2004) 1420

[4] D. Mascali, G. Castro, S. Biri, R. Rácz, J. Pálinkás, C. Caliri, L. Celona, L. Neri, F. P. Romano, G. Torrisi and Santo Gammino, Electron cyclotron resonance ion source plasma characterization by X-ray spectroscopy and X-ray imaging, Review of Scientific Instruments 87 (2016) 02A510

[5] R. Rácz, S. Biri, J. Pálinkás, D. Mascali, G. Castro, C. Caliri, F. P. Romano and S. Gammino, X-ray pinhole camera setups used in the Atomki ECR Laboratory for plasma diagnostics, Review of Scientific Instruments 87 (2016) 02A741

[6] S. Biri, R. Rácz and J. Pálinkás, Status and special features of the Atomki ECR ion source, Review of Scientific Instruments 83 (2012) 02A341

ISBN 978-3-95450-186-1

SPIRAL1 CHARGE BREEDER: PERFORMANCES AND STATUS

L. Maunoury#, P. Delahaye, M. Dubois, O. Bajeat, C. Barthe-Dejean, R. Frigot, P. Jardin, A. Jeanne, O. Kamalou, P. Lecomte, B. Osmond, G. Peschard, and A. Savalle
GANIL, bd Henri Becquerel, BP 55027, F-14076 Caen cedex 05, France
J. Angot, T. Lamy, and P. Sole
Laboratoire de Physique Subatomique et de Cosmologie - Université Grenoble Alpes - CNRS/IN2P3 - 53, rue des Martyrs, 38026 Grenoble Cedex, France

Abstract

In the framework of the SPIRAL1 upgrade under progress at the GANIL lab, the charge breeder based on a LPSC Phoenix ECRIS, first tested at ISOLDE [1] has been modified as to benefit of the last enhancements of this device from the 1+ / n+ community [2].

Prior to its installation in the middle of the low energy beam line of the SPIRAL1 facility, it has been tested at the 1+/n+ LPSC test bench to validate its operation performances. Charge breeding efficiencies as well as charge breeding times have been measured for noble gases and alkali elements. The experimental results demonstrated that the modifications done were on the right track leading the SPIRAL1 charge breeder to the top worldwide in terms of performances. The experimental outcomes have shown a strong interrelationship between the charge breeding efficiency and the charge breeding times which is still under active discussion.

This paper will summarize the experimental results obtained and will discuss the specific phenomenons observed but still not fully explained as the charge breeding time evolution, the depletion of highly charged ions in the buffer gas etc.

INTRODUCTION

The SPIRAL 1 facility is under operation since 2001 and almost 35 Radioactive Ion Beams (RIBs) have been delivered to the Physicist. The first Target Ion Source System (TISS) developed at GANIL [3] was very chemically selective: only gaseous elements as noble gases, N, O and F could be ionized. These RIBs allowed numerous results in Nuclear Physics [4] but physicists need an enlarged palette to study the nuclear properties and to test the nuclear models including isotopes of condensable elements. The 1+/n+ [5] technique has been chosen as many different TISS providing 1+ beams can be developed for specific chemical family elements with high efficiency. The charge breeder is requested to boost the charge state from 1+ to n+ prior to the post-accelerator: the cyclotron CIME [6] is delivering a RIB with energy in the range 2 – 20 MeV/u suitable for the nuclear physicists. The charge breeder is based on one developed at LPSC and modifications have been already described in other papers [7, 8]. In the following, the experimental results of the charge breeder operation on the LPSC test bench will be presented as well as its status at the SPIRAL1 facility.

EXPERIMENTAL RESULTS

The installation of the SPIRAL1 charge breeder in the middle of the 1+/n+ test bench at LPSC needed a modification thereof. The Figure 1 is the layout of the experiment at LPSC. The Reference 8 describes the experimental conditions.

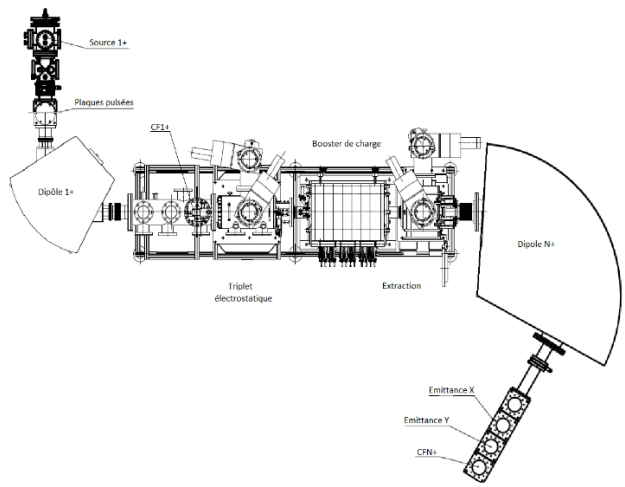

Figure 1: Layout of the Spiral1 charge breeder at LPSC laboratory.

Effect of the Residual Gas Pressure

The residual gas pressure value plays a major role on the charge breeding efficiencies as demonstrated at the CARIBU facility: charge breeding efficiencies get their higher values as soon as the pressure drops down to the level of few 10^{-8} mbar. The Figure 2 reports the evolution of the charge breeding efficiency of the Rb^{19+} versus the product of the pressure at injection times the pressure at extraction. The charge breeding efficiency drops continuously with the increase of the residual gas pressure. The CB has been modified such the conductances to the plasma chamber are optimized.

Effect of the 1+ Injected Current

The question is the following: is the charge breeding efficiency measured with a stable beam in the nA range still valid with RIBs in the pA even less range?

ISBN 978-3-95450-186-1

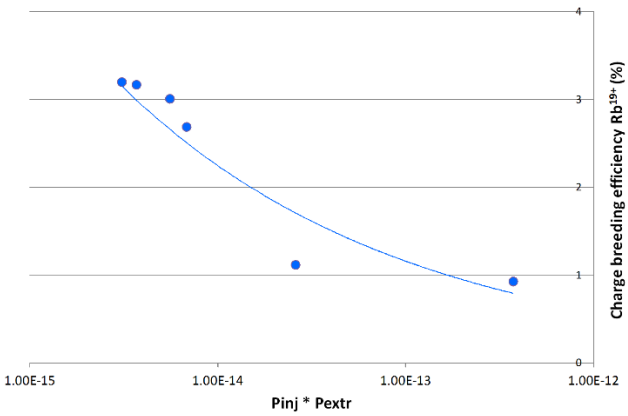

Figure 2: Influence of the residual gas pressure onto the charge breeding efficiency for the case Rb^{19+}.

Figure 3 shows the evolution of the Rb^{17+} current versus the Rb^{1+} injected. There is a plateau followed by a fall-off around 1500 nA. It means that as long as the RIB 1^+ intensity is small enough compared to 1 µA, the charge breeding efficiency is constant and can be used to determine the yields of RIBs. That conclusion is corroborated by a 1+/n+ carbon measurement [9] done with the CB of the LPSC lab.

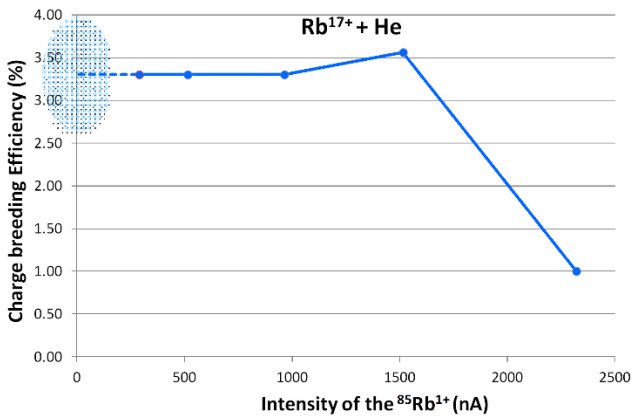

Figure 3: Evolution of the RB17+ charge breeding efficiency with the injected 1+ current (the light blue zone corresponds to the RIB work area).

Effect of the Deceleration Tube Position

The deceleration tube at the injection side is mobile. In the case of $^{39}K^{9+}$, it has been moved over a 50 mm range. For a wide domain of 30 mm, the charge breeding variation is tiny and a regular decline occurs afterwards. The best position of the exit of the deceleration tube is a little ahead from the entrance of the CB iron plug as it is displayed on the Figure 4. This parameter has not a dramatic effect on the charge breeding efficiency.

Effect of the Buffer Gas

The Figure 5 exhibits the charge state distributions of the ^{39}K with three different buffer gases O_2, He and H_2. Lighter is the buffer gas used narrower is the charge state distribution and higher is the charge breeding efficiency for the potassium case. That result opens up a new way to tune the booster depending on the final energy of the requested post-accelerated RIB. As the final energy is function of the Q/M ratio, higher is the charge state higher will also be the final energy. Thus, for a low energy RIB using the 8+ charge state, He should be chosen. In contrast for a higher energy RIB requiring the 9+ charge state H_2 is more suitable. Consequently, the buffer gas type is a new parameter to tune in order to deliver the RIB with the highest yields at the right energy.

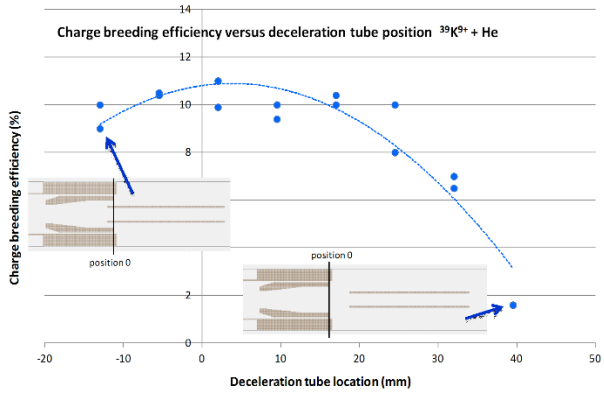

Figure 4: Evolution of the $^{39}K^{9+}$ charge breeding efficiency with the position of the deceleration tube.

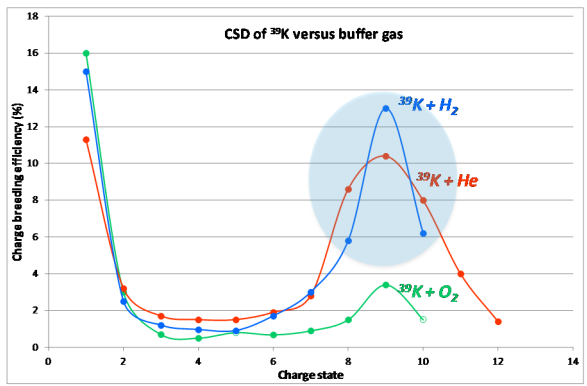

Figure 5: Charge state distributions of the 39K versus the buffer gas.

Charge Breeding Efficiencies

The Figure 6 is a summary of the charge breeding efficiencies measured depending on the ratio of A/Q. The yellow points, corresponding to the measurements of the CARIBU facility, are almost always on the top but mostly the SPIRAL1 CB results are on second position (red points) excepted for the case of $^{40}Ar^{8+}$ with 18.9% of charge breeding efficiency. Within the domain of the light element (Na, K zone), there is still a margin of a factor 2 to gain if one compares to the CARIBU facility. As SPIRAL1 targets this area, a deeper comparison of both machine conditions should be undertaken as to find out the relevant parameters which limit the charge breeding efficiency in our case. Among the possible parameters, the double frequency heating, which has not yet been tested with the SPIRAL 1 charge breeder, could possibly help in increasing the capture efficiency.

ISBN 978-3-95450-186-1

CHARGE BREEDING TIME

The physicists are interested by exotic nuclei far away from the stability valley, with ratios of protons over neutrons depending on the case as large or as small as possible, meaning often isotopes with short half life (<100ms). The production of an accelerated RIB using such isotopes requiring a charge breeder implies a real care on the charge breeding time. We are taking the following examples: for the first experiments, the ^{30}Na ($T_{1/2}$=48 ms) and ^{35}K ($T_{1/2}$=190 ms) are expected to be requested. Using the charge states 7+ and 9+, their charge breeding times are expected to be 52 ms and 117 ms respectively, as observed with the corresponding stable isotopes and H_2 as support gas, inducing yield losses by radioactive decay.

But depending on the tuning of the charge breeder, the charge breeding time can vary over a wide range. For the $^{39}K^{9+}$, two charge breeding times have been measured: 35 ms and 117 ms, the major difference between both measurements being the use of two types of buffer gas: He and H_2 respectively while the other parameters (coil current, drain current, injected current etc.) were quite similar with a global charge breeding efficiency of ~50%. At the same time the charge breeding efficiency decreases from 13% down to 11.7% with a smaller ratio: 0.9 (charge breeding efficiency) compared with 3.3 (charge breeding times). Similar dramatic changes in the charge breeding time were also observed at at the CARIBU facility for the Xe-132 case [10], originating this time from a small change of the RF frequency.

Figure 7 is another demonstration of the large variation of this parameter according to the experimental conditions. Figure 7 displays the evolution of the charge breeding time with the charge state in the case of the ^{39}K + He and for two Phoenix charge breeder types. As it is shown; the values vary up to a factor 2.

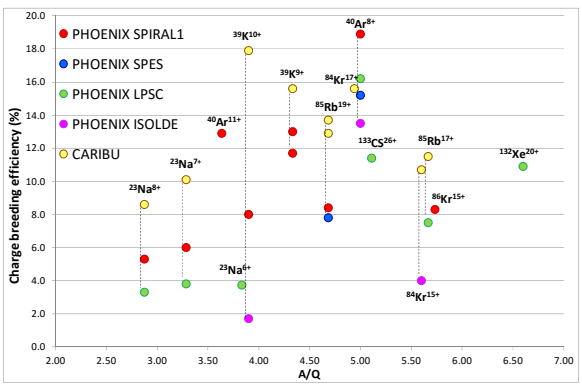

Figure 6: Recapitulation of the charge breeding efficiencies obtained with the SPIRAL1 charge breeder and compared with the results obtained with similar Charge breeders.

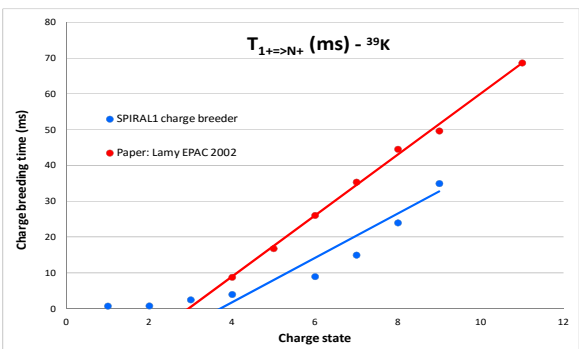

Figure 7: Charge breeding time (ms) of the $39K^{n+}$ charge states.

Figure 8: Top: low energy beam line before modifications Bottom: low energy beam line after inclusion of the Spiral1 charge breeder.

At GANIL, within the framework of a PhD work program, studies will be focusing on this specific, topic to gain control over the charge breeding time. A new simulation will be started involving recent results [11, 12] and based on realistic coulomb collisions modellisation. In parallel, an experimental work will be started either with stable or radioactive charge bred ions for collecting data on the dependence of the charge breeding time versus the various CB relevant parameters.

STATUS AND COMMISSIONNING

Currently, the Spiral1 CB came back to Caen to be assembled inside the Spiral1 facility. As it can been seen on the Figure 8 (bottom), the charge breeder as well as its injection and extraction boxes are in the middle of the low energy beam line. The comparison with the low energy beam line before the modification (Figure 8 top) shows clearly how the magnetic quadrupoles have been moved to insert the charge breeder leading to a new beam optic which must be tested during the commissioning.

The last optimizations done on the Spiral1 CB are

- ✓ firstly a fine pure Al (99.999%) layer (few µm) which was deposited on the plasma wall chamber,
- ✓ secondly a new plasma electrode using a grid to enhance the global conductance to the plasma chamber.

ISBN 978-3-95450-186-1

Those last adjustments have been done, on the one hand, as to go on decreasing as much as possible the residual gas pressure and, on the other hand, to improve the charge bred beam purity.

The commissioning program is defined and will last around four months. The final goal is to deliver a low energy RIB to the LIRAT facility [13] as well as a post-accelerated RIB to physicists at the end of the first semester of 2017. Several challenges should be overcome to reach the final goal:

- ✓ getting a residual gas pressure close to 1.10^{-8} mbar within the Spiral1 CB,
- ✓ validating all the beam optics downstream the Spiral1 CB: as a large modification has been done with insertion of new diagnostics, the tuning will be tricky to match the beam requirements before the injection into CIME, especially for keeping a high resolving power,
- ✓ validating the measurements done at the 1+/n+ LPSC test bench; an alkali ion source is under development for the 1+ injection into the Spiral1 CB,
- ✓ validating the operation of the previous TISS Nanogan by reaching a high transmission efficiency (>80%) through the Spiral1 CB.

CONCLUSION

Based on the results obtained, the SPIRAL1 CB matches the characteristic requested for the post-acceleration of the RIBs by the CIME cyclotron.

However, best efforts are to be made for increasing the charge breeding efficiency especially for the light elements as Na and even lighter as Li. To deliver RIB of very short half-life (< 100ms), charge breeding time must be fully controlled to minimize as much as possible losses by radioactive decay through the Spiral1 CB.

In order to keep on enlarging the RIB palette at GANIL as well as the RIB yields, two objectives shall be pursued: development of specific TISS [14] and development of new production targets using material other than carbon.

REFERENCES

[1] P. Delahaye *et al.*, *Review of Scientific Instruments* **77**, 03B105 (2006).
[2] R. Vondrasek *et al.*, *Review of Scientific Instruments* **83** 113303 (2012).
[3] L. Maunoury *et al.*, in *Proc. of the 13th International Workshop on ECR Ion Sources*, College Station, Texas, US, February 26-28, 1997.
[4] A. Navin *et al.*, *Journal of Physics* G: Nuclear and Particle Physics **38** 024004 (2011).
[5] C. Tamburella *et al.*, *Review of Scientific Instruments* **68** 2319 (1997).
[6] M. Duval *et al.*, in *Proc. of the 14th International Workshop on Magnet Technology*, MT-14 Tampere, Finland, June 11-16, 1995.
[7] P. Delahaye *et al.*, *Nuclear Instruments and Methods in Physics Research* A **693** 104 (2012).
[8] L. Maunoury *et al.*, *Review of Scientific Instruments* **87** 02B508 (2016).
[9] L. Maunoury *et al.*, *Review of Scientific Instruments* **85** 02A504 (2014).
[10] R. Vondrasek *et al.*, *Review of Scientific Instruments* **85** 02B903 (2014).
[11] O. Tarvainen *et al.*, *Physical Review Accelerators and Beams* **19** 053402 (2016).
[12] A. Galata *et al.*, *Plasma Sources Science and Technology* **25** 045007 (2014).
[13] F. Varenne, Technical Report on Operation Accelerators 2003-2004, internal report GANIL R-05-01 (2005).
[14] P. Jardin *et al.*, *Nuclear Instruments and Methods in Physics Research* B **B376** 64 (2016.

ISBN 978-3-95450-186-1

THE PROTON SOURCE FOR THE EUROPEAN SPALLATION SOURCE (PS-ESS): INSTALLATION AND COMMISSIONING AT INFN-LNS

L. Celona†, L. Allegra, A. Amato, G. Calabrese, A. Caruso, G. Castro, F. Chines, G. Gallo, S. Gammino, O. Leonardi, A. Longhitano, G. Manno, S. Marletta, D. Mascali, A. Massara, M. Mazzaglia, A. Maugeri, L. Neri, S. Passarello, G. Pastore, A. Seminara, A. Spartà, G. Torrisi, S. Vinciguerra,
Instituto Nazionale di Fisica Nucleare-Laboratori Nazionali del Sud, Catania, Italy
S. Di Martino, P. Nicotra, Si.a.tel., Catania, Italy

Abstract

A 2.45 GHz – 0.1 T microwave discharge Proton Source has been designed and assembled at INFN-LNS for the European Spallation Source (PS-ESS) in order to produce pulsed beams of protons up to 74 mA nominal current, at 75 keV of energy, with a transverse emittance containing 99 % of the nominal proton current below 2.25 π mm mrad and a beam stability of ± 2 %. The challenging performances of the machine have triggered specific studies on the maximization of the proton fraction inside the plasma and of the overall plasma density, including dedicated modelling of the wave-to-plasma interaction and ionization processes. The plasma conditioning phase started in July and excellent RF to plasma coupling, more than 99.5% is evident since the beginning. Reflected power fluctuation less than 0.05 % was measured providing a great starting point to reach the beam stability requested by the ESS accelerator.

INTRODUCTION

The European Spallation Source will be one of the most advanced technological tools for scientific and industrial development in Europe in the next decades. A linear accelerator is going to be built for the production of 2 GeV protons to be used for neutron production via nuclear spallation. Peak beam power will be 125 MW. Neutrons will be finally used for fundamental science and applied research.

The source named Proton Source for ESS (PS-ESS) [1] was designed with a flexible magnetic system and a compact tetrode extraction system with the goal to minimize the emittance and the time needed for the maintenance operations. Figure 1 shows a picture of the High Voltage (HV) platform fully assembled with the source body and magnetic system, the microwave injection line, all power supplies, control system devices, cooling system, gas injection and measurement devices. The ESS injector design has taken advantage of recent theoretical updates together with the new plasma diagnostics tools developed at INFN-LNS. The improved know-how will permit to fulfil the requirements of the ESS normal conducting front-end; the proton beam should be 74 mA which can be obtained with a total beam current of about 90 mA. The beam stability during the normal operations (in terms of current and emittance) shall be within ± 3.5 % as for pulse to pulse variation and ± 2 % of the beam current if averaged over a period of 50 us. The pulse duration is 2.86 ms with 14 Hz repetition rate. The requirements for the proton source and the LEBT are summarized in Table 1 and Table 2.

A detailed study of the beam transport in regime of space charge compensation was done and experimentally verified [2, 3, 4]. A reliability better than 95% is requested for the whole accelerator, thus meaning that the source reliability is expected to be greater than 99%. For that reason, the mechanical design was driven also to maximize the MTBF and minimize the MTTR.

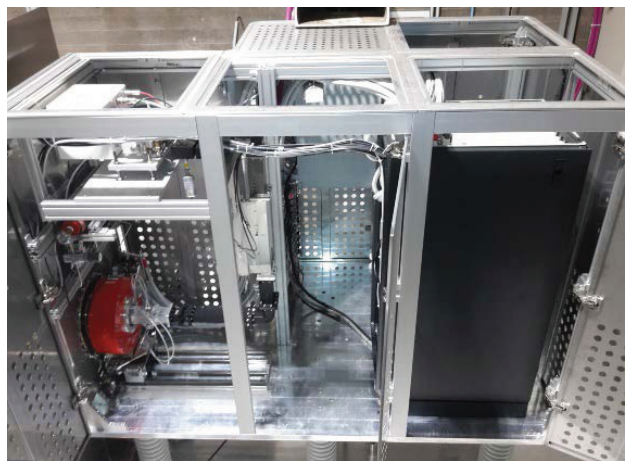

Figure 1: PS-ESS, high voltage platform detail.

Table 1: PS-ESS Requirements

Parameters	Value
Proton current range	67 – 74 mA
Proton fraction	> 75 %
Current stability (50us avr.)	± 2 %
Pulse to pulse stability	± 3.5 %
Beam energy	70 – 80 ± 0.01 keV
Repetition rate	1 – 14 Hz
Pulse length	5 – 2860 ± 1 us
Current reduced (with iris)	2 – 74 ± 1 mA
Restart after vacuum break	< 32 h
Restart after cold start	< 16 h

† celona@lns.infn.it

ISBN 978-3-95450-186-1

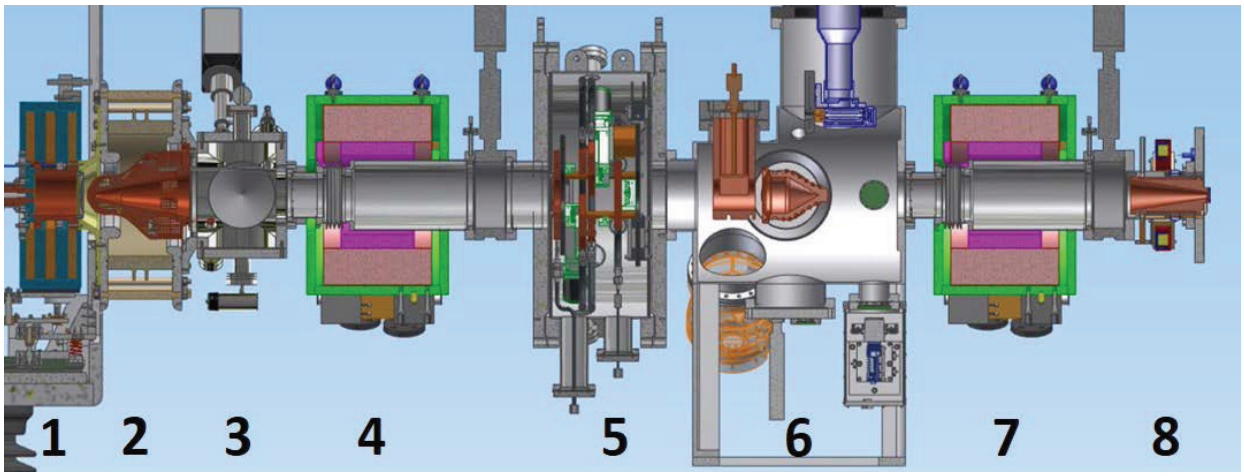

Figure 2: PS-ESS and LEBT layout.

Table 2: LEBT Requirements

Parameters	Value
Emittance (99 % normalized)	< 2.25 π.mm.mrad
Twiss parameter α	1.02 ± 20 %
Twiss parameter β	0.11 ± 10 %
Beam pulse rise and fall time	< 20 us
Gas type	≤ 28 g/mol
Pressure	$< 6 \cdot 10^{-5}$ mbar

PS-ESS AND LEBT LAYOUT

Figure 2 shows the PS-ESS and LEBT layout that today is arrived to a final stage. Every details are finalized, most of the element was already delivered to Catania and the other part are under fabrication in different manufacturing companies.

Description of the layout will follow the notation inserted in the Figure 3:

1. Plasma chamber with flexible three coils magnetic system, matching transformer for optimized microwave to plasma coupling and double pin joint support for the free alignment of this part to the first element of the LEBT
2. Insulating column made with a single alumina piece. The external surface has an innovative design that permit to reduce the electric field up to 6.5 kV/cm. The shape around the junction between the alumina the metal and the vacuum, commonly named triple point, was completely redesigned to achieve an electric field lower than 5.5 kV/cm in correspondence of the ground side. Inside this element the tetrode extraction system can be seen. It is composed by the plasma electrode located in the plasma chamber wall, and a set of three electrodes supported by the first element of the LEBT. There are two grounded electrodes and one repeller electrode that will avoid to inject free electrons from the LEBT to the plasma chamber. All three electrodes are water cooled.
3. The first element of the LEBT house two turbo molecular pumps (TMP), water and electrical utilities for the extraction system, a Residual Gas Analyzer (RGA), three different type of vacuum gauges, a burst disk and the gas injection needed to improve the space charge compensation of the LEBT. The design of this part was focused to be as compact as possible. This element is the most important peace for the alignment of the entire machine.
4. First LEBT solenoid with two magnetic steerers inside to reduce the total length of the LEBT. The two solenoids are identical.
5. The Iris is a six blade diaphragm that will be used to reduce the beam current injected inside the following part of the accelerator (Radio Frequency Quadrupole, RFQ) without change the condition of the source. This was designed to use the most stable working condition of the source even during the start-up of the accelerator when the beam transport is checked with reduced power.
6. The diagnostic box will house two Emittance Measurement Units (EMU), one Doppler Shift Measurement (DSM), a Faraday Cup (FC), a Non-invasive Profile Measurement (NPM), two TMP, three vacuum gauges and a burst disk. Inside this part that was designed by the ESS beam diagnostic group there is also housed a chopper designed by INFN-LNS, it will deflect and defocus the beam out from the LEBT collimator (part 8) hole to speed up the rise and fall time of the beam pulse injected into the RFQ.
7. The two LEBT solenoid are identical as well are identical the two beam pipes that are inside. A bellow and a gas injection is integrated in their design. Both pipes are followed by a gate valve that will permit maintenance operations without break the vacuum where is not needed.
8. Two are the main function of the LEBT collimator, the first is to work as a beam dump for the for proton beam when it is deflected by the chopper electric field and for the H_2 beam. The latter scope is a vacuum break between the LEBT that can work with a pressure up to $6 \cdot 10^{-5}$ mbar and the RFQ that need to work under $1 \cdot 10^{-7}$ mbar. Additionally, in this element there are also

ISBN 978-3-95450-186-1

integrated a repeller electrode that avoid the transmission of free LEBT electron to the RFQ and a beam current transformer that measure the beam current injected in the RFQ.

9. In the ESS accelerator layout, after the LEBT collimator will be the RFQ, while during the commissioning in Catania will be a diagnostic tank with the same characteristics of the LEBT diagnostic tank.

The source is actually fully assembled (Figure 1) while only the first part of the LEBT is actually assembled (Figure 3) and ready for the first two commissioning phases. This setup is able to house one FC, one DSM, one EMU and a beam stop. The first phase will be the characterization of the current produced by the source using the FC and the DSM. In November the EMU delivery is planned and the emittance of the beam produced by the source will be characterized for different source parameters configuration.

Figure 3: LEBT configuration for the first two beam commissioning phases.

FIRST PLASMA CONDITIONING RESULTS

Plasma conditioning is the first operation that must be done after the assembly of a new source. It consists in the gradually turn on of the RF power to slowly increase the plasma density. The plasma is cheeped for different hours and for different times it is switched on and off. It is needed to clean the plasma chamber walls using the plasma sputtering and heating. Even if it is only a cleaning procedure we tried to used it also as a test to evaluate the goodness of some technical choices.

The three coils magnetic system of PS-ESS was designed to be a very flexible system. By using the same code used for the design of the magnetic system, COMSOL Multiphysics, we are able to choose a magnetic field profile and obtain, as an output, how to energise the three coils to be as close as possible to the request. The code provide also how much the obtained profile differs from the requested. Figure 4 is an example of how much precise can be the definition of the magnetic field profile. We requested a flat field of 900 G inside the plasma chamber and the ECR resonance (875 G) at the injection side of the plasma chamber wall. This is the most common magnetic field profile used for the Microwave Discharge Ion Source (MDIS) and with this profile we observed an excellent behaviour since the beginning. During the commissioning of the source we will have the time to test different magnetic profiles in a very easy way.

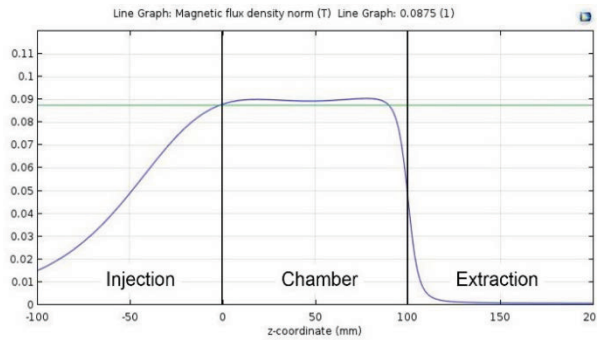

Figure 4: On axis magnetic field profile used during the plasma chamber conditioning.

The PS-ESS microwave injection line is composed by the magnetron head that produce the microwave, an Automatic Tuning Unit (ATU) that work as impedance matching between the wave guide and the plasma chamber, a directional coupler where two probes are connected to measure the forward and the reflected microwave power, the matching transformer and the plasma chamber. The data acquired with the two RF probes shows that the design is correct and an optimum match of power inside the plasma chamber is reached. Figure 5 shows that plasma ability to adsorb incoming microwave power increase gradually from 20 W to 120 W. After this value the plasma density is enough to adsorb more that 99.5 % of the injected power. This behaviour is promising for the future.

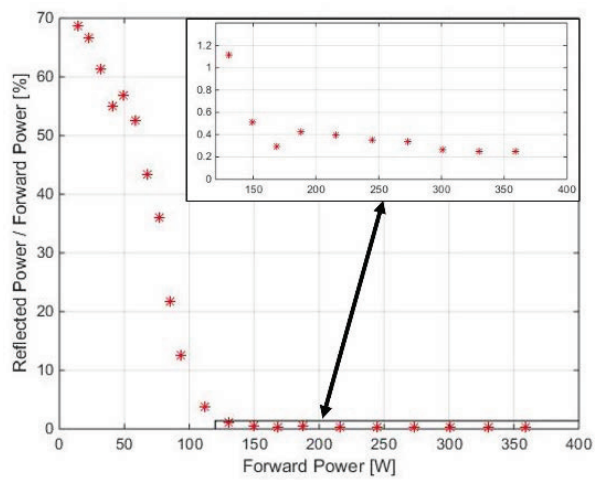

Figure 5: Fraction of reflected microwave power vs injected.

ISBN 978-3-95450-186-1

The software used for the data acquisition of the RF probes gives us also the possibility to extract the stability of the two measured power values. We select a data acquisition length of 10 us and an acquisition rate of 10 Hz, after 2000 of counts the standard deviation was calculated. Figure 6 shows the fraction between the standard deviation and the adsorbed power (forward minus reflected) versus the forward power. The result shows that with an injected power greater that 120 W the plasma sows a very stable condition with a fluctuation less than 0.05 %. This is a fundamental parameter that will help to reach the ± 2 % of beam stability requested by ESS.

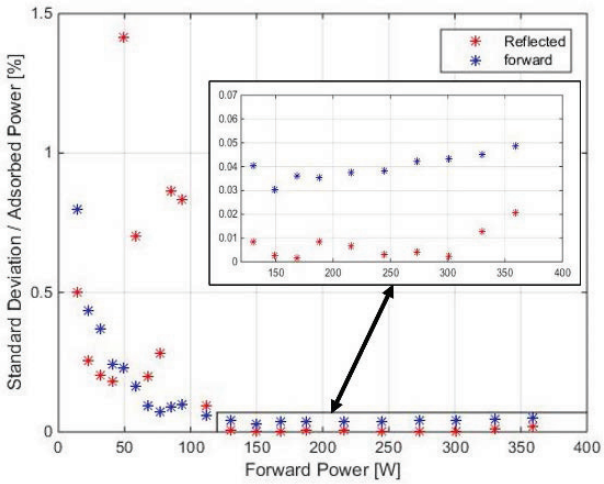

Figure 6: Stability of microwave absorbed power.

CONCLUSION

The design of PS-ESS and the LEBT is completed, the manufacturing of all components is almost completed and the installation is ready for the first beam commissioning. The first plasma conditioning stage produces comfortable result that confirm the technical choses inserted in the design of the microwave injection line. The stability of the microwave power adsorbed by the plasma, greater than 99.95 %, is a promising result that will work to obtain the beam stability requested by ESS. Everything seems going in the right direction and we are confident for reach the performance requested by the ESS accelerator.

ACKNOWLEDGEMENT

The authors would like to acknowledge the support of INFN technical staff and of the mechanical workshop for the valuable work done in the design and manufacturing of several items of the ESS setup. The valuable support of different ESS and CEA groups was continuous and fundamental for all phases of the project.

REFERENCES

[1] L. Neri, L. Celona, S. Gammino, D. Mascali, G. Castro, G. Torrisi, B. Cheymol, A. Ponton, A. Galatà, G. Patti, A. Gozzo, L. Lega, and G. Ciavola. Rev. Sci. Instrum. 85, 02A723 (2014)

[2] R. Gobin, P.Y. Beauvais, R. Ferdinand, P.A. Leroy, L. Celona, G. Ciavola and S. Gammino, Improvement of beam emittance of the CEA high intensity proton source SILHI, Rev. Sci. Instrum. 70(6) (1999) 2652–2654

[3] L. Neri, L. Celona, S.Gammino, D. Mascali, A. Caruso, A. Longhitano, L. Calabretta, B cheymol, A. Ponton. Proc. Of Linac conference, Tel Aviv 2012

[4] Y.I. Levinsen, M. Eshraqi, L. Neri, L. Celona. Proc. IPAC conference 2016, Busan, Korea

ISBN 978-3-95450-186-1

SECRAL II ION SOURCE DEVELOPMENT AND THE FIRST COMMISSIONING AT 28 GHz*

L. Sun#, W. H. Zhang, X. Fang, J. W. Guo, W. Wu, Y. C. Feng, X. Z. Zhang, Y. M. Ma, H. Y. Ma, Z. Shen, T. J. Yang, Y. Yang, B. Zhao, H. W. Zhao, L. Z. Ma
IMP/CAS, Lanzhou, 730000, China

Abstract

SECRAL II ion source has been successfully designed and developed at IMP. This ion source is a 3rd generation ECR machine optimized for the operation at 28 GHz. As a second superconducting ECR ion source developed at IMP with the identical cold mass design as SECRAL ion source, which has the sextupole coils external to the axial solenoids, the magnet performance is more robust according the training test. After a short time beam test at 18 GHz, SECRAL II has been commissioned at 28 GHz, and some preliminary results have been achieved with high charge state ion beam production. This paper will present the magnet design and test results. The first beam at 28 GHz will also be given.

INTRODUCTION

ECR ion sources have been used in IMP as the heavy ion injectors for over 20 years. Absolutely, the incorporation of ECR ion source to the heavy ion accelerator complex has already improved the machines' performance. The existing facility HIRFL (Heavy Ion Research Facility in Lanzhou) as shown in Fig. 1, which is mainly composed of one K69 cyclotron SFC, one K450 cyclotron SSC, RIBLL1 for radioactive beam production, cooler storage rings CSRm and CSRe, and the radioactive beam line RIBLL2 to connect the two rings [1, 2], has 3 injector ion sources, i.e. all permanent magnet ion source LAPECR1 for intense light ion beam beams, room temperature ion source LECR3 for intense medium charge state heavy ion beams (A≤40), and SECRAL the superconducting ion source for intense highly charged heavy ion beams (A≥40). SECRAL is now the main working horse of heavy ion beam for HIRFL, therefore in case of any big failure with the ion source, especially the superconducting magnet that has been in operation for over 11 years, the facility would be impossible to run heavy ion beams heavier than Ar, and the performance of the facility will be greatly affected. It has been highly recommend having a second high performance superconducting ECR ion source as the spare one. Additionally, as an upgrade program to boost the performance of the SSC cyclotron and also the storage ring, a project proposal has been issued to build a dedicated injection linac injector for SSC. The most interested ion beam for the design is several puA of U^{34+}, and the more preferred one is U^{37+}. Fundamentally, only with a 3rd generation ECR ion source, the goal could be achieved. Therefore, for a dual-purpose strategy, SECRAL II project was initiated.

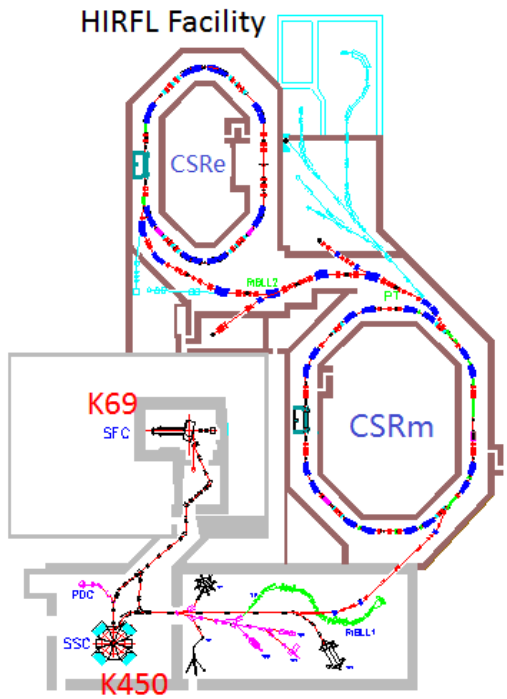

Figure 1: Layout of HIRFL facility.

SECRAL was connected to the injection line of HIRFL complex in 2007 and as of early 2016, more than 24,000 hours' beam time has been accomplished. It has been demonstrated as a very reliable and high performance ECR ion source. Especially, the recent progress with high intensity Ar and Xe beams, such as 1.42 emA Ar^{12+}, 1.1 emA Xe^{26+}, 0.67 emA Ca^{12+}, 0.68 emA Bi^{31+} and etc., has demonstrated its performance and capacity [3]. Logically, SECRAL II will be a duplicated one of SECRAL.

MAGNET DESIGN

The SECRAL II cold mass is almost a duplicated one of SECRAL. In that case, the axial fields inside the plasma chamber wouldn't be different from SECRAL. The radial field gradient would be the same as SECRAL. Therefore, the sextupole field at the same chamber wall would be the same. SECRAL was initially designed with 63 mm inner radius of plasma chamber, but after 1.5 mm thickness Ta shielding cylinder was integrated to do bremsstrahlung X-ray shielding to protect the main insu-

*Work supported by the 100 Talents Program of the CAS (No. Y214160BR0), NSF (contract No. 11221064) and MOST (contract No. 2014CB845500).
#sunlt@impcas.ac.cn

ISBN 978-3-95450-186-1

lator column, the radius was lowered down to ~60 mm with a SS plasma chamber and 58 mm with a Al chamber. And as a result, the radial field on the plasma chamber wall is much lower than designed value of 2.0 T, however it is sufficient for 24 GHz optimization of highly charged ion beams production, but not enough for a 28 GHz plasma, which needs at least ~2.0 T on the inner chamber wall. For this reason, SECRAL II magnet has to find a way to get a higher radial field on the chamber wall. By decreasing the gap between the warm bore and the copper thermal shield, the warm bore size is enlarged to ϕ142 mm. With a ϕ125 mm ID plasma chamber, ~2.0 T field could be achieved. Since SECRAL was designed and built without He recondensation system, the operation efficiency has been greatly affected, especially at high power. Even after the upgrade with an external recondensation system, the continuous operation at high power of 24 GHz is not promising. Therefore, SECRAL II should be designed with integrated LHe recondensation cryogenic system so as to be able to tolerate large dynamic heat load under high microwave power heating conditions. The typical continuous operation of SECRAL II at 28 GHz would be 4-5 kW, and according to the experience with SECRAL [4] and VENUS [5], this will give an approximately 4~5 W heat load to the 4.2 K cold mass. It is quite comfortable to design the cryogenic system with a cooling capacity of over 5 W. For this goal, 5 GM 1.5 W@4.2 K coolers have been utilized in the design. The main design parameters are given in Table 1.

Table 1: Main Design Parameters of SECRAL II

ω_{ecr}	28 GHz
B_{inj}	3.7 T
B_{ext}	2.2 T
Mirror Length	420 mm
Radial field at inner chamber wall	~2.0 T
Warmbore ID	Ø142 mm
Coldmass length	810 mm
Dynamic cooling capacity	> 5 W

MAGNET FABRIATION AND TEST

Cold Mass Fabrication

Cold mass is the critical part of the magnet, and it is also the most technically challengeable part of the project. SECRAL II magnet cold mass is mainly composed of three axial solenoids wounded on a stainless steel bobbin, six sextupole coils rested on the axial coils bound with 0.3 mm×3.3 mm stainless steel strip, cold iron blocks to boost the radial field and also to minimize the stray field, two iron flanges to connect and fix the position of the sextupole coils and axial coils, and the outer most aluminium rings to clamp the sextupole coils. Figure 2 gives the Solidworks sketch of the cold mass. Both the sexupole coils and axial solenoids are using the same type of NbTi wire from WST (Western Superconducting Technologies Co., Ltd). The typical features of the adopted wire are given in Table 2. The guaranteed superconducting performance is 668.7 A@7 T (4.2 K). Calculation with TOSCA 3D shows that the highest superimposed field on the coils is situated on the sextupole coils of 7.8 T@191.0 A which corresponds to the loading factor of ~87.5%. The highest field on the injection solenoid is 7.3 T@308.7 A which also corresponds to a loading factor of ~87.6%.

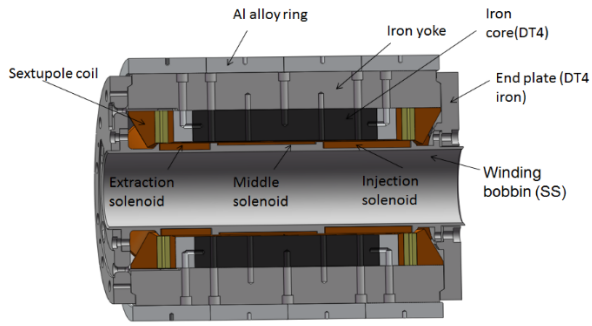

Figure 2: Sketch plot of SECRAL II cold mass.

Table 2: Typical Features of the Rectangular Wire from WST Used for SECRAL II Fabrication

Item	Specs.
Type	Monolith
Insulation	Formvar
Bare size (mm^2)	1.20 × 0.75
Insulated size (mm^2)	1.28× 0.83
Cu/Sc ratio	1.3:1
RRR	>100
No. of Filaments	630
Filament size (μm)	27.6
Pitch size (mm)	15

All the coils are wounded through wet winding with Stycast 2850FT black epoxy. After the solenoids were finished, stainless steel strip is used to do the coil binding. Fiberglass cloth is adopted for insulation purpose. Sextupole coil winding is more complicated and difficult because of the special cross-section configuration and the racetrack layout. Each coil was wound around a 5-piece core, the central portion being an iron pole to enhance the radial field, two aluminium ends designed to compensate for thermal contraction from room temperature to 4.2 K and two G10 fillers to avoid the localized highest field region. The picture of one of the sextupole coils is given in Fig. 3. After curing, the sextupole coils were also formed to have even external shape for assembly by vacuum impregnation. The finished sextupole coils were bolted to cold iron segments separately, and thus 6 completed sextupole blocks were ready for assembly. The sextupole blocks were positioned around the solenoid bobbin through two end iron plates to fix the position and do pre-clamping. One of the very obvious virtues of SECRAL type configuration is that the Lorentz forces at the sextupole coils ends are all pointing outwards radially instead of being inwards and outwards periodically with traditional configuration magnet, therefore no radial support of the sextupole coil ends were needed provided that the coils are robust enough after curing. Very efficient

ISBN 978-3-95450-186-1

pre-clamping of the sextupole coils were made by tight fitting installation of the aluminium rings. The negative tolerance designed aluminium rings were installed externally to the cold iron cylinder through hot shrinkage fit at about 150℃. Figure 4 is the picture of the completed cold mass at the assembly site.

Figure 3: Picture of one of the sextupole coils.

Figure 4: Completed cold mass at the assembly site.

Cold Mass Test

The solenoids were tested in test Dewar separately when they were ready in 2013. Limited by the current power supply, all the three solenoids were only energized to 115% of the design currents without any quenches. 18 months after the fabrication contact being signed, the cold mass was ready for test Dewar training. The magnet system was supported vertically from the top of the magnet test Dewar. A set of quench protection system was installed, which is identical to the final one to be utilized in the real Dewar. The voltage on each coils were monitored to diagnose the quench triggering. Cold mass temperature and LHe depth were also monitored during the training. Since the stored energy of SECRAL is about 0.7 MJ at the designed currents, most of the LHe filled in the test Dewar (~220 liters) were evaporated when a quench happed at ~90% of the designed currents.

Energized separately, the sextupole coils reached 85% of the designed currents with 6 quenches. Then they were energized together with the axial coils. During the whole system training, all the elements were energized evenly together, which was realized by matching the ramping rate of each superconducting coil controllers and going in steps. 8 quenches were detected before the cold mass trained to 90% of the designed currents. It seems that more quenches are predicted if the magnet needs to be further trained to the designed values.

Cryogenics

The cold mass is housed in a Ø817 mm ID 821 mm long LHe tank. Cold mass, LHe and the helium tank all together weighs about 1.54 tons, which will be supported by 8 support rods. To minimize the heat load to 4.2 K region, G10 material is utilized. 6 auxiliary SUS304 rods are also considered in the design to have redundant supports to ensure transportation safety. External to the 4.2 K reservoir, generally two thermal installation stages are designed. The first one is the 60 K copper thermal shield, and second one is the vacuum buffer between 60 K and room temperature. MLI solution is also considered in the design. The MLI are used between LHe tank and the 60 K shield, and inside the vacuum vessel. A typical layer density of 25 layers/cm is adopted. Evaporated helium gas will be recondensed to LHe by 5 condensers bolted to the 2nd stage of five 1.5 W GM coolers individually. To realize quick maintenance of the GM coolers without warming out the whole system, cryocooler sleeves are introduced in the design with the sacrifice of about 0.13 W extra heatload induced by the each of the sleeves. 5 HTS leads are used to minimize the ohmic and conduction heat load between 60 K and 4.2 K stages. 5 Sumitomo RDK-415 D coolers can provide about 200 W cooling capacity at 60 K that is sufficient for the 60 K thermal shield cooling. The estimated total static heat load at 4.2 K is about 1.86 W, which allows a maximum dynamic heat load of 5.64 W. Figure 5 is the sectional plot of SECRAL II magnet with most of the subsystems integrated.

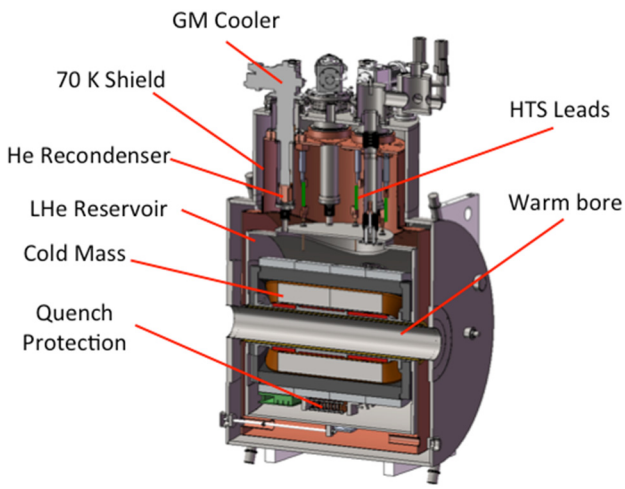

Figure 5: Side view of the magnet sectional plot.

Magnet Test

The magnet arrived at IMP in October 2015. User's site test had been completed in that December after about one month's preparation. The magnet was eventually ener-

ISBN 978-3-95450-186-1

gized to ~100% design currents after 9 quenches, which announced the success of this magnet fabrication. A comparison between the SECRAL and SECRAL II magnets on user's site test results is given in Fig. 6. SECRAL II magnet indicates more robust coil clamping as it reaches 95% of the design currents via 3 quenches. But it has to overcome the preloading while releasing the stress caused by slight movement during ramping to higher currents, which might be a stepwise process if the preloading is high. The cryogenics system was tested during the system cooling down and static condition at 4.2 K. According to the test with embedded heaters at 4.2 K region, a dynamic heat load capacity of ~6.0 W is estimated.

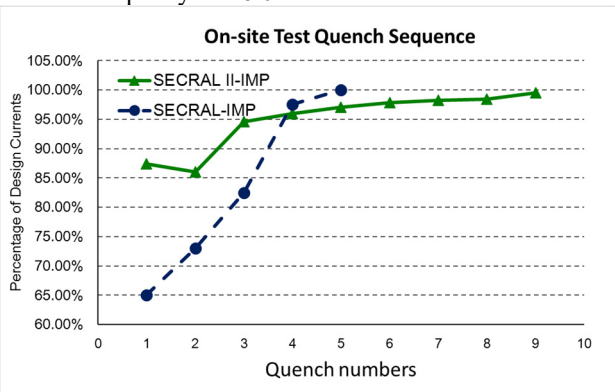

Figure 6: User's site training results of SECRAL and SECRAL II magnets.

SECRAL II TEST BENCH

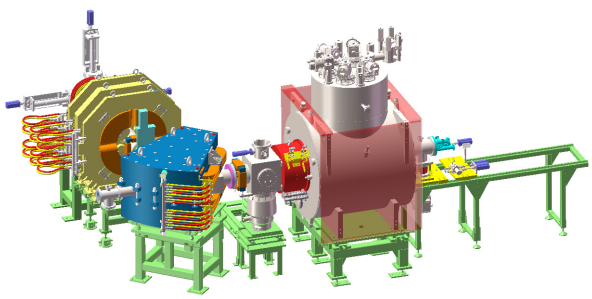

Figure 7: Layout of the SECRAL II test bench.

SECRAL II plasma will be heated by the microwave power from a CPI 10 kW/28 GHz gyrotron amplifier. The plasma chamber is floated to a 25 kV high voltage so as to have efficient beam extraction. A triode extraction system will be adopted to have flexibility on beam extraction optics optimization and suppression of secondary electrons entering the acceleration region. Ion source vacuum is pumped by oil free pumps. A 700 L/s turbo pump is to be installed at source injection tank and a 2000 L/s pump is going to be mounted on the source extraction box. Extracted beam will be focused by a solenoid with aberration correction design. Extracted ion beams will be analysed by a 180 mm gap, 510 mm bending radius, 90° double focusing bending magnet. Knowledge from beam line design of VENUS [6] and experimental results from SECRAL [7] indicates that large vertical gap can maximize the beam transmission efficiency through the M/Q analyzer and minimize the high order aberration pickup at the meantime. A set of triplet quadrupole magnets are utilized after the bending magnet so as to have optimal tuning of the analysed beam twiss parameters and also to improve the beam optical resolution, especially for high intensity very heavy ion beams, such as Bi and U beams. The layout of the test bench is given in Fig. 7.

FIRST COMMISSIONING RESULTS

SECRAL has been mainly commissioned at 28 GHz with O and Xe plasma. The 1st plasma with beam extraction at 18 GHz has produced 1.75 emA O^{6+}. At 28 GHz, with even 1 kW, about 2.2 emA O^{6+} has been extracted, which is obviously a strong frequency effect against that of 18 GHz. The plasma responds linearly to microwave power input. At 4.5 kW, 5.4 emA O^{6+} has been obtained at the source potential of 25 kV. At 3.5 kW, a 1.57 emA O^{7+} beam has also been extracted. Intense beam production wouldn't be possible without dense plasma having been built. A 20 emA total drain is detected when 5.4 emA O^{6+} created. For Xe^{27+} production, 3.5 kW has been used to give a result of 510 eμA beam intensity. Given more microwave power, this intensity could be further increased according to the beam tuning. Thanks to the high beam acceptance provided by this larger gap dipole. When 8.0 emA drain current of O+He ions transmitting in the system, a 84% transmission efficiency was observed. For 7.0 emA Xe+O ion beams, a transmission efficiency of 86% was also achieved. Since sufficient M/Q separation has been made on the faraday cup, the slits are almost fully open to allow full transmission. The typical Xe spectrum is given Fig 8 when Xe^{27+} is optimized.

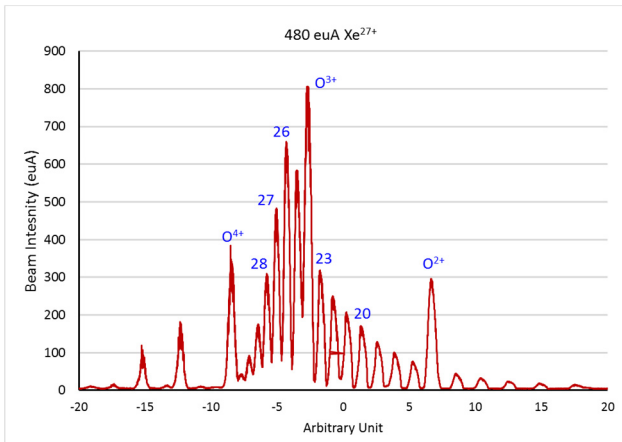

Figure 8: Typical spectrum optimized for 480 eμA Xe $^{27+}$ beam production.

During the commission at 28 GHz, the SS plasma chamber was burnt by the plasma twice at the locations of lowest |B| inside the plasma chamber wall (Fig. 9), i.e. one at the source extraction and the other one at the source injection (for the same plasma chamber). SECRAL had been tested at even much higher microwave power for several years without any burnt holes in the plasma chamber. And the field mapping of SECRAL II is quite consistent with the design value. Under those conditions,

ISBN 978-3-95450-186-1

plasma chamber cooling was doubted. A later water flow rate test of the plasma chamber showed that the water channels of the damaged chamber are not functioning well as a possible cause of fabrication mistake. Just before this workshop, a newly fabricated plasma chamber has been installed.

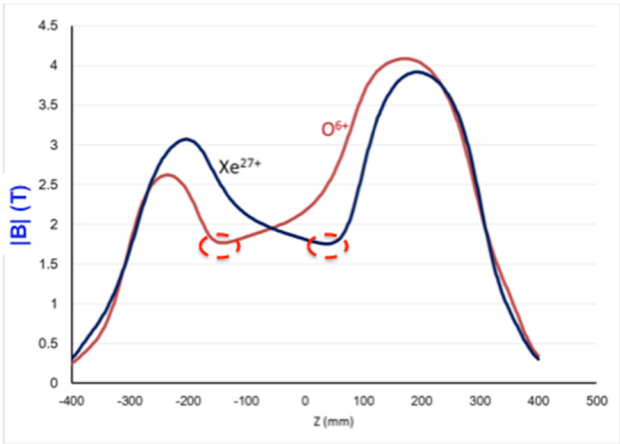

Figure 9: Two burnt holes' locations, one at the extraction side for O^{6+} plasma and one at the injection side for Xe^{27+} plasma.

CONCLUSION

SECRAL II ion source has been successfully developed after 3.5 years. The preliminary test of this ion source at 28 GHz has given quite promising results with 5.4 emA O^{6+}, 1.57 O^{7+} and 510 euA Xe^{27+}. But a malfunctioning plasma chamber gives trouble during high microwave power test with burnt holes. Here listed the key milestones of this project:

- 2013.01: Project contract
- 2014.07: Cold mass successfully tested
- 2015.08: Cryostat and magnet integration
- 2015.09: Factory test and acceptance
- 2016.01: 1st plasma at 18 GHz
- 2016.06: First oxygen plasma at 28 GHz and a plasma burnt hole at 5 kW

This project indicates that SECRAL structure is reliable and also reproducible with proper design and engineering.

ACKNOWLEDGMENT

Dr. Detlef Krischel from DK-Ing Consult, Dr. Ito Satoshi from KOBELCO, Dr. D. Xie from LBNL, Dr. Li Wang from SINAP and Dr. Linhui Gong from IPC are well acknowledged for their fruitful suggestions on SECRAL II magnet fabrication. The authors would also like to thank the team in XSMT (Xi'an Superconducting Magnet Technique) company for their great work on SECRAL II magnet fabrication.

REFERENCES

[1] J. W. Xia *et al.*, "HIRFL Status and HIRFL-CSR Project in Lanzhou", in *Proc. APAC'98*, Tsukuba, Japan, March 1998, p.342 (1999); http://www.JACoW.org

[2] Y. J. Yuan *et al.*, *Nucl. Instr. Meth.* B 317, 217 (2013);

[3] L. Sun *et al., Rev. Sci. Instrum*. 87, 02A707 (2016);

[4] H. W. Zhao *et al., Rev. Sci. Instrum*. 81, 02A202 (2010);

[5] D. Leitner *et al., Rev. Sci. Instrum*. 77, 03A302 (2006);

[6] M. Leitner, S. R. Abbott, D. Leitner, C. Lyneis, "A High Transmission Analyzing Magnet for Intense High Charge State Beams", ECRIS'02, Jyvaskyla, Finland, June 2002, p. 32 (2002);

[7] Y. Yang, L. T. Sun, Q. Hu, Y Cao, W. Lu, Y. C. Feng, X. Fang, H. W. Zhao, and D. Z. Xie, *Rev. Sci. Instrum*. 75, 02A719 (2014).

ISBN 978-3-95450-186-1

FIRST PLASMA OF THE PHOENIX V3 ECR ION SOURCE *

T. Thuillier†, J. Angot, L. Bonny, J. Jacob, A. Leduc, T. Lamy, P. Sole, LPSC, Grenoble, France
L. Maunoury, J.-L. Flambard, GANIL, France
C. Peaucelle, IPNL, France
T. Kalvas, JYFL, Finland

Abstract

PHOENIX V3 is an upgrade of the PHOENIX V2 ECR ion source granted by the European CRISP project. This new ECRIS features a larger plasma chamber and a reduced vacuum pressure under operation. The V3 source will replace the V2 one on the SPIRAL2 accelerator in 2018. The first plasma of PHOENIX V3 was achieved on May 9th 2016. The early commissioning of the V3 source at low 18 GHz power demonstrates as expected an enhancement of the high charge state production and Ar^{14+} intensity already exceeds the V2 one. Further enhancements are expected the outgassing will be achieved and the full RF power will be injected in the source.

MOTIVATION FOR THE SOURCE UPGRADE

The new SPIRAL2 accelerator at GANIL (Caen, France) includes a nuclear physics program dedicated to heavy ions with the S3 collaboration [1]. The present acceleration scheme of the LINAC imposes the production of ion beams with M/Q=3. High intensity beams are possible with such a M/Q up to M~40. Above this mass, the charge state is so high for a given mass that the achievable intensity collapses rapidly when the mass increases. S3 collaboration is thus interested in the procurement of ion beams with an intensity of several pμA up to the mass M~60. The availability of a European fund (CRISP Project) made an upgrade of the existing PHOENIX V2 source possible. The goal is to enhance the high charge state production to fulfil the need expressed by the S3 collaboration. The strategy of the upgrade is:

- to enhance the plasma chamber volume radially to increase the ion confinement time,
- to reduce the vacuum pressure in the source to decrease the charge exchange process, by adding a pumping system on the injection side of the source.

These two effects are expected to increase by 50 to 100% the M/Q=3 ions up to the mass 60 with respect to the existing V2 source.

V3 DESIGN

The magnetic simulation of V3 and some information on the mechanical design can be found here [2, 3]. For completion, a summary of the information is proposed below. The available funding allowed designing a new hexapole, a new plasma chamber and a vacuum box located on the injection side of the source. An overview of the V3 design is displayed in Fig. 1 (see next page). In order to minimize the impact of the modifications, the axial magnetic structure of the existing V2 source was kept unchanged. The main design difference came from a new hexapole providing a much larger radius at the plasma chamber wall of 45 mm (31 mm for V2). The new chamber volume is 1.4 liter, being ~2.2 time larger than the V2. The radial intensity at wall with the bare hexapole is 1.18T. Later, a special plasma chamber including soft iron slits on its outer part will be installed to reach ~1.25T along the magnetic poles at the aluminium wall. The source can accept new generation ovens up to Ø20 mm. The oven axis is slightly pointing toward the sky to prevent any liquid metal spill toward the plasma chamber. Two WR 62 waveguide ports are available (see Fig. 2). One is currently fed with an 18 GHz 2 kW RF Klystron. The second will be used to inject a 14 GHz power when it will be available for the project. A bias disk with some water cooling is also installed on the injection flange. Two new ovens will be tested in the source. The first, developed at LPSC, is a low temperature oven working up to ~600°C with a design similar to the one used in LBNL and MSU. The new oven will be commissioned in the early 2017 with calcium. The second oven is a new high temperature large capacity oven developed by GANIL. This oven is also expected to be commissioned in 2017 to feed the source.

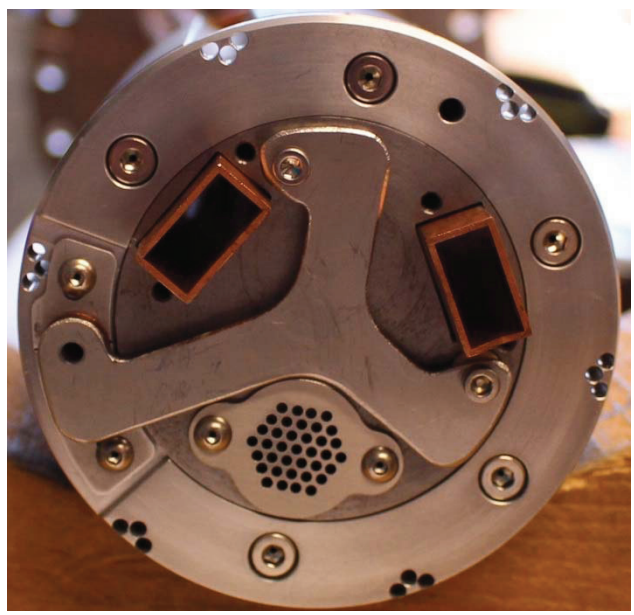

Figure 2: Photograph of the source injection flange.

* Work supported by EU Grant Agreement 283745
† thuillier@lpsc.in2p3.fr

ISBN 978-3-95450-186-1

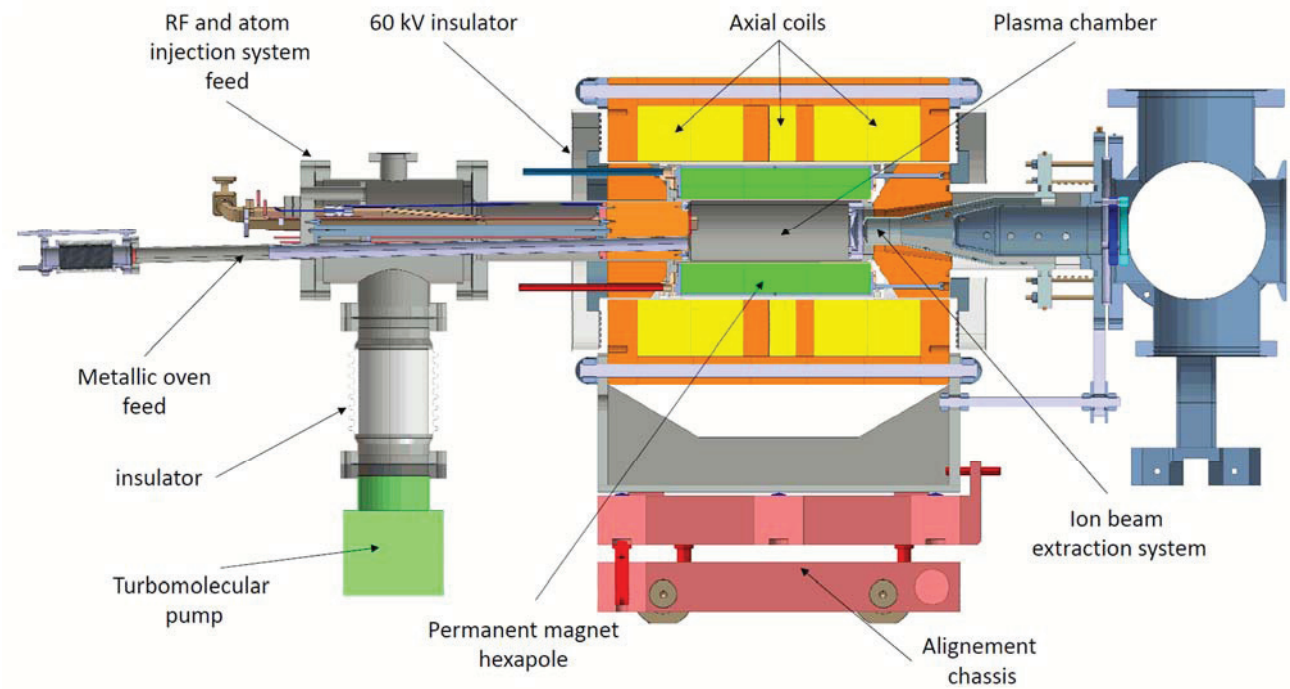

Figure 1: Sectional view of the PHOENIX V3 ion source mechanics.

FIRST PLASMA AND EARLY COMMISSIONING

The first ion source plasma was achieved on May 2016. A water flow measurement of the plasma chamber revealed an insufficient water velocity along the magnetic pole. So the early commissioning was limited to a conservative 50 W of 18 GHz power. Despite this dramatically reduced operation condition, it was possible to produce argon charge state distributions higher than what the V2 source can do. A simulation was performed to find the place where the hot electrons touch the wall (see Figure 3).The water channel geometry was then optimized to grant a turbulent flow along the poles on a sufficiently large surface covering the area of high power density electron deposition. A new plasma chamber was built to correct the flaw and the normal operation could start in August 2016. The first weeks of experiments were used to commission the LEBT which command control system was totally rebuilt in parallel to the source assembly. The residual gas pressure at the injection vacuum box is 2×10^{-8} mbar, provided by a 360 l/s turbomolecular pump. The new source responds normally to pressure and power. So far, the ion currents produced were limited to 500 W and were 100 µA of Ar^{12+}, 60 µA of Ar^{14+}, 450 µA of Ar^{8+}, 400 µA of O^{6+}. It is noticeable that the Ar^{14+} intensity is already higher than the one obtained with V2 (50 µA Ar^{14+}). The outgassing is still not over and better results are expected in a near future with higher RF power and better vacuum pressure. Extensive source operation will be performed in 2017 in collaboration with the GANIL team to study metallic beam production.

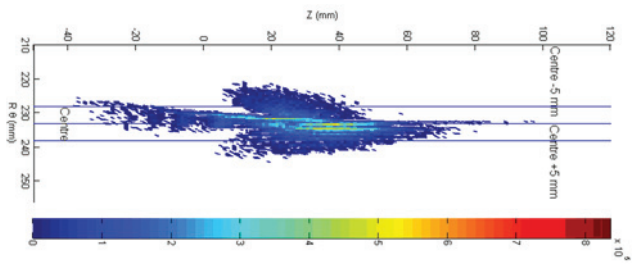

Figure 3: Hot electron impact at the wall and water channel limits (blue lines).

ACKNOLEDGEMENT

The authors wish to thank G. Machicoane from MSU for providing a piece of explosive bonding bi-metallic plate for the low temperature oven completion.

REFERENCES

[1] H.Savajols et al., S3: The Super Separator Spectrometer for SPIRAL2 stable beams Tours 2009 Proceedings, AIP conference series.

[2] T. Thuillier, J. Angot, T. Lamy, M. Marie-Jeanne, C. Peaucelle, C. Barue, C. Canet, M. Dupuis, P. Leherissier, F. Lemagnen, L. Maunoury, B. Osmond, "Recent results of phoenix v2 and new prospects with phoenix v3", in Proc. XXth Int. Conf. on ECR Ion Sources (ECRIS'10), Sydney, Australia, Sept. 2010, paper WEZO03, pp. 117-120.

[3] T. Thuillier, J. Angot, C. Barué, P. Bertrand, J. L. Biarrotte, C. Canet, J.-F. Denis, R. Ferdinand, J.-L.Flambard, J. Jacob, P. Jardin, T. Lamy, F. Lemagnen, L. Maunoury, B. Osmond, C. Peaucelle, A. Roger, P.Sole, R. Touzery, O. Tuske, and D. Uriot, Rev. of Scient. Instrum., 87, 02A733 (2016).

ISBN 978-3-95450-186-1

RECENT DEVELOPMENTS WITH THE GTS-LHC ECR ION SOURCE AT CERN

V. Toivanen*, G. Bellodi, C. Fichera, D. Küchler, A. M. Lombardi,
M. Maintrot, A. Michet, M. O'Neil, S. Sadovich, F. Wenander
European Organization for Nuclear Research (CERN), Geneva, Switzerland
O. Tarvainen, University of Jyväskylä, Department of Physics (JYFL), Jyväskylä, Finland

Abstract

Linac3 is the first link in the chain of accelerators providing highly charged heavy ion beams for the CERN experimental program. The beams, predominantly lead, are produced with the GTS-LHC 14.5 GHz Electron Cyclotron Resonance (ECR) ion source, operated in afterglow mode. In the framework of the LHC Injector Upgrade program (LIU), several activities have been carried out to improve the GTS-LHC and Linac3 performance, in terms of delivered beam current.

The extraction region of the GTS-LHC has been upgraded with redesigned apertures and the addition of an einzel lens, yielding improved Linac3 output. Also, a series of measurements has been performed to study the effects of double frequency heating on the afterglow performance of the GTS-LHC. A Travelling Wave Tube Amplifier (TWTA) with variable frequency and pulse pattern was utilized as a secondary microwave source. The double frequency effect commonly reported with CW operation of ECR ion sources boosting high charge state ion production was also observed in afterglow mode. Lastly, for studies of metal ion beam production, a dedicated test stand has been assembled to characterize the GTS-LHC resistively heated miniature oven performance.

INTRODUCTION

In order to prepare for the future high luminosity operation of the Large Hadron Collider (LHC), all the accelerators providing beam for the LHC experiments are undergoing an extensive upgrade program; the LHC Injector Upgrade (LIU). For the heavy ion accelerator chain this includes, from the lowest beam energy to the highest, the Linac3 linear accelerator, the Low Energy Ion Ring (LEIR), the Proton Synchrotron (PS) and the Super Proton Synchrotron (SPS). As part of the Linac3 upgrades, several activities have been carried out with the GTS-LHC Electron Cyclotron Resonance (ECR) ion source [1], which produces the primary heavy ion beams for the CERN experiments.

GTS-LHC is a 14.5 GHz second generation ECR ion source which is based on the Grenoble Test Source (GTS) by CEA, Grenoble [2]. The main differences to the GTS include a modified magnetic field structure with an added center coil and a stronger Halbach-style 36-piece permanent magnet hexapole. GTS-LHC is exclusively operated in afterglow mode to produce mainly lead ion beams, although also argon beam was delivered for experiments in 2015 and xenon is planned for 2017. The afterglow operation is performed with a 10 Hz RF heating cycle at 50 % duty factor. A ~200 µs ion beam pulse is selected and accelerated through the linac from the afterglow burst which is exhibited by the extracted ion beam after the microwave switch-off. The lead beam is produced as $^{208}Pb^{29+}$ with 2.5 keV/u initial energy, as it provides the highest particle current during afterglow, and is stripped to $^{208}Pb^{54+}$ at the end of the linac for injection into LEIR with 4.2 MeV/u energy.

This paper presents three activities that have been recently carried out with the GTS-LHC; the GTS-LHC extraction region upgrade, double frequency plasma heating combined with afterglow operation and oven studies for metal ion beam production. These topics are discussed in the following chapters.

EXTRACTION REGION UPGRADE

Following a dedicated simulation study [3–5] the beam extraction region of the GTS-LHC was modified in the beginning of 2016. The goal of this upgrade was to increase the beam currents out of Linac3 by mitigating the beam losses immediately after the ion source and by improving the flexibility of the ion source tuning and matching to the following low energy beam transport (LEBT) section.

One of the main issues of the original extraction system that was observed with the simulations and verified with inspection of the extraction chamber was the strong divergence of the extracted ion beams. Due to the limited tuning capabilities of the extraction system this resulted in the collimation of a significant part of the extracted ion beam at the entrance of the beam pipe at the end of the ion source extraction chamber [4]. In order to improve the beam transmission in this region, the section immediately downstream from the extraction electrodes was redesigned with two main modifications. Firstly, in order to improve the transport flexibility and to mitigate beam collimation, the aperture restrictions were relaxed by increasing the beam pipe bore through the first beam line solenoid from 65 to 100 mm. Secondly, a new bipolar einzel lens was installed inside the extraction chamber to provide additional beam focusing and matching to the following beam transport section. A comparison of the original and the upgraded extraction regions are presented in Fig. 1. Further details of the designs are given in Ref. [5].

The performance of Linac3 has improved steadily after the implementation of the extraction region upgrade, as experience has been gained on how to optimize the ion source matching to the new beam transport conditions. The present

* ville.aleksi.toivanen@cern.ch

ISBN 978-3-95450-186-1

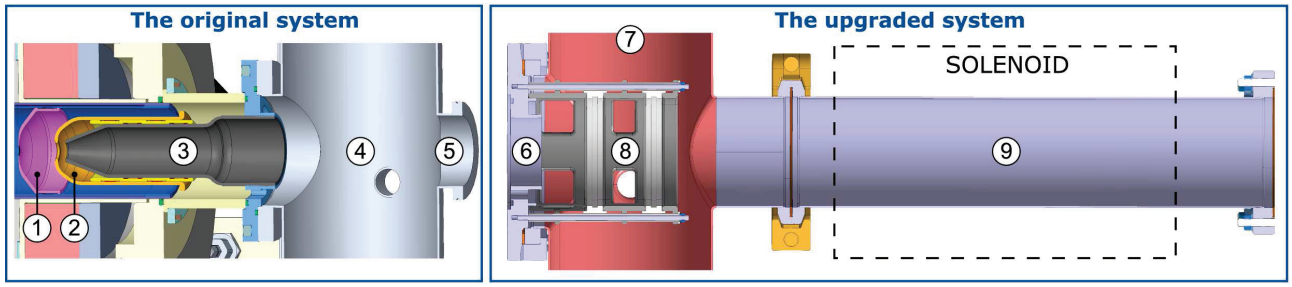

Figure 1: Comparison of the original and the upgraded GTS-LHC extraction regions. In the original design the intermediate (2) and grounded electrodes (3) are supported in front of the plasma electrode (1) on a flange which is connected to the extraction chamber (4). The chamber is followed by a 65 mm diameter beam pipe (5). In the upgraded system the flange (6) and the extraction chamber (7) have been redesigned to allow the installation of an einzel lens (8) and a larger 100 mm diameter beam pipe through the first beam line solenoid (9).

Table 1: Comparison of typical lead beam currents from the ion source and out of Linac3 before and after the extraction region upgrade. The values for the original system before upgrade are from the 2015 lead run.

Ion species and location	*Original system (2015 run)*	*Upgraded system*	*Improvement*
$^{208}Pb^{29+}$ from the ion source	170 µA	210 µA	24 %
$^{208}Pb^{54+}$ out of Linac3	25 µA	35 µA	40 %

performance with lead downstream from the ion source and at the output of Linac3 is presented in Table 1. Compared to the 2015 lead run, the beam currents of $^{208}Pb^{29+}$ delivered from the ion source through the spectrometer have increased over 20 %, and the Linac3 output current for $^{208}Pb^{54+}$ is up to 40 % higher than before. The increased flexibility in the ion source tuning allows operation with different source settings than before without compromising the beam transmission. This has led to improved beam stability and matching to the rest of the linac, as is evident from the fact that the linac output current exhibits greater improvement than the current out of the ion source.

DOUBLE FREQUENCY OPERATION IN AFTERGLOW MODE

Using multiple discrete frequencies simultaneously for ECR plasma heating is a well-established method to improve ECR ion source performance with high charge state ion beam production (see e.g. Refs. [6, 7]). However, the experiments with multiple frequencies have been mainly performed with ECR ion sources operated in CW mode, and especially detailed data with afterglow operation is not readily available. As this is the main operation mode to produce beams at Linac3, a set of experiments have been performed to study the effects of double frequency heating on the afterglow performance of GTS-LHC. A comprehensive description of the studies is reported in Ref. [8].

The measurement setup used in the experiments is presented in Fig. 2. The microwave radiation at the primary 14.5 GHz frequency is delivered from a klystron amplifier through a WR62 rectangular wave guide assembly. In normal operation the klystron is operated in pulsed mode at 10 Hz repetition rate and 50 % duty factor, providing ~2 kW of power during the RF pulse. The secondary WR62 wave guide of the ion source, normally used for a spare 14.5 GHz klystron, was connected to a Travelling Wave Tube Amplifier (TWTA) to provide microwaves at a variable secondary frequency. The transmission and reflection characteristics of the HV break and the vacuum window between the TWTA and the plasma chamber were measured to determine the limits for the frequencies that could pass through the system. As a result, the frequency range for the secondary microwaves was limited to 12–18 GHz. For these frequencies the maximum power delivered from the amplifier was ~300 W. A directional isolator was installed at the output of the TWTA to protect it from the pulsed main microwave radiation. The input signal was generated with a variable frequency oscillator driven with a digital pulse and delay generator. The pulse generator was triggered by the klystron timing signal, allowing pulsed operation of the TWTA with respect to the klystron pulse pattern, as well as CW operation.

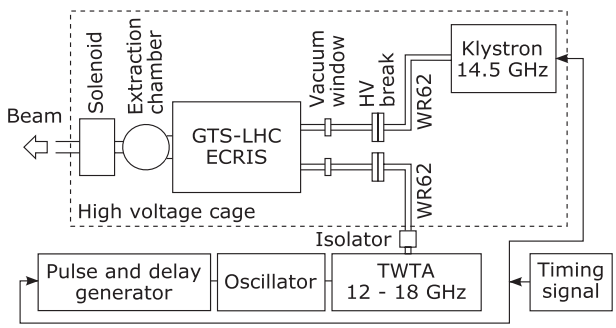

Figure 2: A schematic presentation of the double frequency measurement setup at Linac3.

ISBN 978-3-95450-186-1

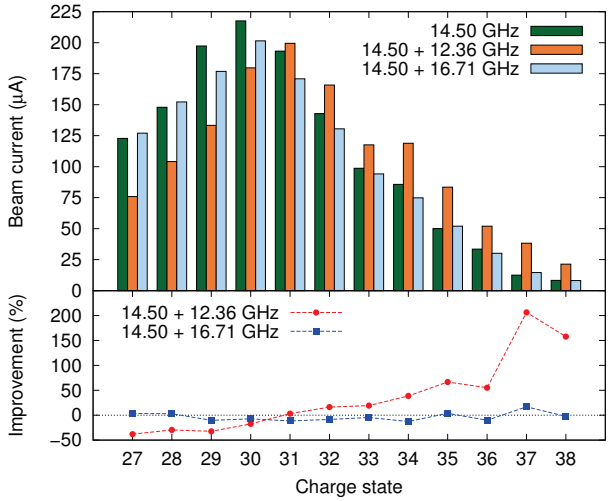

Figure 3: Top: Afterglow CSDs measured with single and double frequency operation. Klystron output at 1920 W, TWTA at 180 W and 185 W for 12.36 GHz and 16.71 GHz, respectively. Bottom: Beam current improvements with two frequencies compared to the single frequency case.

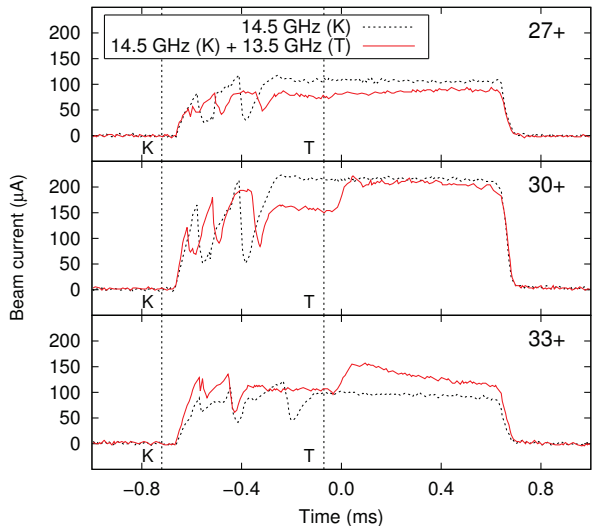

Figure 4: Beam currents of Pb^{27+}, Pb^{30+} and Pb^{33+} with single and double frequency heating. 13.50 GHz secondary frequency with 0.65 ms trailing edge delay (indicated with the dashed vertical lines for klystron (K) and TWTA (T)). To avoid beam-loss induced interference with the linac RF systems, the steady state part of the beam pulse at $t < -0.68$ ms and the tail of the afterglow at $t > 0.63$ ms have been actively removed from the beam pulse.

When both the primary and the secondary microwave sources are pulsed synchronously and a suitable secondary frequency is chosen, a shift to higher charge states was observed in the charge state distribution (CSD) measured during the afterglow. Concerning the frequency dependency of this effect, the shift in CSD was in general seen when the secondary frequency was chosen to be lower than the primary one, whereas with higher frequencies the influence to the beam currents was significantly weaker and no clear shift was evident in the measured data. An example of this is presented in Fig. 3. It was verified that the shift to higher charge states is not simply due to increased total microwave power, as this effect was observed also when the combined power in double frequency operation was matched with the power level used in the single frequency case. However, an increase in the total power in the double frequency case does provide a further improvement for the high charge states.

Introducing a time delay between the trailing edges of the primary and the secondary microwave pulses leads the afterglow current to exhibit a second step-like increase following the switch-off of the TWTA. This reflects the two-stage collapse of the plasma, indicating that part of the ion population remains trapped until the secondary microwaves are switched off. Figure 4 showcases this current behaviour for selected lead charge states.

When the TWTA is switched to CW mode while keeping the klystron pulsed, an afterglow burst is still observed after the trailing edge of the primary microwave pulse, but the beam current during the discharge is reduced compared to pulsing of both frequencies. This mitigation is explained by the secondary microwaves sustaining the plasma between the primary microwave pulses and consequently part of the ion population is constantly retained inside the trap.

Pb^{29+} was studied in more detail, as it is the primary beam from GTS-LHC. Best response was observed with 14.2 GHz pulsed secondary frequency, yielding beam current improvements in the order of $10 - 20$ % after the source.

With the ion source solenoid settings used in the experiments, the lowest value of the minimum B field inside the plasma chamber was 0.47 T, which corresponds to a lower limit of 13.16 GHz for the microwave frequencies that fulfil the electron cyclotron resonance condition for non-relativistic electrons. This limit excludes the frequencies around 12.36 GHz which experimentally provided the best improvement to the high charge state beam currents. For these frequencies the resonance only exists for electrons with energies >30 keV. Further heating of this population should not directly improve the ionization efficiency of the measured ion species, because these electron energies are significantly higher than the energies corresponding to the maxima of the electron impact ionization cross section for the lead charge states in question (<8 keV [9, 10]). However, it is noted that improved performance with secondary off-resonance frequencies has recently also been reported with CW operation [11]. It has been suggested that this effect is caused by suppression of plasma instabilities through the interaction of the secondary microwave radiation with the hot electron population in the plasma. However, further studies are required to identify the exact mechanisms behind this observed behaviour.

ISBN 978-3-95450-186-1

MINIATURE OVEN STUDIES

The lead ion beams delivered by Linac3 are produced with GTS-LHC using resistively heated miniature ovens. The oven design consists of an aluminium oxide crucible, tantalum heating filament, tantalum oven body and stainless steel cane to allow axial insertion through the ion source injection plug. The oven structure is presented in Fig. 5.

The GTS-LHC features two oven ports through the injection plug. In normal operation the two ovens provide 2 – 3 weeks of lead beam operation between refills. However, it has been observed that when refill is required due to degrading beam performance, typically about 2/3 of the lead is still left in the oven. In some instances the operation is also interrupted by blockage of the oven tip, either by formation of lead oxide or droplets of metallic lead. In order to study the oven performance and failure mechanisms in more detail, a dedicated offline test stand has been constructed with capabilities to measure the oven temperatures and lead evaporation rates in varied input power and vacuum or gas atmosphere conditions. The lead evaporation from the oven is measured using an INFICON surface deposition detector with quartz crystal sensor. Temperature measurement are primarily performed with vacuum grade thermocouples. ZnSe viewports with high infrared transmission are an additional option for temperature monitoring with a thermal camera and borosilicate viewports are used for visual inspection during measurements.

Figure 6 presents a temperature characterization of the oven, measured in the test stand. For lead beam production the oven is normally operated with power levels above 6 W, which translates to temperatures over 600 °C based on the measurement. With 20 W, which is the maximum power used in operation, the temperature inside the crucible reaches about 950 °C. It is observed that the measured oven temperatures T follow a $T \propto P^{1/4}$ relationship, where P is the oven input power. This indicates that radiative losses dominate the oven thermal behaviour. In addition, the measurements have shown that the oven is slow to respond to input power changes, and several hours are required to reach temperature equilibrium at lower power levels. This delayed response is also observed in GTS-LHC operation.

The normalized lead evaporation rate is presented in Fig. 7 as a function of the crucible temperature. The measured data shows steady response in the lead output and the observed temperature dependency agrees well with the shape

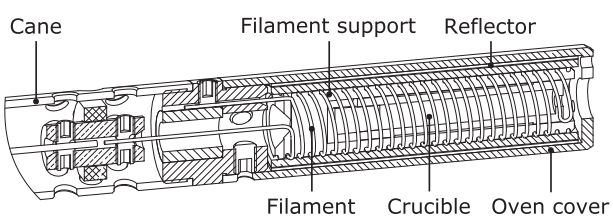

Figure 5: A schematic of the GTS-LHC miniature oven. The outer diameter of the oven is 14 mm and the total length with the cane (partially shown) is 870 mm.

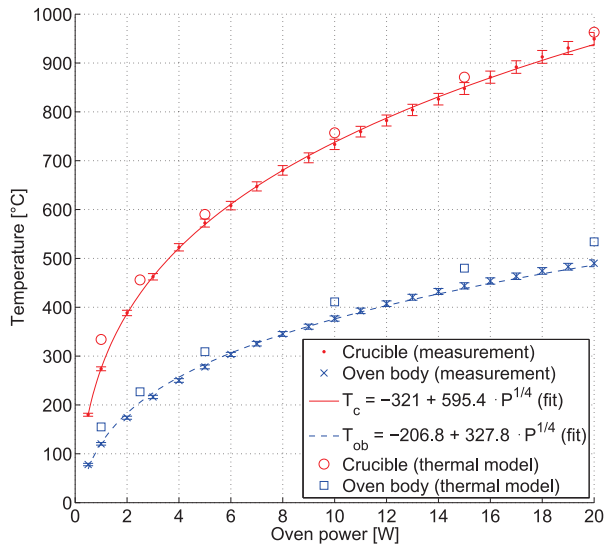

Figure 6: Measured crucible and oven outer body temperatures as a function of the oven input power. Temperatures predicted by the oven thermal model are also presented.

predicted by theory. The theoretical calculation is based on the Hertz-Knudsen equation for evaporation flux and an empirical formula for the estimation of the lead vapour pressure [12]. Figure 8 presents the long term behaviour of the lead output from the oven operated at a constant power of 12.5 W. Two phenomena observed with the measured evaporation rates are demonstrated in the figure. For the first 120 hours, the oven output decreases steadily over time with an average slope of about −0.3 unit-%/hour. This is then followed by instabilities characterized by sudden step-like decreases with plateaus of stable output between them. The latter behaviour could be connected to the dynamics and redistribution of the remaining lead inside the crucible, but further studies are necessary to give a more detailed explanation. The implication of the decreasing trend is that the oven power needs to be adjusted regularly to keep the evaporation rate at a constant value. This is indeed what is done in the GTS-LHC operation to maintain the extracted lead beam current at a constant level.

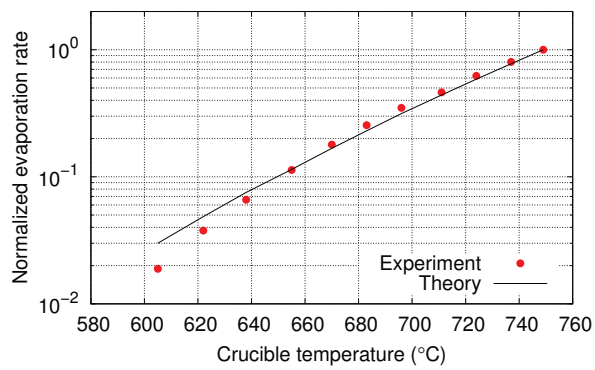

Figure 7: Measured and theoretically calculated normalized evaporation rates with varied crucible temperature. The temperature range for the measured data corresponds to oven powers between 6 W and 11 W.

ISBN 978-3-95450-186-1

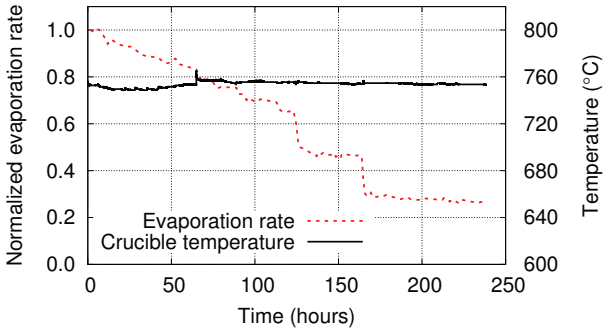

Figure 8: Evolution of the lead evaporation rate and crucible temperature over time with a constant oven heating power of 12.5 W.

A numerical thermal model of the miniature oven has been developed with the ANSYS simulation tools [13] to complement the measurements and provide insight into the temperature distributions inside the oven. The model is benchmarked against measured temperature behaviour at selected locations on the oven body and the model predictions agree well with the measured values (see Fig. 6).

Figure 9 presents calculated temperature distributions inside the oven with 10 W and 15 W heating powers. It is observed that a good temperature uniformity is achieved for the lead sample inside the crucible, while the tip of the oven remains significantly colder. The colder tip is presumed to be one of the issues contributing to the oven blockages experienced during operation.

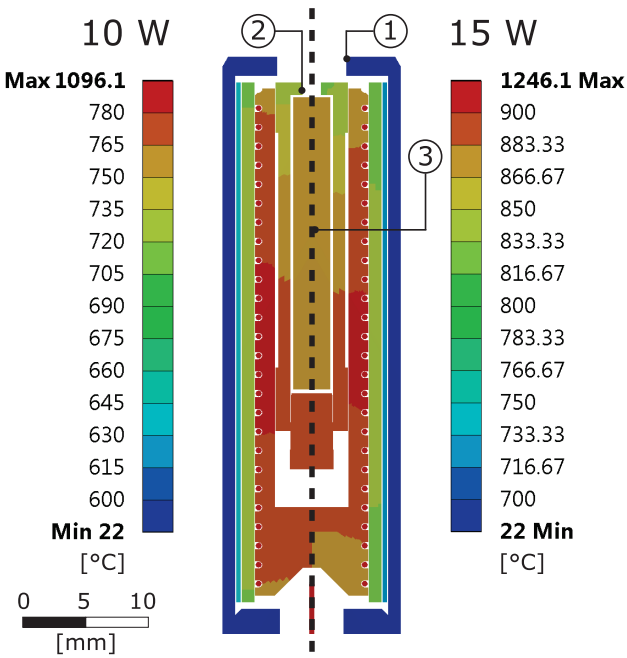

Figure 9: Simulated temperature distribution inside a lead filled oven with 10 W and 15 W powers. Temperatures at locations 1, 2 and 3 are 413, 729 and 756 °C for the 10 W case and 482, 833 and 870 °C for the 15 W case.

CONCLUSIONS

Thanks to the successful upgrade of the GTS-LHC extraction region, Linac3 is now routinely operated with improved beam currents and beam stability. The new beam conditions have also proven to be easier to reach and maintain owing to the increased flexibility in the ion source tuning. The present performance now fulfils the Linac3 output goal set in the LIU project, but studies to further improve the heavy ion performance will continue.

The double frequency experiments show that this method improves the high charge state ion currents also in afterglow mode. This combination is thus a viable option to improve ion source performance in applications where pulsed beams of high charge state ions are required. An improvement was also seen with Pb^{29+}, the main ion produced with GTS-LHC. Further studies are planned to assess if this method would be advantageous in normal Linac3 operation.

Concerning the miniature oven studies, the first basic characterization of the GTS-LHC oven has been carried out. The results show that the oven behaves mostly in the expected way in terms of temperature and evaporation rate trends. In addition, the thermal modelling has given the first hints to possible causes of the observed oven failure mechanisms. The future studies will focus on the details of these mechanisms and the different factors that impact the oven output behaviour (both magnitude and stability) during operation.

REFERENCES

[1] L. Dumas et al., in *Proc. of ECRIS'06*, Lanzhou, China, published in *HEP & NP, Vol.* 31, Suppl. 1, pp. 51-54 (2007).

[2] D. Hitz *et al.*, in *Proc. of ECRIS'02*, Jyväskylä, Finland (2002).

[3] V. Toivanen *et al.*, in *Proc. of ECRIS'14*, Nizhny Novgorod, Russia (2014).

[4] V. Toivanen *et al.*, *Rev. Sci. Instrum.* 87, 02B923 (2016).

[5] V. Toivanen *et al.*, *Rev. Sci. Instrum.* 87, 02B912 (2016).

[6] R. Vondrasek *et al.*, in *Proc. of ECRIS'02*, Jyväskylä, Finland (2002).

[7] R. Vondrasek *et al.*, *Rev. Sci. Instrum.* 77, 03A337 (2006).

[8] V. Toivanen *et al.*, "The effect of double frequency heating on the afterglow performance of the CERN GTS-LHC electron cyclotron resonance ion source", to be published.

[9] I. G. Brown (Ed.), "The physics and technology of ion sources", John Wiley & Sons, Inc., 2004.

[10] NIST Atomic Spectra Database, `http://physics.nist.gov/PhysRefData/ASD/ionEnergy.html`

[11] V. Skalyga *et al.*, *Phys. Plasmas* 22, 083509 (2015).

[12] D. R. Lide (Ed.), "CRC Handbook of Chemistry and Physics", 76th Edition, CRC Press, 1995.

[13] The official ANSYS simulation tools website, `http://www.ansys.com`

ISBN 978-3-95450-186-1

PRACTICAL COMPARISON OF TWO-FREQUENCY HEATING PHENOMENA IN DIFFERENT ECR ION SOURCES

A. Kitagawa#, M. Muramatsu, NIRS, QST, Chiba, Japan
R. Rácz, S. Biri, ATOMKI, Debrecen, Hungary
Y. Kato, Osaka Univ., Osaka, Japan
W. Takasugi, AEC, Chiba, Japan

Abstract

Plasma heating in electron cyclotron resonance ion sources (ECRIS) with the injection of two microwaves having different frequencies has been studied. An 18 GHz ECRIS installed in the Heavy Ion Medical Accelerator in Chiba (HIMAC) at the National Institute of Radiological Sciences (NIRS) and a 14 GHz ECRIS at the Institute for Nuclear Research (ATOMKI) were utilized for this study. One was operated with the frequencies close together each; the other was tested with the two frequencies being even far from each other. The tendencies of the phenomena at both ECRISs were similar, and the output currents of highly charged ions increased with increasing the sum of two microwave powers.

INTRODUCTION

In order to improve highly charged ion production, the two-frequency heating technique was initiated by ECR pioneers Jongen and Lyneis in Berkeley, and some years later more successfully by Xie and Lyneis, again at Berkeley [1]. Since then, many ECR laboratories have tested this technique. The two-frequency heating technique has several advantages: it is effective for any kind of ion species, it is coexistent with almost all other techniques, and no modification of the existing structure is necessary, except for an additional microwave feeding.

Between 1998 and 2014 numerous experiments were carried out at NIRS; in each experiment a positive effect of the second microwave was demonstrated [2, 3]. Our basic observation concerning the productions of C, Ar, Fe, Ni, Kr, and Xe ions is that when the primary microwave power increases, the plasma shows instability, and it is difficult to keep. When an additional microwave with a different frequency is added in the above situation, the plasma stability is improved at greater microwave power. Our conclusion is that the output current of the highly charged ion beam is proportional to the total power of both microwaves. The dependence on the additional frequency showed fine structure. Since this structure depended on the magnetic field, vacuum pressure, and so on, precise frequency adjustment for the maximum output was required under each condition.

It is considered that the plasma instability of the ECR heating plasma is a 'microscopic instability'; like the velocity space instability. In an ECR ion source for the production of highly charged ions, a great deviation of the electron energy distribution from the Maxwell-Boltzmann distribution and the anisotropy of its velocity distribution may adversely affect the plasma stability [2].

Our group has focused on studying the mixture of two microwaves of which the two frequencies are each close together (close 2f) since 2008 at NIRS-HEC. An interest has arisen as to whether the above-mentioned phenomenon can be demonstrated using a different ion source where the two frequencies are even far apart from each other (far 2f). That is why we installed a 17.75-18.25 GHz microwave system in addition to the 14.3 GHz klystron amplifier of the ATOMKI ECRIS. The argon output currents at various values of the microwave power and frequency were recently studied.

TECHNICAL METHOD

18GHz NIRS-HEC ECRIS

The heavy ion medical accelerator in Chiba (HIMAC) at the National Institute of Radiological Sciences (NIRS) was constructed as the first medical-dedicated heavy-ion synchrotron in 1994. HIMAC has treated more than 10,000 patients as of 2016 [4]. It has also been utilized as a second essential task to operate as a user facility for basic experiments in e.g. physics, chemistry, material science, and other life-science studies. In order to extend the range of available ion species for HIMAC, an 18 GHz ECRIS, named NIRS-HEC, was constructed in 1996. The detailed specifications of NIRS-HEC are described in reference [5].

The primary microwave source is an 18 GHz fixed-frequency Klystron (KLY) amplifier system with a maximum power of 1500 W. The additional source is a travelling-wave tube (TWT) amplifier system with a frequency range from 17.10 to 18.55 GHz and with the maximum power of 1200 W. Since the power stability is important for the reproducibility, both microwave systems have been equipped with power feedback. Pulse operation is available with both microwave sources.

14GHz ATOMKI ECRIS

A multi-purpose ECR ion source has been operating since 1996 at the Institute for Nuclear Research (ATOMKI). The ATOMKI-ECRIS does not serve as an injector for an accelerator; instead, it was designed and has been used for low-energy atomic physics research, for plasma studies and for medical and industrial applications [6,7]. The mechanical and electrical structures of the ATOMKI-ECRIS are not fixed; depending on the actual application goal, it has several configurations. During the present experiment, two external microwave sources are

#kitagawa.atsushi@qst.go.jp

ISBN 978-3-95450-186-1

coupled to the plasma chamber. A 14.3 GHz fixed-frequency klystron (KLY) amplifier with a maximum output power of 1500 watt and an additional 17.75-18.25 GHz variable frequency TWT amplifier with a maximum power of 500 watt.

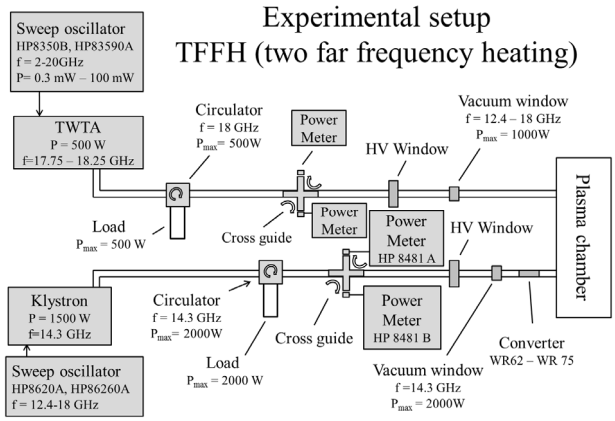

Figure 1: Schematic drawing of the two-frequency heating system at ATOMKI-ECR.

Comparison of the Configurations of NIRS-HEC and ATOMKI-ECR

Table 1 gives the specifications of NIRS-HEC and ATOMKI-ECR. The major differences between both sources are the frequency bandwidth and the maximum power of the additional microwave. The extraction voltages in these experiments were about 20 kV at NIRS-HEC and about 10 kV at ATOMKI-ECR, respectively

Table 1: Specifications of NIRS-HEC and ATOMKI-ECR

	NIRS-HEC	ATOMKI-ECR
Main microwave frequency (GHz)	18.0	14.3
Maximum power (kW)	1.5	1.4
Additional microwave Frequency (GHz)	17.10-18.55	17.75-18.25
Maximum power (kW)	1.2	0.5
Maximum mirror magnetic field at injection side (T)	1.3	1.2
at extraction side (T)	1.2	0.95
Mirror field peak-peak distance (mm)	165	235
Radial magnetic field on the surface of chamber (T)	1.1	1.1
Hexapole magnet length (mm)	200	200
Plasma chamber length (mm)	200	210
Plasma chamber diameter (mm)	61	58
Maximum extraction voltage (kV)	56	30

Figure 2 shows typical geometrical configurations of both NIRS-HEC and ATOMKI-ECR in the experiments. The contours of ECR zones, calculated by TrapCAD [8], are drawn.

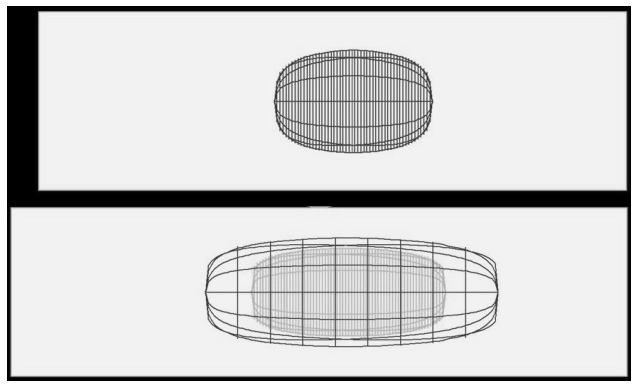

Figure 2: Typical configurations for the plasma confinement of NIRS-HEC (up) and ATOMKI-ECR (down) with the same scale. Left; injection side.

EXPERIMENTAL RESULTS

Production of Ar Ions at ATOMKI-ECR

Experimental data of "far 2f" at ATOMKI were obtained with Ar gas. Initially, the single microwave from KLY was fed, and the operation parameters, i.e., microwave power, amount of gas, magnetic field, extraction voltage, and so on, were optimized. Then, the second microwave from TWT was added and the frequency dependence of TWT was measured. The other parameters were optimised again at the best frequency. This procedure was iterated several times; thus, all parameters were fixed. The typical frequency dependence is shown in Figure 3. The fine structure appeared in this "far 2f" experiment similar to the case of the "close 2f" experiments at NIRS-HEC.

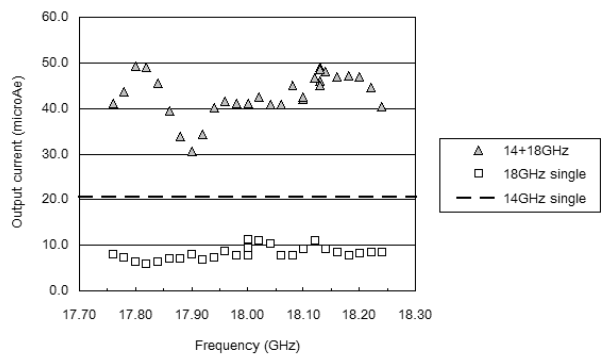

Figure 3: Typical frequency dependence of the output current of Ar^{11+} with the single TWT and the mixture of KLY and TWT. The KLY power was 700 watt; the TWT power was 400 watt.

The microwave power dependences of the output currents of some charge states of Ar ions were measured. The output currents of Ar^{11+} and Ar^{13+} were almost proportional to the power. On the other hand, the dependence of Ar^{7+} and Ar^{1+} were saturated at lower powers. Figure 4 shows an example of the power dependence of the output currents of Ar^{13+}. The square and triangle markers mean the

ISBN 978-3-95450-186-1

single KLY microwave and two frequency by KLY and TWT, respectively. In this figure, the total power is determined by the sum of the two microwave powers, measured by RF crystal detectors. Since the coupling between a microwave and a plasma depends on the operation parameters, this determination is usually too simple. However, it must be noted that the x axis has an ambiguity: the output current increased with increasing the total power. This characteristic in "far 2f" is also similar to "close 2f" at NIRS-HEC [3, 4].

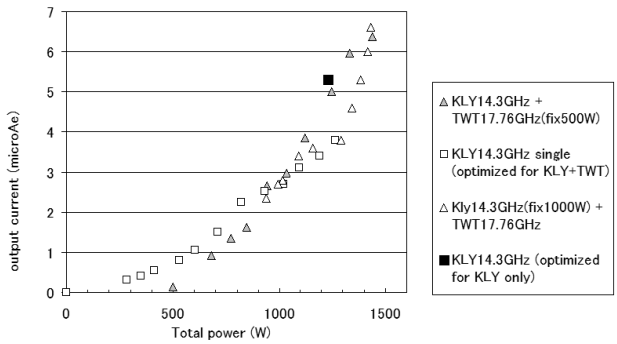

Figure 4: Typical power dependence of Ar^{13+} with the single KLY and the mixture of KLY and TWT.

Since the maximum total power was limited to bellow 1.5 kW (due to the limited cooling capacity), no plasma instability appeared during this measurement. It has not been confirmed that the mixture of two frequencies suppresses the plasma instability and improves the output currents of highly charged ions. If the cooling capacity is improved, it is expected the output currents increase with increasing the total power.

Production of Ar Ions at NIRS-HEC

We tried to observe the plasma instability in the case of "close 2f" at NIRS. The plasma instability strongly depends not only on the microwave power, but also on the vacuum pressure. The increasing pressure provides a stable plasma, and at the same time reduces the output current of highly charged ions. In order to decrease the pressure as much as possible, we carried out a pulse-mode operation, and measured the output currents of the afterglow in this experiment. Because the lower outgas was expected, all operation parameters were optimised for Ar^{13+}. The instability did not appear with the single frequency from KLY or TWT. When the total power increased up to 2 kW, the plasma became instable. This is larger than around 1 kW in the previous cases for Kr and Xe. The maximum output current of Ar^{13+} in the stable region was obtained in the case for the KLY power being 1.15 kW and the TWT power of 0.8 kW. The afterglow also improves the output currents of highly charged ions, as shown in Table 2.

Table 2: Improvement of the Output Currents (eμA) for Ar Ions at NIRS-HEC

Technique		Charge state of Ar ions				
frequency	afterglow	11+	12+	13+	14+	16+
Single	No apply	130	50	21	-	-
Two	No apply	200	116	42	15	-
Two	Add	300	242	118	47	2.3

DISCUSSION

It is usually considered that the plasma instability of ECR heating plasma with a minimum B structure is not magnetohydrodynamic instability called 'macroscopic instability', but 'microscopic instability' like velocity space instability. Especially, in an ECR ion source for the production of highly-charged ions, a great deviation of electron energy distribution from Maxwell-Boltzmann distribution and anisotropy of its velocity distribution may adversely affect the plasma stability. The additional microwave with a different frequency may cause various modes of waves and also causes unexpected resonant absorptions as an origin of microscopic instability. For example, when the 14 GHz microwave penetrated through the 18 GHz resonance zone which surrounded 14 GHz plasma, the plasma instability grew with increasing 18 GHz microwave power. It is likely that the 14 GHz microwave was disturbed by the dense plasma maintained with 18 GHz microwave. In the case of lower 18 GHz microwave power, a similar phenomena was not appeared. Although the interference in two far discrete frequency microwaves shows the complex phenomena, it is curious that an additional microwave with a well-tuned close frequency supports the stability of plasma. However, we did not observe any conflict or disturbance between the two microwaves. It was guessed that our present experiment at ATOMKI has not reached such conditions.

Although the improvement on the plasma instability was not demonstrated at the ATOMKI-ECR, due to the cooling capacity in the case for Ar, we think that it will appear in the case of a lower gas flow for a higher charge state or heavier ions. The other tendencies of the observed phenomena in the "far 2f" experiment are very similar to the "close 2f" experiments. Both the tuning of the additional frequency and the increasing of the total power are necessary for producing highly charged ions. This similarity between "far 2f" and "close 2f" also suggests that the geometrical configuration is not a dominant parameter for the two-frequency heating.

Many reports pointed the importance of fine tuning of microwave frequency, for example in Ref. [9]. A detailed study on frequency tuning effects was performed by INFN, GSI, and JYFL group [10-13]. Here the emphasis in the explanation was set to the RF properties of the plasma chamber. The authors' another work also gave similar results for more simple system [14]. On the other hand, a typical ECR ion source has a steep gradient of magnetic field. One percent of frequency change gives almost no spatial difference less than one mm. It suggests

ISBN 978-3-95450-186-1

that the optimising frequency of additional microwave displays behaviour different from the cavity mode of chamber in the case of two frequency heating technique. From the comparison between the X-ray photographs and spatial distribution of the simulated warm electron component of the plasma, the highly charged ions probably occupy much larger volume around the resonance zone than the ionising electrons [15] and collect cold electrons due to quasi-neutrality. These spatial distributions will be taken into account for the frequency tuning. Our trials to verify the assumption, that the additional frequency controls the anisotropy of the electrons' velocity distribution which may affect the plasma instability, have not been yet confirmed by a computer simulation [3]. Recently Skalyga and Tarvainen group showed the interesting observations and proposed the similar explanation [16, 17].

When NIRS-HEC produced an output current of 42 eμA for Ar^{13+} (Table 2), it was estimated that a total power of 1.5 kW was fed into the 18 GHz ECR zone. Figure 4 shows that 6.6 eμA was obtained at ATOMKI-ECR with a 14 GHz power of 1 kW and an 18 GHz power of 0.5 kW. This big difference is partly caused, of course, by the significant differences between the two ion sources: main frequency, magnetic fields and its peak-peak distance, extraction voltage, plasma chamber material, horizontal slit width of analyser magnet, and so on. That is why the "basic" HCI currents at Atomki-ECR are much lower than at NIRS-HEC. Another difference comes from the geometry of ECR zones. Calculations shown in Figure 2, under the present experimental conditions, the typical diameter, length, volume, and surface area of the ECR zones at ATOMKI-ECR and NIRS-HEC are shown in Table 3. The surface area and volume of ECR zone at 18GHz ATOMKI-ECR are roughly two times larger than that of NIRS-HEC and 14 GHz ATOMKI-ECR. It might cause the decreasing the beam-extraction efficiency towards the magnetic field line.

Table 3: The Geometry of ECR Zones at ATOMKI-ECR and NIRS-HEC

	ATOMKI-ECR		NIRS-HEC
Mirror magnetic field at injection side (T)		1.2	1.3
at extraction side (T)		0.95	1.08
Frequency (GHz)	18	14	18
Diameter (cm)	3.8	3.1	3.5
Length (cm)	10.0	6.6	5.0
Volume (cm^3)	85	36	35
Surface (cm^2)	112	61	51

However, from a practical point of view, at both cases large improvement was observable (to the basic currents) if the microwave power was increased, regardless close-2f or far-2f mode was applied. Considering the above mentioned numerous geometrical differences between the two ECRISs, from these experiments it could not be clearly concluded which combination (near or far 2f) is better or worse. On the other hand, Figure 4 shows a non-linear correlation. We expect it will suggest useful information concerning more detailed coupling between the microwaves and the plasma in order to understand the phenomena. In order to learn how to adapt or to design a source suitable for two-frequency heating, we would like to more precisely measure the power dependence in various cases: mirrored 2f at both ECRISs (near 2f in Atomki, far 2f in NIRS), higher microwave power at Atomki-ECR by improving cooling, etc.

ACKNOWLEDGMENT

The authors would like to express our special thanks to Dr. Arne Drentje for discussions on understanding the phenomena. The authors also thank Prof. Masayuki Sekiguchi, who passed away on April 2nd, 2016, for his continuous encouragement in this study.

REFERENCES

[1] Z. Q. Xie and C.M. Lyneis, "Improvements on the LBL AECR source", ECRIS1995, RIKEN, April 1995, INS-J-182, p 24 (1995).
[2] S. Biri *et al.*, Rev.Sci.Instrum. **85**, 02A931 (2014).
[3] A. Kitagawa *et al.*, "Improvement of Beam Intensities for Ion Beams with Charge-to-Mass Ratio of 1/3 with the Two-Frequency Heating Technique", in *Proc. of ECRIS'14*, Nizhny Novgorod, August 2014, p.83 (2014); http://www.JACoW.org
[4] H. Tsujii and T. Kamada, *Jpn. J. Clin. Oncol.* 42, 670 (2012).
[5] A. Kitagawa *et al.*, *Rev. Sci. Instrum.* **87**, 02C107 (2016).
[6] S. Biri *et al.*, *Rev. Sci. Instrum.* **83**, 02A341 (2012).
[7] R. Rácz *et al.*, "Application of an ECR ion source for ionic functionalization of implant materials on the nanoscale", in *Proc of ECRIS'14*, Nizhny Novgorod, August 2014, p.135 (2014); http://www.JACoW.org
[8] S. Biri, R. Rácz, J. Imrek, A. Derzsi, and Zs. Lécz, *IEEE Transactions on Plasma Science* **39** (2011) 2474.
[9] P. Sortais *et al.*, in *Proc. of ECRIS'95*, p.44.
[10] L. Celona *et al., Rev. Sci. Instrum.* 79, 023305 (2008).
[11] V. Toivanen *et al.*, *Rev. Sci. Instrum.* 81, 02A319 (2010).
[12] D. Mascali *et al.*, *Rev. Sci. Instrum.* 81, 02A334 (2010).
[13] F. Maimone *et al.*, *Rev. Sci. Instrum.* 82, 123302 (2011).
[14] Y. Kato *et al.*, *Rev. Sci. Instrum.* 75, 1470 (2011).
[15] R. Racz *et al.*, *Plasma Sources Sci. Technol.* 20, 025002 (2011).
[16] V. Skalyga *et al.*, *Phys. Plasma* 22, 083509 (2015).
[17] O. Tarvainen *et al.*, *Rev. Sci. Instrum.* 87, 02A703 (2016).

ISBN 978-3-95450-186-1

AN ECRIS FACILITY FOR INVESTIGATING NUCLEAR REACTIONS IN ASTROPHYSICAL PLASMAS

M. Kreller*, G. Zschornack[1], C. Baumgart, Dreebit GmbH, Großröhrsdorf, Germany
[1] also at Dresden University of Technology, Dresden, Germany
K. Czerski, M. Kaczmarski, N. Targosz-Ślęczka
University of Szczecin Institute of Physics, Szczecin, Poland
A. Huke, G. Ruprecht, D. Weißbach, Institute for Solid State Nuclear Physics, Berlin, Germany

Abstract

Nuclear reactions at low energies can be strongly enhanced due to screening of the Coulomb barrier by the surrounding electrons. This effect was studied for the deuteron fusion reactions taking place in metallic environments as a model for dense astrophysical plasmas. Experimentally determined screening energies corresponding to the reduction of the Coulomb barrier height are much larger than the theoretical predictions. One possible explanation is the excitation of a hypothetical threshold resonance in the ^{4}He nucleus. As the energy dependence of the resonant reaction cross section differs to that of the electron screening effect, one can distinguish between both processes expanding measurements down to the deuteron energies of 1 keV. A novel ion accelerator was implemented at the University of Szczecin. Ions are produced by a Dresden ECRIS-2.45M as a high-current, low-Z ion source. The associated beamline designed to work on HV potential is combined with an ultra-high vacuum target chamber on ground potential. This setup enables decelerating ions below a kinetic energy of 1 keV and reduces target impurities. The ion irradiation facility as well as first experimental results are described and discussed.

INTRODUCTION

Hydrogen and Deuterium ions are used in various scientific and technical applications. An area of interest is for example the cold fusion research. Recent cold fusion experiments are based on chemonuclear Deuterium-Deuterium (D-D) and Hydrogen-Deuterium (H-D) fusion reactions in metals [1] or transition metals like palladium [2]. An important aspect for solid-state fusion is a sufficient Deuterium density [3] in the target made of palladium or other materials. Often ion implantation of Deuterium or Hydrogen is used to reach the required density [3–5].

The enhanced electron screening effect was observed for the first time in the ^{2}H(d,n)^{3}He and ^{2}H(d,p)^{3}H reactions preceding in metallic environments [6]. An exponential-like increase of experimental reaction cross sections for decreasing projectile energies could be explained as a result of shielding nuclear charges by surrounding electrons leading to a reduction of the Coulomb barrier in terms of a so-called screening energy U_e. The screening energies experimentally determined for the (D-D) fusion reactions in metals are about a factor of ten larger than that obtained for gas targets [7] and up to a factor of two larger than the theoretical predictions [8]. The results are particularly interesting for nuclear astrophysics since deuterized metals represent a good model for strongly coupled plasmas where the kinetic energy of plasma particles is smaller than the mean Coulomb repulsion energy. In such a case, nuclear reaction rates can be increased by many orders of magnitude as probably realized in White and Brown Dwarfs or Giant Planets [9].

Our first experimental results have been confirmed by other groups [10, 11]. Especially, the data obtained by the LUNA collaboration for almost 60 different target materials [12] allow to compare the experimental results of different groups and to look for a theoretical description of the observed target material dependence as well as for the absolute screening energy values. However, there are significant discrepancies between the data of different groups.

As discussed in previous papers [13], the strong variation of the experimental screening energy arises from the contamination of the target surfaces by Carbon and Oxygen. Even small amounts of the Oxygen contamination correlated with high deuteron densities lead to vanishing screening energies and thick contamination layers connected with low and unstable deuteron densities result in artificially high values of U_e. Thus, new experiments performed under ultra-high vacuum (UHV) conditions at the lowest possible energies with atomically clean targets are required.

In this work we present a newly developed electron cyclotron resonance ion source (ECRIS) and demonstrate the production of Hydrogen and Deuterium ions which are used to investigate (D-D) reactions in a Zirconium environment. Zirconium as a target has been chosen because of its high affinity to form oxides so that it is of advantage to perform measurements under UHV conditions. The screening energy for Zirconium determined in our previous high-vacuum experiment amounted to about 300 eV. This is in contradiction to the experimental result obtained by the LUNA collaboration with $U_e < 40$ eV [14]. The new experiment was intended to clear up this discrepancy.

EXPERIMENTAL SETUP

Ion Source

For the production of Hydrogen and Deuterium ions an electron cyclotron resonance ion source has been developed.

* martin.kreller@dreebit.com

ISBN 978-3-95450-186-1

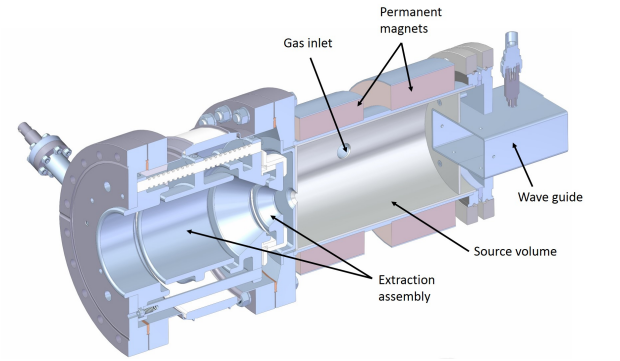

Figure 1: Schematic view of the Electron Cyclotron Resonance Ion Source (Dresden ECRIS-2.45M).

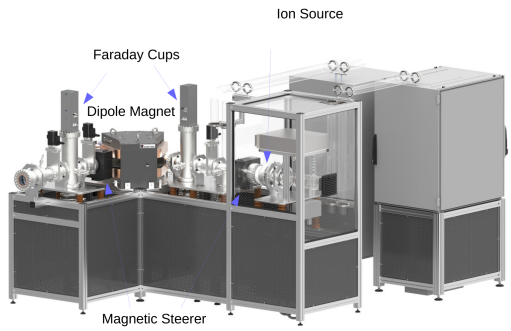

Figure 2: Schematic view of the beamline with the Dresden ECRIS-2.45M ECR ion source, the Faraday cups and the analyzing dipole magnet.

The so called Dresden ECRIS-2.45M is shown schematically in Figure 1. It is a permanent magnet electron cyclotron resonance ion source with a compact design, i.e. a length of 290 mm and a diameter of 210 mm. The axial magnetic field required for the plasma confinement is generated by two NdFeB magnet rings.

The plasma is heated by means of a solid state microwave generator with a tunable RF frequency of 2.45(15) GHz and a maximum RF power of 200 W. The rectangular wave guide, shown in Figure 1 is used to enable a stable microwave injection into the plasma and thus a stable plasma heating.

For the extraction of the ions an extraction assembly system had been designed. As shown in Figure 1 the extraction system consists of a plasma aperture, a puller electrode, and an Einzel lens for focusing the extracted ion beam. The maximum source potential amounts to 30 kV while the puller electrode can be biased up to −6 kV. The puller electrode and the first element of the Einzel lense were made of a soft magnetic material. The magnetic field lines are collected within the material. Hence, a low magnetic field is realized in the extraction system which results in an increased high voltage stability in the extraction region. Using hard magnetic materials for the puller electrode and the Einzel lens element instead lead to high voltage instabilities and plasma ignition in the extraction region.

Including extraction assembly and the corresponding high voltage feed throughs the Dresden ECRIS-2.45M has a length of 460 mm and a diameter of 340 mm.

Ion Irradiation Facility

In Figure 2 the beamline of the applied ion irradiation facility is shown. The ion source with extraction assembly is followed by a magnetic steerer which enables deflection of the extracted ion beam in horizontal and vertical direction. By means of the magnetic steerer the extracted ion beam can be optimized in the front focus point of the analyzing dipole magnet. At this position a Faraday cup (FC1) is mounted which enables the measurement of the integral ion current extracted from the Dresden ECRIS-2.45M.

In the focus point behind the analyzing dipole magnet a second Faraday cup (FC2) is positioned. The analyzing dipole magnet enables the charge to mass (q/A) separation and thus the precise selection of the ions of interest. The corresponding ion current can then be optimized by means of the second magnetic steerer and be measured in the FC2.

Vacuum Concept

From the experimental point of view, the biggest challenge is to combine a high current accelerator system with a working pressure below 10^{-10} mbar in the target chamber. The corresponding vacuum scheme is shown in n Figure 3. Differential pumping stages are used to guarantee the low vacuum pressure in the target chamber. The turbomolecu-

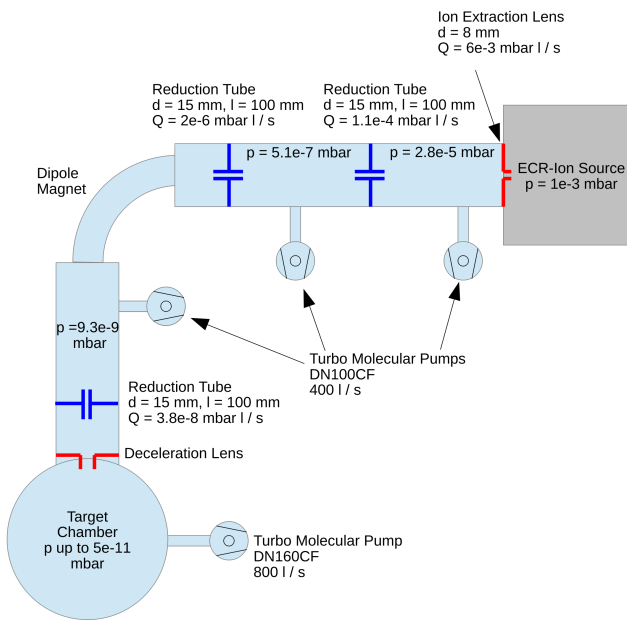

Figure 3: Schematic view of the vacuum concept including the differential pumping stages.

lar pumps in the beamline are backed with a combination of a membrane pump and a small tubomolecular pump to realize a suitable end vacuum. The turbomolecular pump of

ISBN 978-3-95450-186-1

the ion source is backed by a multi-stage roots pump with a high pumping speed. The whole vacuum system operates on oil-free conditions.

Experimental Chamber and Procedure

The beams of D^+ and $D_2{}^+$ ions produced in the ECRIS were magnetically analyzed by the double focusing 90° analyzing dipole magnet and directed on a Zirconium target to a spot of 5 mm diameter by adjusting the magnetic beam steerers, Einzel lenses and a series of apertures. The long-term stability achieved for the deuteron energy was about a few eV. The charged products of the (D-D) reactions (protons, tritium ions and ionized ^{3}He particles) were detected by Si-detectors located in the reaction plane at backward angles 90°, 125° and 150° with respect to the beam at 8 cm distance from the target as it is shown in Figure 4.

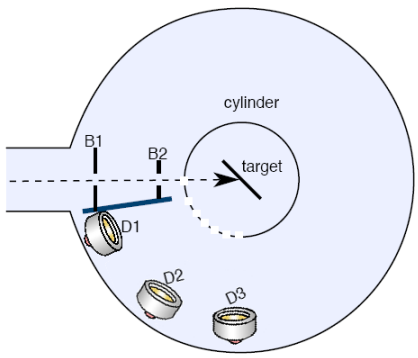

Figure 4: Schematical view of the target and detector positions.

Aluminum foils with a thickness of 150 µg cm^{-2} in front of the detectors prevented elastically scattered deuterons from entering the detectors. The beam charge collected by the target was determined by a measurement of the electric current on the target holder. A negative voltage of about −150 V was applied to a ring surrounding the target for suppression of secondary electrons. The Zirconium target (foil, 1 mm thick) was implanted up to the saturation level close to the chemical stoichiometric ratio of about two (two Deuterium atoms per one metal atom).

Before the yield measurements started, the target surface was cleaned by means of surface sputtering using 10 keV Ar^+ ions. Atomic cleanness of the target surface was controlled by applying Auger electron spectroscopy which is sensitive for a surface contamination down to one monolayer. The experimental chamber including the residual gas analyzer for vacuum characterization, the energy analyzer, the sample manipulator, the target exchange system and the detector manipulator are shown in Figure 5. A detailed experimental procedure is presented in [13].

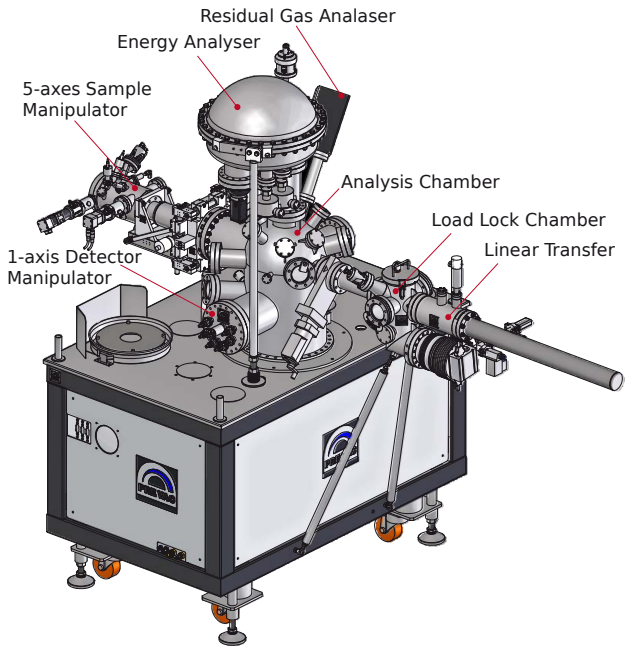

Figure 5: Schematic view of the target chamber. The ion beamline is connected to the backside of the analysis chamber.

RESULTS

Extracted Ions

Experiments with different gases were performed for ion source characterization. In addition to the irradiation experiments with Deuterium, Hydrogen, argon, helium and neon was injected into the Dresden ECRIS-2.45M. Example of the extracted ions are shown in Figure 6. The ion beams have been produced with a source potential of 20 kV and an extraction voltage of −1.8 kV. The optimum microwave power was found to be 200 W.

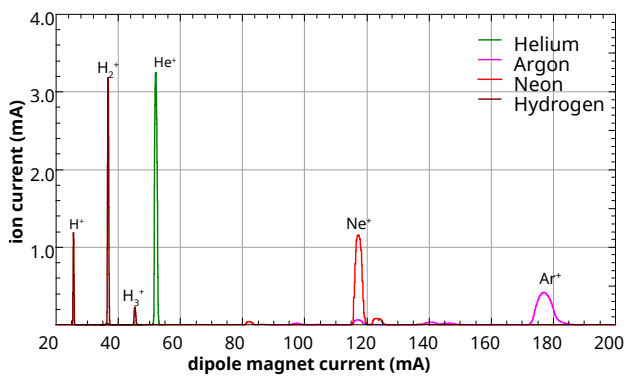

Figure 6: Extracted ion currents in the Dresden ECRIS-2.45M. The ion current measured in FC2 in dependence on the dipole magnet current is plotted.

Significant high ion currents in the mA range of Hydrogen, Helium, Neon and Argon are measured in Faraday

ISBN 978-3-95450-186-1

cup 2 behind the differential pumping stage having a diameter of 15 mm.

The ion source parameters were optimized for ionization of Deuterium. The q/A measurement results shown in Figure 7 revealed that additional to the expected Deuterium ions also Hydrogen ions and charged molecules are present. The detected Hydrogen may be residual gas from the previous Hydrogen ionization but also might be a part of the injected Deuterium gas. This aspect will be part of future studies.

A D^+ ion current of 650 µA is measured. Here must be noted that this peak may be overlapped by simultaneously extracted $H_2{}^+$ ions. Nevertheless, from the H^+ peak with an ion current of 30 µA and the $H_3{}^+$ peak with an ion current of 70 µA a maximum ion current of about 50 µA for $H_2{}^+$ ions can be deduced. Therefore, a minimum D^+ ion current of 600 µA can be assumed.

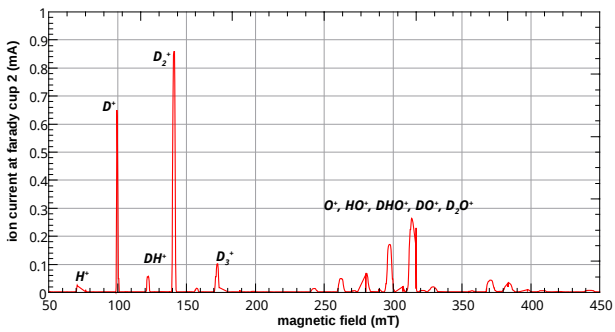

Figure 7: Deuterium ionization in the Dresden ECRIS-2.45M. The ion current measured in FC2 in dependence on the dipole magnetic field is plotted. The ion beam current peaks between dipole magnet currents of 230 mT and 400 mT are assigned to residual gas as water, hydrocarbons, Oxygen and Nitrogen.

Additional to the charged ions charged molecules are observed for Deuterium injection. In particular, a $D_2{}^+$ ion current of 850 µA and a $D_3{}^+$ ion current of 100 µA is measured.

The observed ion species, the corresponding dipole magnet current as well as the measured ion current in FC2 are listed in Table 1.

Table 1: Ion Species and Corresponding Dipole Magnet Current and Measured Ion Current in the FC2

Ion species	Dipole magnet current (A)	Ion current in FC2 (µA)
H^+	20.60	30
D^+ (and H_2^+)	29.60	650
H_3^+	36.60	70
D_2^+	42.30	850
D_3^+	52.20	100

Enhancement Factor

The experimental results are presented as a total, angle integrated, thick-target yield Y_{scr} which is compared to the theoretical value Y_{bare} based on the gas target experiments for which the screening contribution can be neglected [15]. The ratio of both determines the enhancement factor $F(E)$ at different deuteron energies (see Fig. 8) in the central mass (CM) system, given by:

$$F(E) = \frac{Y_{\mathrm{scr}}(E)}{Y_{\mathrm{bare}}(E)} = \frac{\int_E^0 \sigma_{\mathrm{scr}}(E)\left(\frac{dE}{dx}\right)^{-1} dE}{\int_E^0 \sigma_{\mathrm{bare}}(E)\left(\frac{dE}{dx}\right)^{-1} dE} \quad (1)$$

The enhancement factor can be also calculated theoretically using the expression for the screened cross section σ_{scr} [8]

$$\sigma_{\mathrm{scr}}(E) = \frac{1}{\sqrt{E(E+U_{\mathrm{e}})}} \cdot \exp\left\{-\sqrt{\frac{E_{\mathrm{G}}}{E+U_{\mathrm{E}}}}\right\} \quad (2)$$

$$= \frac{1}{\sqrt{(E \cdot E_{\mathrm{G}})}} \cdot P(E+U_{\mathrm{e}}) \cdot S(E) \quad (3)$$

The relation above results from the definition of the astrophysical S-factor $S(E)$ and takes into account that the electron screening effect reduces the height of the Coulomb barrier by the screening energy U_{e}. It can be added to the center mass energy E in the expression for the S-wave penetration $P(E)$. The Gamow energy E_{G} reaches the value of 986 keV for the (D-D) system.

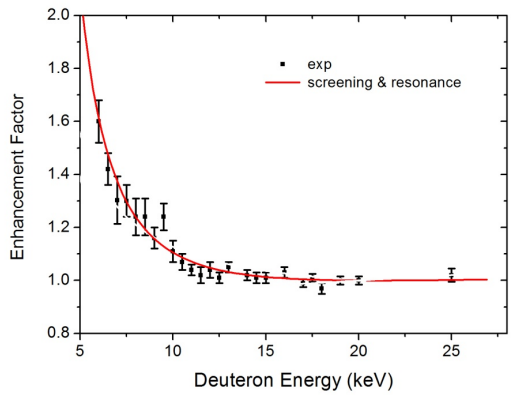

Figure 8: Enhancement Factor.

CONCLUSION

A newly developed electron cyclotron resonance ion source has been introduced and first results on Hydrogen and Deuterium ionization have been presented. Thereby, a D^+ ion current of 600 µA was measured. It was also observed that charged molecules of Hydrogen and Deuterium are generated and can be easily extracted and transported.

The measurement of the enhancement factor provides new experimental data that are much more precise than

ISBN 978-3-95450-186-1

those obtained previously due to better vacuum conditions and higher deuteron currents. They could not be fitted by a simple screening curve using only the screening energy U_e as a free parameter. In agreement to the (D-D) threshold resonance hypothesis [16], a contribution resulting from the single-particle resonance in the compound nucleus ^{4}He, placed close to the (D-D) reaction threshold at the excitation energy of about 24 MeV had to be included. The resonance component considerably reduced the fitted value of the screening energy $U_e = 105(15)$ eV which is now very close to the theoretical one of about 80 eV [8]. As the (D-D) threshold resonance is of great importance for nuclear astrophysics and applied studies concerning the future energy sources based on the fusion reactions, further experiments performed at even lower deuteron energies are highly required. This is the future task of the new accelerator system at the University of Szczecin, Poland [17].

REFERENCES

[1] V. F. Zelensky, ISSN 1562-6016, *Problems of Atomic Science and Technology* N3(85), Series: Nuclear Physics Investigations (60) p.76-118, (2013).

[2] S. N. Hosseinimotlagh and N. Tavallaee, *International Journal of Modern Theoretical Physics*, 3(2), 114-134, (2014).

[3] Han S. Uhm and W. M. Lee, *Fusion Science and Technology*, Vol. 21, NO. 1, p. 75-81, (1992).

[4] J. Roth, R. Behrisch, W. Möller, and W. Ottenberger, *Nucl. Fusion* 30, 441, (1991).

[5] F. Raiola *et al.*, "Enhanced d(d,p)t fusion reaction in metals", *Eur. Phys. J.* A 27, s01, 79-82, (2006).

[6] K. Czerski, A. Huke, A. Biller, P. Heide, M. Hoeft, and G. Ruprecht, *Europhys. Lett.* 54 449, (1998).

[7] U. Greife *et al.*, *Z. Phys.* A 351 107, (1995).

[8] K. Czerski, A. Huke, P. Heide, and G. Ruprecht, *Europhys. Lett.* 68 363, (2004).

[9] S. Ichimaru and H. Kitamura, *Phys. Plasmas* 6 2649, (1999).

[10] J. Kasagi *et al.*, *J Phys. Soc. Japan* 71 2281,(2002).

[11] F. Raiola *et al.*, *Phys. Lett.* B 547 193, (2002).

[12] F. Raiola *et al.*, *Eur. Phys.* J. A 19 283, (2004).

[13] A. Huke, K. Czerski, and P. Heide, *Nucl. Instrum. Methods* B 256 599, (2007).

[14] F. Raiola *et al.*, *J. Phys.* G: Nucl. Part. Phys. 31 1141, (2005).

[15] R. E. Brown and N. Jarmie, *Phys. Rev.* C 41 1391

[16] N. Targosz-Ślęczka, K. Czerski, A. Huke, L. Martin, P. Heide, A. i. Kilic, D. Blauth, and H. Winter, *J. Phys.* CS 202, (2010).

[17] M. Kaczmarski, A. i. Kilic, K. Czerski, A. Kowalska. D. Weissbach, and N. Targosz-Ślęczka, *Acta Phys. Pol.* B 45, (2014).

ISBN 978-3-95450-186-1

DESIGN OF COMPACT ECR ION SOURCE FOR C^{5+} PRODUCTION

M. Muramatsu†, A. Kitagawa, E. Noda, Y. Iwata, M. Sekiguchi, NIRS, QST, Chiba, Japan
K. Fukushima, K. Takahashi, T. Suzuki, T. Sasano, AEC, Chiba, Japan
N. Takahashi, H. Murata, SHI, Yokosuka, Kanagawa, Japan

Abstract

The Heavy Ion Medical Accelerator in Chiba (HIMAC) was constructed as the first medical dedicated heavy ion accelerator facility at National Institute of Radiological Sciences (NIRS). Over 10000 cancer patients have been treated with 140-430 MeV/u carbon beams since 1994. Compact ECR ion source with all permanent magnets, named Kei2, was developed for production of C^{4+} ions for medical treatment at NIRS. A compact ECR ion source for Gunma University (Gunma University Heavy Ion Medical Center: GHMC), Saga carbon-ion radiotherapy (Saga Heavy Ion Medical Accelerator in Tosu: SAGA HIMAT) and Kanagawa carbon-ion radiotherapy (Ion-beam Radiation Oncology Center in Kanagawa: i-ROCK) facility has been operated for medical use. It is a copy of the Kei2 which was developed by NIRS.

In order to reduce operation cost of the injector for next designed carbon ion facility, we start design of new compact ECR ion source for C^{5+} production. Some dependence (mirror field, microwave power and frequency) were checked for optimal parameter of C^{5+} production at 18 GHz NIRS-HEC.

INTRODUCTION

Four ion sources have been operated in HIMAC for medical treatment, physics and biological experiments at NIRS. Two ECR ion sources with normal conducting mirror coils, named 10 GHz NIRS-ECR [1] and 18 GHz NIRS-HEC [2], produce carbon ion for treatment and heavier ions (i.e. Ar, Fe, Xe) for experiment. Compact ECR ion source with all permanent magnet, named Kei2 [3], was installed to HIMAC with prototype injector [4] for backup of existing injector. Cold cathode type of PIG source, named, NIRS-PIG, produces ions of hydrogen, helium and neon from gases. Boron and aluminium ions are also produce by spattering method at NIRS-PIG.

There are five carbon ion radiotherapy facilities in Japan and two are under construction. If we can reduce the size and the operating cost of a facility, the spread of carbon ion radiotherapy is expected. Compact ECR ion sources (Kei series) at Gunma University, Saga carbon-ion radiotherapy and Kanagawa carbon-ion radiotherapy facility have been operated for medical use. Those are copies of the Kei2 which was developed by NIRS. Mirror magnetic field of the Kei series is optimized for production of C^{4+} under the experiment of 10 GHz NIRS-ECR. It is possible to reduce of the size of injector Linac when an ion source produces carbon 5+ or 6+ for a next facility. However, it is difficult to separate C^{6+} from other ions such as nitrogen and oxygen. Therefore, we design a new compact ECR ion source with all permanent magnets to produce C^{5+} ions with an output current of 300 eμA. The other requirements are similar as the Kei series.

† muramatsu.masayuki@qst.go.jp

TRIAL EXPERIMENTS

NIRS-HEC has produced C^{5+} with 500 eμA. So the size of the magnets and their arrangement of the new ion source were determined in such a way that both the maximum peak and B minimum values of the mirror field would become close to those of the NIRS-HEC. For design of the magnetic field, beam test was done for production of the C^{5+} at NIRS-HEC. NIRS-HEC are usually operated with two microwave amplifiers, 18 GHz klystron power amplifier and 17.10 – 18.55 GHz Traveling-Wave-Tube (TWT) amplifier. Output power of these amplifier are 1400 W and 1200 W, respectively. However, we plan that the frequency of the new ion source is around 14 GHz because high magnetic field is difficult to produce by using permanent magnets. Therefore we used other TWT amplifier for this trial experiment. Microwave frequency and output power are 10 – 18 GHz and 300 W, respectively.

In this experiment, some dependences (mirror field, microwave power and frequency) were checked for optimal parameter of C^{5+} production.

Production of Carbon Ion with CH_4 and CO_2

Usually, CH_4 gas is used at Kei series in carbon-ion medical facility. At first, we compared between CH_4 and CO_2 gas for production of C^{5+}. Figure 1 and 2 show charge state distribution (CSD) of carbon with CH_4 and CO_2 gases, respectively. Operation parameters were optimized for C^{5+}. Extraction voltage was 30 kV. In the case of CH_4, there was little oxygen peak from residual water. Beam intensity of C^{5+} was 160 eμA. in the case of CO_2, beam intensity of C^{5+} was only 36 eμA. CSD of CH_4 was better than CO_2.

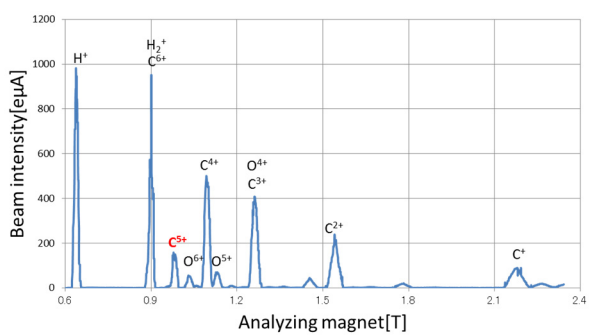

Figure 1: Charge state distribution under the CH_4 gas.

ISBN 978-3-95450-186-1

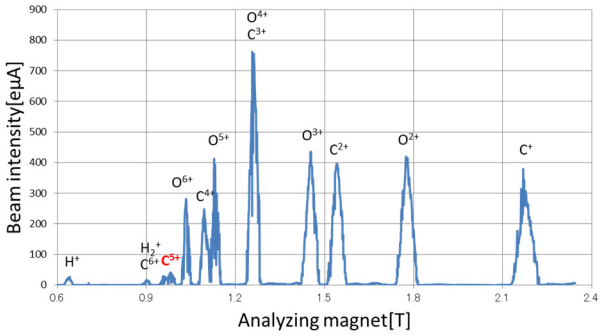

Figure 2: Charge state distribution under the CO_2 gas.

Dependence of Mirror Field

Figure 3 and 4 show dependence of mirror magnetic field for C^{5+} with CH_4 and CO_2 gases. Operation parameters except coil current were optimized for production of C^{5+}. Microwave frequency and power were 14.6 GHz and 300 W. Extraction voltage was 30 kV.

Maximum beam intensity of C^{5+} was obtained under the upstream mirror coil current of 840 A and downstream 500 A with CH_4 gas. Beam current of C^{5+} was 160 eμA. In the case of CO_2, coil currents of 840 A and 530 A were good for C^{5+} production. However, beam intensity of C^{5+} was lower than the case of CH_4. Higher coil current of upstream coil was better for the production of C^{5+}. Otherwise, for downstream coil current, around 500 A was best.

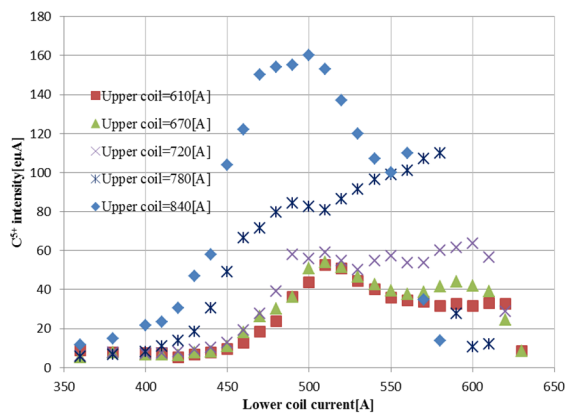

Figure 3: Mirror magnetic field dependence under CH_4 gas.

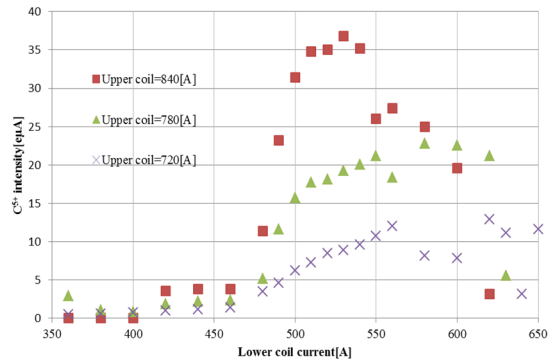

Figure 4: Mirror magnetic field dependence under CO_2 gas.

Microwave Frequency Dependence

Figure 5 shows microwave frequency dependence at C^{5+} under the upstream coil current of 610, 670, 720, 780 and 840 A. From this result, characteristics of frequency dependence at all case of coil current were similar, however, beam intensity changed dramatically at high coil current. Maximum beam intensity of C^{5+} was over 200 eμA at frequency of 14.45 GHz. But other beam tests use frequency of 14.60 GHz, because beam stability is better than 14.45 GHz. It is evident that the fine tuning of frequency is necessary for the operation of the new ion source.

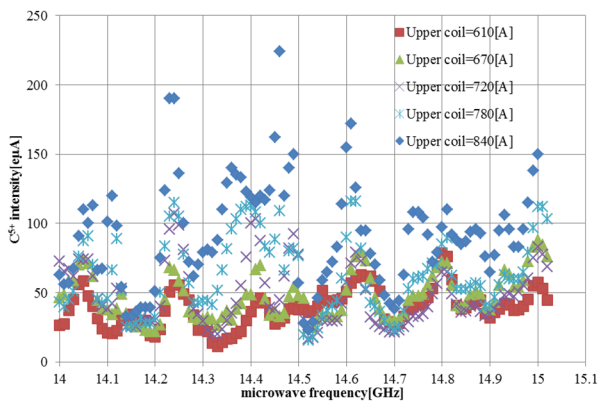

Figure 5: Microwave frequency dependence.

Microwave Power Dependence

Figure 6 shows microwave power dependence for C^{5+} under the upstream coil current of 610, 780 and 840 A. Maximum beam intensity of C^{5+} was obtained when microwave power becomes the highest at each coil current. In this experiment, it is evident that the present microwave power was not enough for production of C^{5+}. In order to increase the C^{5+} intensity, we estimate that a high power microwave amplifier with 500 W is necessary, at least.

ISBN 978-3-95450-186-1

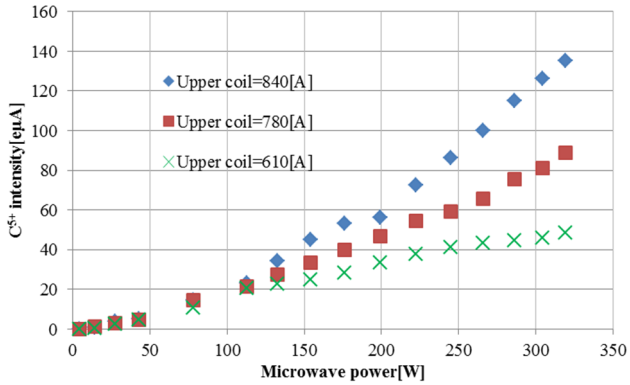

Figure 6: Microwave frequency dependence.

CONCLUSION FOR THE NEXT STEP

Some dependences (mirror field, microwave power and frequency) were checked for the design of the new compact ECR ion source at NIRS-HEC with the 14 GHz operation. From the present result, we guess that 1) necessary coil currents of upstream and downstream mirror coil for production of C^{5+} were around 840 and 500 A, 2) CH_4 gas was better than CO_2 gas for the production of C^{5+}, 3) microwave power of over 500 W will be necessary.

We verified that the above necessary magnetic field distribution was able to be realized by permanent magnets from the calculation by POISSON/SUPERFISH code [4]. Figure 7 shows a typical schematic drawing of the permanent magnets. Four ring magnets produce mirror magnetic field. A hexapole magnet produces radial confinement field.

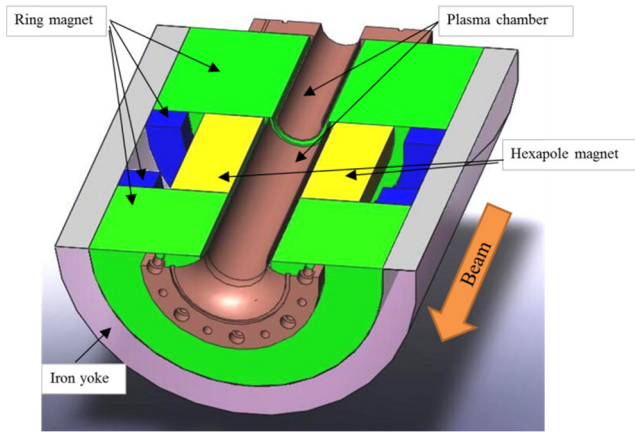

Figure 7: Schematic drawing of permanent magnets and plasma chamber.

In order to fix the design structure of permanent magnets, we plan the next trial at NIRS-HEC with higher power 14 GHz operation since September 2016. We will check more detailed dependences of an extraction voltage, a distance between puller and plasma electrode, other and so on. We also have tried to use other ionisation gasses. It seems that C_4H_{10} is promising and we would like to test the long-term operation.

REFERENCES

[1] A. Kitagawa *et al., Rev. Sci. Instrum*. 65, 1087 (1994).

[2] A. Kitagawa *et al., Rev. Sci. Instrum*. 69, 674 (1998).

[3] M. Muramatsu *et al., Rev. Sci. Instrum*. 76, 113304 1-6 (2005).

[4] James H. Billen and Lloyd M. Young, “Poisson Superfish (version 6.28)” Rev. Nov. 6 (2002).

ISBN 978-3-95450-186-1

INTERMEDIATE COMMISSIONING RESULTS OF THE REQUIRED 140 mA/100 keV CW D^+ ECR INJECTOR OF LIPAC, IFMIF'S PROTOTYPE

B. Bolzon†, N. Chauvin, R. Gobin, F. Harrault, F. Senée, CEA, Gif-sur-Yvette, France
J. Knaster, A. Marqueta, K. Nishiyama, Y. Okumura, G. Pruneri, F. Scantamburlo, IFMIF/EVEDA Project Team, Rokkasho, Japan
L. Bellan[1], M. Comunian, E. Fagotti, A. Pisent, INFN, Legnaro, Italy
P-Y. Beauvais, P. Cara, H. Dzitko, R. Heidinger, F4E, Garching, Germany
R. Ichimiya, A. Ihara, A. Kasugai, T. Kitano, M. Komata, K. Kondo, K. Sakamoto, T. Shinya, M. Sugimoto, QST, Rokkasho Fusion Institute, Rokkasho, Japan
[1]also at Dipartimento di Fisica e Astronomia, Università degli Studi di Padova, Padova, Italy

Abstract

The LIPAc accelerator aims to operate in Rokkasho Fusion Institute a 125 mA/CW deuteron beam at 9 MeV to validate the concept of IFMIF's accelerators that will operate in CW 125 mA at 40 MeV. The 2.45 GHz ECR injector developed by CEA-Saclay is designed to deliver 140 mA/100 keV CW D^+ beam with 99% D^+ fraction ratio. Its LEBT relies on a dual solenoid focusing system to transport and match the beam into the RFQ. The normalized RMS emittance at the RFQ injection cone is required to be within 0.25π mm·mrad to allow 96% transmission through the 9.81 m long RFQ. An equal perveance H^+ beam of half current and half energy as nominal with D^+ is expected to be used to avoid activation during commissioning. The injector commissioning at Rokkasho is divided into three phases to characterize the emittance between the two solenoids of the LEBT (A1) and just downstream the RFQ injection cone (A2) and the extraction system of the source (A3). Phase A1 has been achieved and phase A2 continues in 2016 in order to reach the required beam parameters and to match the beam into the RFQ. This paper reports the commissioning results of phase A1 and the intermediate ones of phase A2 for H^+ and D^+ beams.

INTRODUCTION

IFMIF (International Fusion Materials Irradiation Facility) is a projected accelerator-driven-type neutron source for qualifying fusion reactor materials. It is characterised by its beam current frontier accelerator producing two sets of 125 mA/CW deuterium ion beams up to 40 MeV [1]. The current EVEDA (Engineering Validation and Engineering Design Activities) phase is developed to validate the IFMIF accelerator with a challenging 125 mA/9 MeV CW deuteron accelerator called LIPAc (Linear IFMIF Prototype Accelerator). LIPAc was designed and constructed mainly by European laboratories with the participation of QST in the RFQ couplers and the control system. It is being assembled, commissioned and will be operated at Rokkasho [2, 3]. It is composed of an injector delivered by CEA-Saclay [4], a RFQ [5] delivered by INFN on April 2016, a superconducting SRF Linac designed by CEA-Saclay [6], RF power, Medium and High Energy Beam Transfer lines and a beam dump designed by CIEMAT.

The injector is composed of a 2.45 GHz ECR ion source based on the CEA-Saclay SILHI source design [7] and a LEBT line to transport and match the beam into the RFQ using a dual solenoid focusing system with integrated H/V steerers. Its commissioning started in November 2014 at Rokkasho and continues in 2016 interleaved with the RFQ installation to optimize the project schedule. It has to deliver to the RFQ 140 mA/100 keV CW D^+ beam to meet LIPAc requirements. Moreover, simulations showed that the normalized RMS emittance at the RFQ injection cone has to be no higher than 0.30π mm·mrad [8] with well-matched Twiss parameters in order to minimize losses to less than 10% in the RFQ (target of 0.25π mm·mrad for 4% of losses).

Commissioning program plans to use an equal perveance H^+ beam of half current and half energy as deuterons at nominal conditions to avoid activation and ease maintenance activities. However, it has to be stressed that the injector design has been optimized to produce high intensity 100 keV D^+ beam. In terms of beam extraction and transport at low energy, the performance of the injector can thus be lower by operating this one with 70 mA/50 keV H^+ beam due to lower plasma density.

The injector commissioning is divided in different phases. During phase A1, the emittance was measured in the first diagnostic chamber located between the two solenoids of the LEBT while it is measured in the second diagnostic chamber located downstream the RFQ injection cone at phase A2 (for both phases, the RFQ cannot be placed at its final position). The realization of a third phase A3, where the emittance is measured just downstream the 5-electrode beam extraction system to characterize the source itself, is still under discussion.

This paper presents the results of phase A1 with D^+ beam (completed at the beginning of September 2015) and the intermediate ones of phase A2 with D^+ and H^+ beams. In view of machine protection system during the RFQ commissioning, the injector was operated at low duty cycle with sharp beam pulses down to 100 µs length (use and test of an electrostatic chopper) up to CW operation. The different diagnostics of the injector used to characterize the beam are described in [9].

†benoit.bolzon@cea.fr

ISBN 978-3-95450-186-1

PHASE A1 WITH 100 keV D^+ BEAM

Plasma Electrode of 10 mm Diameter

Phase A1 commissioning started with the use of a plasma electrode of 10 mm diameter to limit the maximum current that can be extracted as a first step.

After enough ion source conditioning at high duty cycle with a beam, the ECR coils currents (COIL1, COIL2) and the tuners of the source can be optimized to maximize the plasma efficiency, i.e. the extracted current for a given RF power. Figure 1 shows the measured extracted current which increased with the increase of ECR coil 1 current for a RF power of 700 W. Plasma discharges appeared at higher coil 1 currents but the operation range of the coils currents allowing a stable plasma became wider day after day with high duty cycle conditioning of the ion source.

By adjusting also carefully the flow rate of D_2 gas injected into the ion source chamber, the extracted current can increase linearly with the injected RF power, see Fig. 5. Beam currents up to 113 mA were extracted at 1000 W of injected RF power with a very similar plasma efficiency at low (40%) and high duty cycle (91%). This corresponds to 158 mA for hydrogen (113 mA $\times \sqrt{2}$), which is very similar to the plasma efficiency obtained during the proton beam operation at 100 keV.

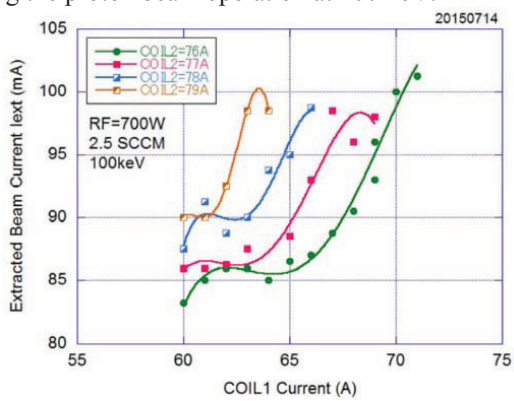

Figure 1: Optimization of the ECR coils currents in order to maximize the plasma efficiency for D^+ beam operation.

The voltage of the first accelerating gap (VIE) of the 5-electrode beam extraction system has to be optimized in order to minimize the beam divergence at the exit of the extraction system, and to avoid thus emittance growth. It exists an optimum VIE for a given extracted current. For instance, the emittance could be minimized down to 0.11π mm·mrad with VIE around 30-35 kV and for an extracted current of 105 mA (9.5% duty cycle), see Fig.2.

The D^+ fraction ratio was measured with two diagnostics, the Doppler-shifted spectroscopy and the Allison scanner (Emittance Measurement Unit - EMU). With this last device, the D^+ fraction ratio is estimated by integrating the emittance diagram of each ion species (mass separation measurement) [9]. With both diagnostics, it was shown experimentally that the D^+ fraction ratio increases usually with the extracted current or the plasma density in the ECR ion source [10]. It reached already a high value of 93% (mass separation measurement) for the extracted current of 105 mA at 9.5% duty cycle, which confirms that the injector design was well optimized for 100 keV D^+ beam.

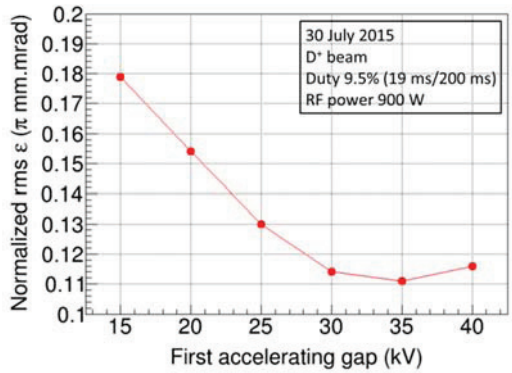

Figure 2: D^+ beam emittance as a function of the first accelerating gap voltage for an extracted current of 105 mA.

The duty cycle was increased step by step up to CW operation with an extracted current of around 65-75 mA to study if the beam characteristics remain the same while keeping the same injector parameters. Emittance increased significantly with the duty cycle when the flow rate of D_2 gas injected into the ion source chamber was kept low. However, the emittance degradation up to CW operation was reduced when the gas flow rate was increased, see Fig. 3. This trend of emittance growth with the duty cycle may be connected to various experimental conditions (including starting conditions).

The emittance could be improved at high duty cycle (only) by injecting Krypton gas between the two solenoids of the LEBT, see Fig. 3. Moreover, space potential measurements of the beam plasma were performed with the 4-Grid Analyzer (FGA) device located between the two solenoids of the LEBT. Measurements were performed at 9.5% and at 80% duty cycle where it was observed a significant degradation of the emittance. The D_2 gas flow rate was kept to 2.1 sccm for both duty cycles. The extracted current was lower at 80% duty cycle, i.e. 72 mA compared to 85 mA at 9.5% duty cycle. The space charge potential was centred on 11 eV at 10% duty cycle. It increased to 16 eV at 80% duty cycle but it decreased to less than 10 eV with Krypton gas injection, see Fig. 4. Space charge was thus compensated at high duty cycle.

A study of neutrons yield from D-D reactions in the LEBT is reported in [11] as a function of the duty cycle.

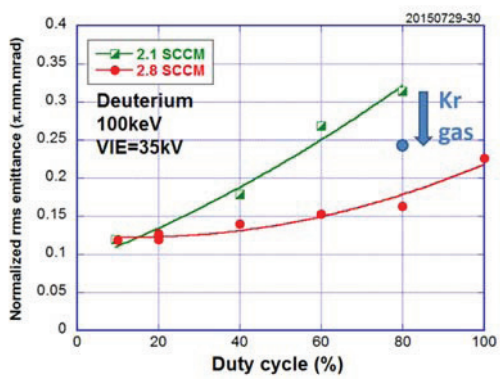

Figure 3: Emittance of D^+ as a function of duty cycle for two different D_2 gas flow rates and with Krypton injection.

ISBN 978-3-95450-186-1

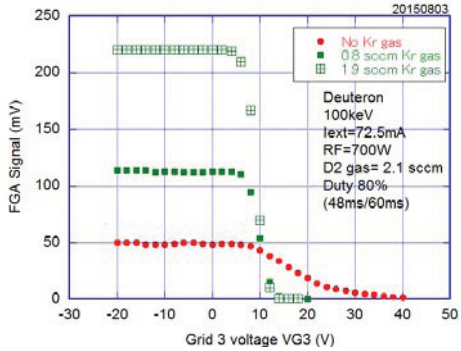

Figure 4: Measured Faraday cup signal in the FGA showing the space potential of the beam plasma (D^+ beam) with and without Krypton gas injection at 80% duty cycle.

Plasma Electrode of 12 mm Diameter

After enough experience taken on the injector behaviour, a plasma electrode of 12 mm diameter was installed.

From a plasma electrode of 10 mm diameter to one of 12 mm diameter, the extracted current should increase following the extraction surface factor (i.e. 1.44). After optimizing the plasma source parameters, currents as high as 186 mA could be extracted with an injected RF power of 950 W at 9.8% duty cycle, which is more than 1.44 times higher than the currents obtained with the plasma electrode of 10 mm diameter at 91% duty cycle. In Fig. 5, the extracted current was measured as a function of the injected RF power for a plasma electrode of 10 mm and of 12 mm. For a plasma electrode of 12 mm diameter, the measurements were done at three different dates, showing that the plasma efficiency was improving with ion source conditioning.

For an extracted current of 153 mA at 9.5% duty cycle, the emittance was minimized down to 0.27π mm·mrad between the two solenoids of the LEBT (VIE= 40 kV). This measurement was performed by maximizing the beam current transmission through the RFQ injection cone with the coils currents of the two solenoids of the LEBT (SOL1= SOL2= 280 A). Under this condition, D^+ ion beam is focused while D_2^+ and D_3^+ ion beams are divergent, see Fig. 6. The analysis of emittance data with the presence of three ion species is described in [9]. The D^+ ratio was of 90% (mass separation measurement) and the current measured on the Faraday cup (located between the two solenoids) was of 134 mA.

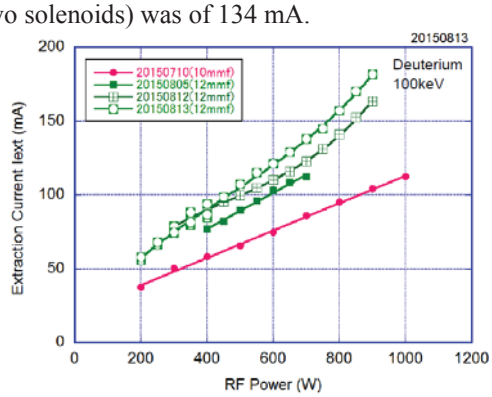

Figure 5: Extracted current as a function of the injected RF power for a plasma electrode of 10 mm and of 12 mm (D^+).

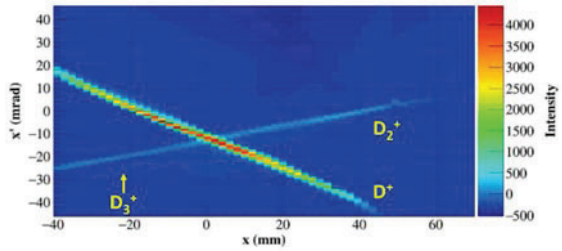

Figure 6: Raw emittance data of D^+, D_2^+ and D_3^+ beams for an extracted current of 153 mA at 9.5% duty cycle.

PHASE A2: IMPROVEMENTS TO BRING

Space Charge Compensation After RFQ Cone

A study of space charge compensation was done with 50 keV H^+ beam at 10% duty cycle (extracted current of 86 mA) in the second diagnostic chamber. In fact, the vacuum level is more than ten times lower at this location than in the first diagnostic chamber. By increasing the pressure inside the second diagnostic chamber (shutdown of the turbomolecular pump of this chamber), the emittance decreased of 20%. This study was performed for three very different beam focalizations to confirm the reproducibility of the results. Compensation of space charge thus occurred at least partially. In Fig. 7 and Fig. 8, the measured emittance diagrams are plotted (background subtracted) with respectively low pressure and higher pressure (SOL1= 134 A and SOL2= 145 A).

Unfortunately, this test was done very recently and all the other measurements were performed with low vacuum level in the second diagnostic chamber. The results presented in this paper can be thus most probably improved simply by increasing this vacuum level. In fact, the emittance has to be within specifications at the RFQ entrance and the EMU is placed ~300 mm downstream from it. For the next commissioning campaign in October 2016, modifications will be done in order to be able to inject D_2 / H_2 gas and Krypton gas directly into this diagnostic chamber and to know the real emittance value at the RFQ entrance.

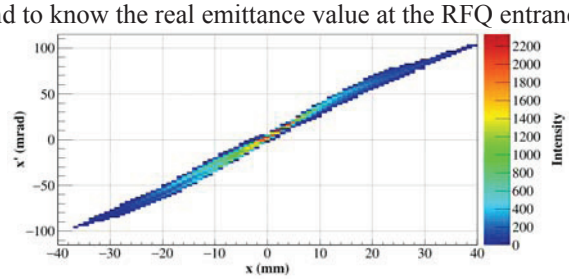

Figure 7: Emittance data without space charge compensation in the second diagnostic chamber (50 keV H^+ beam).

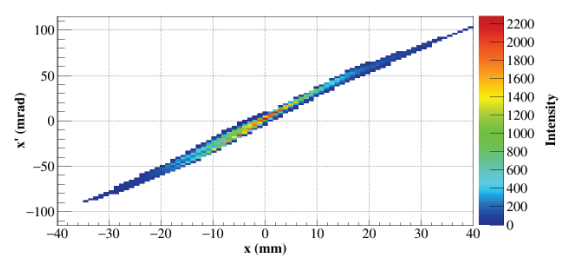

Figure 8: Emittance data with space charge compensation in the second diagnostic chamber (50 keV H^+ beam).

ISBN 978-3-95450-186-1

Improvement of Current Measurement on BS

In this article, results of currents measured on the beam stop (BS) are from electrical measurements (same principle as for a Faraday cup), which can be tricky with such an injector. Although a repeller electrode for electrons is located just upstream the end of the RFQ cone, the results of currents may be underestimated due to secondary electrons hitting the self-biased BS. These electrons can be generated by the interaction of the beam with the end of the cone and with the second diagnostic chamber [9]. In addition, autopolarisation of the BS leads to the modification of the electron trapping in the second diagnostic chamber. A magnetic secondary electrons suppressor will be thus added for the next commissioning campaign.

A calorimetric measurement system at the BS was available but modifications were needed to get sufficient resolution especially at low duty cycle. In the next campaign, the improved calorimetric measurement system will be commissioned [12] and results will be cross-checked with the ones of electrical measurements.

PHASE A2 COMMISSIONING

Commissioning with 100 keV D^+ Beam

Commissioning of phase A2 with 100 keV D^+ beam was performed with a plasma electrode of 12 mm diameter in order to extract enough current and to reach the requirements at the entrance of the RFQ.

For an extracted current of 150 mA, the BS current was measured at 10% duty cycle as a function of SOL1 & SOL2 after adjusting finely the injector parameters (see Fig. 9). The emittance was measured at three settings of SOL1 & SOL2 (with the same injector parameters) in the weak focusing area at 10% duty cycle (VIE= 43 kV). It was under specifications while the BS current was of 104-112 mA, see Fig. 9 which reports the emittance values in π mm·mrad. However, the Twiss parameters should be the best matched for the RFQ somewhere in the strong focusing area according to recent simulations [13]. In the next commissioning campaign, the emittance will be measured also in this area with as objective to keep it within specifications. With the Doppler-shifted spectroscopy, D^+ ratio was measured to be of 92%, D_2^+ ratio of 5% and D_3^+ ratio of 3%. D^+ ratio measurements give the same results with the Doppler-shifted spectroscopy and the EMU (mass separation measurement) at 100 keV (see the results reported for phase A1 with the same extracted current of ~ 150 mA). This gives thus confidence on these results.

A study at high duty cycle was also performed. The emittance was measured at 50% duty cycle (SOL1= 277 A and SOL2= 270 A) and was of 0.31π mm·mrad for an extracted current of 158 mA (BS current of 108 mA). Unfortunately, HV breakdowns occurred at that time and prevent to continue this study. High duty cycle operation will be done in the next campaign up to CW operation.

Experimental data show that the emittance tends to increase with the extracted current. Higher BS currents were obtained with higher extracted currents but the emittance was over specifications. These experiments need to be however repeated in the next campaign with calorimetric measurements (and electrical measurements using a magnetic secondary electrons suppressor) and with D_2 or Krypton gas injection into the second diagnostic chamber.

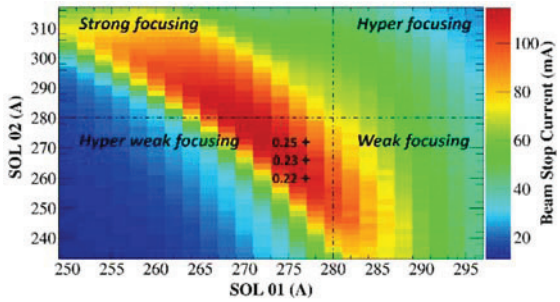

Figure 9: BS current as a function of SOL1 & SOL2 and emittance measured at 3 settings of SOL1 & SOL2 (D^+).

The electrostatic chopper was operated to provide sharp beam pulses of 100 µs for source pulses of 2 ms (repetition rate of 60 ms). Figure 10 shows the chopped beam current measured on the BS, the source pulse, the voltage supplied to the chopper plate and the chopper gate signal.

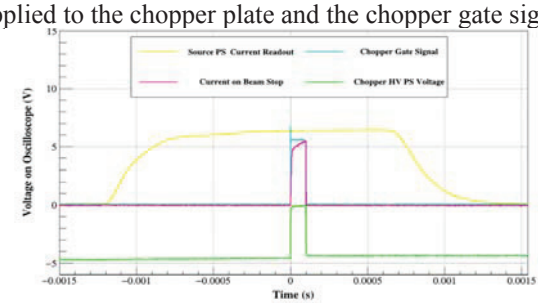

Figure 10: Chopped beam current of 100 µs measured on the BS (purple curve), source pulse of 2 ms (yellow curve), voltage supplied to the chopper plate (green curve) and signal of the chopper gate (blue curve).

Commissioning with 50 keV H^+ Beam

Commissioning with 50 keV H^+ beam used a plasma electrode of 10 mm diameter since only half of the current is required compared to 100 keV D^+ beam.

The highest currents obtained on the BS were of 55 mA (10% duty cycle) but these results have to be cross-checked with calorimetric measurements (and electrical measurements using a magnetic secondary electrons suppressor). To maximize BS currents, extracted currents had to be set to values no higher than 85 mA to avoid beam losses due to large beam divergence. Also, the plasma parameters were carefully tuned in order to obtain a quite high H^+ fraction ratio of 73%. Note that this measurement was done with Doppler-shifted spectroscopy, which gave a lower H^+ fraction ratio at 50 keV respect to the 100 keV. Investigations are on-going about that.

The emittance was measured at 10% duty cycle for an extracted current of 85 mA and was under specifications in the weak focusing area (VIE= 37 kV). However, the emittance increased from the weak to the strong focusing area as predicted by simulations and it was below 0.30π mm·mrad in only half of the strong focusing area. Figure 11 summarizes these results with the BS current

ISBN 978-3-95450-186-1

measured as a function of SOL1 & SOL2. On the same plot, the results of emittance measured at 25 settings of SOL1 & SOL2 are reported with as units π mm·mrad. In Fig. 12, the results of emittance are overlapped with an emittance contour plot (measured points are indicated by crosses) and the boundary delimiting an emittance of 0.30π mm·mrad is plotted. By injecting H_2 or Krypton gas into the second diagnostic chamber, the emittance can be probably reduced and may be within specifications for any settings of SOL1 & SOL2. During the RFQ commissioning, there will be in this case no limitations to find the best matched Twiss parameters which should be located in the strong focusing area as reported previously.

A study up to CW operation showed that the emittance and the H^+ fraction ratio were degrading with the increase of duty cycle. However, the emittance may be recovered at least partially at high duty cycle by injecting Krypton gas into the first diagnostic chamber as it was observed for D^+ beam in phase A1. Krypton gas injection into the second diagnostic chamber at high duty cycle may also help to recover the emittance obtained at low duty cycle.

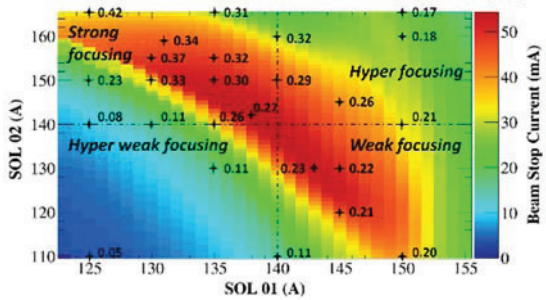

Figure 11: BS current as a function of SOL1 & SOL2 and emittance measured at 25 settings of SOL1 & SOL2 (H^+).

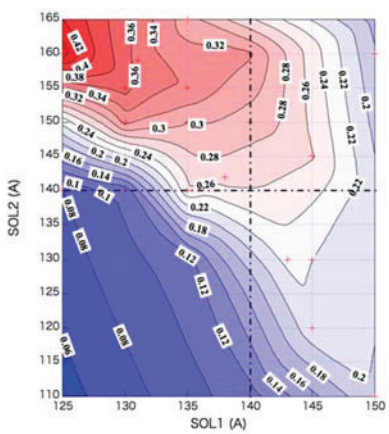

Figure 12: Emittance contour plot as a function of SOL1 & SOL2 from the emittance values reported on Fig. 11 (H^+).

CONCLUSION

Intermediate results of phase A2 commissioning of 100 keV D^+ and 50 keV H^+ beams reported an emittance within specifications for BS currents of 110 mA and 55 mA respectively (electrical measurements) at 10% duty cycle. For H^+ beam, these results were valid for any settings of SOL1 & SOL2 maximizing the current transmission except in half of the strong focusing area (best matched Twiss parameters for the RFQ according to recent simulations). For D^+ beam, the emittance was measured only in the weak focusing area and BS currents higher than 110 mA were obtained by increasing the extracted current but the emittance was then over specifications.

Very recent experiments showed that by increasing the pressure in the second diagnostic chamber, the emittance decreased by 20% due to space charge compensation. The results reported in this article can be thus improved. In fact, it is to be stressed that the EMU is placed ~300 mm downstream from the RFQ entrance, where the emittance values are to be within specifications.

The emittance and the H^+/D^+ fraction ratio were degraded with the increase of duty cycle. However, commissioning results of phase A1 with D^+ beam showed that the emittance was improved at high duty cycle by injecting Krypton gas between the two solenoids of the LEBT. Injecting Krypton gas (or D_2 / H_2 gas) into the second diagnostic chamber at high duty cycle may also help to retrieve the emittance obtained at low duty cycle.

The LIPAc injector has been designed to produce 100 keV D^+ beam of high intensity. H^+ beam operation at half current and half energy can lead to lower plasma density and can explain the difference of extraction and of transport at low energy between H^+ and D^+ beams.

In October 2016, commissioning of H^+ and D^+ beams will thus continue with the objective to reach the requirements at the RFQ entrance from chopper operation up to CW operation with well-matched Twiss parameters. To achieve this goal, injection of Krypton gas (or D_2 / H_2 gas) into the second diagnostic chamber will be possible to learn the real emittance value at the RFQ entrance. Also, a calorimetric BS measurement system of high resolution is now available and a magnetic secondary electrons suppressor will be added to the electrical BS measurement system. Results of electrical and calorimetric measurements will be compared in the next campaign.

ACKNOWLEDGEMENT

The present work has been performed in framework of the Broader Approach Agreement. The authors gratefully acknowledge the support of their home institutions and research funders in this work. Views and opinions expressed herein do not necessarily reflect those of QST, Fusion for Energy, or of the authors' home institutions or research funders.

REFERENCES

[1] J. Knaster *et al.*, *Nuclear Fusion* 55 (2015) 086003.
[2] P. Cara *et al.*, in *Proc. IPAC'16*, paper MOPOY057, Busan, Korea.
[3] A. Mosnier *et al.*, in *Proc. IPAC'12*, paper THPPP075, New Orleans, LA, USA.
[4] R. Gobin *et al.*, in *Proc. IPAC'13*, paper THPWO003, Shanghai, China.
[5] M. Comunian *et al.*, in *Proc. LINAC'08*, paper MOP036, Victoria, BC, Canada.
[6] H. Dzitko *et al.*, in *Proc. IPAC'15*, paper THPF006, Richmond, VA, USA.
[7] R. Gobin *et al.*, *Rev. Sci. Instrum.*, 79 (2008) 02B303.

ISBN 978-3-95450-186-1

[8] M. Comunian *et al.*, in *Proc. IPAC'11*, paper MOPS031, San Sebastián, Spain.
[9] B. Bolzon *et al.*, in *Proc. IBIC'15*, paper TUPB008, Melbourne, Australia.
[10] K. Shinto *et al., Rev. Sci. Instrum*., 87 (2016) 02A727.
[11] Y. Okumura *et al., Rev. Sci. Instrum*., 87 (2016) 02A739.
[12] K. Nishiyama *et al.*, Proc. SOFT 2016, to be submitted.
[13] L. Bellan *et al.*, presented at LINAC 2016, East Lansing, MI, USA, (to be published).

ISBN 978-3-95450-186-1

DEVELOPMENT OF A COMPACT HIGH INTENSITY ION SOURCE FOR LIGHT IONS AT CEA-SACLAY

O. Delferrière†, R. Gobin, Y. Gauthier, F. Harrault, O. Tuske
Commissariat à l'Energie Atomique et aux Energies Alternatives, CEA/Saclay, DSM/IRFU, 91191-Gif/Yvette, France

Abstract

During the past 5 years, a R&D program has been launched to improve the beam quality of ECR 2.45 GHz high intensity light ion sources for high power accelerators. The main goal was to minimize the divergence and emittance growth of intense beams due to the space charge as early as possible on the low energy transfer line for a better injection in the second stage of acceleration (RFQ). This has been achieved by reducing the length of the extraction system, to be able to put the first solenoid as close as possible to the extraction aperture. This was performed with the ALISES [1] concept (Advanced Light Ion Source Extraction System). Encouraging results have been obtained in 2012 but with limitations due to Penning discharges in the accelerating column. Taking advantages of ALISES geometry, intensive studies and simulations have been undertaken to eliminate the discharge phenomena. An Innovative and compact source geometry has been found and the source has been fabricated. This new prototype and its performances will be described, as well as magnetic field configuration studies and its influence on the extracted beam.

INTRODUCTION

The ALISES concept developed at CEA/Saclay is based on the use of the stray field of a solenoid located downstream the extraction system to produce the ECR resonance in the plasma chamber. The other characteristic of ALISES source is that the insulating structure between the source potential and the LEBT potential is located upstream of the plasma electrode. The design of the accelerator column (Fig. 1), reversed compared to standard high current light ions sources like SILHI [2] or IFMIF [3] source, allows a gain of several tens of cm on LEBT length. This also gives available space at the beginning of the LEBT, to put focalizing and/or guiding elements as early as possible to adjust the beam dimensions and angle, in order to minimize the emittance growth due to the beam space charge effects. The ALISES source has produced about 18 mA extracted from a 6mm diameter plasma extraction hole at 23 keV during the commissioning in 2011-2012 [4], but strong limitations were observed [5] due to Penning discharge in the accelerator column.

† Olivier.delferriere@cea.fr

* This source developed at Saclay is under patent number FR 2969371 from 2010/12/15

After two years of intensive work on electromagnetic simulations and design improvement to eliminate the penning discharge process, an innovative and compact source geometry has been developed, fabricated and successfully tested on BETSI [6] test bench in 2015.

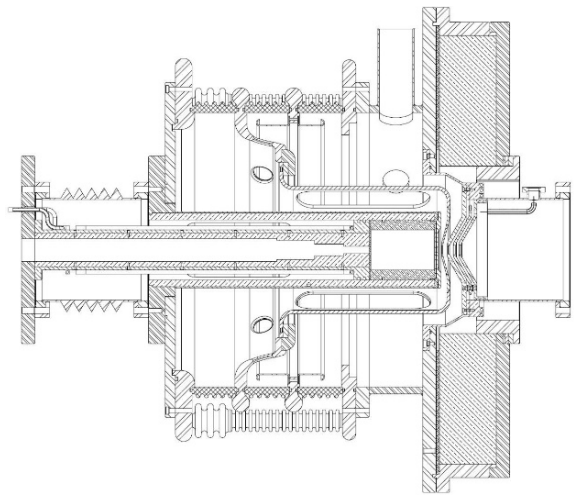

Figure 1: ALISES source geometry characteristic.

ALISES II* INOVATIVE ION SOURCE

The undesirable Penning discharge occurred at different locations in the ALISES accelerator column due to favorable combination of electromagnetic and electrostatic field lines. This was due first, to electrode shape with alternative parts along axial direction and radial direction, and second to higher magnetic field value in the system compare to standard source configuration, because of increasing field from the RF injection up to the extraction end. At the location of changes in direction of electrode shape, Penning trap electromagnetic configuration can occur. Then, at several locations, electrons are accelerated up to several kilovolts and trapped with enough energy to ionize the residual gas, leading to the Penning discharge.

The Insulating structure used for ALISES source was a spare part of SILHI source with a large 410mm internal diameter. In this big volume of vacuum, the electrodes geometry have been designed with smooth shape and sufficient space in between, to prevent from electrostatic sparks, especially the shape of the puller electrode between the plasma chamber at 100 kV, and the first grounded electrode, but not for Penning discharge reason. To eliminate all the sources of Penning discharge, the idea was to reduce the vacuum part as much as possible where they could appear. The main characteristic of this source

ISBN 978-3-95450-186-1

is that now the insulating structure, initially 155mm away from the outer part of the plasma chamber, is now directly in contact with the source body. From the initial ALISES source, the pumping port has been suppressed, but the same solenoid is used as well as the extraction chamber. This chamber hosts the two grounded electrodes, which are cooled, with the repeller electrode in between.

SOURCE ASSEMBLY

Main Parts

The new source ALISES II is a compact system as we can see on Fig. 2 and Fig. 3. A first copper cylinder (A) has been machined to form the plasma chamber (A1) and the RF entrance ridged guide (A2) in one piece. A smooth ceramic cylinder (B) built in two concentric parts realizes the insulating structure, and is in contact of the copper body. Both the ceramic and the source body are screwed on a copper flange (C) and connected to the RF guide. The plasma electrode (D) is fixed on the copper cylinder extremity to close the plasma chamber with an appropriate extraction hole. The puller electrode (E) is fixed to the source body by the mean of an intermediate ring shaped ceramic part (F). During the machining, a collar (G) has been realized on the external part of the insulating structure, to allow the structure to be assembled with the magnetic system (H) and the extraction chamber (I) by the mean of a dedicated flange (J).

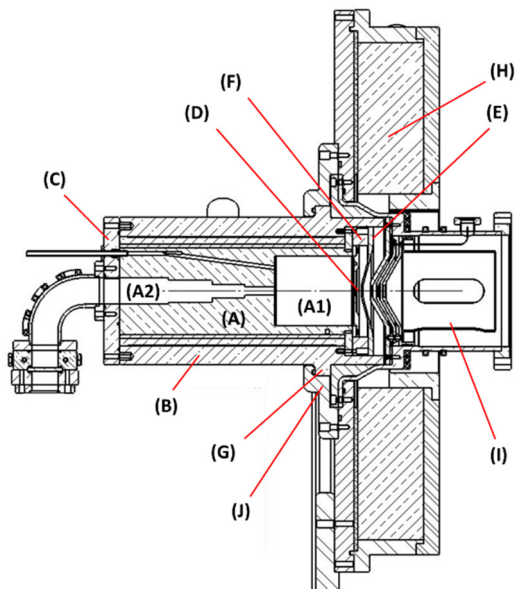

Figure 2: ALISES II source assembly.

The geometry of the five electrode extraction system is now greatly simplified. Electrodes shape is reduced to simple cones that ensure electric field line more or less parallel to the magnetic field lines avoiding any Penning trap problem. The assembly is also easier. The Extraction system has been initially design for high current and high voltage (100mA@100kV) with a 9mm diameter plasma electrode.

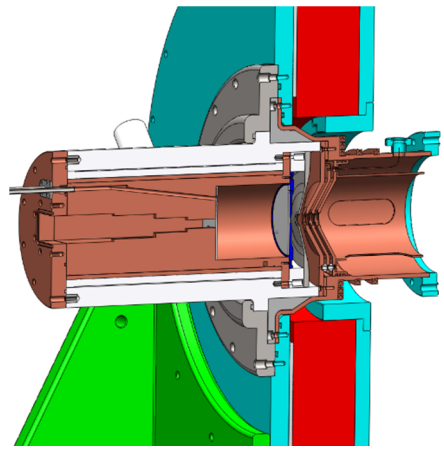

Figure 3: 3D cut of ALISES II source.

Puller Electrode Connection

To connect the puller electrode to high voltage (Fig. 4), a groove has been machined longitudinally on the external surface of the internal ceramic cylinder, and a hole has been drilled radially on the external ceramic cylinder (Fig. 4). The wire goes in the hole (K), then in the groove (L), cross the collar (M) of the source body, pass through the ceramic ring (F) and is plugged on the puller electrode (E) by a screw. Because the source body is at 100 kV, and the wire is at intermediate potential around 70 kV, the wire is inserted in a glass tube when crossing the copper collar, which extend in the ceramic part enough to prevent electrical sparks.

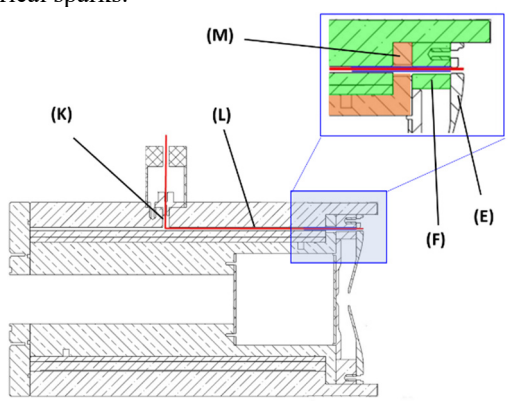

Figure 4: Repeller electrode connection.

COMMISSIONING ON BETSI

The source has been first tested without RF power to verify the lack of Penning discharge by increasing the high voltage, with the magnetic field adjusted at resonance value of 875 Gauss for the 2.45 GHz microwave generation. We observed that no output current occurs on high voltage power supplies, which means that no particle hit the electrodes to induce any fall of the voltage.

ALISES II has then been installed on BETSI test bench in March 2015 (Fig. 5) and has produced its first proton beam very easily with 18mA@35kV in pulsed mode (500ms each s) with a 6mm extraction hole diameter.

ISBN 978-3-95450-186-1

After optimization with the same extraction, the source has produced end of March, a proton beam of 35mA@50 kV in continuous mode with gas injection of 1.65sccm, and a RF power of 980 W. We couldn't explore higher extraction voltage because of High voltage limitation to 50 kV on BETSI.

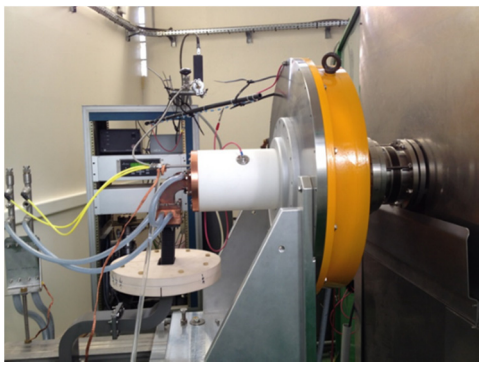

Figure 5: ALISES II on BETSI.

MAGNETIC FIELD PROFILE STUDY

A major characteristic of this source is that over a large range of magnetic field value, the source is producing about the same current even in off-resonance mode inside the plasma chamber (Fig. 6).

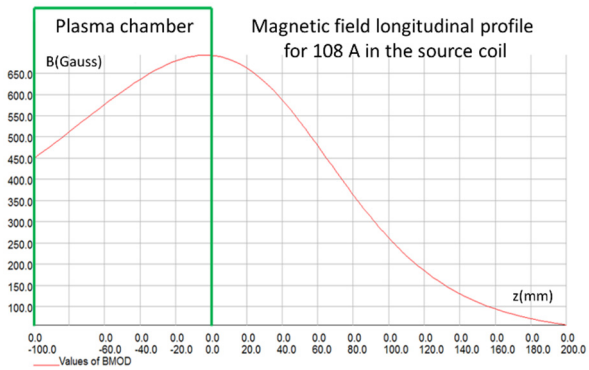

Figure 6: Best magnetic field B(z) for 22.5mA@30kV extracted beam.

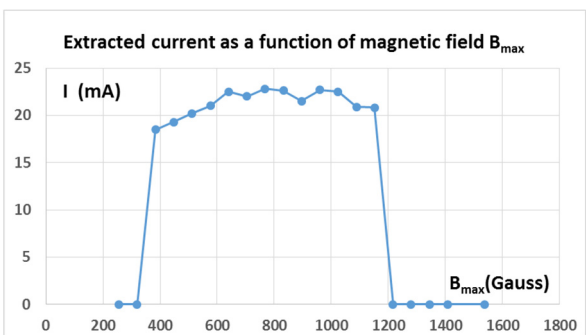

Figure 7: Extracted current function of B_{max} (extraction).

The resonance zone is usually positioned just in front of the RF entrance. To obtain 875 Gauss at this location, the corresponding current in the coil is 181A with Bmax=1150 Gauss at the extraction. As we can see on Fig. 7, we can produce a beam between 18mA to 23mA from Bmax=400 Gauss (I=60A) to Bmax=1150 Gauss, when extraction stops.

As the dimensions of the source body has been dramatically reduced, we tried to understand this production mode by adding a second coil (SILHI type) installed around the ceramic structure (Fig. 8). With the 2 coils, we could test different magnetic profiles, including the SILHI one. The same results were obtained, with the best tuning under the resonance. The latest result was obtained with a current of only 104A in the additional coil, the theoretically current for resonance at the RF entrance being 140A. The extracted beam current was 48.5mA@50kV with 2.1sscm gas and 700W power in continuous mode. Additional work is necessary to understand clearly the mechanism of ion production.

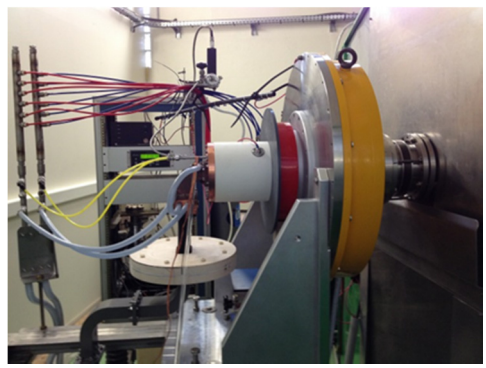

Figure 8: Addition of a second coil surrounding the ceramic and the plasma chamber.

CONCLUSION AND FUTURE WORK

ALISES II ECR light ion source has been successfully tested at Saclay at 50 kV. The BETSI upgrade to 100 kV at the end of this year will give the possibility of higher extraction voltage and performance improvements. Wien filter and Allison scanner will be ready to analyze the beam proton fraction and the beam emittance. Due to the compactness of this source given by its innovative conception, we can now use a small coil around the source body instead of the large initial solenoid. Drawings of ALISES III taking also into account some improvements for an easy plug of the source on the LEBT without any support, have already been realized and fabrications launched. Assembly is foreseen by the end of this year.

REFERENCES

[1] O. Delferrière *et al., Rev. Sci. Instrum.* **83,** 02A307 (2012).
[2] R. Gobin *et al., Rev. Sci. Instrum.* **81**, 02B301 (2010).
[3] Okumura *et al.*, "Operation and commissioning of IFMIF (International Fusion Material Irradiation Facility) LIPAc Injector", presented at ICIS'15, New York, NY, USA, paper WepM04 (2015).
[4] S. Nyckees, "Study and development of a new ECR source creating an intense light ions beam", Thesis-Universite Paris Sud - Paris XI, UFR Sciences, CEA, DSM-IRFU (France).
[5] O. Delferrière *et al., Rev. Sci. Instrum.* **85**(2), 02A939 (2014).
[6] O. Tuske *et al., Rev. Sci. Instrum.* **79**, 02B710 (2008).

ISBN 978-3-95450-186-1

TRANSVERSE COUPLING OF ION BEAMS FROM AN RCR ION SOURCE

Y. Yang#, Y. Liu, L.T. Sun, Y. J. Yuan, H.W. Zhao, IMP/CAS, Lanzhou 730000, China

Abstract

Transverse coupling of ion beams out of an ECR ion source has been studied from two aspects. One is the coupling induced during beam extraction and the other is the coupling effect of a solenoid. Ion beams extracted from an electron cyclotron resonance (ECR) ion source will experience a descending axial magnetic field at the extraction region, resulting in a strong transverse coupling to the extracted beam, with projection root-mean-square (RMS) emittance growth both in horizontal and vertical directions and two eigen-emittances separation. Simulations of particle beam extraction from an ECR ion source in the present of the magnetic field have been carried out to investigate the coupling property. The results indicate the magnetic field in the extraction region can determine the beam emittances and the transverse coupling by affecting the beam formation. In addition, coupling effect of a solenoid on an initially non-round beam has been illustrated by introducing the matrix algorithm, which can qualitatively and indirectly explain the experimental phenomenon of SECRAL (Superconducting Electron Cyclotron Resonance ion source with Advance design in Lanzhou) at institute of modern physics (IMP).

INTRODUCTION

As one of the most powerful devices to produce intense highly-charged heavy ion beams, ECR ion sources are widely adopted by many large accelerator facilities. However, because of its special magnetic confinement fields ECR ion source beam quality has always been concerned and achieved much attention. Since the extraction of the ions takes place in the vicinity of a local magnetic field maximum, the following descending axial magnetic field adds an azimuthal momentum to the beam, leading to the transverse emittances blow up and coupling. It is generally believed that the beam emittance is primarily determined by the axial field strength at the extraction region if the ion temperature in the ECR plasma is low [1, 2]. The magnetic contribution to the (Normalized RMS) emittance can be given by

$$\varepsilon_{mag} = 0.032 \cdot (R_{extr})^2 \cdot (\frac{B_{extr}}{M/Q}), \quad (1)$$

where R_{extr} [mm] is the radius of the effective extraction aperture and M/Q the ion mass-to-charge ratio and B_{extr} [T] the maximum magnetic field at the extraction region. This equation indicates the beam projection emittance is proportional to the extraction field strength. However, beam emittance measurements for the ECR ion source at RIKEN with a pepper-pot scanner do not have a good agreement with the accepted theorem as described above [3, 4]. In their experiment both the projection RMS emittances and the 4-D emittance are lower under a relatively larger B_{extr}, which indicates a more complicated extraction process. Besides the coupling induced by the semi-solenoid field in the ion source extraction region, a complete solenoid, which is usually employed as the initial focusing element, can also lead to beam coupling since the ion density distribution across the extraction aperture is inhomogeneous due to the asymmetric plasma distribution at extraction, resulting in a non-round beam [5].

This paper starts with an introduction of the relationship between the projection RMS emittances and eigen-emittances based on modeling a beam passing through a semi-solenoid field. Afterwards beam extraction simulations are carried out toward SECRAL [6] to investigate the transverse coupling property of the extracted beam. Then coupling effect of a solenoid field on a non-round beam is demonstrated by analytical theory in combination with the experimental results with SECRAL. The last section makes some conclusions and an outlook.

BASIC THEOREM

Beam RMS emittances are defined through the beam second moment matrix [7, 8]

$$C = \begin{bmatrix} <xx> & <xx'> & <xy> & <xy'> \\ <x'x> & <x'x'> & <x'y> & <x'y'> \\ <yx> & <yx'> & <yy> & <yy'> \\ <y'x> & <y'x'> & <y'y> & <y'y'> \end{bmatrix}, \quad (2)$$

where the full 4-D emittance is defined by

$$\varepsilon_{4d} = \sqrt{\det(C)}\,. \quad (3)$$

The projection RMS emittances ε_x and ε_y are defined by the corresponding sub phase space determinants, which can completely characterize the transverse quality when the beam is transversely uncoupled. Diagonalization of the beam matrix yields the eigen-emittances ε_1 and ε_2, whose values can be expressed as:

$$\varepsilon_{1,2} = \frac{1}{2}\sqrt{-tr[(CJ)^2] \pm \sqrt{tr^2[(CJ)^2] - 16\det(C)}}\,. \quad (4)$$

The 4-D matrix J is the skew-symmetric matrix with non-zero entries on the block diagonal off form. A symplectic transformation M obeys

yangyao@impcas.ac.cn.

ISBN 978-3-95450-186-1

$$M^T J M = J\,,\quad J=\begin{bmatrix}0&1&0&0\\-1&0&0&0\\0&0&0&1\\0&0&-1&0\end{bmatrix}. \tag{5}$$

Drifts, solenoids, quadrupoles, and dipoles are all symplectic, through which transformations beam eigen-emittances are invariant. Coupling between horizontal and vertical planes results in

$$\varepsilon_{4d} = \varepsilon_1 \cdot \varepsilon_2 \le \varepsilon_x \cdot \varepsilon_y \tag{6}$$

with equality just for zero inter-plane coupling moments.

The extraction aperture of most ECR ion sources is located near the center of the extraction solenoid coil [6], therefore particles are extracted and accelerated in a semi-solenoid magnetic field, which provides a non-symplectic transformation R_{out}. For simplicity, assuming a very short solenoid, its transfer matrix in the exit fringe can be described by:

$$R_{out}=\begin{bmatrix}1&0&0&0\\0&1&-\kappa&0\\0&0&1&0\\\kappa&0&0&1\end{bmatrix}, \tag{7}$$

where

$$\kappa=\frac{B_{extr}}{2(B\rho)}. \tag{8}$$

B_{extr} is the solenoid on-axis magnetic field strength, and $(B\rho)$ is the particle rigidity. Assuming the initial beam out of the ion source extraction hole has equal horizontal and vertical RMS emittances and no inter-plane correlations, the beam matrix can be simplified to (in the case here, assuming Twiss parameters $\alpha_{x,y}$=0)

$$C_0=\begin{bmatrix}\varepsilon\beta&0&0&0\\0&\frac{\varepsilon}{\beta}&0&0\\0&0&\varepsilon\beta&0\\0&0&0&\frac{\varepsilon}{\beta}\end{bmatrix}. \tag{9}$$

When the beam passes through the exit fringe of the solenoid, the beam matrix C_1 is found as

$$C_1 = R_{out} C_0 R_{out}^T=\begin{bmatrix}\varepsilon\beta&0&0&\kappa\varepsilon\beta\\0&\frac{\varepsilon}{\beta}+\kappa^2\varepsilon\beta&-\kappa\varepsilon\beta&0\\0&-k\varepsilon\beta&\varepsilon\beta&0\\\kappa\varepsilon\beta&0&0&\frac{\varepsilon}{\beta}+\kappa^2\varepsilon\beta\end{bmatrix}. \tag{10}$$

Inter-plane correlations are created in the *xy'* and *x'y* phase spaces and the RMS emittances and eigen-emittances become

$$\varepsilon_x=\varepsilon_y=\sqrt{\varepsilon\beta(\frac{\varepsilon}{\beta}+\kappa^2\varepsilon\beta)}\,, \tag{11}$$

$$\varepsilon_{1,2}=\varepsilon_x\pm\kappa\varepsilon\beta\,. \tag{12}$$

It can be seen that both the RMS emittances ε_x and ε_y have a significant growth and the two eigen-emittances separate, nevertheless, the 4-D emittance preserves.

The realistic semi-solenoid field has a certain integral length, whose transmission matrix can be read as

$$R_{out}=\begin{bmatrix}1&0&0&0\\0&1&-\kappa&0\\0&0&1&0\\\kappa&0&0&1\end{bmatrix}\begin{bmatrix}1&\frac{\sin(\kappa L)}{2\kappa}&0&\frac{\sin(\kappa L/2)^2}{\kappa}\\0&\cos(\kappa L)&0&\sin(\kappa L)\\0&-\frac{\sin(\kappa L/2)^2}{\kappa}&1&\frac{\sin(\kappa L)}{2\kappa}\\0&-\sin(\kappa L)&0&\cos(\kappa L)\end{bmatrix}, \tag{13}$$

where L is the integral length of the whole extraction solenoid of the ion source.

BEAM EXTRACTION SIMULATION THROUGH A SEMI-SOLENOID FIELD

The magnetic confinement fields of an ECR ion source are typically achieved by the superposition of an axial mirror field and a radial sextupole field, resulting in

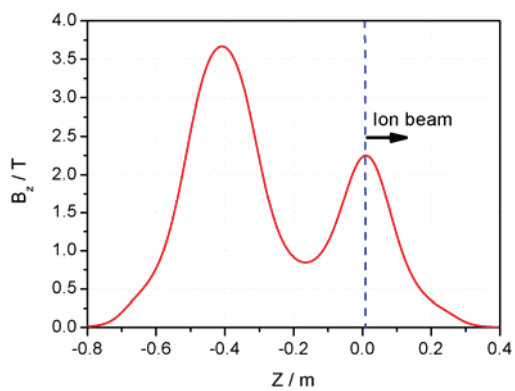

Figure 1: Axial magnetic field distribution of SECRAL.

ISBN 978-3-95450-186-1

a so called minimum-B field configuration. Fig.1 shows the axial magnetic field distribution of SECRAL. The plasma electrode is located in the vicinity of the extraction mirror peak, leading to extraction of ions from a strong magnetic field and subsequent beam formation in decaying fringe field. Extraction simulation in this section will mainly focus on the contribution of the magnetic field to the beam emittance.

The ion beam extraction has been modeled with the ion optical code IBSimu [9, 10, 11]. In the simulation, ions are extracted from plasma that is modeled in a reduced volume. The 3-D magnetic field map, which includes the solenoid and hexapole fields, is calculated with TOSCA and read by the code. The first simulation is aimed at a $^{129}Xe^{29+}$ beam with extraction voltage of 25 kV. Fig. 2 illustrates the simulated ion trajectory densities through the extraction region with three different field strengths of B_{extr}=1.35 T, B_{extr}=2.03 T and B_{extr}=2.7 T. Fig. 3 presents the beam emittances (including the projection RMS emittances ε_x and ε_y and eigen-emittances ε_1 and ε_2) and the corresponding products $\varepsilon_x*\varepsilon_y$ and $\varepsilon_1*\varepsilon_2$ along the extraction path when the B_{extr}=1.35 T. Simulation results agree well with the theoretical prediction that the two eigen-emittances tend to heavily separate, with one value increasing and the other decreasing, but both projection emittances rise up in the strong magnetic field. Finally the difference between ε_1 and ε_2 reaches several hundred times at the end of the extraction region (z=0.38 m), and the value of $\varepsilon_{x,y}$ becomes nearly ten times larger than that at the point of z=0.05 m where the accelerating process is almost accomplished. The 4-D emittance, which is equal to $\varepsilon_1*\varepsilon_2$, keeps constant, but the value of $\varepsilon_x*\varepsilon_y$ has a significant growth.

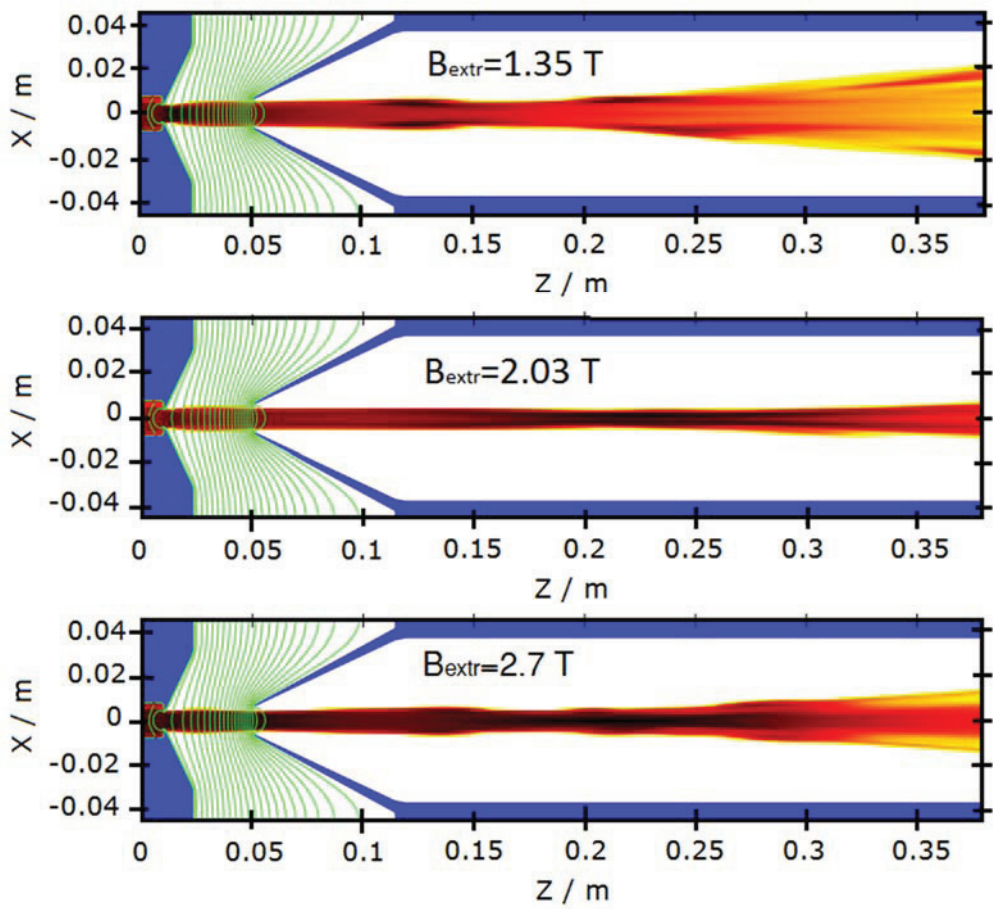

Figure 2: Simulated ion trajectory densities through the extraction region with B_{extr}= 1.35 T, B_{extr}=2.03 T and B_{extr}=2.7 T.

To investigate the effect of the magnetic field in the extraction region simulations with different amplitudes of B_{extr} are performed. Fig. 4 shows the simulated beam emittances and the corresponding products versus B_{extr} at the end of the extraction region (z=0.38 m), in which the expected emittance calculated according to formula (1) is also given (with R_{extr}=5 mm). It is clear the projection emittances do not increase with the magnetic field strength proportionally as predicted by formula (1), but there exist an optimal field (B_{extr}=2.03 T) under which condition the projection emittance $\varepsilon_{x,y}$ reaches minimum and the value of $\varepsilon_x*\varepsilon_y$ is closest to $\varepsilon_1*\varepsilon_2$, and also, the difference between the two eigen-emittances ε_1 and ε_2 is smallest. It means under this condition the coupling in the

ISBN 978-3-95450-186-1

transverse phase space is relatively weak. 4-D matrices (in units of mm and mrad) of the beams at the end of the extraction region in the cases of B_{extr}=1.35 T, B_{extr}=2.03 T and B_{extr}=2.7 T are

$$C_{1.35\,T}=\begin{bmatrix} 105.9975 & 476.0413 & -0.2120779 & -196.2880 \\ 476.0413 & 2466.011 & 175.0482 & -81.79913 \\ -0.2120779 & 175.0482 & 95.20618 & 432.9456 \\ -196.2880 & -81.79913 & 432.9456 & 2330.547 \end{bmatrix}, \quad (14)$$

$$C_{2.03\,T}=\begin{bmatrix} 13.14704 & 70.28109 & -0.4886135 & -37.11058 \\ 70.28109 & 468.760 & 29.29614 & -22.68711 \\ -0.4886135 & 29.29614 & 11.82261 & 66.22893 \\ -37.11058 & -22.68711 & 66.22893 & 468.3700 \end{bmatrix}, \quad (15)$$

and

$$C_{2.7\,T}=\begin{bmatrix} 44.9443 & 238.4365 & -1.350854 & -101.0213 \\ 238.4365 & 1465.950 & 87.37357 & -27.78315 \\ -1.350854 & 87.37357 & 44.73177 & 243.2753 \\ -101.0213 & -27.78315 & 243.2753 & 1519.878 \end{bmatrix} \quad (16)$$

respectively. It is clear that when B_{extr}=2.03 T the absolute values of the off-diagonal sub-matrix elements are much lower than those with B_{extr}=1.36 T or B_{extr}=2.7 T except for the infinitesimal <*xy*>.

The cause of this non-proportional relationship between the beam emittance and the magnetic field strength is that the magnetic field plays an important role in the beam formation in the extraction region, with the transverse coupling changed. The extracted beam profiles with B_{extr}=1.35 T, 2.03 T and 2.7 T are compared in Fig. 2. It is found that the plasma meniscuses under different magnetic fields have the same shapes, however, the magnetic field with strength of 2.03 T, together with the electric field in the acceleration gap, provide a proper focusing effect, resulting in a quasi-parallel beam with a small divergence as well as a small envelope inside the grounded electrode. While in the case of B_{extr}=1.36 T the beam is less focused, but over focused in the field of 2.7 T. According to equation (11) and (12) derived from the simplified semi-solenoid model, for a given particle rigidity, the beam emittances (including the projection emittances and eigen-emittances) out of a exit fringe field are related not only to the field strength B_{extr} but also to the initial beam emittance ε and beam size (equal to $2\sqrt{\varepsilon\beta}$). In another words, besides adding an azimuthal momentum to the beam, the magnetic field can also determine the beam emittances and the transverse coupling by affecting the beam formation in the extraction region. This can be a possible reason of the experimental phenomenon that the beam emittance with lower B_{ext} is larger than that with higher B_{ext} for RIKEN ECR ion source [3, 4].

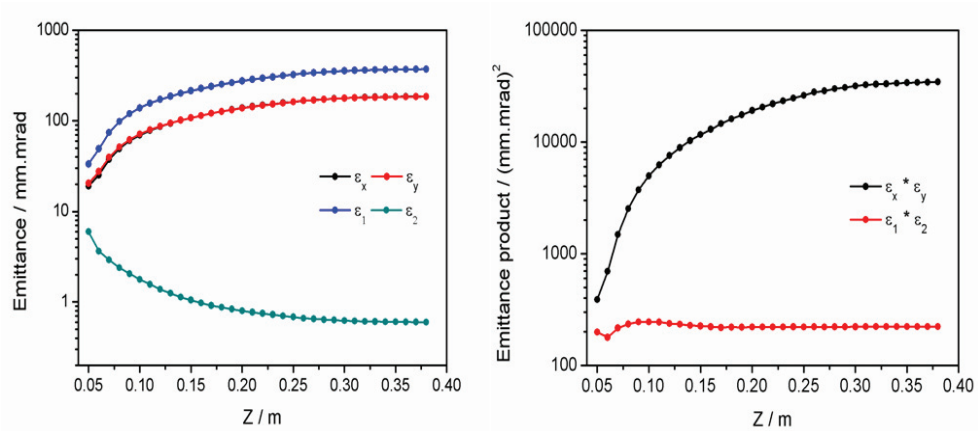

Figure 3: Beam emittances and the corresponding products ε_x*ε_y and ε_1*ε_2 along the extraction path when B_{extr}=1.35 T.

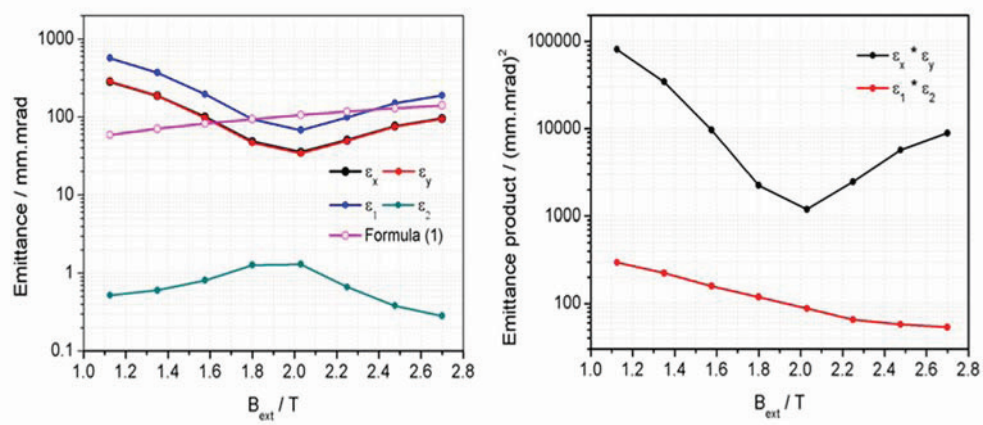

Figure 4: Beam emittances and the corresponding products versus B_{extr}.

ISBN 978-3-95450-186-1

According to the simulations, it is of interest to realize that the 4-D emittance decreases with increasing the extraction magnetic field strength. Since the 4-D emittance keeps constant after accelerating, it is easy to imagine that the magnetic field in the acceleration gap is one of the decisive factors of the 4-D emittance. By observing the beam extraction profiles in Fig. 2, we can find the main reason is that the beam size at the location of the grounded electrode is focused to be smaller with a larger magnetic field, which helps to avoid the large-radius aberration in the einzel lens and improve the beam quality.

COUPLING EFFECT OF A SOLENOID

In the previous section, we have discussed the transverse coupling resulting from the non-conservation of the angular momentum of the beam out of a semi-solenoid field. However, a complete solenoid can also induce beam coupling if it is a non-round beam, although through which beam's angular momentum keeps constant. Our experimental results have indicated that the cross section of extracted beam from ECR is not round along transport path [12]. The experiment is based on the measurement of the projection emittance (for $^{129}Xe^{29+}$ with the extraction voltage of 25 kV) with SECRAL by changing the field strength and the polarity of the solenoid lens which is installed just after the source body. Experimental result is presented in Fig. 5, in which "F" means forward current being loaded on the solenoid, in which case the beam transmits in the direction of the solenoid lens axial field in the beam pipe, while "R" means the polarity of the solenoid lens is reversed. This plot indicates that the emittances tend to transfer between the two orthogonal directions as the solenoid current is increased and in addition, allot values dramatically differ in the two directions when reversing the polarity of the solenoid field. The maximum difference between the two projection emittances can even reach several times. The change of the emittance values with the solenoid current can be due to the fact that the ion beam extracted from the ECR ion source is not round and can produce periodic coupling in a solenoid which has a rotation effect to the beam.

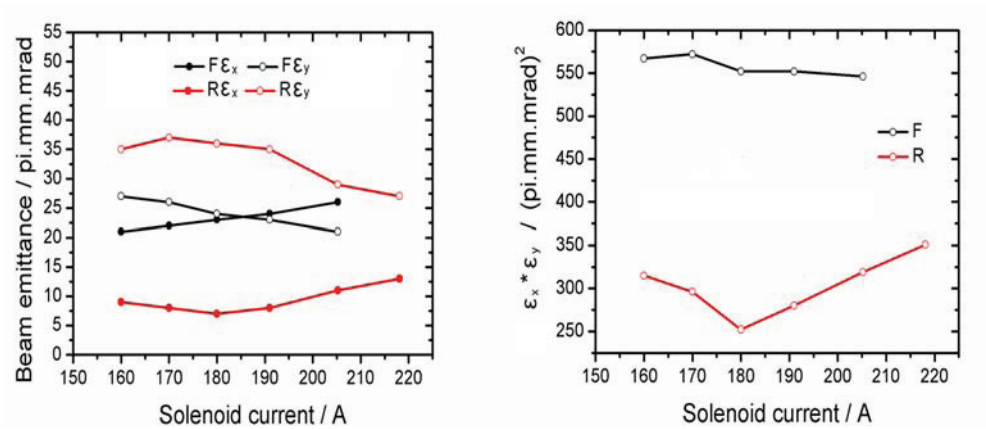

Figure 5: Measured beam emittances and the corresponding product by changing the focusing strength and reversing the polarity of the beam line solenoid.

In order to illustrate the coupling effect of a solenoid on a non-round beam and explain the experimental phenomenon indirectly and qualitatively, matrix algorithm is applied. Firstly, we make an artificial beam matrix with zero inter-plane elements as

$$C = \begin{bmatrix} 10 & 65 & 0 & 0 \\ 65 & 485 & 0 & 0 \\ 0 & 0 & 10 & 65 \\ 0 & 0 & 65 & 432.5 \end{bmatrix}, \quad (17)$$

which has the same envelope in the two projected directions but different emittances, with ε_x=25 mm.mrad and ε_y=10 mm.mrad. Let this beam pass through a solenoid with effective length of L_{eff}=0.18 m, the beam emittances and their products versus the solenoid field are calculated and plotted in Fig. 6 for a particle rigidity of 0.0479 Tm (for $^{129}Xe^{29+}$ with extraction voltage of 25 kV). It is clear that the beam coupling in the transverse phase space has a periodic property, resulting in a periodic change both in the projection emittance and the corresponding product as the field strength of the solenoid is changed. When the value of the projection emittance product $\varepsilon_x*\varepsilon_y$ reaches minimum, equal to the eigen-emittance product $\varepsilon_1*\varepsilon_2$, the coupling is removed.

Besides its focusing effect, a solenoid can bring a phase space rotation to the beam. The rotation angle is

$$\Theta = \kappa L_{eff} = \frac{B_{\max}}{2(B\rho)} L_{eff}, \quad (18)$$

where B_{max} is the on-axis magnetic field strength. When $\Theta = n \cdot \frac{\pi}{2}, \quad n = 0, \pm 1, \pm 2, \pm 3, \cdots$, the beam is uncoupled, in which the horizontal and vertical planes exchange if $n = \pm 1, \pm 3, \pm 5, \cdots$.

The second artificial beam matrix is assumed as

ISBN 978-3-95450-186-1

$$C = \begin{bmatrix} 10 & 65 & 0 & 0 \\ 65 & 485 & 0 & 0 \\ 0 & 0 & 20 & 65 \\ 0 & 0 & 65 & 242.5 \end{bmatrix}, \quad (19)$$

which has equal projection emittances, but different sizes in the horizontal and vertical planes. For this case, a solenoid can also create periodic coupling due to the rotation effect, although the two projection emittances are always equal to each other, as shown in Fig. 7.

For the case that a beam has both unequal emittances and sizes in the two projected directions, with an assumed matrix of

$$C = \begin{bmatrix} 10 & 65 & 0 & 0 \\ 65 & 485 & 0 & 0 \\ 0 & 0 & 20 & 65 \\ 0 & 0 & 65 & 216.25 \end{bmatrix}, \quad (20)$$

the coupling effect of a solenoid is presented by Fig. 8. It is noteworthy that for this case the coupling is much stronger than that in the first and second cases by comparing the value of $\varepsilon_x * \varepsilon_y$.

In a word, the rotation effect of a solenoid field could bring a periodic coupling to a non-round beam, even though it is initially uncoupled. With regard to the experimental result with SECRAL (as shown in Fig. 5), when the solenoid current is -180 A, the value of $\varepsilon_x * \varepsilon_y$ reaches minimum and the beam quality is optimal. That is because under this condition the solenoid (after the ion source) disentangles the coupling by compensating the beam rotation (not rotational momentum) caused by the semi-solenoid field in the extraction region on the premise of initially non-round beam. However, the coupling is not completely removed unless in an opposite magnetic field of the same the particles experienced while they were extracted or by using a skew quadrupole (or a skew triplet) [7, 8].

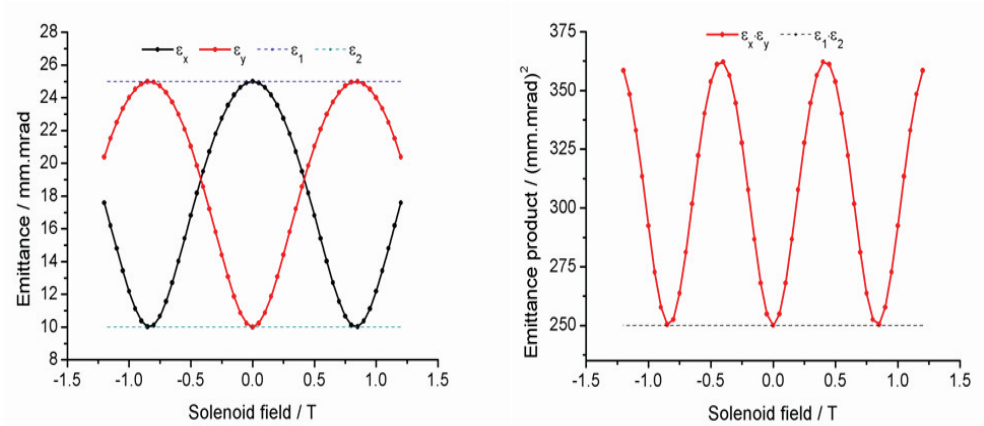

Figure 6: Calculated beam emittances and their products versus the solenoid field for the first case.

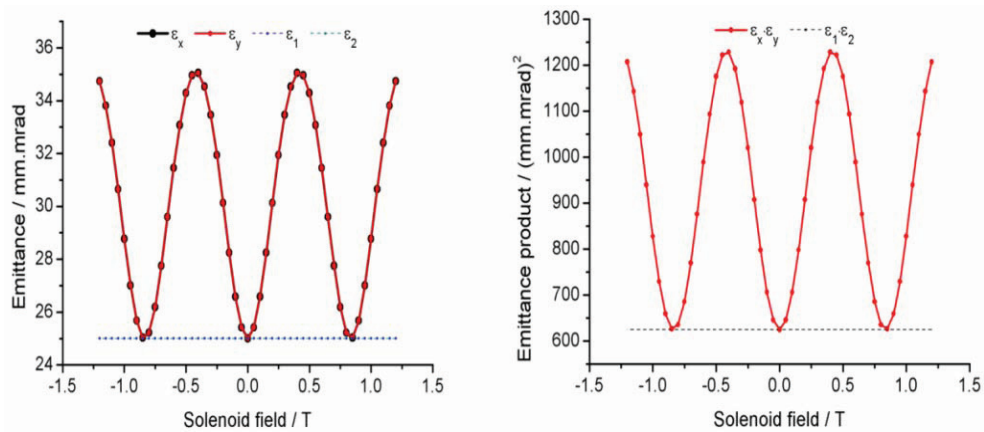

Figure 7: Calculated beam emittances and their products versus the solenoid field for the second case.

ISBN 978-3-95450-186-1

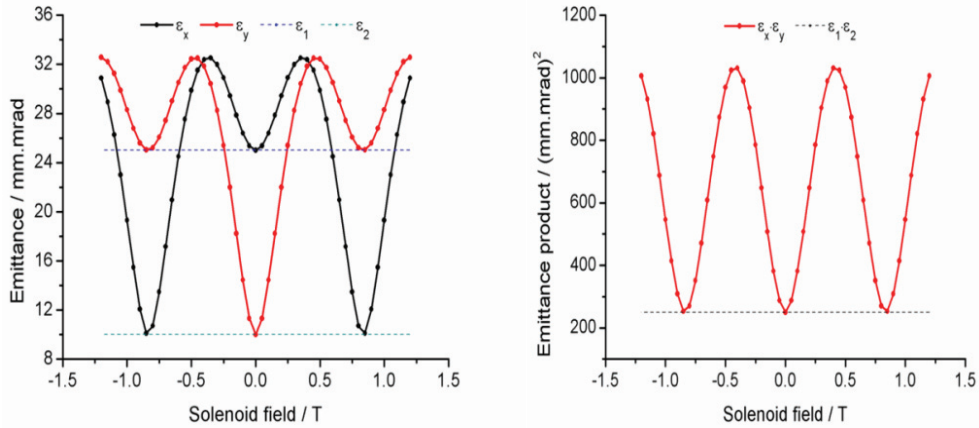

Figure 8: Calculated beam emittances and their products versus the solenoid field for the third case.

CONCLUSION AND OUTLOOK

Transverse coupling of ion beams out of an ECR ion source has been studied from two aspects. One is the coupling induced during beam extraction and the other is the coupling effect of a solenoid. Particle beam extraction from an ECR ion source in the present of magnetic fields has been modeled. A strong coupling in the transverse space is established through the semi-solenoid field in the extraction region, resulting in the projection emittance growth both in horizontal and vertical and the two eigen-emittances separation. Simulations do not show a proportional increasing of the projection emittances with scaling up the extraction field strength, but there exist an optimal field under which condition the coupling is weakest with the projection emittance reaching minimum. The cause of this phenomenon is that the magnetic field takes effect on the beam formation in the extraction region, with the transverse coupling changed. An interesting phenomenon presented in the simulation is that the 4-D emittance decreases with increasing the extraction magnetic field strength, which can be attributed mainly to the fact that the beam size at the location of the grounded electrode is focused to be smaller with a larger magnetic field, helping to avoid the large-radius aberration in the einzel lens and improve the beam quality. In actual adjustment of the extraction magnetic field, it is not used primarily to optimize the extracted beam formation, but to optimize the plasma confinement. Therefore, in order to achieve a high-quality beam, we should optimize the plasma conditions and the electric field in the acceleration gap (by using a moveable extraction electrode) by combination with the local magnetic field to optimize the beam profile. On the other hand, coupling effect on an initially non-round beam due to the rotation function of a solenoid has been demonstrated by introducing the matrix algorithm, which can qualitatively and indirectly explain the experimental phenomenon of SECRAL. However, the fly in the ointment is that the beam extraction simulations do not reflect a non-round beam due to the limited modeling in the ECR plasma distribution. To obtain more comprehensive qualities of ion beams from an ECR, measurements using a pepper-pot scanner are very essential, which is now under development at our institute.

ACCKNOWLEGEMENTS

This work is supported by the National Nature Science Foundation of China (contract No.11405238 and 11575265) and 973 Research program 2014CB845500.

REFERENCES

[1] M.A. Leitner, D.C. Wutte and C.M. Lyneis, in: Proceedings of PAC2001, Chicago, USA, 2001.
[2] M.Strohmeier, J.Y.Benitez, D.Leitner, D.Winklehner, D.S.Todd, C.M.Lyneis, M.Bantel, in: Proceedings of BIW10, Santa Fe, New Mexico, US, 2010.
[3] Y. Higurashi, J. Ohnishi, K. Ozeki, and T. Nakagawa, in: Proceedings of ECRIS2014, Nizhny Novgorod, Russia, 2014.
[4] Y. Higurashi, Oral presentation in: ICIS2015, NewYork, USA, 2015. <http://www.c-ad.bnl.gov/ICIS2015>.
[5] Peter Spädtke, K. Tinschert, R. Lang, J. Mäder, and J. Roßbach, Rev. Sci. Instrum. 79 (2008) 02B716.
[6] H. W. Zhao, L. T. Sun, X. Z. Zhang, Z. M. Zhang, X. H. Guo, W. He, P. Yuan, M. T. Song, J. Y. Li, Y. C. Feng, Rev. Sci. Instrum. 77 (2006) 03A333.
[7] C. Xiao, O.K. Kester, L. Groening, Physics Review Special Topics-Accelerators and Beams 16 (2013) 044201.
[8] L. Groening, Physics Review Special Topics-Accelerators and Beams 14 (2011) 064201.
[9] T. Kalvas, O. Tarvainen, T. Ropponen, O. Steczkiewicz, J. Ärje, H. Clark Rev. Sci. Instrum. 81 (2010) 02B703.
[10] V. Toivanen, G. Bellodi, D. Küchler, A. Lombardi, R. Scrivens, J. Stafford-Haworth, in: Proceedings of ECRIS2014, Nizhny Novgorod, Russia, 2014.
[11] V. Toivanen, T. Kalvas, H. Koivisto, J. Komppula, O. Tarvainen, J. Instrum. 9 (2013) P05003.
[12] Y. Yang, Y.J. Yuan, L.T. Sun, Y.C Feng, X. Fang, Y. Cao, W. Lu, X.Z. Zhang, and H.W. Zhao, Rev. Sci. Instrum. 85 (2014)113305.

ISBN 978-3-95450-186-1

HIGH INTENSITY BEAM PRODUCTION AT CEA/SACLAY FOR THE IPHI PROJECT

R. Gobin*, D. Bogard, O. Delferrière, M. Desmons, Y. Gauthier, F. Harrault, F. Peauger, G. Perreu, B. Pottin, Y. Sauce, J. Schwindling, F. Senée, O. Tuske, D. Uriot, T. Vacher,
Commissariat à l'Energie Atomique et aux Energies Alternatives,
CEA/Saclay, DRF/IRFU,91191 - Gif/Yvette, France

Abstract

CEA/Saclay is involved in high power proton accelerators for many years. This activity started in the 90's, with the development of the SILHI source which routinely produces tens mA of proton beam. Several industrial difficulties led to a very long IPHI RFQ construction process. The 352 MHz RFQ conditioning is presently in progress. Before the completion of the conditioning in CW mode, tests with pulsed proton beam have been performed.

As a consequence, the SILHI source recently produced very short H+ beam pulses in order to allow the first IPHI beam acceleration. Such very short pulses, in the range of few hundred microseconds, allowed analyzing the beam loading of the RFQ cavity as well as conditioning the middle energy diagnostic. This article reports the source parameters and beam characteristics in the low energy beam line leading to the best RFQ transmission as well as several results concerning the accelerated beam at 3 MeV.

INTRODUCTION

In the middle of 90's, CEA and CNRS which are 2 important national research organizations, decided to start a collaboration in the development of high power proton accelerator. It was then decided to concentrate the activities on 3 items: (i) the injector of proton for high intensity (IPHI) which is a prototype of linac front end able to accelerate up to 100 mA cw H+ beam, (ii) construction and test of $\beta<1$ superconducting cavities and (iii) development and improvement of the codes for accurate beam dynamics calculations.

The development and construction of the High Intensity Light Ion Source (SILHI) with its associated low energy beam line were the first steps of the IPHI program. To fulfil the IPHI requests (high intensity cw beam), a 2.45 GHz ECR source has been chosen for the SILHI source producing the H^+ particles.

Then the design and construction of the RFQ and a dedicated diagnostic beam line was decided. In a 1st step, the goal of IPHI was to accelerate the proton beam from 100 keV to 5 MeV with an RFQ and up to 11 MeV with a DTL. For different reasons (mainly economical and strategic ones), the final energy has been reduced from 11 to 3 MeV [1]; as a consequence, the DTL was not needed any more.

In parallel to the long IPHI RFQ construction, the SILHI source was producing high intensity beam. The obtained performance allowed us developing and constructing new injectors for Spiral 2, FAIR and IFMIF. The production of such high intensity beams also permitted the development and improvement of innovative diagnostics.

In the past years, the IPHI project faced industrial (company closure), administrative (end of collaboration) and technical difficulties (RFQ brazing troubles for example); and the completion of the RFQ assembly ended few months ago. Then the 352 MHz RFQ conditioning has been undertaken at very low duty cycle; it is still in progress by increasing the duty cycle. Once the conditioning reached a high enough RF field into the cavity, it has been decided to inject the SILHI beam into the RFQ. And the acceleration of the first proton beam up to 3 MeV has been recently achieved in pulsed mode.

This article briefly recalls the IPHI general design as well as the SILHI and LEBT components. The following section presents the SILHI parameters with very low duty cycle and before to conclude, the last section reports the preliminary 3 MeV H^+ beam results.

IPHI AND SILHI DESIGN

The 4 vane type RFQ of the IPHI project [1, 2] is made of 6 modules (Fig. 1). Each module is 1 meter long and is built in 4 parts brazed together. Large copper pieces with very tight tolerances after machining (10 µm over 1 meter long) and precise brazing pushed to use unconventional technics. The whole RFQ is assembled in 3 segments (made of 2 coupled modules) linked with 2 coupling plates. The 352 MHz RF power, generated by 2 klystrons, is injected in the 4th module via 4 ridges and 4 windows. During the operation, to avoid RFQ detuning due to geometry modifications, the cavity is water cooled by means of 268 different circuits and its temperature is precisely adjusted (0.1° C) by regulating the temperature of several circuits.

The RFQ is followed by a dedicated diagnostic beam line designed to fully characterize the 3 MeV beam. At the end of the beam line, a 300 kW water cooled beam dump has been installed. The beam dump conical shape allows minimizing the beam power density and the inner cone made of nickel allows minimizing the activation.

*rjgobin@cea.fr

ISBN 978-3-95450-186-1

Figure 1: General view of the 6 meter long IPHI RFQ.

Before the acceleration, the proton beam is produced by the SILHI source [3] and transported at the RFQ entrance by a 2 solenoid LEBT. The SILHI ECR source operates at 2.45 GHz; the RF power is injected into the plasma chamber via a quartz window and a 3 step ridged waveguide. The beam is extracted from the plasma chamber through a 5 electrode extraction system. Then the beam is transported and matched into the LEBT thanks to 2 solenoids, steerers, an iris and a cone. The water cooled cone, located between the second solenoid and the RFQ, allows collecting the unwanted particles (H_2^+ and H_3^+). In the LEBT, the high intensity beam interacts with the residual gas; as a result the space charge compensation (due to electron trapping) helps in minimizing the space charge forces. In order to reach the 95 keV energy at the RFQ entrance, the source and its ancillaries are positioned onto a HV platform.

LOW DUTY CYCLE SILHI BEAM

In 1996 the SILHI source produced its 1st high intensity beam. Several months have been needed to reach high performance with routine operation (beam intensity > 100 mA, energy 95 keV, H^+ fraction between 75 and 80 %). Then, in parallel to other projects (Spiral 2 injector with its permanent magnet source, IFMIF injector), the SILHI beam has been used for dedicated experiments like innovative diagnostic developments or material sample irradiation. But the beam has never been fully characterized after the RFQ entrance cone. So, in order to prepare the IPHI commissioning, this characterization has been recently done by measuring the intensity and emittance versus both solenoid scans after the cone. These measurements have been performed in pulsed mode. After the first data analysis, misalignment of the source has been corrected, both boron nitride discs (located at both ends of the plasma chamber) have been changed. Then, new measurements showed the LEBT transmission increased up to 90 %, in close agreement with the simulations. The 0.36 π.mm.mrad measured emittance is higher than the emittance used in the RFQ design simulations. Despite this high emittance value, it has been decided to install the RFQ in its final position with no additional opportunity to analyse the 95 keV beam after the cone. Then the RFQ radiofrequency conditioning has been done in pulsed mode, starting with very low duty cycle (few 10 µs at few Hz).

In parallel, the SILHI source was tuned to produce very short beam pulses and to inject into the IPHI RFQ. Figure 2 shows a 200 µs pulse crossing the DCCT (at the exit of the accelerator column) and collected on the Faraday cup (located in between the 2 solenoids). It is clear that the low bandwidth of the DCCT (yellow curve) does not allow measuring such beam pulses. The Faraday cup signal (which combines H^+, H_2^+ and H_3^+ pulses on the blue curve) showed a small jitter (between 5 and 10 µs) compare to the magnetron RF control signal (curve magenta). The species fraction measurements were done with the Wien filter. With the 200 µs pulse, H^+ beam fraction was as low as 20% and with a 5 ms pulse, by measuring the species fraction on the plateau (Fig. 3), the H^+ fraction reached 75 %.

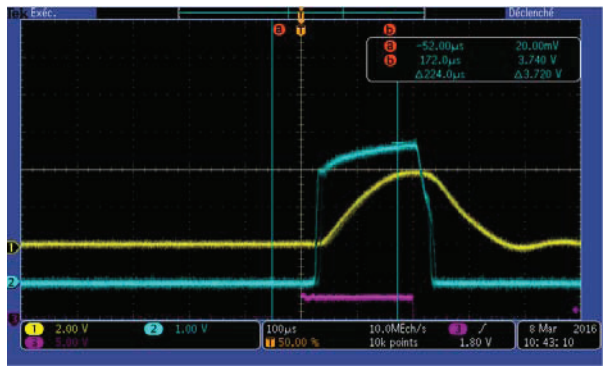

Figure 2: 200 µs beam pulse produced by the SILHI source.

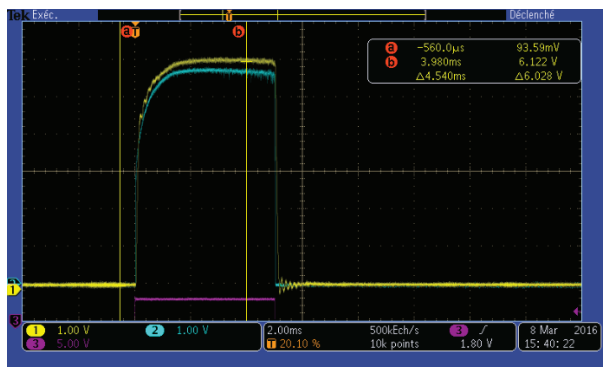

Figure 3: 5 ms beam pulse produced by the SILHI source.

As the beam is injected into the RFQ through the cone which is designed to catch the H_2^+ and H_3^+ particles, the H^+ rise time can be observed on the ACCT signal as the measurement is done between the cone and the RFQ entrance plate.

H^+ ACCELERATION WITH THE IPHI RFQ

Figure 4 presents a schematic view of the whole IPHI installation with the respective position of the different diagnostics [4]. It can be noted the RFQ transmission can

ISBN 978-3-95450-186-1

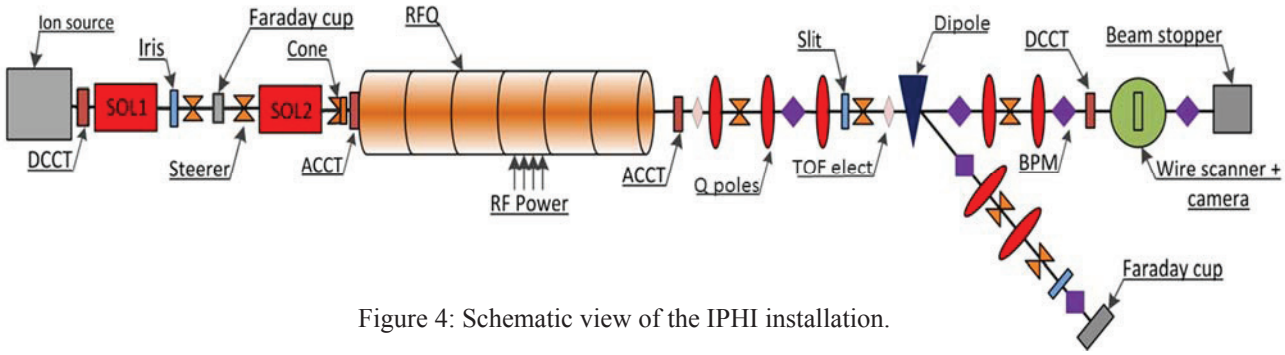

Figure 4: Schematic view of the IPHI installation.

be easily calculated by measuring the ratio between 2 ACCT located very close to both RFQ end plates.

When the nominal RFQ electromagnetic field has been obtained with a 200 µs power pulse, the LEBT gate valve and the Faraday cup have been removed from the beam trajectories. The timing system was tuned to get the same beam and RF pulse fall time.

Figure 5: First accelerated H^+ beam by IPHI RFQ.

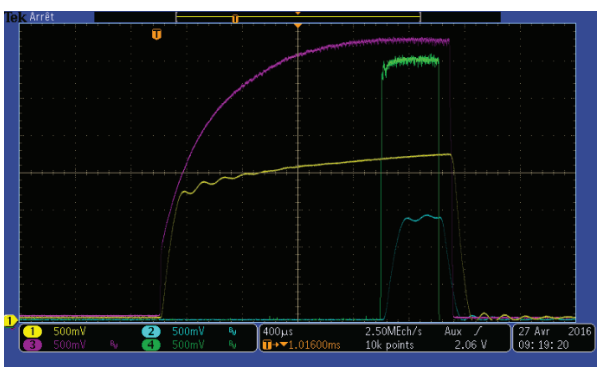

Figure 6: IPHI RFQ transmission reached 92 %.

The beam at the RFQ exit was observed on the ACCT located just at the RFQ exit. Figure 5 presents the signals of different current measurement diagnostics (i) the source DCCT signal with very low bandwidth (yellow curve), (ii) the RFQ entrance ACCT (magenta curve), (iii) the RFQ exit ACCT (blue curve). These signals have been observed after LEBT solenoid and steerer tuning.

In order to overcome the long rise time of the H^+ fraction, the source beam pulse has been enlarged up to 2 ms by keeping a 400 µs short RF pulse located at the end of the beam pulse (Fig. 6). In these conditions, the total current extracted from the source was 100 mA (yellow curve), the RFQ entrance ACCT signal was 82 mA (magenta curve), the RFQ exit ACCT signal was 75 mA (green curve) and the high energy DCCT signal was 64 mA (blue curve). The magenta curve indicates the H^+ fraction rise time is at least equal to 1 ms.

CONCLUSION

For the 1st time, in April 2016, the SILHI source produced a proton beam for IPHI RFQ acceleration. At the beginning of the RFQ conditioning, once the accelerating field map was close to nominal one into the RFQ, very short pulses (of 100 µs at the beginning) have been injected. Such low beam pulses helped us for debugging the high energy diagnostics. Then the short RF power pulse injected into the RFQ has been positioned at the end of a 2 ms source pulse. In these conditions, the RFQ transmission has been estimated around 92 % and the nominal 3 MeV energy has been confirmed by deflecting the short pulse with the dipole.

ACKNOWLEDGMENT

This work was supported by grants from Région Ile-de-France.

In addition, the authors would also like to especially thank the IPN Orsay colleagues who developed the high energy beam line and the numerous persons who are (and/or were) involved for several years in the IPHI project either at CEA/Saclay or in other French and European institutes.

REFERENCES

[1] P-Y. Beauvais, Proceeding of EPAC 2004 Conference (TUPLT053), Lucerne, Switzerland.
[2] B. Pottin et al., Proceedings of LINAC 2012 Conference, (THPB031), Tel Aviv (Israel).
[3] R. Gobin et al., Rev. Sci. Instrum. **75** 1414 (2004).
[4] P. Ausset et al., to be presented at IBIC 2016 Conference.

ISBN 978-3-95450-186-1

COMMISSIONING OF THE HIGH INTENSITY PROTON INJECTOR OF THE FACILITY FOR ANTI PROTONAND ION RESEARCH AT CEA-SACLAY

O. Tuske, O. Delferrière, N. Chauvin, Y. Gauthier, P. Girardot, N. Misiara,
Y. Sauce, F. Senée, C. Simon, T. Vacher
CEA Saclay, France
F. Ameil, R. Berezov, J. Fils, R. Hollinger
GSI, Darmstadt, Germany

Abstract

The Facility for Antiproton and Ion Research (FAIR) located at GSI (Darmstadt) in Germany addresses several fields of physics research within a single installation. These include the physics of exotic nuclei, hadron physics using proton-antiproton collisions, relativistic heavy ion reactions at a few tens of GeV per nucleon, plasma physics, and atomic physics. The FAIR accelerator complex will deliver stable and rare isotope beams covering a huge range of intensities and beam energies. A significant part of the experimental program at FAIR is dedicated to antiproton physics that requires an ultimate number 7.10^{10} cooled pbar/h. The high-intensity proton beam that is necessary for antiproton production will be delivered by a dedicated 75 mA/ 70 MeV proton linac. One of the contributions of Irfu/SACM at CEA-Saclay to the FAIR linear proton accelerator concerns the development and construction of the ion source and the low energy line.

The 2.45 GHz microwave ion source will deliver a 100 mA H^+ beam pulsed at 4 Hz with an energy of 95 keV. A low energy beam transport (LEBT) line based on a dual solenoids focusing scheme allows the injection of the proton beam into the radio frequency quadrupole (RFQ) within an acceptance of 0.3π mm.mrad (norm. rms). An electrostatic chopper system located between the second solenoid and the RFQ is used to cut the beam macro pulse from the source to inject 36 µs long beam pulses into the RFQ.

At the end of 2015, a first plasma of 80 Watt at 4 Hz has been produced by the FAIR proton linac ion source.

Then the commissioning of the injector has started beginning by the characterization of the ion beam just after the accelerating column.

This article reports the finalization of the installation of the injector with the details of dedicated diagnostics, the first beam measurements, and gives a planning of the different commissioning phases

INTRODUCTION

The beam commissioning at CEA/Saclay will be divided in three main phases.

- During the phase one, already started, the beam intensity, emittance and species proportion extracted from the source are measured at the source exit, just behind the accelerating column, using a dedicated diagnostic chamber (DIAG2).
- For the phase 2, the LEBT is assembled without the chopper. The same diagnostics are installed first in the FAIR injector diagnostic chamber (DIAG1) between the 2 solenoids, and in a second time the beam is analyzed in the chamber DIAG2 connected at the exit of the second solenoid.
- During the phase 3, the nominal source and LEBT apparatus is assembled. All the diagnostics of the diagnostic chamber DIAG1 are available. The chopper is tested. The beam intensity and emittance are measured after the injection cone. The FAIR p-linac source and LEBT are validated.

INJECTOR LAYOUT

The injector section of the FAIR p-linac [1-2] is composed by an ECR source, delivering a pulsed 100 mA H^+ beam (4 Hz) at 95 keV and a low energy beam transport line required to match the beam for the RFQ injection (Fig. 1). The LEBT is based on a dual solenoids focusing scheme. A dedicated chamber DIAG1 containing several diagnostics (Alisson scanner, Wien filter, SEM grid, Iris, Faraday Cup) will be located between the two solenoids. At the end of the LEBT, an electrostatic chopper system is foreseen to inject 36 µs beam pulses into the RFQ.

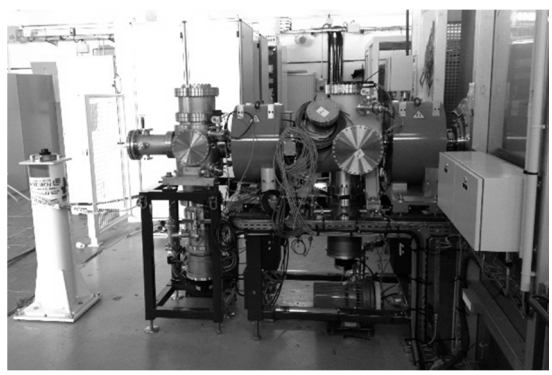

Figure 1: FAIR p-linac injector at Saclay.

ION SOURCE & LEBT REQUIREMENTS

The FAIR p-linac source & LEBT is aimed to produce a 100 mA/95 keV proton beam and to transport and match it for its injection into the RFQ. The main beam parameters that are required are summarized in Table 1.

ISBN 978-3-95450-186-1

Table 1: FAIR p-linac Ion Source & LEBT Requirements

Parameters	Values
Specie	Proton
Energy	95 keV
Intensity	100mA
Time structure	Pulsed at 4 Hz
Energy spread	< 60 eV
Final emittance	$\leq 0.33\ \pi$ mm.mrad
α Twiss parameter	$0.27 \leq \alpha \leq 0.59$
β Twiss parameters	$0.037 \leq \beta \leq 0.046$ mm/π.mrad

Before the commissioning, the ion source accelerator column has been assembled with great care: the system is composed of 5 electrodes non-water cooled. Two plasma electrodes have been designed with aperture of diameter 6 and 9 mm. The 6 mm electrode has been installed for the beginning of the bias test and first plasma. The second electrode called "puller electrode" is biased negatively compared to the HT plate-form up to -50kV. The third electrode is a ground electrode followed by the reppeler electrode negatively biased. This electrode produces an electrostatic field to avoid LEBT free electrons to get accelerated by the positive electric field of the accelerating column and thus produce Bremsstrahlung radiation when they get stopped in the matter. The last electrode is also at ground potential.

BEAM DIAGNOSTICS

Beam Intensity Measurements

The LEBT will be equipped by several diagnostics in order to qualify the beam during the commissioning period but also for daily operation.

In order to measure the beam intensity (Fig. 2), two Alternative-Current Current Transformers (ACCT) have been installed. The first one is located after the source extraction and the second one, after the second solenoid before the chopper. These ACCTs have been designed by Bergoz Company in close collaboration with CEA, taking in account magnetic perturbation aspects. Because of the very short LEBT length (2.4m), ACCTs have been placed close to the solenoids and magnetically shielded to be operated in the solenoids fringe field environment. Bergoz Company did the manufacturing and ACCTs have been in the fringe field of IPHI LEBT second solenoid in order to verify the efficiency of the magnetic shielding and validate the ACCTs design before mounting on FAIR LEBT [3].

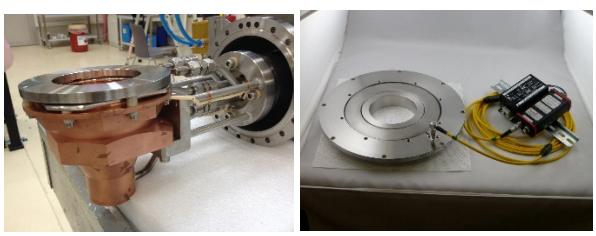

Figure 2: Faraday cup and Bergoz ACCT.

Emittance Measurements

An Allison scanner has been developed by IPHC Strasbourg to measure the beam emittance. The principle is to deviate a beamlet selected by a slit with the electric field produced by 2 bias plates and collect it on a faraday cup equipped with an electron repeller after passing through a second slit. A voltage ramp is applied to collect all the ions with their different initial divergence. All the beam is scanned by moving the system with a step by step motor. The Allison scanner could be placed either in vertical or horizontal position. Several modifications are undergoing to modify the command-control (in Labview FPGA) and also to increasing the shielding of the measurement head against free electrons perturbation.

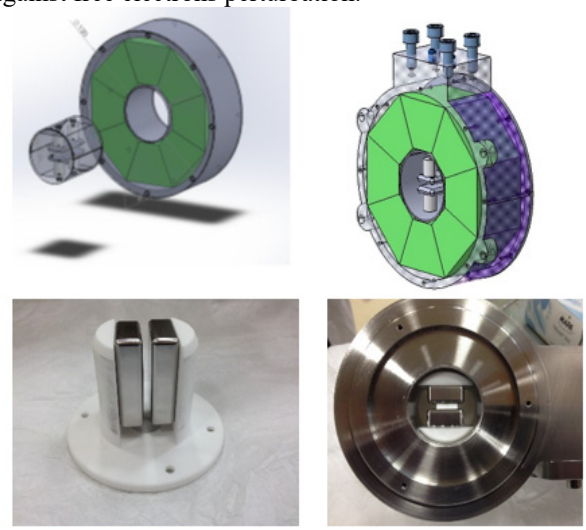

Figure 3: Wien filter, electrodes and Halbach permanent magnet dipole.

Beam Species Measurements Resolved in Time

A Wien filter (Fig. 3) to measure the proportion of the different ion species (H^+, H_2^+, and H_3^+) extracted from the ion source has been design at Saclay. It is a small device with a Halbach permanent magnet structure producing a dipole: configuration with 6 blocks encapsulated in a stainless steel shell. Two small plates for electric deviation with 6 mm space in between installed in the dipole magnetic field. The Wien filter is magnetically shielded by two 3 mm ARMCO plates at both extremities and protected by a tungsten thermal shield at the entrance, which has been assembled on a copper support with HIP technic (Hot Isostatic Pressure – 1200 °C, 1500 bars) by LITEN in Grenoble. The maximum magnetic field is 0.5 T and the field integral reaches 16.90 T.mm. In these conditions 6445 V between the 2 plates are necessary for H^+ selection. A sample hole of ∅0.25 mm trough the thermal shield defines the beam fraction to be analyzed. The selected specie exit the Wien filter through a ∅0.5 mm hole and collected on a plate. A negative polarized electrode before collection is used to eliminate secondary electrons emission. This device is aimed to be used on beam axis. All collected pulses are timed resolved and thus can reconstruct the beam species fraction at any moment during the pulse.

ISBN 978-3-95450-186-1

FIRST COMMISSIONING PHASE

The source and LEBT in its final configuration up to the second solenoid has been mounted, aligned and vacuum tested. The first plasma of hydrogen has been produced the 5th of November 2015, with 80 W power of the magnetron at 4 Hz. Then, the high voltage tests have been performed up to 100 kV with gas injection in the plasma chamber without any failure. From that time, the LEBT has been dismounted to allow mounting the DIAG2 chamber in order to fully characterize the beam extracted at the source exit.

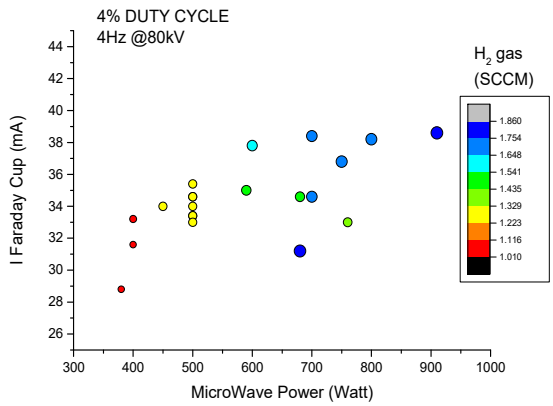

Figure 4: Measured current on the Faraday cup versus Injected Microwave Power in Watt.

A dedicated command-control has been written under Labview in order to remote control equipment on the high voltage platform, leading us to realize several commissioning tests before installing the GSI specific command control system. Several magnetic configurations where tested at 80kV extraction voltage in pulse mode, optimizing:

- the stability of the tuning over time,
- the extracted current pulse shape or the beam noise in CW mode,
- the maximal extracted current value.

In order to increase extracted current of the source, the injected microwave power and the injected gas flux must also be increased as well (Fig. 4). But what was not expected is that the magnetic coil tuning also has a quasi-linar behavior with the gas injection (Fig. 5). The magnetic calculations showed up that for all coils configurations, the resonant zone at 87,5mT is always positioned at the microwave injection point in the plasma chamber.

Maximal current extracted with the 6 mm aperture hole in the plasma electrode was 60 mA measured on the faraday-cup but this specific configuration is not reported on the figure because the tuning point was not stable enough. This extracted current lead to a density current equivalent to the SILHI source.

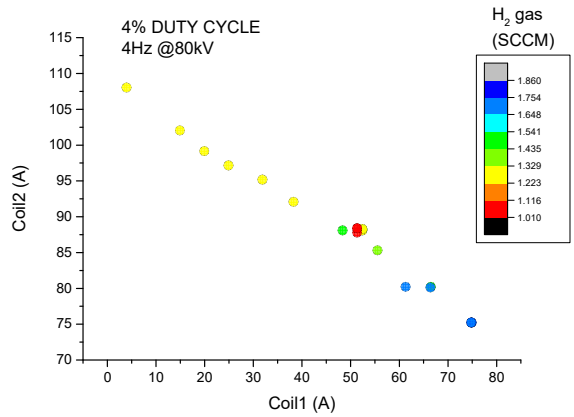

Figure 5: Source Coil Tuning for maximal Extraction recorded on the Faraday cup.

CONCLUSION AND PLANNING OF THE FUTURE WORK

The FAIR proton source has been installed in CEA Saclay with the whole LEBT. The first plasma and first beam where produced this year and preliminary measurements were carried out with only a current transformer and a faraday cup. As the other diagnostics are not completely fully operational at this moment, the next step will be to install the 9 mm aperture hole plasma electrode to achieve the expected beam current in pulsed mode. The source will be fully characterized before the end of the year 2016.

ACKNOWLEDGEMENT

Great thanks to the ion source team in INFN Catania for the lending of the 100kV power supply (L. Celona, S. Gamino, and L. Neri).

REFERENCES

[1] R. Berezov *et al.*, “High intensity proton injector for facility of antiproton and ion research”, *Review of Scientific Instruments.* Vol. 87. 02A705, (2016).

[2] N. Chauvin et al., “Status of the FAIR Proton Source and LEBT”, in *Proc. LINAC’14*, Geneva : Switzerland, p. 863.

[3] H. Bayle et al., “Effective shielding to measure beam current from an ion source”, *Review of Scientific Instruments.,* Vol. 85. 02A713, (2014).

ISBN 978-3-95450-186-1

NEVER RUN YOUR ECR ION SOURCE WITH ARGON IN AFTERGLOW FOR 6 MONTHS!

D. Küchler, J. Ferreira Somoza, A. Michet, V. Toivanen
European Organization for Nuclear Research (CERN), 1211 Geneva 23, Switzerland

Abstract

The fixed target experiment NA61/SHINE in the North Area of the SPS at CERN studies phase transitions in strongly interacting matter using the primary beams available from the CERN accelerator complex (protons and lead ions). In order to explore a wider range of energies and densities a primary argon beam was requested for the physics run in 2015. The GTS-LHC ECR ion source was running for many months during 2013 and 2014 to study the source behaviour and to set-up the accelerator chain with argon ions.

This paper reports the long term effects of the argon operation on the GTS-LHC ion source and the Low Energy Beam Transport (LEBT). Heavy sputtering inside the source caused a degradation of the plasma chamber and metal coating of insulators inside the beam extraction system. Iron ions could be found in the extracted beam. Also the pumping performance of ion getter pumps in the LEBT degraded significantly. Additional preventive maintenance was necessary to be able to run for long periods without risking serious damage to the ion source.

INTRODUCTION

NA61/SHINE [1] is a fixed target experiment in the North area of the Super Proton Synchrotron (SPS). NA61/SHINE studies the hadron production in hadron-nucleus and nucleus-nucleus collisions. The aim of this experiment is to study phase transitions in strongly interacting matter (quark gluon plasma), the onset of deconfinement and to take reference measurements for the hadron production.

In the last years proton and lead as primary beams and light ions from fragmented beams were used. In 2015 a primary argon beam was delivered to be able to explore a wider range of energies and densities in the experiment. In preparation the accelerator chain was set up with the argon beam in the second half of 2014.

In 2013 a test run was done at the linear accelerator Linac3 to find and optimize the settings for the source and the linac, to measure the beam parameters (intensity, stability, emittance) and to study the long term behaviour of the source and the linac [2].

The GTS-LHC ion source [3,4], running at 14.5 GHz, was set-up to provide an $^{40}Ar^{11+}$ beam. The source is running in the afterglow mode with a heating pulse of 50 ms and a repetition rate of 10 Hz. No mixing gas was used. The beam was extracted with an extraction voltage of 9.6 kV to match the injection energy of 2.5 keV/u into the RFQ. In the linac a pulse of 200 µs cut out of the afterglow discharge was accelerated. At the end of the linac the beam reaches the final energy of 4.2 MeV/u.

The source delivered around 100 eµA of Ar^{11+}. At the exit of the linac the current was around 70 eµA (this is more than 10 times the particle current compared to the lead operation). The intensity varied up to 20 % during operation [2].

The total time operated with argon was nearly 12 months, 24 h per day, 7 days a week. But as the first tests in 2013 showed already after 10 weeks of operation some degradation of the source hardware, it was decided to do a preventive maintenance after roughly 6 months of operation where plasma chamber and extraction system were replaced with spare parts.

INVESTIGATIONS

Operating with argon the source can be tuned to a stable operation point (more stable over long periods than during Pb ion production) and also returns to the same conditions quickly after a source stop. The fixed target physics programme was limited by event pile up, and therefore high intensities were not requested from the accelerator chain. Therefore the tuning of the source could also be made with low power parameters (for example the ECR source microwave power was kept below 500W). This allowed to reduce the hardware degradation (known from the 2013 experiment) and to maximize the source lifetime.

The different parts of the source and the linac were affected by the argon operation in different ways. The three main issues will be described in the following.

The Plasma Chamber

As already reported in Ref. [2], after 10 weeks of operation first sputter marks could be seen in the plasma chamber and in the ion beam co-extracted iron ions could be found (several eµA).

After a period of 6 months the plasma chamber was taken out and measured (Fig. 1). The spots where the plasma is lost dominantly are clearly visible and along these loss lines grooves up to 100 µm deep were measured (the chamber has a wall thickness of 2mm). During the lead operation only some marks were visible at the same spots.

The Extraction System

The GTS-LHC source operates with a 3 electrode extraction system. After the replacement of the extraction system during the maintenance two observations could be made.

The aperture of the intermediate electrode showed clear sputter marks and some metal flakes after removal from the source (Fig. 2).

ISBN 978-3-95450-186-1

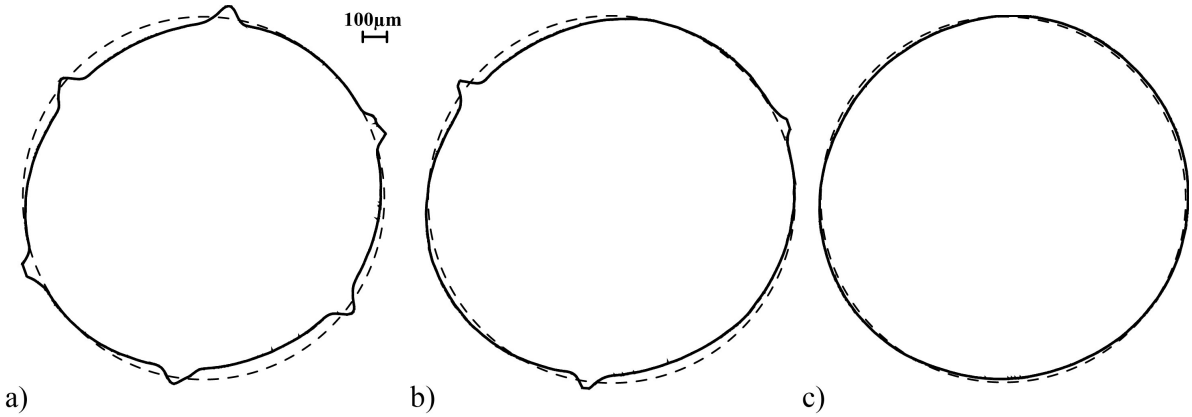

Figure 1: The measured deviation of the plasma chamber surface from the ideal circle (dashed). The values are amplified by a factor 100. The inner diameter if the chamber is 78 mm.
The measurement was taken a) roughly in the middle of the chamber, b) at around a quarter of the chamber length and c) at the extraction end of the chamber.

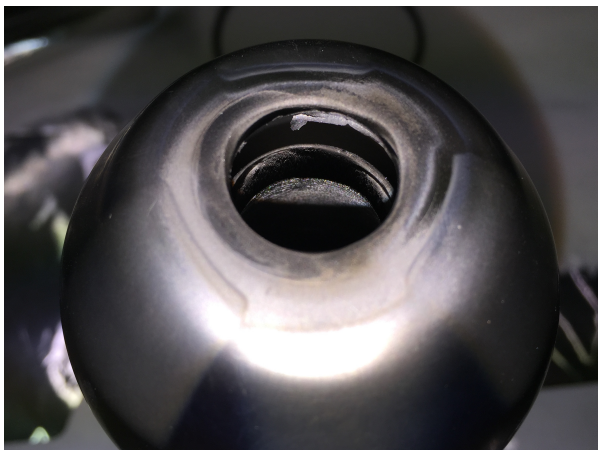

Figure 2: Tip of the intermediate electrode with clear signs of erosion.

The insulator between the intermediate and the ground electrode was partially metallized on the side which is facing the extraction aperture (Fig. 3).

An indication that there is some metallization of the insulators was there already during the operation. It could be seen at the behaviour of the current of the extraction high voltage. While the extracted ion current stayed quite constant and therefore also the fraction of the high voltage current related to the ions the drain current went up over time (Fig. 4). The change of the high voltage current was relatively constant most of the time and could be fitted with a cubic function. Why it is a cubic function is not well understood.

The Vacuum System

The vacuum in the linac is maintained by ion getter pumps. There are 4 pumps in the LEBT and 2 at the RFQ. Only at the source and at the first diagnostic box after the source there are in addition turbo molecular pumps.

During normal operation the pressure in the linac is in the order of 10^{-8} mbar. Only in the source extraction region and in the first part of the Low Energy Beam Transport (LEBT) it is in the order of 10^{-7} mbar.

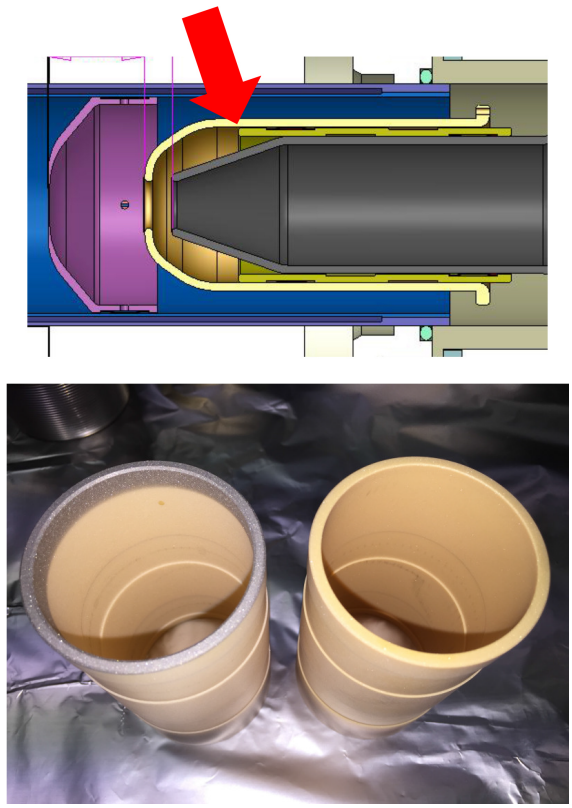

Figure 3: The insulator between the extraction electrodes. The top part of the figure shows the position of the insulator and the side of the metallization. The electrodes from left to right: plasma electrode (purple), intermediate electrode (yellow) and ground electrode (grey). In the lower part of the figure the left insulator shows a clear metallization on the top after around 6 months of argon beam operation. The right lower part shows for comparison an insulator that was used around 8 months during lead beam operation.

ISBN 978-3-95450-186-1

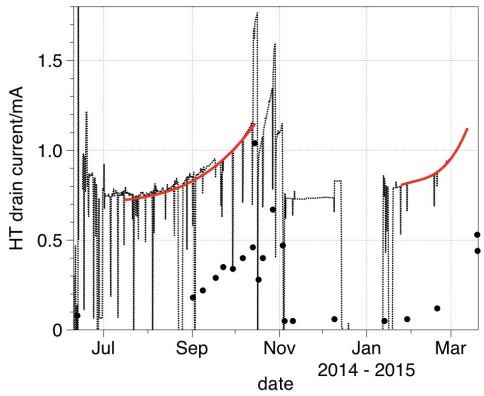

Figure 4: The current of the extraction power supply. The dotted line is the total current when the plasma is on, the dots show some selected values of the drain current when the plasma is off. The red curve represents a cubic fit of the current. In November there was the source maintenance. Due to the clean insulators the drain current dropped down, but over time started to rise again.

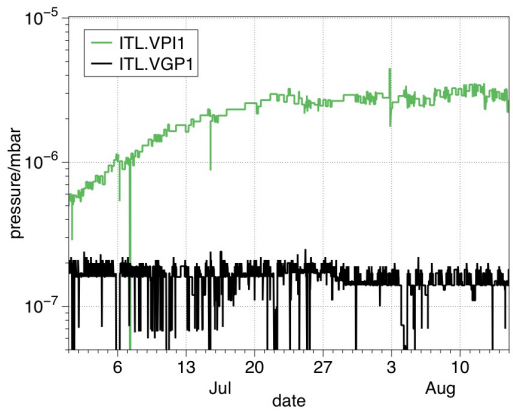

Figure 5: Vacuum measured in the LEBT with a Penning gauge (ITL.VGP) and in one of the of the ion getter pumps in the LEBT (ITL.VPI). The current measured in the ion getter pump is taken as measure for vacuum pressure.

During the running period it was realized that while the pressure in the linac stayed quite constant the current in the ion getter pumps was rising (see Fig. 5). The effect was very pronounced in the LEBT but could be seen also in the ion getter pumps of the RFQ. This behaviour is not fully understood, but it may be related to leakage currents inside the ion getter pumps due to the coating of insulators.

In addition there was the counter-intuitive observation, that when the gas injection into the source was stopped or the source was separated from the LEBT by closing a valve, the current/pressure in the ion getter pumps near to the source went up (for an example see Fig. 6).

Ion getter pumps can pump noble gases only by ion implantation. That's why the pumping speed for noble gases is lower compared to other gas species and it drops after short operating time [5].

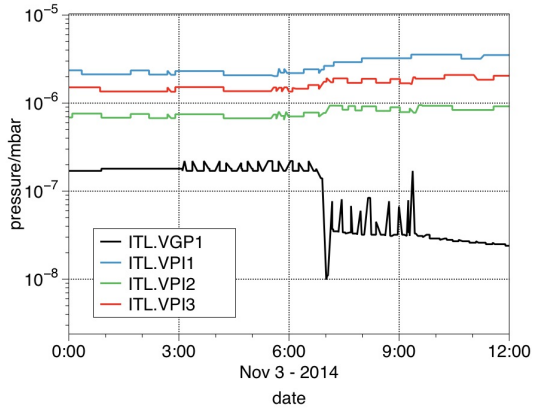

Figure 6: Vacuum measured in the LEBT with a Penning gauge (ITL.VGP) and in the ion getter pumps (ITL.VPI). At 7:00 the LEBT was separated from the source with a valve.

After the argon ion run the pumps recovered slowly (partially supported by baking). But the ion getter pumps directly after the source which have seen most of the argon had to be replaced.

CONCLUSION

The argon ion run in 2014/2015 was a very successful physics run. The injector chain could deliver over the whole period a stable argon ion beam of sufficient intensity.

But it was revealed as well that such a long term operation can be quite detrimental for parts of the source and the linac. Preventive maintenance is essential under such conditions. Eroded and metallized parts need to be replaced in time. The vacuum pumps need to be closely surveyed as the pressure in the machine is not the only indicator of the healthiness of the vacuum system.

All in all one can say that the performance in terms of beam properties may not always be the challenging part of the operation.

ACKNOWLEDGEMENTS

The authors like to thank the colleagues of the ABP/HSL section supporting the operation of the source and the linac.

REFERENCES

[1] NA61/SHINE, http://shine.web.cern.ch/

[2] D. Küchler, M. O'Neil, R. Scrivens, and R Thomae, "Preparation of a Primary Argon Beam for the CERN Fixed Target Physics", *Rev. Sci. Instrum.* 85 (2014) 02A954.

[3] C.E. Hill, D. Küchler, C. Mastrostefano, M. O'Neil, R. Scrivens, *et al.*, "Experience with the GTS-LHC ion source", LHC Project Workshop - Chamonix XV, (2006) 240–242.

[4] L. Dumas, C.E. Hill, D. Hitz, D. Küchler, C. Mastrostefano, M. O'Neil, *et al.*, "Operation of the GTS-LHC Source for the Hadron Injector at CERN", LHC Project Report 985, (2007).

[5] Karl Jousten (Ed.), Handbook of Vacuum Technology, Whiley-VCH, 2008.

ISBN 978-3-95450-186-1

STATUS REPORT ON METALLIC BEAM PRODUCTION AT GANIL/SPIRAL 2

C. Barué †, O. Bajeat, J.L. Flambard, R. Frigot, P. Jardin, N. Lechartier, F. Lemagnen, L. Maunoury, V. Métayer, B. Osmond, GANIL, CEA/CNRS, Caen, France
P. Sole, T. Thuillier, LPSC, CNRS, Grenoble, France
C. Peaucelle, IPNL, CNRS, Lyon, France

Abstract

Primary ion beams from metallic elements are routinely produced at GANIL using ECR4 [1] and ECR4M [2] room temperature (RT) ECR ion sources. Ionization efficiency measurements, partially presented in the past, are summarized in this paper together with updated and new results obtained with Cd, Mo and Ta. Preliminary results obtained at Grenoble with the PhoenixV2 [3] ion source for Ni and Ca beam production [4] are also included. These ionization efficiencies are compared according to the ordinary production methods: oven, sputtering, MIVOC, gaseous compounds. The present SPIRAL 2 heavy ion injector designed for ions Q/A=1/3 is of interest to accelerate metallic ions up to the mass ~60. Above this value, the achievable intensities are dramatically limited by the atomic physics processes in the ECR plasma (intensities << 1 pμA). This limitation will be overcome with the future Q/A=1/6,1/7 injector. In order to choose the best ion source for such an injector, best world results have been compiled for different existing RT (Room temperature) and superconducting (SC) ECR ion sources.

ECR4/4M AND PHOENIX V2 ION SOURCES

In this section, the main differences between ECR4/4M (ECR4 or ECR4M) and Phoenix V2ion sources are presented. Although the global magnetic structure of these ion sources is comparable, i.e. superposition of an axial magnetic field created by resistive coils and of a radial field created by permanent magnets, some differences have to be pointed out:

RF Injection

Phoenix V2 is working at 18 GHz (instead of 14 GHz for ECR4/4M) with a direct rectangular RF injection (coaxial RF injection for ECR4/4M) allowing more RF power to be injected into the source.

Magnetic Confinement

Due to its direct RF injection, a massive iron plug can be placed behind the injection flange of Phoenix V2, leading to a much stronger injection magnetic field: 2 T for Phoenix-V2 compared to the 1 T for ECR4/4M. Moreover, Phoenix-V2 is equipped with a third coil located at the middle, helping to get a better shaped axial magnetic field.

† barue@ganil.fr

Access to the Plasma

The internal diameter of the plasma chamber is about the same for ECR4/4M and Phoenix V2 (~63 mm). Using ECR4/4M, the oven used to evaporate metals can be placed only on axis (in front of the hot plasma) without any bias voltage, unlike Phoenix V2 where the oven is located off axis (beside the hot plasma) while keeping the biased disk functionality.

Beam Extraction

The beam is extracted at 60 kV from Phoenix V2 (2 accelerating gaps) instead of 25 kV for ECR4/4M (1 accelerating gap). The beam line inner diameter is higher for Phoenix V2 than the one of ECR4/4M, resp. 150 mm and ~65 mm. These differences lead to a better beam transmission for Phoenix V2 (~80-90%) than for ECR4/4M (~50%).

For Phoenix V2, the use of high speed turbo molecular pumps (2x1000 L/s) at the extraction leads to a vacuum level one order of magnitude lower than ECR4/4M (10^{-8} mbar for Phoenix V2 and 10^{-7} mbar for ECR4/4M). This is a crucial requirement to reduce the charge exchange process in the source and in the beam line, and therefore to keep alive the high charge states escaping the source.

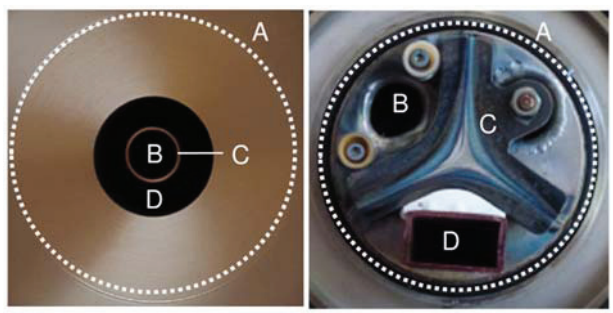

Figure 1: Injection view of ECR4/4M (left side), injection view of Phoenix V2 (right side). (A): inner diameter of the plasma chamber; (B): oven port and gas injection, (C) left side: biased tube, (C) right side: biased disk, (D) left side: 14 GHz coaxial RF injection, (D) right side: 18 GHz rectangular RF injection.

METALLIC BEAM PRODUCTION METHODS

In view of the very high charge states required for SPIRAL 2 (Q/A=1/3 => $^{14}Ca^{14+}$, $^{48}Ca^{16+}$, $^{58}Ni^{19+}$), the choice of the oven method and the use of pure metallic samples seems to be the most relevant alternative: the buffer gas

ISBN 978-3-95450-186-1

flow, required to shift the distribution on high charge state, can be controlled regardless of the metal vapor injected into the source.

Primary beam production at GANIL (ECR4/4M), requiring a smaller Q/A (1/3 → 1/8), the MIVOC (Metal Ions from VOlatile Compound) method can also be used [5]. For very low vapor pressure elements (Ta for example), dismissing the use of an oven for evaporation, the sputtering method can be another alternative [6].

IONISATION EFFICIENCY DEFINITION

The ionization efficiency of a specific atomic species is defined as the ratio of the extracted ion flow over the injected neutral flow.

Extracted Ion Flow

The ion flow extracted from the ion source is deduced from the spectrum obtained downstream in the Faraday cup by summing I/q for all charge states (I being the beam intensity for the charge state q). This value expressed in pμA is corrected by the beam transport from the ion source to the Faraday cup, i.e. the total electrical intensity in the spectrum (sum of I for all charge state and species) divided by the drain current of the high voltage power supply.

Let us keep in mind, that the beam transport is assumed to be the same for all species and charge states, which is probably not the case. Since the spectra contain mainly ions coming from the buffer gas (see Fig. 2,3,6 and 7), the deduced beam transport is mainly the one of the buffer gas.

Because the transport efficiency of the ions coming from the light buffer gas is probably lower than for the heavier metallic ions, the ionization efficiencies given in this paper could be over-estimated. Some errors could come from this transport efficiency correction, especially for low values.

RESULTS FOR LEAD

Extracted Ions

The $^{208}Pb^{28+}$ beam has been produced during 17 days with a mean intensity of 1.4 μA (I_q^{mean}) at faraday cup location. The ^{208}Pb ion flow reaching the faraday cup (over all charge states) can be deduced from the spectrum Fig. 2:

$$\frac{I_q^{mean}}{I_q} \times \sum_q \frac{I_q}{q} = \frac{1.4}{4.5} \times 2.5 \approx 0.78\ \text{p}\mu A$$

Taken into account the beam transport efficiency of 50% (T) - assumed to be the same for all charge state and species - leads to an ion flow extracted from the source of:

$$\frac{1}{T} \times \frac{I_q^{mean}}{I_q} \times \sum_q \frac{I_q}{q} = \frac{1}{0.5} \times \frac{1.4}{4.5} \times 2.5 \approx 1.55\ \text{p}\mu A$$

Injected Neutrals

The material consumption of 38 mg measured by weighting the sample after 17 days, leads to a mass flow of 93 μg/h injected into the source, equivalent to 12.0 pμA.

Therefore, the ionization efficiency of the ion source ε is:

$$\varepsilon = \frac{1.55}{12.0} \approx 0.13 = 13\%$$

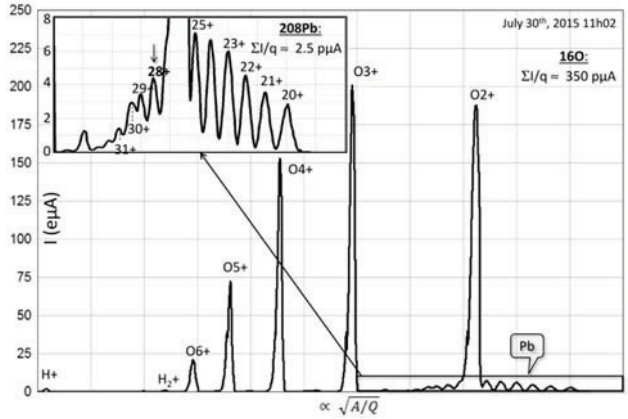

Figure 2: Spectrum obtained with ECR4M and optimized on $^{208}Pb^{28+}$ (4.5 μA). RF power: 380 W (120 W reflected), buffer gas O_2: 8.5×10^{-6} mbar at injection, 2.0×10^{-7} mbar at extraction, 18.5 kV/1.8 mA, axial magnetic coils: 960A/729A, oven power 1.9 W (~200°C off-line), oven position: +6 mm inside the plasma chamber, no bias. Transport efficiency up to the faraday cup: ~50%.

RESULTS FOR MOLYBDENIUM

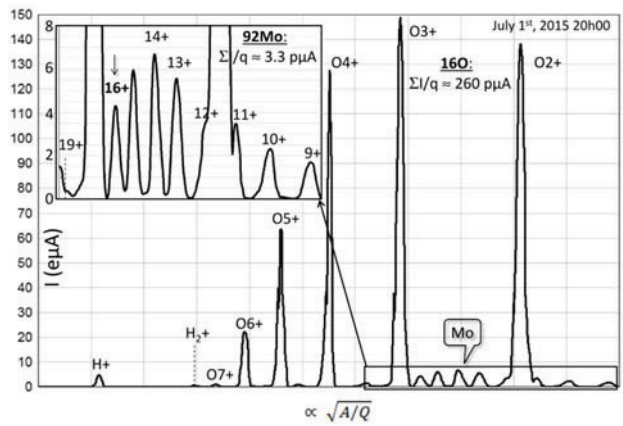

Figure 3: Spectrum obtained with ECR4M and optimized on $^{92}Mo^{16+}$ (4.1 μA). RF power: 140 W (37 W reflected), 18 kV/1.8 mA, buffer gas O_2: 8.5×10^{-6} mbar at injection, 2×10^{-7} mbar at extraction, oven power 3.5 W (~250°C off line), oven position: 0 mm inside the plasma chamber, no bias, coils: 940A/730A. Transport efficiency up to the faraday cup: ~40%.

Extracted Ions

The $^{92}Mo^{16+}$ beam has been produced with a mean intensity of 1.25 μA for 6 days. Following the same calculation method previously detailed, the ion flow extracted from the source is:

$$\frac{1}{0.4} \times \frac{1.25}{4.1} \times 3.3 \approx 2.51\ \text{p}\mu A$$

ISBN 978-3-95450-186-1

Injected Neutrals

The measured consumption for $^{92}MoO_3$ was 1.34 mg/h, i.e. 0.88 mg/h for ^{92}Mo, leading to a neutral flow injected into the source of about 256 pμA.

Therefore, the ionization efficiency ε of the ion source is:

$$\varepsilon = \frac{2.51}{256} \approx 0.0098 \approx 1\%$$

Figure 4: Aspect of the Mo fed oven after the 6 days run.

RESULTS FOR TANTALUM

Extracted Ions

The $^{181}Ta^{24+}$ beam has been produced with a mean intensity of 4.5 μA for 17 days. Following the same calculation method previously detailed, the ion flow extracted from the source is:

$$\frac{1}{0.5} \times \frac{4.5}{5.5} \times 2.0 \approx 3.3\ \text{p}\mu A$$

Injected Neutrals

The measured consumption for ^{181}Ta was 3.0 mg/h, leading to a neutral flow injected into the source of about 444 pμA.

Therefore, the ionization efficiency ε of the ion source is:

$$\varepsilon = \frac{3.3}{444} \approx 0.0074 \approx 0.75\%$$

Figure 5: Aspect of the Ta electrode after the 17 days run.

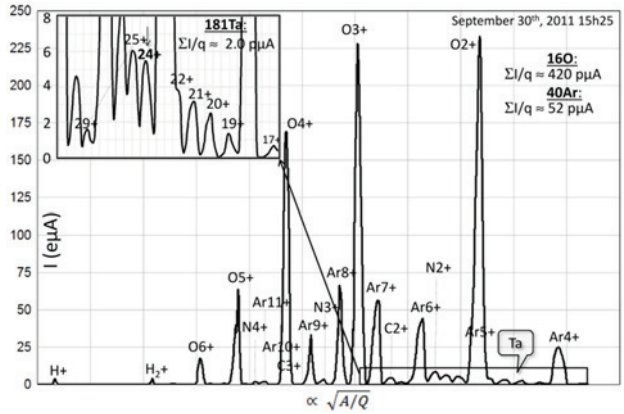

Figure 6: Spectrum obtained with ECR4M and optimized on $^{181}Ta^{24+}$ (5.5 μA). RF power: 371 W (22 W reflected), 19 kV/2.4 mA, buffer gas Ar + O_2: 2×10^{-5} mbar at injection, 2×10^{-7} mbar at extraction, sputtering voltage: –1200 V/1.4 mA, sputtering electrode position: +16 mm inside the plasma chamber, coils 895A/755A. Transport efficiency up to the faraday cup: ~50%.

RESULTS FOR CADMIUM

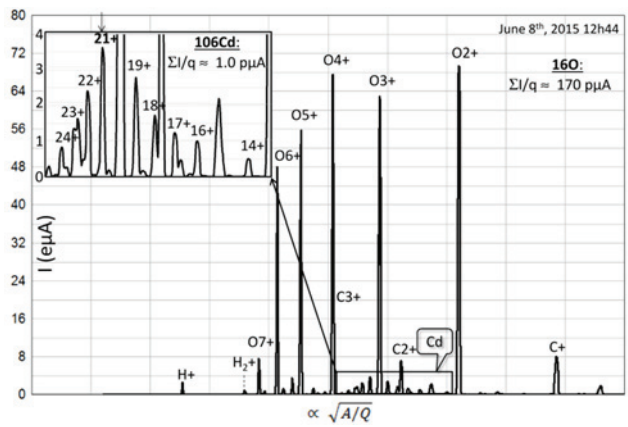

Figure 7: Spectrum obtained with ECR4 and optimized on $^{106}Cd^{21+}$ (3.7 μA). RF power: 139 W (17 W reflected), 25 kV/1.0 mA, buffer gas O_2: 6×10^{-6} mbar at injection, 2.0×10^{-7} mbar at extraction, oven power 0.5 W (~100°C off line), oven position: +6 mm inside the plasma chamber, no bias, coils 1071A/1044A. Transport efficiency up to the faraday cup: ~50%.

Extracted Ions

The $^{106}Cd^{21+}$ beam has been produced with a mean intensity of 1.4 μA for 11 days. Following the same calculation method previously detailed, the ion flow extracted from the source is:

$$\frac{1}{0.5} \times \frac{1.4}{3.7} \times 1.0 \approx 0.75\ \text{p}\mu A$$

Injected Neutrals

The measured consumption for ^{106}CdO was 34 μg/h, i.e. 30 μg/h for ^{106}Cd, leading to a neutrals flow injected into the source of about 7.6 pμA.

ISBN 978-3-95450-186-1

Therefore, the ionization efficiency ε of the ion source is:

$$\varepsilon = \frac{0.75}{7.6} \approx 0.099 \approx 10\%$$

IONISATION EFFICIENCIES COMPILATION

These ionization efficiencies and previously published data obtained with ECR4/4M [7][8][9][10] are graphically represented in Fig. 8, according to the production methods. Some results, published only in GANIL internal reports, and preliminary results obtained with Phoenix V2 at Grenoble for Ca and Ni [4] have also been included.

It is important to keep in mind that the ionization efficiency for a given element may easily vary by a factor of 2, depending on how the ion source is tuned. For example, a too fast tuning could lead to a temporary over-evaporation and significantly decrease the ionization efficiency.

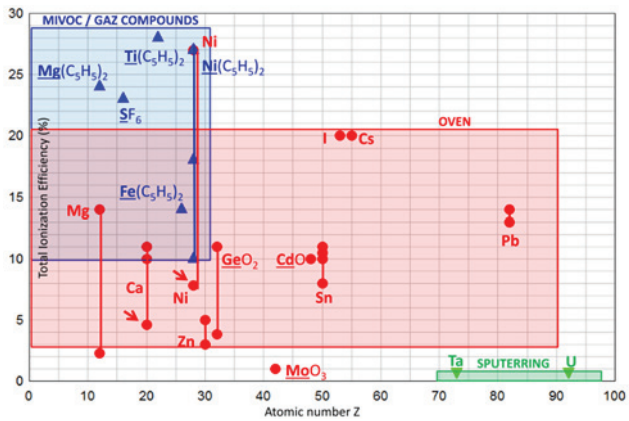

Figure 8: Total ionization efficiencies compilation obtained with ECR4/4M and Phoenix V2 (red arrows).

Therefore, the Fig. 8 must be interpreted from a statistical point of view. It appears that:

- The ionization efficiencies obtained by the (MIVOC/Gas compound) method (~20%) is higher than those obtained by the oven method (~10%). With the sputtering method, the ionization efficiency drastically shuts down by one order of magnitude (~1%).
- Very high ionization efficiency for Ni (~27%) has been measured using the oven method (internal report GPI-2010-138). More tests have to be done to confirm this result.
- Very low ionization efficiency (~1%) has been obtained for Mo using the oven method with the compound MoO_3.
- The ionization efficiencies obtained for Ca and Ni with Phoenix V2, respectively 4.6% and 7.5% (corrected by a beam transport of ~ 80%), are a bit lower than those obtained with ECR4/4M. No clear conclusion could be drawn. More tests over longer periods, should start in the next months coming with Phoenix V2 installed in the SPIRAL 2 Q/A=1/3 injector.

IONISATION EFFICIENCIES INTERPRETATION

In order to be captured by the plasma, the atoms or molecules must be ionized during their first crossing through the plasma, otherwise they remain stuck onto the cold plasma chamber walls.

When using the MIVOC method, the molecules lost on the walls can be re-evaporated into the plasma due to the high vapour pressure of the compound (~10^{-2} mbar at 25°C). This leads to a higher probability to be ionized, and therefore to a better ionization efficiency for the MIVOC method.

Concerning the much lower ionization efficiency obtained with the sputtering method (~1%), the interpretation is much unclear. With the sputtering method, the condensable atoms of the rod are mainly injected into the plasma under a neutral form and with energy in the order of eV [11]. This energy, much higher than the thermal energy of atoms produced by the oven method (1273 K ↔ 0.1 eV), could explain the very low ionization efficiency.

IMPROVEMENT OF THE IONIZATION EFFICIENCY

In addition to the reduction of the material consumption of importance for the use of rare and expensive isotopes, the improvement of the ionization efficiency will reduce the plasma chamber contamination and could result in a better beam stability. As the metal vapor injected into the plasma will be decreased, could we expect a better charge state distribution? This remains an open question.

At least two parameters are not under control when using the oven, MIVOC or sputtering methods:

- The energy of the metallic atoms sent into the plasma (probably not optimum).
- The trajectory of the metallic atoms injected into the plasma (wide angular atom dispersion as they are neutral, hence insensitive to electric and magnetic field).

Injecting 1+ metallic ion into the plasma source, i.e. controlling the energy and trajectory, could be a way of improving the ionization efficiency by targeting the best place to trap and multi-ionize the ions. It has been already proved using charge breeder devices [12] that the injection of low intensity (<1 µA) 1+ metallic ions leads to ionization efficiencies close to those obtained with gaseous ions.

The first question that arises is to estimate by calculations the maximum 1+ intensity that can be injected while keeping good ionization efficiency. To be of interest for stable beam production a mono-charged beam with a threshold intensity of a few tens of µA should be injected.

ISBN 978-3-95450-186-1

FUTURE Q/A=1/6, 1/7 SPIRAL 2 INJECTOR

The SPIRAL 2 LINAC has been designed to accelerate 5 mA deuterons at 40 MeV (Q/A=1/2). This deuteron beam will produce high neutrons flux via a carbon converter that will be used either directly for physics (NFS: Neutrons For Science) or for the delivery of high intensity RIB produced by neutron-induced fission of a uranium target (up to 10^{14} fissions/s).

The RFQ injector of the LINAC has been designed to accelerate also Q/A=1/3 ions that will be used for the in-flight radioactive ion production system named S3 (Super Separator Spectrometer). In order to accelerate beams up to the uranium mass, a separate cave has been built to later host a second injector including a RFQ able to pre-accelerate Q/A=1/6, 1/7 ions (much more easy to produce with an ion source) at the required entrance energy of the LINAC.

The best world results represented in Fig. 9 highlights some rules:

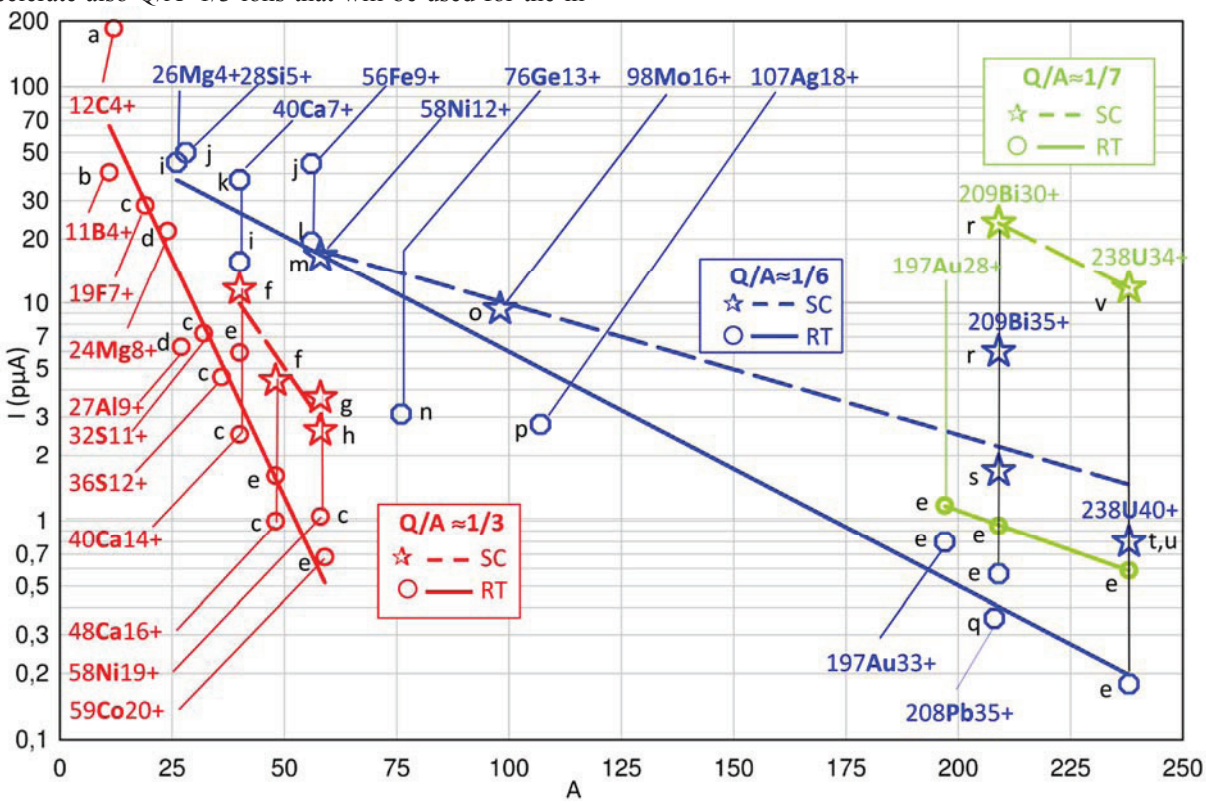

Figure 9: Best world intensities obtained for Q/A=1/3, 1/6 and 1/7 with RT (room temperature) and SC (Superconducting) ion sources. The letters a, b, c...make reference to publications (see references).

The best world results represented in Fig. 9 highlights some rules:

- Above A=60, the intensities fall below 1 pμA, which are comparable to those already obtained with the existing GANIL facility.
- Up to A=25, the choice of Q/A=1/3 is justified. However no data are available for Q/A=1/6, 1/7.
- For A=25, the choice of Q/A=1/6, 1/7 is evident, and the gain in intensity becomes much more important when the mass increases.
- For A between 25 and 60, a RT Q/A=1/6,1/7 ion source seems the most suited and cheapest solution. However, no results from Q/A=1/6, 1/7 SC ion sources are available since they have been developed for heavy ions. Tests should be done.
- For A higher than 60, the choice of a Q/A=1/6,1/7 SC ion source becomes more and more evident when the mass increases.
- For A above 200, the best choice is clearly a Q/A=1/7 SC ion source.

Table 1: Best ion charge state (Q/A=1/3 or 1/6, 1/7) and best ion source (RT: room temperature or SC: Superconducting) to get the maximum intensity for SPIRAL 2.

Ion mass	Best ion source	Comment
A < 25	Q/A=1/3 , RT	
25 < A < 60	Q/A=1/6? 1/7? RT a priori	- No data for Q/A=1/7 - No optimized data with SC ion sources
60 < A < 200	Q/A=1/6-1/7 , SC	- No data for Q/A=1/7 - Too few data
A > 200	Q/A=1/7 , SC	- Bi, U

ISBN 978-3-95450-186-1

Although the choice is clear for A<25 and A>200, the conclusion for intermediate masses would need more data with SC ion sources not build and optimized for such masses. In addition, physics requests have to be taken into account for the final choice.

It is important to keep in mind that the best intensities presented in Fig. 9 are the best never obtained, so that they have to be divided by a factor of 2 to get intensity in operation.

REFERENCES

[1] P. Sortais et al., Rev. Sci. Instrum. 61, 228 (1990). http://dx.doi.org/10.1063/1.1141324

[2] R. Leroy et al., Proceedings of 12th ECRIS Workshop (Riken 1995).

[3] C. Peaucelle et al., Proceedings of 19th ECRIS Workshop (Grenoble 2010). http://accelconf.web.cern.ch/AccelConf/ECRIS2010/papers/tucoak01.pdf

[4] C. Barué et al., Proceedings of the 15th ICIS (Chiba), Rev. Sci. Instrum. 85, 02A946 (2014). http://dx.doi.org/10.1063/1.4847236

[5] H. Koivisto et al., Proceedings of 13th ECRIS Workshop (College Station 1997).

[6] R. Harkewicz et al., Rev. Sci. Instrum. 66, (1995) 2883. http://dx.doi.org/10.1063/1.1146501

[7] P. Lehérissier et al., Proceedings of the 9th ICIS (Oakland 2001). Rev. Sci. Instrum. 73, 558 (2002). http://dx.doi.org/10.1063/1.1429316

[8] P. Lehérissier et al., Proceedings of the 11th ICIS (Caen 2005). Rev. Sci. Instrum. 77, 03A318 (2006). http://dx.doi.org/10.1063/1.2164888

[9] P. Jardin et al., Proceedings of 13th ICIS (Gatlinburg 2009). Rev. Sci. Instrum. 81, 02A909 (2010). http://dx.doi.org/10.1063/1.3267296

[10] F. Lemagnen et al., Proceedings of the 21th ECRIS (Nizhny Novgorod 2014). http://accelconf.web.cern.ch/AccelConf/ECRIS2014/papers/mopph002.pdf

[11] A. Arnau et al., Surface Science Reports 27, 113-239 (1997). http://dx.doi.org/10.1016/S0167-5729(97)00002-2

[12] L. Maunoury et al., Proceedings of the 15th ICIS (Chiba), Rev. Sci. Instrum. 85, 02A504 (2014). http://dx.doi.org/10.1063/1.4828374

REFERENCES IN FIG. 9

[a] M. Muramatsu et al., Proceedings of the 12th ICIS (Seoul), Rev. Sci. Instrum. 79, 02A328 (2008). http://dx.doi.org/10.1063/1.2816706

[b] H. Koivisto et al., Proceedings of the Workshop on the Production of Intense Beams of Highly charged ions, Catania (2000).

[c] C. Barué et al., Proceedings of the 15th ICIS (Chiba), Rev. Sci. Instrum. 85, 02A946 (2014). http://dx.doi.org/10.1063/1.4847236

[d] D. Wutte et al., Proceedings of the 9th ICIS (Oakland), Rev. Sci. Instrum. 73, 521 (2002). http://dx.doi.org/10.1063/1.1425781

[e] Z.Q. Xie et al., Proceedings of the 13th ECRIS workshop (College Station 1997).

[f] H.W. Zhao et al., Proceedings of 18th ECRIS workshop (Chicago 2008) (data in the talk only).

[g] H.W. Zhao et al., Proceedings of 19th ECRIS workshop (Grenoble 2010). http://accelconf.web.cern.ch/AccelConf/ECRIS2010/papers/mocoak01.pdf

[h] L.T. Sun et al., Proceedings of 19th ECRIS workshop (Grenoble 2010). (data in the talk only).

[i] R. Lang et al., Proc. of 15th ECRIS workshop (Jyvaskyla 2002).

[j] A. Kitagawa et al., Proc. of 19th ECRIS workshop (Grenoble 2010). (data in the talk only). http://lpsc.in2p3.fr/Indico/getFile.py/access?resId=11&materialId=slides&confId=467

[k] D. Hitz et al., Proceedings of the 12th ECRIS workshop (Riken 1995).

[l] S.L. Bogomolov, Physics of Particles and Nuclei Letters, Vol. 12, n°7 (2015). https://www.researchgate.net/publication/286522922

[m] L.T. Sun et al., Proceedings of 19th ECRIS workshop (Grenoble 2010). http://accelconf.web.cern.ch/AccelConf/ECRIS2010/papers/mocoak02.pdf

[n] P. Lehérissier et al., Nuclear Instrum. and Methods B211 (2003). http://www.sciencedirect.com/science/article/pii/S0168583X03012138

[o] G. Machicoane et al., Proceedings of the 15th ICIS (Chiba), Rev. Sci. Instrum. 85, 02A957 (2014). http://dx.doi.org/10.1063/1.4858095

[p] R. Scott, Proceedings of 19th ECRIS workshop (Grenoble 2010) (data in the poster only). http://lpsc.in2p3.fr/Indico/getFile.py/access?resId=17&materialId=poster&confId=467

[q] R.C. Vondracek, Proceedings of the 10th ICIS (Dubna), Rev. Sci. Instrum. 75, 5 (2004). http://dx.doi.org/10.1063/1.1691507

[r] L.T. Sun, Proceedings of 21th ECRIS workshop (Nizhny Novgorod 2014). http://accelconf.web.cern.ch/AccelConf/ECRIS2014/papers/tuommh03.pdf

[s] D. Leitner et al., Proceedings of 16th ECRIS workshop (Berkeley 2004).

[t] D. Leitner et al., Proceedings of the 12th ICIS (Seoul), Rev. Sci. Instrum. 79, 02C710 (2008). http://dx.doi.org/10.1063/1.2816790

[u] L.T. Sun, Proceedings of 21th ECRIS workshop (Nizhny Novgorod 2014). http://accelconf.web.cern.ch/AccelConf/ECRIS2014/papers/tuommh03.pdf

[v] J. Benitez et al., Proceedings of 20th ECRIS workshop (Sydney 2012). http://accelconf.web.cern.ch/AccelConf/ECRIS2012/papers/thxo02.pdf

ISBN 978-3-95450-186-1

DEVELOPMENT OF COMPACT H^+ ECR ION SOURCE WITH PULSE GAS VALVE

Y. Fuwa*†, Y. Iwashita, H. Tongu, E. Miyawaki, Kyoto University, Uji, Kyoto, Japan
M. Ichikawa, QST, Tokai, Ibaraki, Japan

Abstract

A compact H^+ ECR ion source is under development. For reduction of the gas load to vacuum evacuation systems, the gas flow into the plasma chamber is chopped by a piezo-electric gas valve. To achieve the enough short time constant of gas flow, a small plasma chamber with 50 cm^2 is adopted and the chamber is operated in 6 GHz TE111 mode. The magnetic field is generated by permanent magnet for reduction of the required volume. For the evaluation of the ion source performance, a Wien filter is fabricated and the ion species distribution is measured. As the result of experiments, the population of protons in the extracted beam was about 15 %.

INTRODUCTION

Ion sources using gas discharge eject not only ion beam but also neutral gas. Most of the neutral gas is evacuated by the vacuum system in Low Energy Beam Transport (LEBT) region and some of the gas diffuse into the accelerator tanks. For pulsed ion sources, the ion beams are extracted from the ion source in just pulse duration, while the neutral gas get out of the plasma chamber constantly. Considering the ion accelerator with high intensity, the length of the LEBT should be as short as possible to reduce the space charge effect. However, with the short LEBT, the quantity of the neutral gas flow into the accelerator tank would become large. The gas flow in the tank may lead discharge and disturb stable operation. For the reduction of the gas flow, the supply of the gas into the plasma chamber should be chopped.

COMPACT ECR ION SOURCE WITH PULSE GAS VALVE

For evaluation of the performance of the ion source with pulsed gas system, a prototype ion source is developed. Proton was chosen as the ions produced in the prototype, supposing that the ion source would applied to compact neutron sources. The ECR plasma production scheme was adopted intending to achieve high H^+ fraction in the extracted beam. A piezo-electric gas valve was developed to chop the gas supply into the plasma chamber. The volume of the chamber is about 50 cm^2 to set the time constant of gas filling and gas evacuation enough small. The chamber was designed to have resonance at the 6 GHz. The magnetic field for the ECR condition at 6GHz is about 2.2 kG and the magnetic field is generated by permanent magnets. The detailed description about the prototype ECR ion source can be found in Reference [1].

RECENT UPDATE ON THE ECR ION SOURCE AND THE TEST BENCH

RF System

The RF power is fed into the cavity through a coaxial line. To couple the coaxial line with the plasma chamber, the tip of the inner conductor inserted into the chamber as a antenna. The radius of the inserted antenna is 0.3 mm and the length of that is about 12.5 cm, which corresponds to the quarter wavelength of light at 6 GHz. The cross-sectional view of the plasma chamber is shown in Figure 1. For evaluation of the coupling condition, a frequency domain analysis with CST microwave studio was performed. The calculated S_{11} parameter is shown in Figure 2. From the result, it was found that the chamber had resonance at 6.038 GHz and the mode of the resonance was TE111 mode.

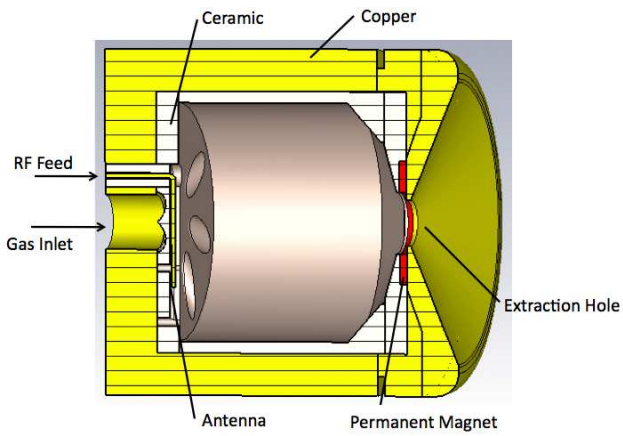

Figure 1: Cross-sectional view of the plasma chamber.

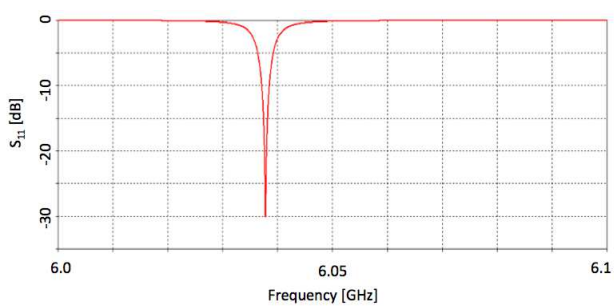

Figure 2: Calculated S_{11} parameter. The plasma chamber has resonance at 6.039 GHz with TE111 mode.

* Research Fellow of Japan Society for the Promotion of Science
† fuwa@kyticr.kuicr.kyoto-u.ac.jp

ISBN 978-3-95450-186-1

Charge-to-Mass Analyzing System

For measurement of the ion species distribution in the extracted beam, a charge-to-mass analyzing system with a Wien filter is fabricated. The analyzing system consists of the Wien filter, field clamp plates and a Faraday cup (see Figures 3 and 4). The length and the cross-section dimensions of the Wien filter are 30 mm and 60 mm × 40 mm, respectively. The area of the filter aperture is 25 mm^2. The magnetic field in the aperture is generated by permanent magnets and the strength of the field is 4 kG. The electrodes in the filter can be applied electric potential with ± 1 kV and the generated electric field is up to 400 kV/m. With the maximum applied voltages (± 1 kV), protons with up to 4.5 keV kinetic energy can be transported through the filter. The shapes of the magnetic pole tips and the electrode tips have grooved structure to flatten the transverse field distribution. The field clamp plates are made of iron plates with 1 mm thickness to form the fields in fringe region. The field clamp also collimate the beam. The field clamp at the upstream of the filter has slit with 1 mm gap. That at the downstream of the filter has aperture with 2 mm aperture. The Faraday cup is made of an SMA receptacle connector and the shape of detection surface is ϕ1.2 mm.

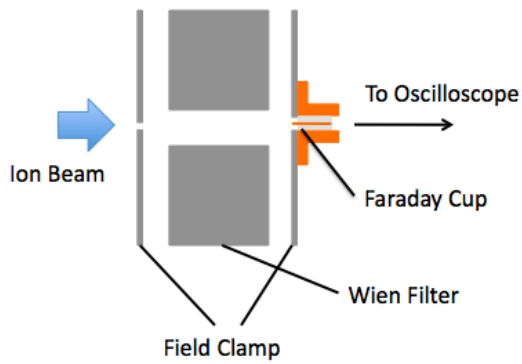

Figure 3: Schematic view of the charge-to-mass analyzing system.

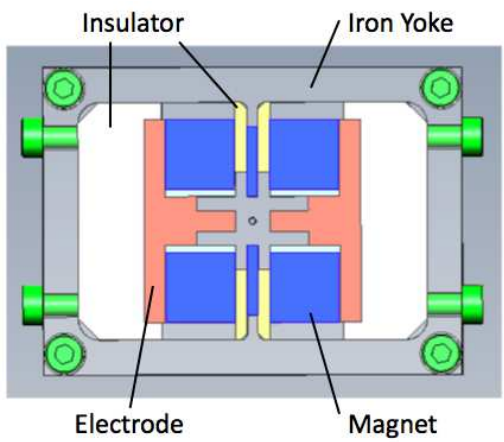

Figure 4: Cross-sectional image of the Wien filter. Magnets (blue part in the figure) are magnetized downward.

PRELIMINARY RESULTS

The ECR ion source was mounted on the test bench for evaluation of the beam production performance. The 6 GHz RF power was generated by a solid state amplifier with magnitude up to 30 W. The RF power was fed through a DC break between waveguides. Waveguide-to-coaxial adopters were attached at the end of the waveguide. The hydrogen gas was supplied from a hydrogen generator for gas chromatography and the gas was stored in a gas buffer tank to control the gas feed pressure to the pulsed gas valve. The gas flow into the plasma chamber can be tuned by the gas feed pressure. The gas flow can be estimated from the difference of the pressure in the test bench in cases pulsed gas valve is on/off. The estimated dependence of the gas flow (with 1 % gas pulse duty; 2 ms pulse duration with 5 pps) on the gas feed pressure is shown in Figure 5.

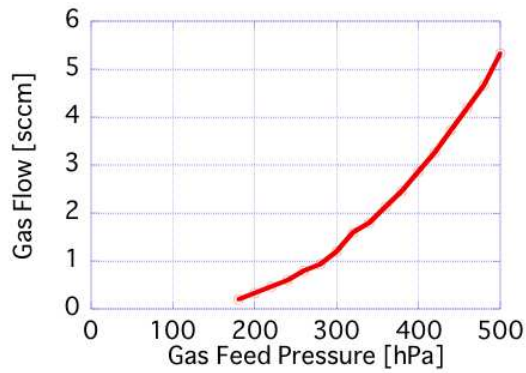

Figure 5: Estimated gas flow into the plasma chamber as the function of the gas feed pressure.

With the gas flow more than 0.2 sccm, the plasma was generated in the plasma chamber. Applying the extraction voltage, ion beams can be provided. The measured ion beam current with 3 kV extraction voltage is shown in Figure 6. The extracted current was saturated with increasing the RF power and the saturated value was increased as the gas flow increased. Figure 7 shows the saturated current value as the function of the gas flow. The extracted current as the

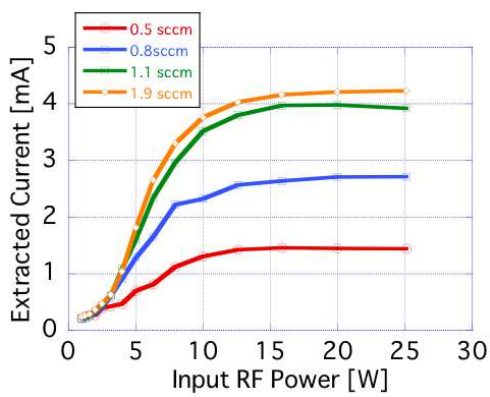

Figure 6: Extracted ion beam current with 3 kV extraction voltage.

ISBN 978-3-95450-186-1

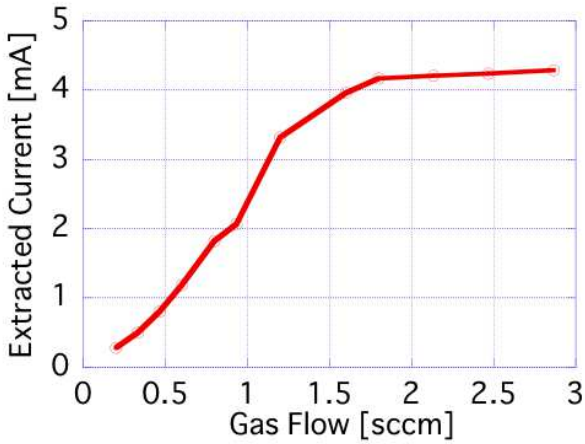

Figure 7: The extracted beam current with 25 W RF power as the function of gas flow.

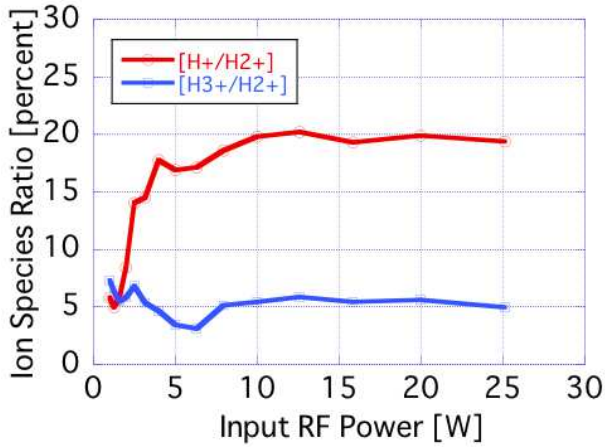

Figure 8: The current of H^+ beam and H_3^+ beam normalized by H_2^+ beam current.

function of of the gas flow is also saturated to 4.2 mA beyond the 1.8 sccm gas flow.

The charge-to-mass analyzing system was installed in the test bench at about 15 cm downstream from the extraction electrodes. Changing the applied voltage on the electrodes in the Wien filter, current of H^+, H_2^+, H_3^+ was measured. Figure 8 shows the measured current of H^+ and H_3^+ normalized by H_2^+ current with 0.8 sccm gas flow. With RF power more than 10 W. The ratio of the population of the ions in the beam become constant. The measurements with other gas flow value also showed that the population of the ions was constant with RF power up to 25 W. Figure 9 is the result of the ion population measurements as the function of gas flow. The population of the H^+ was almost constant as 15 %, and the population of the H_3^+ was increased as the gas flow increased.

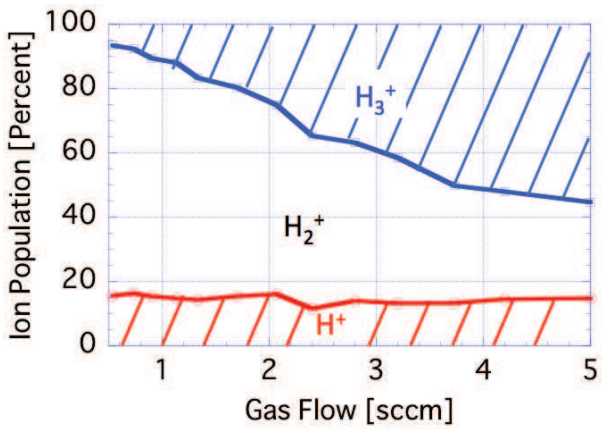

Figure 9: The current of H^+ beam and H_3^+ beam normalized by H_2^+ beam current.

DISCUSSION

Considering the practical operation of the ion source, the gas flow should be set as 1 sccm. From the experimental result, the extracted current with about 2 mA with the gas flow condition. Because the 15 % of the total current is the proton current, the extracted proton current would 300 µA. For the application of the ion source to the compact ion sources, the proton current should be more than 1 mA. The result of the ion species population measurement, the temperature of the plasma is suggested to be too low to generate the large amount of protons. To generate more protons in the ion source, more heating of the plasma is needed. For more efficient plasma heating, the modification of the magnet seems to be effective. In the current ion source test model, the magnetic field distribution is almost uniform to make the volume of the ECR zone large (see Ref. [1]). However, the high temperature electrons are supposed to hit the chamber wall due to the absence of the mirror field. The performance test with additional magnet to generate mirror field is planned.

REFERENCES

[1] Y. Iwashita, H. Tongu, Y. Fuwa, and M. Ichikawa, *Rev. Sci. Instrum.* 87, 02A718 (2016).

ISBN 978-3-95450-186-1

DEVELOPMENT OF A NEW COMPACT 5.8 GHz ECR ION SOURCE*

J. Angot†, L. Bonny, J. Jacob, T. Lamy, P. Sole, T. Thuillier, F. Villa, LPSC – Université Grenoble Alpes – CNRS/IN2P3, 53, Avenue des Martyrs, 38026 Grenoble cedex, France
P. Sortais, Polygon Physics, 53, Avenue des Martyrs, 38026 Grenoble cedex, France

Abstract

LPSC is developing a new 5.8 GHz compact ion source to produce low charge state ion beams and study their capture into the PHOENIX charge breeder plasma. The source was designed to meet criteria like stability, compactness, and low cost. It is mounted on a NW200 flange and is fully under vacuum during operation. The technology brings modularity to ease the development. It operates up to 60 kV. The plasma is heated by a 100 W solid state amplifier. The ECRIS produces 1 mA of H^+ beam with 20 W of HF power and can produce too, low charge state argon ions. It was tested under several microwave and magnetic configurations on a test bench equipped with a mass spectrometer and diagnostics. Given its good performances, this source is being installed to drive the accelerator-based neutron source, GENEPI 2, at LPSC. The developments of the source together with the results of the experiments are presented. Future plans for this ion source are also discussed.

INTRODUCTION

To characterise a charge breeder, a test bench has to be equipped with reliable and easy to install sources producing singly charged ions [1]. Such sources, regarding their performances, must ensure beam stability and quality (emittance) as well as produce the desired species with the required beam intensity. In order to study the capture of low charge state ions into the PHOENIX charge breeder plasma, one LPSC task of the EMILIE project aims to develop a new ion source targeting the specifications listed above.

Since 2013, many developments and experiments have been carried out to improve the 1^+ source. As good performances were obtained, the source was duplicated and installed in order to produce D^+ beams for the accelerator-based neutrons source operating at LPSC, GENEPI2. In parallel, developments will continue to improve the performances and to test innovative configurations.

5.8 GHz ION SOURCE DEVELOPMENT

To develop this new source, the first idea was to use a socket type connexion to obtain a compact and easy to dismount assembly. We also opted for a modular design to easily change the magnetic structure and the microwave coupling. Thus, the first configurations were based on the compact microwave ion sources technology (COMIC 2.45 GHz) [2] using a 5.8 GHz microwave (μw) frequency and with a larger plasma chamber to optimize the coaxial μw coupling. Recently, a minimum-B configuration with a waveguide coupling has been tested.

Design

The source is fixed on a NW200 flange and its length is about 400 mm (Fig. 1). The plasma chamber is water-cooled and surrounded by a container enclosing the permanent magnets. The microwave circuit passes through the flange and is axially connected to the plasma chamber. The extraction system is composed of a plasma electrode and a polarized puller allowing extraction electric field (E) tuning, a set of three electrodes (one with a negative potential inserted between two grounded electrodes) allowing space charge compensation during beam transport.

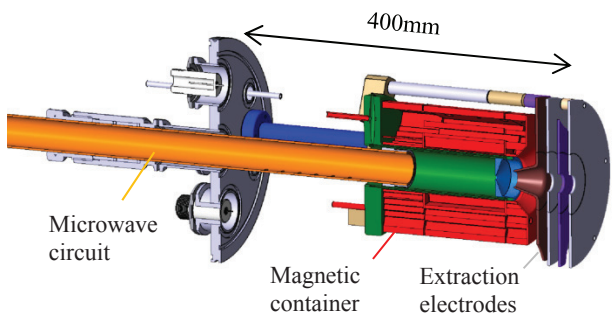

Figure 1: Cut view of the 5.8 GHz ion source modular structure.

Compact Microwave Configuration

In the compact microwave design, the goal is to produce high microwave electric field in the plasma chamber, at the ECR surface. This is done using a resonant μw structure composed of antennas and couplers with a coaxial input. The gas pressure is tuned to reach the Paschen's condition to ignite and sustain the plasma. These sources produce stable beams with a low beam emittance at low power [2].

The 5.8 GHz μw coupling assuring a high electric field at the plasma electrode hole was simulated with HFSS [3]. It is done with a 14 mm long antenna in a 41 mm inner diameter cavity. The maximum E field on the axis is 15 kV/m (Fig. 2a). Another microwave coupling using a longer antenna with 4 radial couplers has also been designed and tested. In this configuration, the μw E electric field reaches 100 kV/m on the axis, close to the plasma chamber hole, for 1 W of injected power (Fig. 2b).

*Work supported by ERA-NET NuPNET in the framework of the EMILIE project.
†julien.angot@lpsc.in2p3.fr

ISBN 978-3-95450-186-1

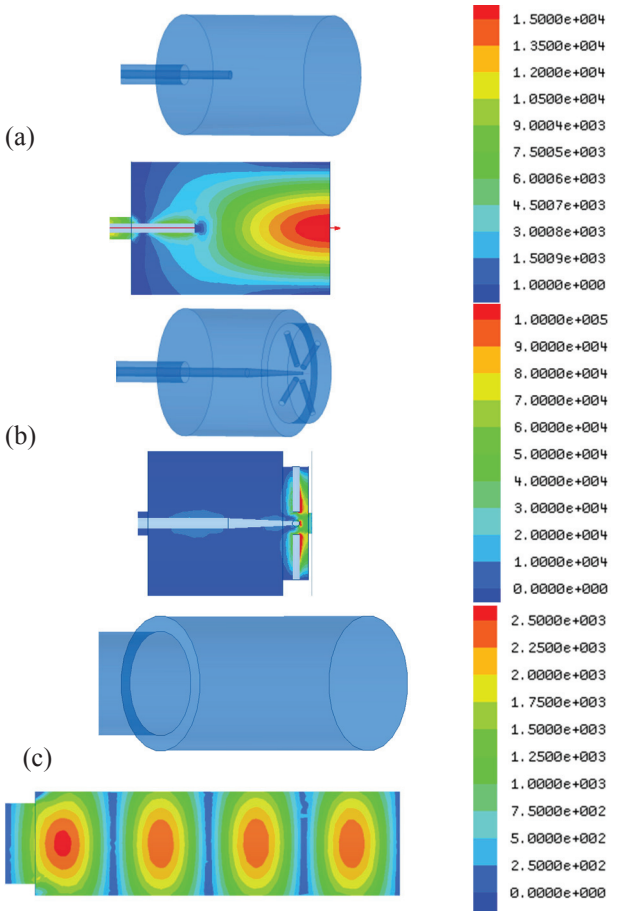

Figure 2: HFSS simulations of microwave couplings and electric field distributions (a) single antenna, (b) antenna with couplers, (c) circular waveguide.

Regarding the magnetic structure, an axial field gradient is generated by a permanent magnet ring alternating axial and radial orientation (Fig. 3). The axial peak is located at the extraction electrode, shaping one ECR resonant surfaces in the cavity while the other is in the accelerating gap outside of the source.

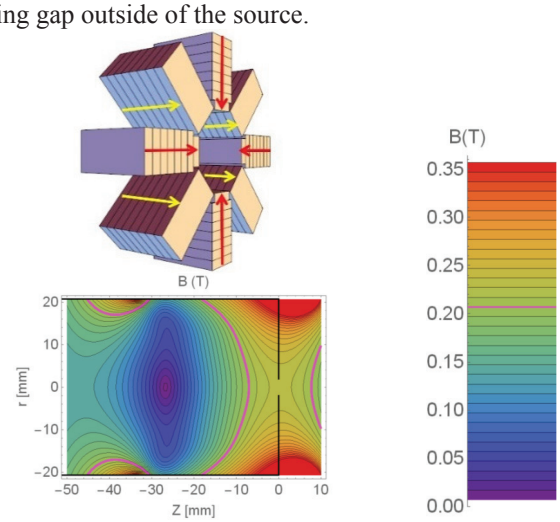

Figure 3: Gradient magnetic structure (top) and magnetic field map simulated with Radia - Mathematica (bottom).

Classical ECR configuration

A minimum-B structure has then been designed using a set of standard 12x12x12 cm^3 permanent magnets. A 0.43 T magnetic field is obtained at the injection point A, 0.24 T at the extraction point B, with a minimum of 0.15 T at point C. (Fig. 4).

The µw coupling has been replaced by a circular waveguide (TE11 mode) (Fig. 2c). A coaxial to waveguide transition has been simulated with HFSS, realized, tested, and validated before the mounting on the source.

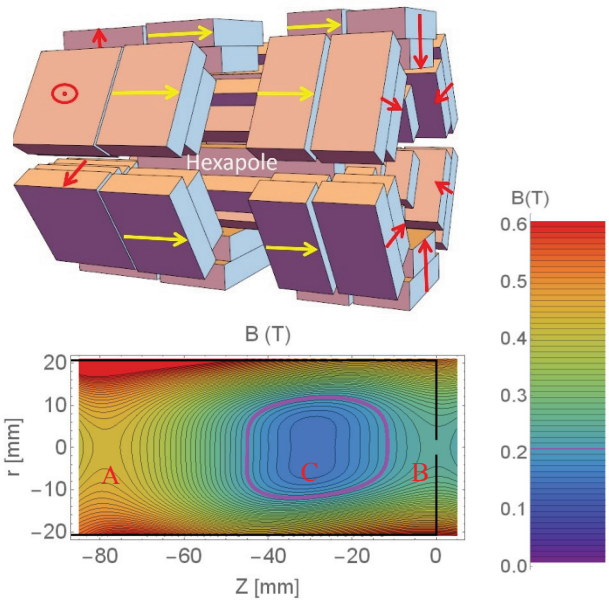

Figure 4: Minimum B magnetic structure (top) and magnetic field map simulated with Radia - Mathematica (bottom).

Results and Discussion

Table 1 presents some results in several configurations. The magnetic gradient configuration with the coaxial antenna and couplers showed very good ability to produce single charge argon beam at low power. For low charge states beams, the magnetic container was replaced by the minimum-B structure. The source generated beams up to charge 4+, the 1+ beam being predominant. The base vacuum will be improved in order to enhance the low charge state beam intensities, the plasma electrode hole will be reduced to produce some µA beams within an emittance compatible with the charge breeder acceptance. The minimum-B magnetic configuration was also tested for the production of mA range proton beam. It was clearly noticed that more H^+ current could be extracted using the waveguide coupling, with less power compared to the antenna coupling. By adjusting the microwave power, the source is to produce intensities ranging from a few µA up to 1.45 mA extracted from a 4 mm hole in the plasma electrode.

To compare the two coupling efficiencies in the minimum-B magnetic structure without plasma, we computed the efficient part of the electric field on the ECR surface (B=0.207 T at 5.76 GHz).

ISBN 978-3-95450-186-1

Table 1 : Extracted Currents with a Φ=4 mm Plasma Electrode Hole

Magnetic and HF configurations	Species	Current (mA)	HF power (W)	Extraction voltage (kV)
Gradient coaxial antenna + couplers	Ar^+	1	25	40
MinB coaxial antenna	H^+	1	63	30
MinB Waveguide	Ar^+ / Ar^{2+} / Ar^{3+} / Ar^{4+}	0.185 / 0.142 / 0.044 / 0.01	81	30
MinB Waveguide	D^+	1.15	17	30
MinB Waveguide	H^+	1.45	45	35

As the electrons trajectories are following the magnetic field lines, the efficient part of the electric field providing ECR heating is defined as:

$$E = \frac{\vec{E} X \vec{B}}{B} \quad (1)$$

The ECR surface is meshed with Radia-Mathematica, at each node the points coordinates and the magnetic field vectors are recorded, then the electric field is obtained using the field calculator of HFSS and imported in Radia-Mathematica to compute E.

The results are plotted on the ECR surfaces in Fig. 5 and Fig. 6, using a color scale to represent the intensity. The average value of E is also calculated to compare the two configurations.

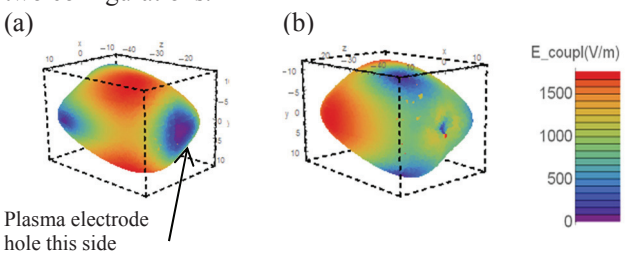

Figure 5: Front (a) and rear (b) views of the efficient E field distribution on the ECR resonance surface for the antenna coupling.

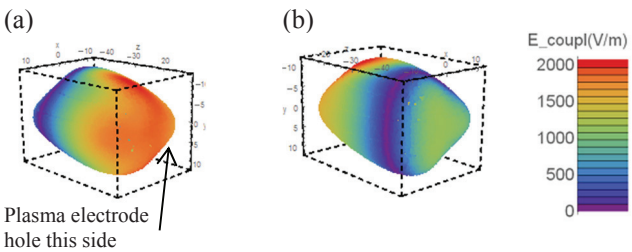

Figure 6: Front (a) and rear (b) views of the efficient E field distribution on the ECR resonance surface for the waveguide coupling.

Without plasma, in the case of the antenna, the average efficient E field is 1267 V/m and, in the case of the waveguide, it is 1072 V/m. Comparing with the experimental results, this indicates that the significant parameter is not the average coupling but rather the location on the surface, or that the plasma presence strongly affects the microwave coupling in these operating conditions. One can note that in the case of the waveguide the E intensity is much higher close to the cavity axis where the dense ECR plasma is located. While in the case of the antenna, the strongest E intensity is obtained on the peripheral part of the ECR zone (large radius), providing energy transfer to electrons playing a secondary role in ECR ion source performance.

Further simulations, including a plasma model, would be necessary to better simulate the coupling.

5.8 GHz ION SOURCE ON GENEPI2

At LPSC, GENEPI2 is an accelerator-based neutron source for multipurpose applications (nuclear physics experiments, irradiation platform, neutrons detector calibration) [4]. The neutron flux is produced by the impact of a 220 keV D^+ beam onto a tritium target.

Up to now, the accelerator was operated in a pulsed mode, driven by a duoplasmatron source (50 mA peak D^+, 700 ns pulse width, repetition rate from 100 to 4000 Hz) [5].

In order to increase the beam power and operate in CW mode, the 5.8 GHz ECR ion source has been retained to produce a 100 to 1000 µA D^+ beam. The source is set on a 250 kV platform (see Fig. 7). The beam is first extracted with a 35 kV potential and then accelerated through a set of 5 electrodes.

On the platform, the source socket flange is fixed on a trolley making its mounting and dismounting easy on the vacuum chamber. A 0.5 kW water chiller was also added on the platform and connected to the plasma chamber to regulate its temperature.

ISBN 978-3-95450-186-1

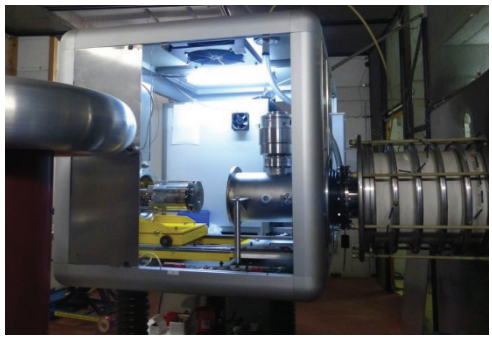

Figure 7: 5.8 GHz ion source mounted on the 250 kV platform of GENEPI2.

To start in safe conditions and qualify the accelerator operation, the extracted current was limited using a 1 mm hole diameter in the plasma electrode instead of the 4 mm one. The assembly of the source on the platform was completed in June 2016 and a 50 µA D^+ beam has been successfully accelerated in July. The plasma electrode will now be replaced to increase the D^+ current up to 1 mA.

CONCLUSION

The 5.8 GHz ion source shows a good ability to produce low charge state ion beams at low microwave power. Tuning this parameter, a wide range of intensities is achievable for H^+ and D^+. Thanks to the modular configuration and in order to improve the performances, new microwave couplings and new magnetic configurations will be tested. This could lead to configurations allowing frequency increase and therefore frequency scaling studies. To produce higher charge state currents, the vacuum and the plasma chamber pumping will also be improved.

The compactness and the simplicity of the source eased the integration of the source on the GENEPI2 high voltage platform. This reduced the time and cost required to upgrade this facility.

REFERENCES

[1] T. Lamy et al., "Fine frequency tuning of the phoenix charge breeder used as a probe for ECRIS plasmas", in *Proc. 19th Int. Conf. on ECR Ion Sources (ECRIS'19)*.

[2] P. Sortais *et al.*, "Ultracompact/Ultralow power electron cyclotron resonance ion source for multipurpose applications", in *Proc. 13th Int. Conf. on Ion Sources (ICIS'13)*, Gatlinburg, USA, Sept. 2009, paper RSI 81, 02B314 (2010).

[3] HFSS, ANSYS, http://www.ansys.com/Products/Electronics/ANSYS-HFSS.

[4] F. Villa *et al.*, "Multipurpose applications of the accelerator-based neutron source GENEPI2", in *Proc. UCANS-V*, paper Il nuovo cimento 38 C (2015) 182.

[5] C.Destouches *et al.*, "The GENEPI accelerator operation feedback at the MASURCA reactor facility", in *Proc. 7th Int. Conf. on Accelerator Applications(AccApp05)*, paper NIM 562, Issue 2 (2006).

ISBN 978-3-95450-186-1

A NEW ECRIS INSTALLATION AT THE ARGONNE TANDEM LINAC ACCELERATOR SYSTEM*

R. H. Scott†, C. A. Dickerson, R. C. Pardo, R. C. Vondrasek
Argonne National Laboratory, Lemont IL, 60439, USA

Abstract

An existing all permanent magnet ECRIS, the BIE100 [1], will be installed at ATLAS to recover operational flexibility by providing ATLAS with a second ECR ion source for stable beams. For years ATLAS has operated with two ECR ion sources, ECR2 and the ECR charge breeder as well as a tandem electrostatic injector. The tandem was retired in 2013 and in mid-2015 the ECR charge breeder was decommissioned to make room for a new Electron Beam Ion Source exclusively for charge breeding radioactive ion beams. This left the facility with a single ECR source for virtually all stable ion beam production. Design, installation plans and anticipated operational parameters are discussed.

ATLAS MULTI-SOURCE HISTORY

The Argonne Tandem-Linac Accelerator System (ATLAS) has mostly relied on the use of multiple ion sources since inception in 1985. This has allowed for enhanced operational flexibility and time to develop new beams and improve ion source performance. One source can be prepared, maintained and conditioned while another is in use for the experimental program. If there is a major failure of an ion source system another one can be called into duty to continue accelerator operations and reduce overall downtime.

Early on two negative ion source injector platforms (east and north) were used to feed the Tandem Vandegraff Accelerator, stripping to positive ion beams and subsequently feeding the Booster and Atlas superconducting linac sections (see Fig. 1). In 1992 the Electron Cyclotron Resonance Ion Source (ECRIS) ECR1 and Positive Ion Injector (PII) linac were commissioned to also feed into Booster, while the east injector was retired. Through the years, and a variety of upgrades, ATLAS has maintained multiple ion sources for the production of stable beams as can be seen in Fig. 2. Recently the ECRCB (charge breeding upgrade of ECR1) was only used for stable beams that did not affect the low background essential for effective charge-bred radioactive beam delivery. In the summer of 2013, the tandem injector was retired and in June of 2015 the ECRCB was retired from part time stable beam operation to be dismantled a few months later and replaced with an Electron Beam Ion Source (EBIS) dedicated solely to radioactive beam charge breeding.

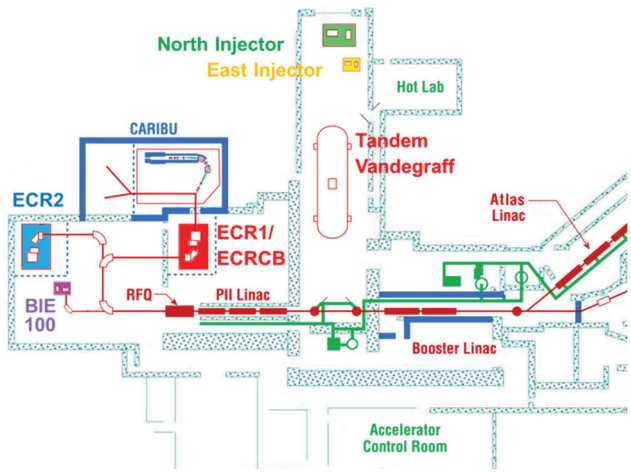

Figure 1: Layout of ATLAS accelerator section.

PRESENT SOURCE OPERATIONS

Since ECRCB removal, ATLAS has been left with a single source, ECR2, for all stable beam production. This source limitation has been very taxing for ATLAS operations. ATLAS essentially follows a 24 hour 7 day/week operational schedule. Typical experiments last 3-7 days with a very quick turnaround time expected of less than 24hrs for a new ion species to be tuned on target. Scheduling of beam time has become more complicated with more consideration needed for outside user schedules in relation to ion source preparation demands. Some of the scheduling burden will be lifted from ECR2 when the EBIS is brought online in late 2016 for breeding CARIBU radioactive ions, but there will still be no alternate ion source for stable beam production.

Carbon-14 Beams

Carbon-14 ion beam production ended at ATLAS with the retirement of the tandem in 2013. The demand for this beam has not diminished, and experiments delivering ^{14}C have been approved by the ATLAS program advisory committee. Until now, resumption of ^{14}C beam production in ECR2 has been avoided, mostly due to time prohibitive radioactive contamination procedures that would make maintenance and operation very difficult. Based on experience with the tandem ion sources, ^{14}C contamination also continues into the beamline past the ion source for quite some distance.

* Work supported by U.S. Department of Energy, Office of Nuclear Physics, under contract No. DE-AC02-06CH11357.
† scott@phy.anl.gov

ISBN 978-3-95450-186-1

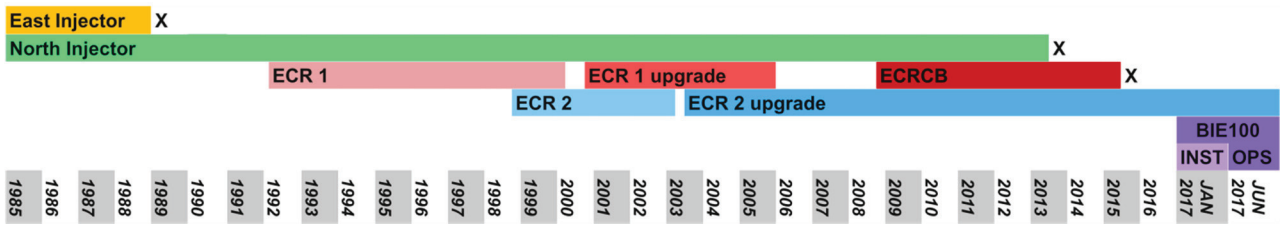

Figure 2: Timeline of stable beam production from ion sources for the ATLAS facility experimental program.

BIE100 PROJECT

The need for ion source flexibility and the need to return to ^{14}C production are the performance goals which drive a project to install the BIE100 [1] ECRIS as a second 'stable' beam source for ATLAS. It is an all permanent magnet (NdFeB) design that was developed for a DOE small business innovation research (SBIR) project from 1999 thru 2002 [2] by Dan Xie at Berkeley Ion Equipment, Inc. The BIE100 was most recently used within the Argonne Physics Division for demonstration of a multi-charge state low energy beam transport (LEBT) system. The simple plasma chamber design and the compact nature (47 cm Ø, 32 cm L) of this ion source are suited for ^{14}C contamination clean-up when needed (see Fig. 3).

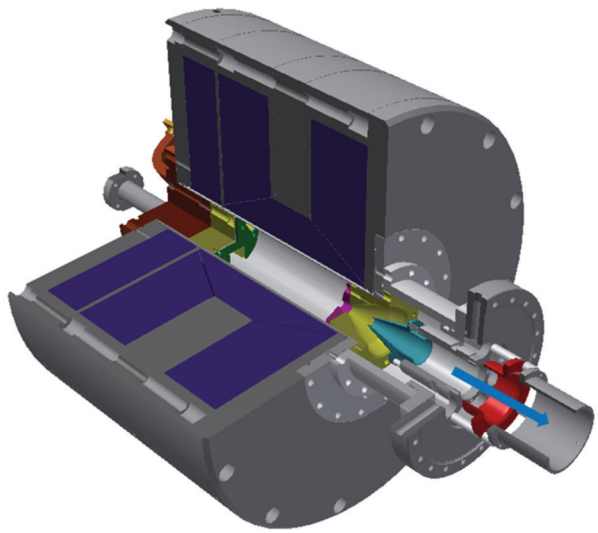

Figure 3: BIE100 ECRIS sectioned perspective view, the blue arrow denotes ion beam extracted from source.

Operations

The BIE100 has measured injection, extraction and radial magnetic fields of 12.7, 6.5 and 10 kG respectively. It typically ran with RF power ≤1.3 kW at 2 frequencies: 12.7 and 13.5 GHz during development, but will run at a single frequency between 11-13 GHz at up to 350 W for current ATLAS needs. The purchase of another TWTA, that would provide a second frequency of plasma heating, can be delayed if needed. This source will operate at 15-25 kV source potential with 1-10 mA of drain current. The HV platform will operate as high as 175 kV to meet the energy required for injection into the first accelerating section. The maximum mass to charge ratio is currently limited to ~6.5.

When the source becomes operational, it will not only produce the highly desired ^{14}C beam from $^{14}CH_4$, but can also be tasked for beams from all of the elemental gases, other molecular gases, and materials with a high vapor pressure. Usage of this source is expected mostly for lighter beams (Z ≤18). As a benchmark, the BIE100 has produced 200 eμA or more for Argon charge states up to 8+ with 330 W single frequency RF power [2]. For reference, approximately 50% of the experimental runs from FY2016 could have been produced using the BIE100 at the requested beam current, all without venting the ion source.

Installation

The preliminary beamline design from the source into the existing ATLAS LEBT is shown in Fig. 4. The small size of the BIE100 will allow it to fit next to ECR2 (see Fig. 1) requiring no new building construction. A number of items from ECRCB that will be reused include a travelling wave tube amplifier (TWTA), gas leak valves/controllers, vacuum pumps, waveguides, power supplies, a small high voltage (HV) platform and insulators as well as existing beamline elements such as dipole magnets and accelerator tubes. A major beam optics difference compared to existing and previous sources at ATLAS is that the mass analysing magnet will be moved off of the HV platform resulting in full beam loading of the HV power supply and accelerator tubes. Electrostatic beam focusing elements are important to keep the beam loading small. A new vacuum chamber for the convergence of the new beamline with the PII LEBT at a 90 degree dipole magnet has already been constructed. It has new beam entrance and optical alignment ports for the intersection point.

Timeline

Plans have already begun for the installation of the BIE100 ECRIS at ATLAS. Items for reuse have been identified and placed into an initial design layout. Beam optics were calculated using TRACK beam dynamics code [3]. The timing of many of the activities will be somewhat fluid with availability of personnel and needs of ATLAS. The next step shall be a finalization of layout of ion source and HV platform placement, which should be completed by end of September 2016. After a safety review is performed, placement of beamline stands, HV platform, vacuum and optics components will follow

ISBN 978-3-95450-186-1

without interruption to ATLAS beam delivery. The new intersecting 90 degree vacuum chamber will be installed during a scheduled downtime period over December 2016 or January 2017. Electrical, vacuum control, safety interlocks, fencing, and control system hardware will be installed in early 2017. It is anticipated that beam tests can begin April-May followed by experiments at ATLAS using the BIE100 in June 2017.

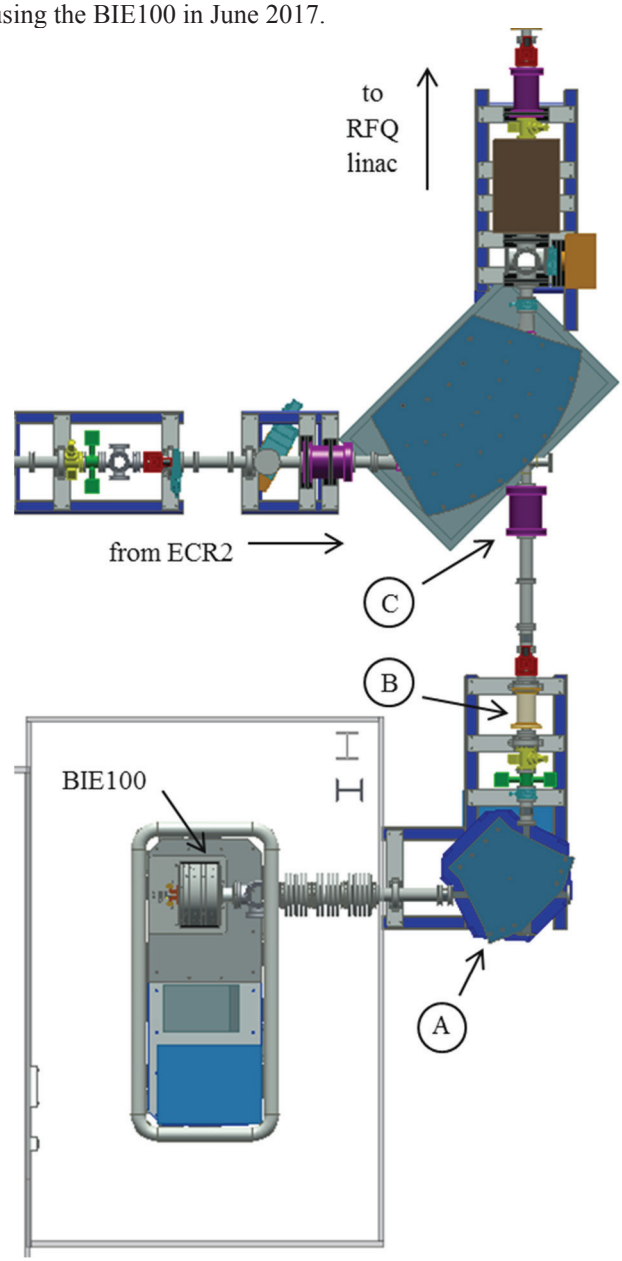

Figure 4: Planned BIE100 at ATLAS. Note the initial mass analysis off the HV platform (A), followed by a simple beamline design with steerer (B) and electrostatic quadrupole triplet (C) to match into existing LEBT.

CONCLUSION

A new ion source for ATLAS will be installed and made operational in the next year using an existing permanent magnet source. The source must provide both ^{14}C beams and added flexibility to stable beam operations. The BIE100 ECR ion source has been identified as a solution for the accelerator's current and near future needs. Layout design is underway and installation is to follow. Operations are currently slated for mid-2017.

REFERENCES

[1] D. Z. Xie, "The BIE100 ECR ion source," *Rev. Sci. Inst.*, vol. 73, no. 2, pp. 531-533, Feb. 2002.

[2] D. Z. Xie, "A high efficiency electron cyclotron resonance ion source system for the production of radioactive ion beams," Rep. DOE00 SBIR Phase II Project (Grant No: DE-FG-99ER82750) Nov. 2002

[3] B. Mustapha, V. N. Aseev, P. N. Ostroumov, and E. S. Lessner, "TRACK: the new beam dynamics code," in *Proc. PAC'05*, pp. 2053-55.

ISBN 978-3-95450-186-1

DESIGN, CONSTRUCTION AND COMMISSIONING OF THE NEW SUPERCONDUCTING ION SOURCE AISHA

L. Celona*, S. Gammino, G. Ciavola, F. Chines, F. Noto, G. Costa, G. Torrisi, O. Leonardi, D. Mascali, G. Castro, S. Marletta, G. Pastore, S. Vinciguerra
Instituto Nazionale di Fisica Nucleare - Laboratori Nazionali del Sud, Catania, Italy

Abstract

At INFN-LNS a new superconducting ECRIS named AISHa has been designed with the aim to provide highly charged ion beams with low ripple, high stability and high reproducibility, also fulfilling the needs of hospital installations (e.g. L-He free, easy to use, etc.). It is a hybrid ion source based on a permanent magnet hexapole providing 1.3 T on plasma chamber walls and four superconducting coils for the axial confinement. The axial magnetic system is very flexible in order to minimize the hot electron component and to optimize the ECR heating by controlling the field gradients and the resonance length. The design of the hexapole aimed to minimize the demagnetization due to SC coils. The magnetic system measurement confirmed the effectiveness of the adopted solutions. Innovative solutions have been also implemented as it concerns the RF system design. It will permit to operate in single/double frequency mode, supported by variable frequency high power klystron generators, thus exploiting at the same time the FTE – Frequency Tuning Effect and the Two Frequency Heating. The source has been assembled at the INFN-LNS site and the commissioning phase already started.

INTRODUCTION

The **A**dvanced **I**ons **S**ource for **Ha**drontherapy (AISHa) was designed in 2012 by taking into account the typical requirements of hospital-based facilities, including the minimization of the mean time between failures (MTBF) and the maintenance operations.

In 2013 the proposal of AISHA construction was approved by the Regional Government of Sicily and it was funded within the framework of the program of Sicilian Government named PO FESR 2007-2013 and a pool of Sicilian SME was associated with INFN for its construction. Today the AISHa source is entirely assembled and its complete commissioning is scheduled by the end of 2016.

Figure 1 shows an overall view of the source together with the components of the beamline.

The compact AISHa source has been designed to be an intermediate step between the 2nd generation ECRIS, unable to provide the requested current and/or brightness and the 3rd generation, too complex and expensive.
It is a multipurpose device with the aim to provide highly charged ion beams with low ripple, high stability and high reproducibility.

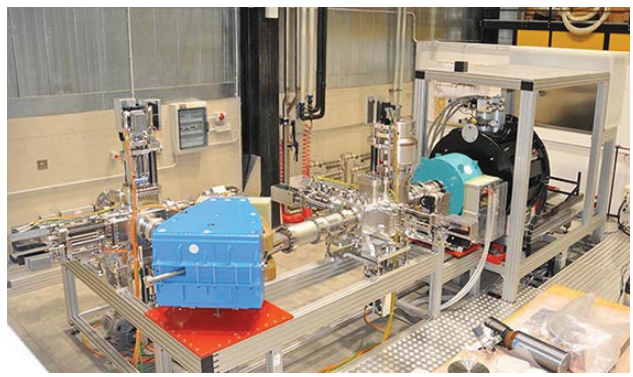

Figure 1: An overall view of the Ions Source and LEBT of the AISHa project.

Furthermore, the introduction of an oven for metallic ion beams will permit the production of new beam for hadrontherapy and for other applications in radiobiology. The main source characteristics are described in Table 1.

Table 1: Major Source Parameters

Radial field (max)	1.3 T
Axial field (INJ/MID/EXTR)	2.6 T / 0.4 T / 1.7 T
Plasma Chamber diameter	92 mm
Operating frequencies	18 GHz
Operating power (max)	1.5 kW
Extraction voltage (max)	40 kV
Cryostat length	620 mm
Cryostat diameter	550 mm
L-He	Free

MECHANICAL DESIGN

The majors mechanical improvements of the AISHa with respect to the usual layout of similar sources concern the use of the carbon fibers and composite materials to realize the hexapole containment chamber and the HV insulation.

* celona@lns.infn.it

ISBN 978-3-95450-186-1

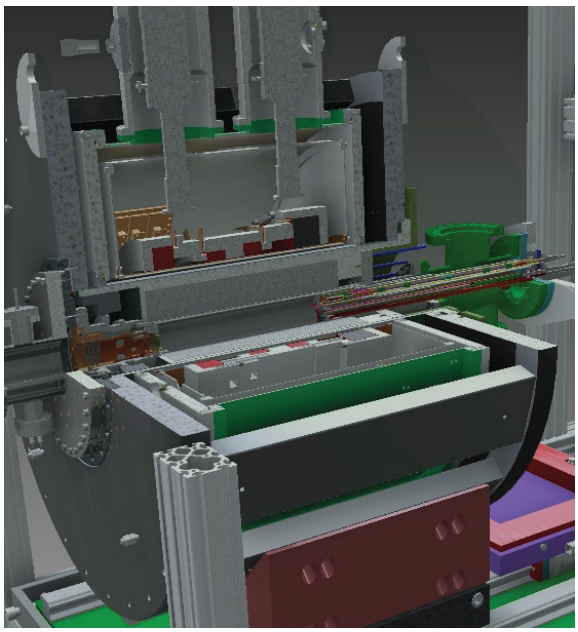

Figure 2: A rendering of core of the AISHa source.

The plasma chamber is made of stainless steel and it was designed to operate at a maximum power rate of 2 kW by using a multi-channel water-cooling system [1].

A laminar water flow into to the plasma chamber allows to not exceed the safe temperature for the permanent magnet hexapole avoiding any possible damage. By optimizing the design of the grooves, the maximum temperature on the outer surface of the plasma chamber is in the order of about 30°C.

The insulation was adapted to 40 kV operation by means of a 20 mm thick Glass Fiber / Carbon Fiber tube surrounding the hexapole, keeping the superconducting magnets and the yoke at ground potential.

Furthermore, the movable extraction system will permit to adapt the AISHa source to other facilities, such as the high voltage platform already present at INFN-LNL.

MAGNETIC SYSTEM DESIGN

The hybrid magnetic system consists of a NdFeB permanent Halbach-type hexapole magnet and four independently energized NbTi superconducting coils.

The maximum radial field on plasma chamber walls is up to 1.3 T, while the axial gradients is about 13 T/m, enough to burn the plasma in strong gradient regime [2].

A deep analysis in the design phase has allowed to overcoming the demagnetization issue of some sectors of hexapole due to the presence of high values of the radial magnetic field components H_x and H_y generated by the SC coils. To avoid the radial confinement magnetic field decreasing, these sectors have been replaced with others having higher coercivity [3].

The tunable magnetic profile, by changing the current in the two middle coils, allows a fine tuning of the mirror ratio and an improvement of the heating efficiency by suppressing the production of quasi-collisionless high energy electrons.

Figure 3 shows the axial magnetic field measurement that confirmed the design specifications [3].

The peak field at the injection side is around 2.6 T and at the extraction it is about 1.7 T, with a minimum value of 0.5 T, about 60% of the ECR resonance field @ 18 GHz.

The superconducting coils are enclosed in a compact cryostat (it is 620 mm long and 550 mm in diameter), the cold mass is cooled down to cryogenic temperatures with two double-stage cryocoolers. Figure 4 shows the typical cool down data: around 40 hrs are needed from room temperature to reach the operating conditions needed to energise the magnet and the time to reach the maximum coil energisation is 24 min.

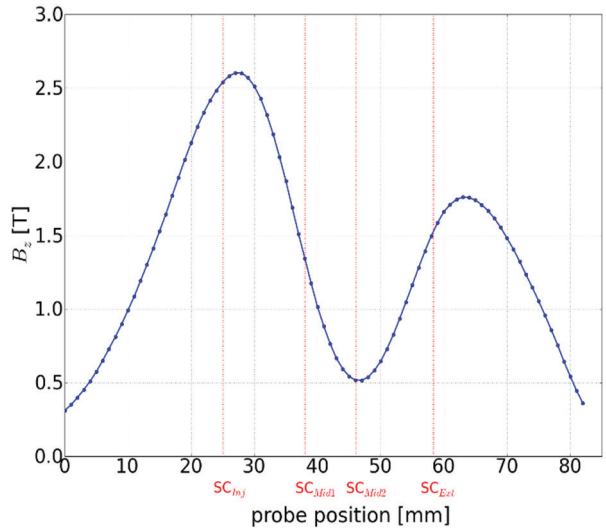

Figure 3: Experimental axial magnetic field measurement.

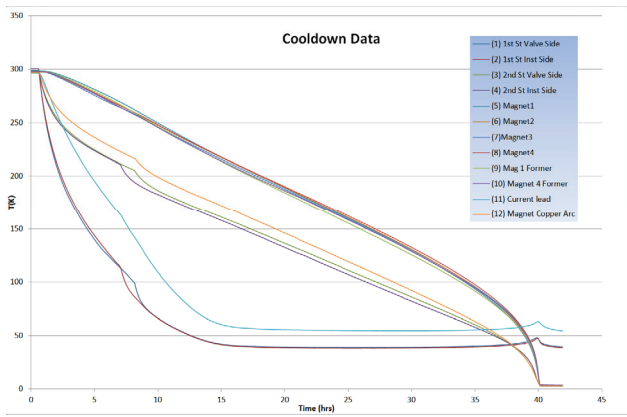

Figure 4: Typical cool down data.

MICROWAVE INJECTION

The source is equipped with two High Power Klystron Amplifiers in order to inject microwave at different frequencies in the chamber, one at 18 GHz and another at higher frequency (~ 21 GHz).

Through a Digital Fast Tuner System (DFTS) it is possible to finely tune the frequency and to exploit the Two Frequency Heating (TFH) and Frequency Tuning Effect to

ISBN 978-3-95450-186-1

generate moderate currents of the highest charge states and optimize the beam brightness.

Figure 5 shows the front side of the injection flange with the different input utilities, the biased-disk and the evaporation oven for metal ion beam production.

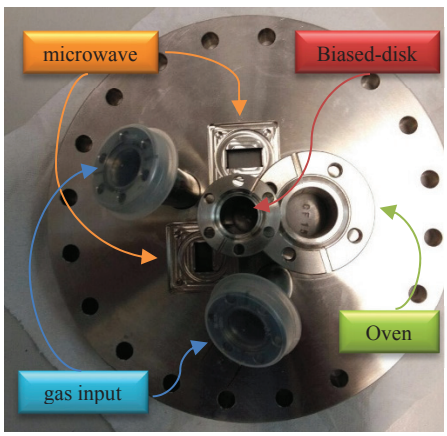

Figure 5: Front side of the injection flange.

Figure 6: Microwave injection system.

Figure 6 shows the plasma injection flange equipped with two waveguides, two different gas inputs, the bias disk and the port for the oven.

In order to insulate the plasma chamber, placed at high voltage, from the microwave amplifier, located at ground, two compact waveguide DC breaks have been designed for the two microwave line to permit reliable operation up to 50 kV.

BEAM LINE

The beamline mainly consists of a focusing solenoid placed downstream the source, a 90° bending dipole for ions selection and two diagnostic boxes. The distance beetwen solenoid and dipole was chosen in oder to minimize the beam losses and increase emittance for the transport of ions with different charge states.

The diagnostic boxes consist of two Faraday Cups, a beam wires scanner and the slits that will allow the characterization of the beam.

Figure 7: Beam line.

CONCLUSION

The assembly and the first tests of vacuum, high voltage and the magnetic system startup with different cycles of cool-down and warm-up has been completed in June. The computer control is going to be finished, this will permit to start the beam commissioning in late September 2016.

ACKNOWLEDGEMENT

The authors acknowledge the valuable support given by all technical staff of INFN-LNS.

REFERENCES

[1] F. Noto et al., Structural Mechanics Optimization of the ASHa Ion Source, ICCM2015, vol.2, 2015 - ISSN 2374-3948 14-17th July, Auckland, NZ.

[2] S. Gammino et al, Plasma Source Sci.&Tech. 18.4 (2009): 045016.

[3] L. Celona et al., ECR Ion Source Development at INFN-LNS, Proceedings of ECRIS-2014, Nizhny Novgorod, Russia.

ISBN 978-3-95450-186-1

INNOVATIVE MECHANICAL SOLUTIONS FOR THE DESIGN OF THE HIGH INTENSITY PROTON INJECTOR FOR THE EUROPEAN SPALLATION SOURCE

G. Gallo, L. Allegra, L. Celona, L. Neri, D. Mascali, G. Torrisi, S. Gammino
INFN/LNS, Catania, Italy

Abstract

The design of the 2.45 GHz, 0.1 T microwave discharge Proton Source for the European Spallation Source (PS-ESS) has required on-purpose solutions in order to maximize the beam brightness, keeping a very high reliability figure. The mitigation of maintenance issues has been the main guideline through the design phase to maximize the MTBF and minimize the MTTR. The mechanical design has been based on advanced solutions in order to reduce as much as possible the venting time for the plasma chamber, to facilitate the replacement of extraction electrodes and/or plasma chamber, and to simplify any after-maintenance alignment procedure. The paper will describe the strategy which has driven the design phase, the solutions adopted to fulfil the project goals and the results of the assembly phase recently concluded at INFN-LNS with successful first plasma.

INTRODUCTION

The Proton Source for ESS (PS-ESS) (see Fig. 1) was designed with a flexible magnetic system and a compact tetrode extraction system with the goal to minimize the emittance and the time needed for the maintenance operations [1].

The PS-ESS source body has been designed with the aim to fulfil the needs of an industrial installation. In particular, in order to maximize the MTBF and minimize the MTTR, the entire assembly has been designed by taking into account the allotted times for maintenance operations. In particular, efforts have been done to optimize the following operations:

- Source opening and closing procedures;
- Easy replacing of the extraction electrodes and plasma chamber;
- Automatic realignment of the plasma chamber on the extraction electrodes, after the maintenance operations;
- Easy replacement of the internal inserts of the matching water-cooled transformer which is used as impedance matching system, maintaining the same outer structure.

MECHANICAL DEVELOPMENT

Hereinafter a description of the mechanical solution adopted is presented for the subsystems constituting the body source. In particular, the extraction electrodes assembly, the suspension based on a pin junction and the water-cooled radiofrequency injection system will be described.

ESS Body Source

The body source is mechanically divided into two distinct parts as it is shown in Fig. 1:

- A movable part consisting of: injection system, plasma chamber, magnetic system and extraction column, called hereinafter “part A”;
- A fixed part consisting of the extraction electrodes together with the first element of LEBT which also houses the vacuum instrumentations, called hereinafter “part B”.

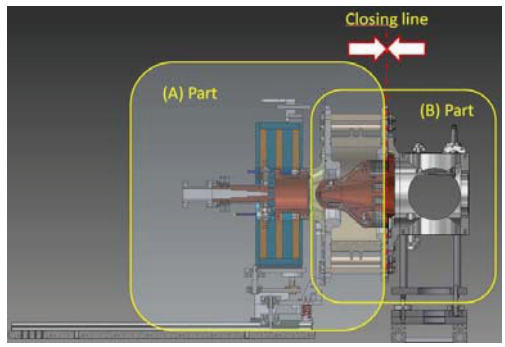

Figure 1: A view of the ESS source body totally assembled on its supports in the high voltage platform.

Part A

The part A consists of:

1) Insulating Al_2O_3 column
2) Oxygen Free High Conductivity Cu plasma chamber (OFHC)
3) RF waveguide and matching transformer
4) Magnetic system

Parts 1, 2 and 3 are rigidly joined together, and mounted on a single block supported on a “pin joint”, as discussed in a next paragraph, which naturally allows several degrees of freedom.

On the other hand, the magnetic system is independent and it has an adjustable position.

The pin joint and the magnetic system can mutually translate along the beam line until the desired position.

Part B

The part B is composed by a stainless steel chamber, which is the first component of the LEBT, rigidly joined to the extraction electrode assembly. The first component is mechanically decoupled from the rest of the LEBT through

ISBN 978-3-95450-186-1

a bellow and it plays an important role in the alignment strategy.

The chamber is very compact (237 mm along the axis line) and it houses the outputs of the cooling channels for the electrodes, the feedthrough for the repeller electrode, the pumping groups and all the vacuum diagnostic components. This is the first element that need to be aligned because it includes the calibrated holes for the coupling with the part A (movable part) equipped with two conical pins.

Figure 2 represents the source body separated in its two parts.

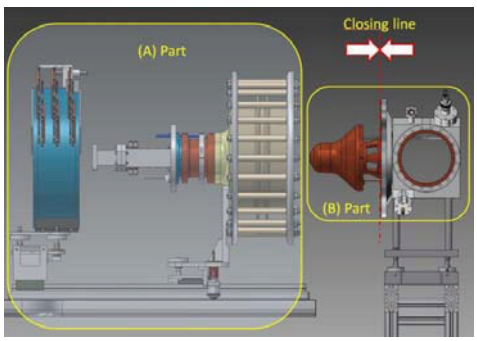

Figure 2: A view of the ESS source body with the extraction column open and with the magnetic system separated parts.

Extraction Electrodes Assembly

The cooled extraction electrodes assembly has been conceived as two separate blocks:

1) the three electrodes assembly which includes the first grounded electrode, the repeller electrode (with insulators) and the second grounded electrode (Fig. 3);
2) the support for part 1, water cooled and connected in the geometric and dimensional tolerance to the LEBT first element (Fig. 3).

The extraction electrodes unit has been designed for a really fast maintenance, preserving at the same time an optimal alignment even after replacing them with a new or regenerated set. This point can be reached thanks to a self-centering conical coupling with a cooled part fixed to the "first component" (see Fig. 1 and 2).

The latter is a key aspect of the mechanical design; in fact it gives the possibility of a quick change of the setup, by using different diameters or shapes of the electrodes; the cooling is obtained by conduction, taking advantage of the large contact surface that comes out from the tapering (see Fig. 3).

This represents a novelty for the ion source mechanical development.

Pin Joint

The “pin joint” has the important role of supporting the Al_2O_3 insulator, the plasma chamber, the RF waveguide; these components are rigidly mounted together in the geometric and dimensional tolerance, keeping them in the concentricity range of $\pm$ 0.1 mm.

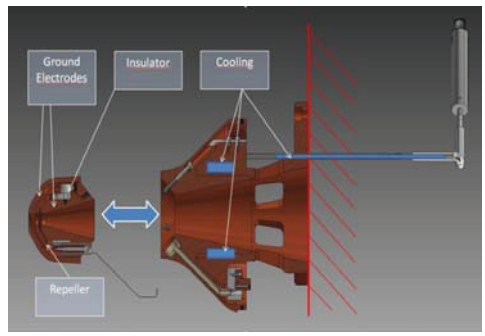

Figure 3: ESS extraction electrode unit: view of the main components and their assembling procedure.

Moreover, this pin joint allows to support and adjust the parts above mentioned in order to fit the position of the LEBT first element.

Looking at Fig. 4, it is evident that the entire load has several degrees of freedom that permit to find an easy and precise coupling with the fixed part "B" (see Fig. 1 and 2).

This suspension gives a very useful flexibility during both the commissioning phase and all the maintenance operations.

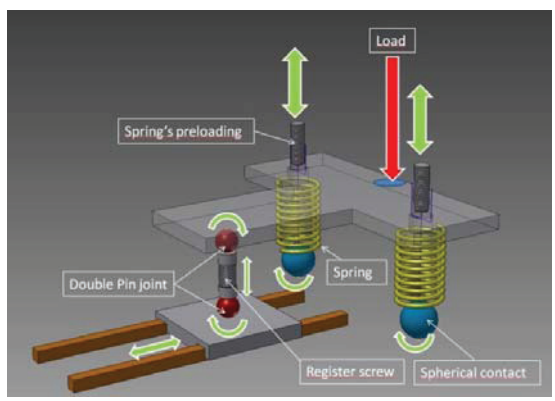

Figure 4: Suspension based on double pin joint.

In this type of suspension, the spherical double joint is really important because it compensates any eventual misalignments; it is equipped with an additional adjusting screw to fit to the theoretical position of the center of the "first component" already previously aligned. The entire system, also including springs and their adjusting screws, makes the system highly versatile and flexible, within 1 mm of diameter.

Moreover, this flexibility allows an automatic alignment because the system can ben rigidly connected to the fixed and already aligned extraction electrodes part.

Microwave Injection System

Even the water-cooled microwave waveguide provides the opportunity to easily change the step geometry to test

ISBN 978-3-95450-186-1

different profiles with the aim to optimize the coupling in operating conditions.

In Figure 5 it is possible to observe that the multisection matching transformer can be easily replaced and it can assume different geometries, the removable internal parts may be realized by using conventional machine tools without using the more complex electric discharge machining.

The matching transformer has also grooves for gaskets used for the cooling system and the vacuum tightness.

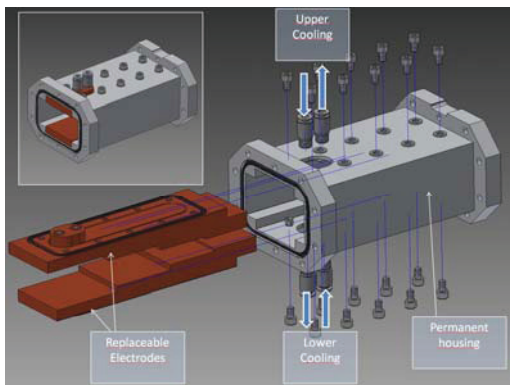

Figure 5: Matching transformer.

MECHANICAL ASSEMBLY AND FIRST TESTS

Figure 6 shows a picture of the two parts A and B before the final assembly of the full source including the insulating column and the extraction electrodes, the plasma chamber, the magnetic and extraction systems and the LEBT components. The first LEBT element houses the water and electrical connections for the repeller electrode, two turbo molecular pumps and vacuum gauges, gas inlet and the residual gas analyser.

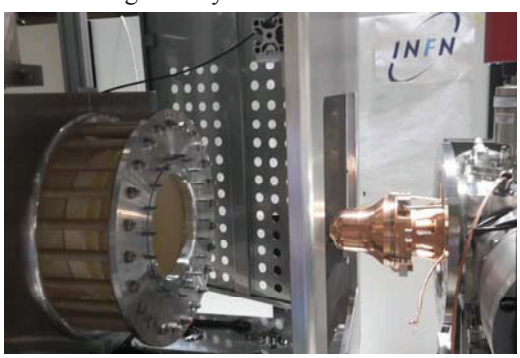

Figure 6: Proton source before the finally assembly of the extraction column.

The insulation of the extraction column and the vacuum tightness has been successfully verified through HV and vacuum leak tests. The extraction column (at operating pressure of $6 \cdot 10^{-6}$ mbar) has been tested without any sparks at 90 kV for 1h e 30' at 19.2 ◦C e 38% humidity level. These promising results have been obtained well above the nominal operating voltage of 75 kV.

The whole assembly has been successfully vacuum tested and the base pressure reached from a cold start is $5 \cdot 10^{-7}$ mbar in 12 hours.

CONCLUSION

The assembly of all mechanical parts was satisfactory for all points of view. The source is now fully assembled and the main disassembly procedure described in this work can be done without removing cooling pipes, sensors cables and all 500A cables of the magnetic system. This result allowed to satisfy the expected time for venting, replacing and mounting that are parts of the requirements specified in the contract signed between ESS and INFN. The plasma chamber conditioning is on-going and the test under thermal load is also satisfactory.

ACKNOWLEDGMENT

The authors would like to acknowledge the support of INFN technical staff and of the mechanical workshop for the valuable work done in the design and manufacturing of several items of the ESS setup.

REFERENCES

[1] L. Neri, L. Celona, S. Gammino, D. Mascali, G. Castro, G. Torrisi, B. Cheymol, A. Ponton, A. Galatà, G. Patti, A. Gozzo, L. Lega, and G. Ciavola. Rev. Sci. Instrum. 85, 02A723 (2014).

ISBN 978-3-95450-186-1

VERSATILE HIGH POWER MICROWAVE SYSTEM FOR FREQUENCY TUNING OF THE CAPRICE ECRIS

F. Maimone, M. Endermann, R. Lang, J. Mäder, P. T. Patchakui, P. Spädtke, K. Tinschert
GSI, Planckstraße 1, 64291 Darmstadt, Germany

Abstract

In the last years it was demonstrated that the variation of the microwave frequency generating the plasma inside ECR Ion Sources (ECRISs) allows to enhance the extracted current of highly charged ions both for gaseous and for metallic elements. In order to use this technique for the performance improvement of the CAPRICE-type ECRIS installed at the High Charge State Injector (HLI) of GSI, the microwave system has been modified. The new arrangement includes - besides the existing Klystron high power amplifier (HPA; max. 2 kW at 14.5 GHz) - two combined Traveling Wave Tube Amplifiers (TWTA) covering a bandwidth of 12.75-14.5 GHz, providing 750 W output power each, which are driven by one or two synthesizer tuners. The new system has been used during the routine operation of the ECRIS for production of different ion beams to be injected into the RFQ of the HLI. A detailed description of the main components of the new microwave system is presented, and the achieved characteristics of ion beam production using different microwave frequencies are described.

INTRODUCTION

In the last years several experiments using the technique of frequency tuning were carried out at the ECR injector test setup (EIS) of GSI in order to investigate the influence on the performance of the CAPRICE-type ECR Ion Source (ECRIS) in terms of enhanced ion currents of high charge states [1, 2]. It was demonstrated that this technique allows increasing the ion current extracted from an ECRIS both for gaseous and for metallic elements [3]. In order to use this technique for the routine operation of the ECRIS installed at the high charge state injector (HLI) of GSI, the microwave injection system has been modified.

At the HLI a CAPRICE-type ECRIS is installed for the production of high charge state ion beams at mass/charge ratios of up to 8.5 for the UNILAC at GSI. The ECRIS is designed to operate at 14.5 GHz and so far Klystron amplifiers were used to send the high power microwaves to the ECRIS to generate the plasma. In order to use the frequency tuning technique at the HLI an upgraded system using wideband high power Traveling Wave Tube Amplifiers (TWTA) has been conceived and assembled. The new arrangement includes two combined TWTAs covering a bandwidth of 12.75-14.5 GHz, providing up to 1500 W CW power, which are driven by one or two synthesizer tuners. In the following the upgraded system and the achieved results of ion beam production using different microwave frequencies are described.

HLI UPGRADED MICROWAVE SYSTEM DESCRIPTION

The schematic view of the upgraded microwave system installed at HLI is shown in Fig. 1. A sweeping signal generator provides the microwave signal to be amplified by two TWTAs. Each of them provides up to 750 W in the frequency range 12.75-14.5 GHz. When the required power is higher than 750 W, the power of the two amplifiers is summed up through a WR62 waveguide power combiner. Otherwise the power combiner is replaced by a high power wideband isolator. Both, the isolator and the power combiner have an insertion loss lower than 0.5 dB and an isolation higher than 20 dB. This last feature allows running the frequency sweeping without interruption of forward power due to the high reflected power amplifier protection in case of power mismatch. For the maximum summed power at the high power combiner, a phase shifter is used and the phase shift is adjusted whenever the frequency is tuned to an optimized condition. The system is integrated into the existing waveguide system with a WR62 mechanical switch. With this versatile setup the microwave input can be switched from the waveguide line connected to the klystron HPA to the one where the upgraded system including the TWTAs is installed. A high power load able to handle up to a CW power of 3000 W is connected to the switch and is used to test and perform measurements of the amplifiers.

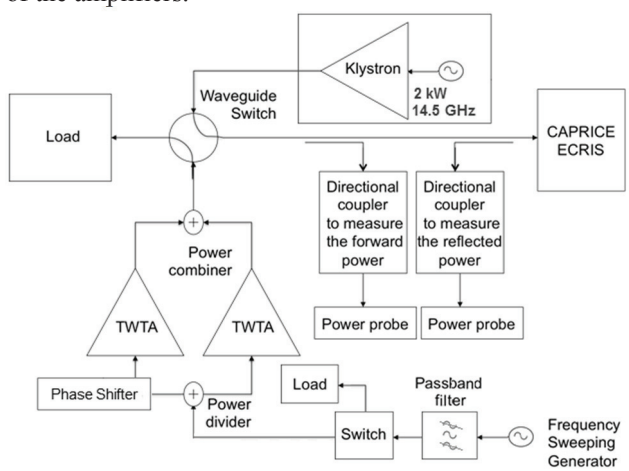

Figure 1: Block diagram describing the main components of the microwave injection system at HLI.

Two directional couplers are inserted between the switch and the ion source. Microwave power probes are connected to each directional coupler to measure the forward power to and the reflected power from the

ISBN 978-3-95450-186-1

ECRIS. The knowledge of the reflection coefficient is beneficial to optimize the microwave coupling to the plasma, which is a fundamental condition for a good performance and stable operation of the ECRIS [1].

In order to maintain the lifetime of the vacuum tubes of the amplifiers, together with the use of a low insertion loss band-pass filter (the bandwidth is corresponding to the amplifiers) a protection system has been developed. The main components of this system are a coaxial SMA switch controlled by a logic board connected to the amplifiers. Figure 2 shows the electric scheme resuming the elements and the interconnections of the protection system of the TWTAs. Since there are two TWTAs which can operate simultaneously, the interlock signal is doubled from the interlock circuit.

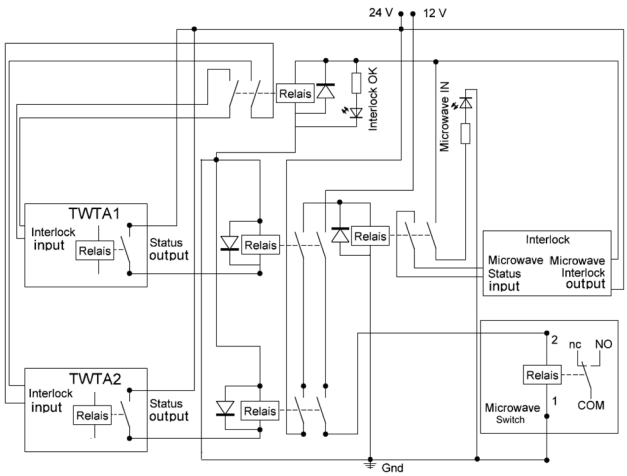

Figure 2: Circuit diagram describing protection system of the TWTAs.

The interlocking system communicates with the amplifiers and as long as they are in stand-by mode or a fault (i.e. high reflected power or for arcing events) or another interlock event (i.e. high pressure or low magnetic field) occurs, the system will toggle the microwave switch to send the input power to a load. As long as the TWTAs status is on high voltage mode, the communication system acts on the switch to provide the input power to the amplifiers.

By avoiding sending power to the tubes when they are not under high voltage status, this arrangement will prevent damages of the tubes and will save their lifetime.

EXPERIMENTAL RESULTS

Since the upgraded microwave system was installed at HLI, it was used several times for the beam production whenever the Klystron amplifier was in maintenance or repair status. In Fig. 3 the ion beams so far produced with the TWTA system are reported.

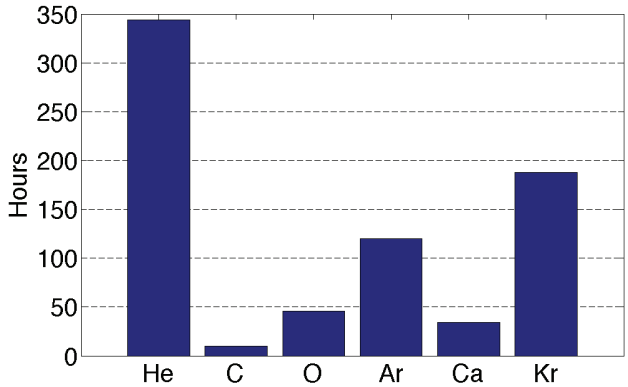

Figure 3: Ion beams produced with the upgraded system at HLI.

For the production of $^{4}He^{1+}$ and $^{16}O^{3+}$ no frequency optimization was required and the requested beam intensities of 300 μA and 180 μA were achieved with 50 W, and 300 W, respectively.

A $^{40}Ar^{9+}$ beam was requested with moderate intensity, and 80 μA were obtained with 300 W microwave power at 14.5 GHz. The spectrum of Argon is shown in Fig. 4.

If higher charge states of Argon, i.e. $^{40}Ar^{11+}$ or $^{40}Ar^{12+}$, will be required, the frequency can be optimized to get higher intensities as reported in [2].

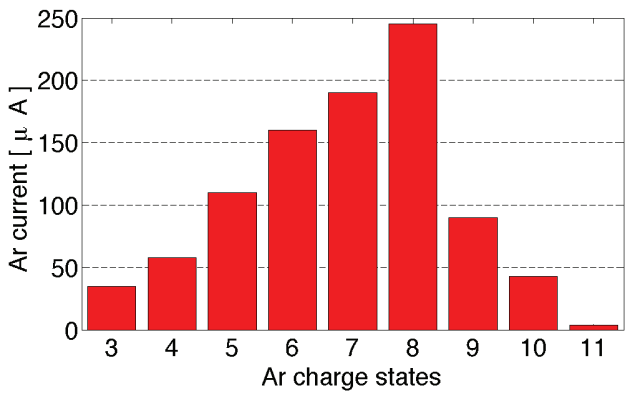

Figure 4: Charge state distribution of Argon.

During several days of ion beam production of $^{48}Ca^{10+}$, a beam intensity of around 50 μA was achieved with 600 W power by setting the synthesizer at the optimized frequency of 14.366 GHz. This setting guaranteed a stable beam with sufficient intensity in a very short setup time. However, for Calcium operation, a further extensive test campaign is required to identify the optimized frequencies for the long term beam production.

The new TWTA-based microwave system was also utilized during a $^{84}Kr^{13+}$ beam time. This operation opened the opportunity to perform further investigations on microwave frequency tuning at the CAPRICE ECRIS under operating conditions using the ^{84}Kr ion beam with its broad charge state distribution. By tuning the microwave frequency to 14.464 GHz up to 40% more current of $^{84}Kr^{13+}$ was provided with respect to the standard operating frequency of 14.500 GHz. The charge state distributions shown in Table 1 confirm that the

ISBN 978-3-95450-186-1

frequency tuning can be used to increase the intensity of higher charge states (i.e. $^{84}Kr^{n+}$ with n>11) for operating.

At the operating frequency of 14.444 GHz the highest intensity of the highest detected charge state, $^{84}Kr^{19+}$, was measured and a current gain of 16 times was obtained with respect to the normal operating frequency. This result is reported in Fig. 5 which shows the Krypton current gain for the optimized frequencies with respect to the normal operation frequency [4].

Table 1: Intensities of Krypton Charge States at Different Frequencies

KRYPTON CHARGE STATE	ION CURRENT AT 14.444 GHz [μA]	ION CURRENT AT 14.464 GHz [μA]	ION CURRENT AT 14.500 GHz [μA]
6+	7.9	8.7	9.7
7+	9	10.6	12.2
8+	13.9	17.5	21.5
9+	19.4	24.2	28.6
10+	23.5	28.1	31
11+	26.1	30.9	30.3
12+	30.6	33.3	28.7
13+	29.5	29.8	21.2
14+	27.8	25.7	15.6
15+	21.3	17.8	7.7
16+	13.7	10	3.4
17+	7.8	5	1.2
18+	4.4	3.2	0.8
19+	1.6	0.8	0.1

The upgraded microwave system was also used for an investigation concerning the production of $^{12}C^{5+}$ beams. For the generation of hydrogen like C ions all L-shell electrons plus one further K-shell electron have to be removed in the plasma by successive electron impact ionization. This requires high power operation of the ECRIS. Besides the standard configuration for $^{12}C^{2+}$ ion beam with CO_2 as working gas and O_2 as auxiliary gas, respectively, CH_4 was investigated as alternative working gas, while He was used as auxiliary gas.

With respect to the fixed frequency operation with the klystron amplifier slightly higher intensities could be obtained by careful frequency tuning of the TWTA. Using the klystron amplifier at 14.5 GHz the highest intensity of $^{12}C^{5+}$ current was around 40 μA, and by switching the microwave system to the TWTA, a $^{12}C^{5+}$ beam current around 60 μA could be achieved with the same setting of the ion source and at 13.470 GHz [5].

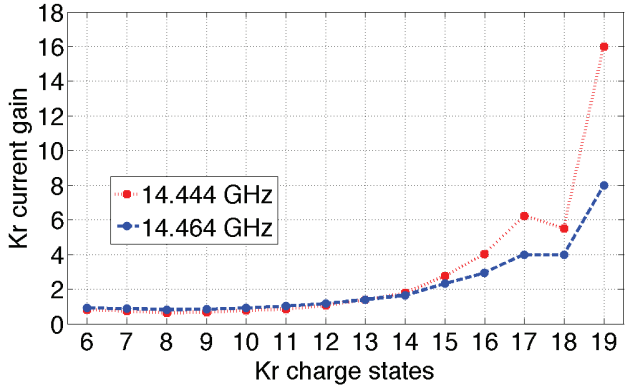

Figure 5: Kripton current gain for optimized frequencies over the normal operating frequency.

CONCLUSIONS

An upgraded microwave injection system has been commissioned for the high charge state injector HLI of the UNILAC accelerator. The new versatile system has been integrated in the existing microwave system. During the operation of the new system an enhancement of the CAPRICE performance has been observed. The capabilities of the frequency tuning for routine operation have been verified.

The arrangement allows making also use of the double frequency heating technique by connecting two separate signal generators to the amplifiers. As long as the TWTAs and the synthesizer will be integrated in the remote control system of GSI, the new system will be fully operational for standard ion beam production.

REFERENCES

[1] F. Maimone, L. Celona, R. Lang, J. Mäder, J. Roßbach, P. Spädtke, K. Tinschert, Rev. Sci. Instrum. 82,123302, (2011).
[2] F. Maimone, K. Tinschert, L. Celona, R. Lang, J. Mäder, J. Roßbach, and P. Spädtke, Rev. Sci. Instrum. 83, 02A304 (2012).
[3] K. Tinschert, R. Lang, J. Mäder, F. Maimone, J. Roßbach, Proc. of ECRIS2012, Sydney Australia, Sep 25-28, 2012.
[4] R. Hollinger et al, GSI Scientific Report 2015.
[5] K. Tinschert, R. Lang, P., J. Mäder, F. Maimone, J. Roßbach, P. Spädtke, GSI Scientific Report 2013.

ISBN 978-3-95450-186-1

MAGNETIC FIELD DESIGN FOR 2.45 GHz NEGATIVE HYDROGEN PMECRIS CHAMBER USING FEM SIMULATION

Chinmoy Mallick†, Somesh V Tewari, Rajesh Kumar, Mainak Bandyopadhyay
Institute for Plasma Research, HBNI, Gandhinagar-382428, Gujarat, India

Abstract

Negative hydrogen ECRIS plasma is confined by NdFeB permanent magnet antenna around cylindrical cavity wall. A combination of four axially magnetized ring magnets of remanence flux density of 1.17T is simulated using bounded current ampere's law technique. Gradient of radial and axial magnetic flux density is calculated to estimate the leaking out fraction of lighter ions from the plasma wall sheath region. Measured axial and radial magnetic fields are benchmarked with the simulated data. The peak values of radial magnetic field gradient between plasma sheath region and cavity outer wall surface increases from 0.1×10^7 A/m^2 to -0.2×10^7 A/m^2 respectively. Axial magnetic field gradient along inner ECR chamber wall increases from -2.1×10^7 A/m^2 to 2.5×10^7 A/m^2. ECR contour dimensions of 0.0875 T which corresponds to microwave plasma, having resonating frequency of 2.45 GHz. The thickness of resonating surface is ~1 mm and having major and minor radius of 30 mm and 28 mm respectively.

INTRODUCTION

Gaseous plasma has a significant role in the fabrication of semiconductor chips and sputtering purposes. Since last few decades, rigorous research work has been carried out in generation of capacitive and inductively coupled plasma for these industrial applications. Negative ion beam is being extensively used in accelerator and fusion related applications. Microwave ECR plasma is also important for these applications but one limitation is when large substrate are used but for smaller substrate it is an excellent technique. Low pressure (in the range of 10^{-3}mbar) microwave ECR plasma is very useful in the removal of impure material from semiconductor materials. Negative ion plasma demand is increasing in the reduction of air pollution [1]. Low pressure microwave plasma under ECR conditions can produce beams having high etching rates which are crucial for semiconductor fabrication technology [2, 3, and 4].

Permanent magnet ECR ion source (PMECRIS) will use microwave power of 500W at frequency 2.45 GHz to produce primary hydrogen plasma inside the source, which will further be optimized to generate negative hydrogen ions through surface conversion technique using cesium catalyst. Design optimization of ion source taking into account of minimum-B magnetic field configuration, microwave E-field launching and effects of Doppler

Broadening on resonance is demonstrated. This compact four ring magnet based ECR ion source is easy to handle because it eliminates all the high voltage active components as is required in solenoid based electromagnets. The only system component that crosses the high voltage boundary is the microwave waveguide section and gas feed section, all other components are at high voltage situations. PMECRIS system can produce high charge state ion beams which has wide applications ranges from nuclear physics research to the material processing [3 and 4]. Four permanent magnet based ECR ion source is designed to construct a compact linear RFQ accelerator for research purposes. Magnetic field design is important for the expected performance of the ECR ion source system.

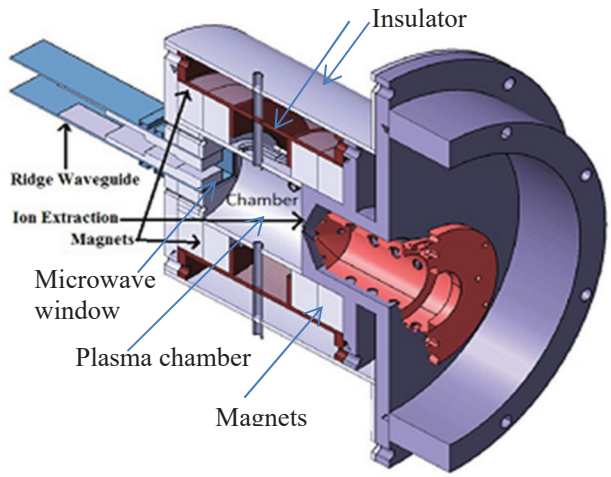

Figure 1:Section cut-view of negative PMECRIS.

MAGNETOSTATICS THEORY

This 2D axis symmetric model describes the magnetic field distribution inside the plasma chamber in cylindrical coordinates (Using azimuthal symmetry). The magnetic field of the NdFeB ring magnets is obtained from Ampere's law (bounded current) technique by the use of magnetic vector potential A which has only azimuthal non zero component [5]. The rare earth ring magnets are defined as two surface currents at inner and outer radial surfaces directed azimuthally in the opposite direction to each other. In this 2D axis-symmetric model, because of no variation of magnetic flux density at each point in the azimuthal direction, there exist only azimuthal component of the magnetic vector potential [5 and 6]. This is justified analytically as well as with simulation results. Axial component of magnetic field is given as $B_z = \frac{1}{r}\frac{\partial(rA_\theta)}{\partial r}$ and radial component of magnetic field calculated as $B_r = -\frac{\partial A_\theta}{\partial z}$

†chinmoy.mallick@ipr.res.in

ISBN 978-3-95450-186-1

Where $B = \mu_0\mu_r H + B_r$. From Ampere Law curl of magnetic field after some calculations is given as follows [5 and 7].

$$\nabla \times \left(\mu_0{}^{-1}\mu_r{}^{-1}(B - B_r)\right) = \mu_0{}^{-1}\mu_r{}^{-1}\left[\frac{A_\theta}{r^2} - \frac{\partial A_\theta}{\partial r^2} - \frac{1}{r}\frac{\partial A_\theta}{\partial r} - \frac{\partial^2 A_\theta}{\partial z^2}\right] = J_e \quad \ldots\ldots\ldots\ldots\ldots (1)$$

Here, J_e is external current density which comes from bounded surface currents on magnets, r, Θ and z are radial, azimuthal and axial coordinates respectively.

DESIGN OF PMECRIS MAGNETIC FIELD CONFIGURATION

The compact negative hydrogen PMECRIS is ring permanent magnet sources in which axial and radial mirror field is created by four axially magnetized NdFeB(Grade N48) magnets having dimensions of length=30 mm, ID=100 mm and OD=180 mm. The plasma chamber made of copper has diameter of 86 mm and length of 109 mm is inserted into the magnetic structure.

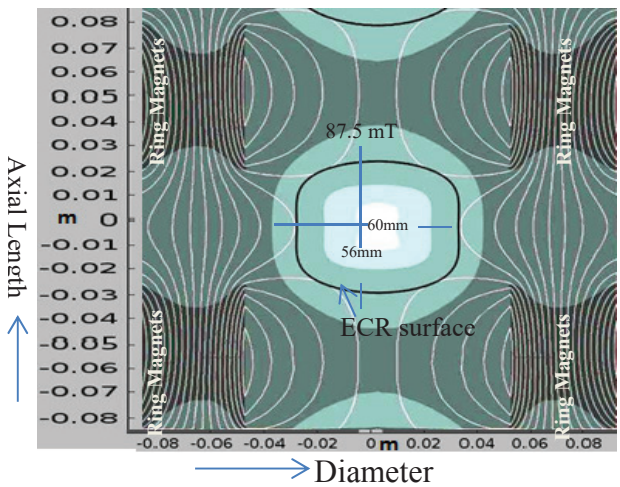

Figure 2: Magnetic field configuration of the inside chamber (Mirror 2D taken of computational domain) showing the ECR resonance surface (87.5mT, thick black line). ECR zone is around that dark line. White line represents the magnetic vector potential (A_{phi}) lines (Web/m). Surface intensities inside the source indicate the normalized magnetic flux density in the log scale ($\log_{10}(B_{normalized})$).

The plasma chamber is closed by a plasma electrode having an extraction hole of 5 mm and other side is closed by a boron nitride plate with a thickness of 6.4 mm. The volume of ECR zone is very small as compared to the whole volume of the plasma chamber. The ECR contour has major diameter 60 mm and minor diameter 56 mm and a thickness approximately 1 mm. In FEM model, infinite element domain is chosen as boundary condition as if magnetic vector potential lines are perfectly absorbed at the boundary and there is no interference of external magnetic field other than the magnet sources. Inherent remanence flux density of each magnet 1.17T is oriented axially (z-direction) during modeling.

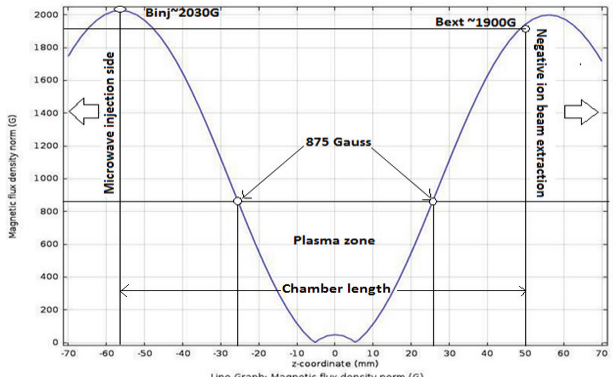

Figure 3: Axial B-field (simulation).

Because of the azimuthal symmetry B_z , B_r and A_θ are decoupled from the A_z , A_r , B_θ components and more interestingly the latter three terms are zero. The magnetic field at the microwave injection side is 0.203 T which is more than two times than the resonant magnetic field so that microwave travel downstream the magnetic field intensity and deposit power exactly on the ECR surface (0.0875 T).The magnetic field at the plasma electrode aperture is 0.19 T which should be somehow less (near to 0.0875 T) for the efficient ion extraction. But to get maximum microwave E-field at 2.4 GHz frequency in the plasma chamber, length of chamber limits plasma electrode position.

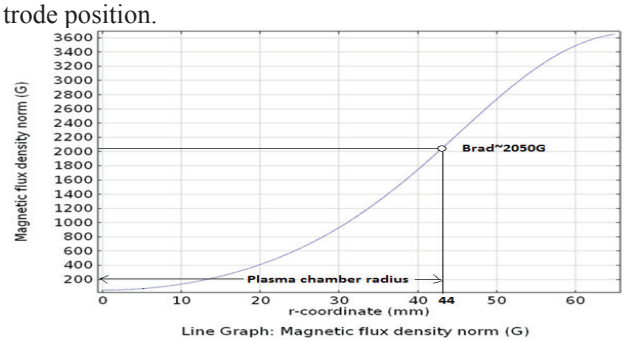

Figure 4: Radial B-field (simulation).

Radial magnetic field along the center of the plasma chamber is 0.205T(Fig.4) at the wall which is also two times more than the resonant magnetic field required to prevent the radial loss of ions.

B-Field Gradient: Resonance Characteristics

The location, flatness and dimension of the ECR zone is dependent on the magnetic field distribution inside the chamber corresponding to the frequency, microwave launching direction and also the type of mode in which the wave is propagating into the plasma. For microwave resonance heating in ECR zone electron energy distribution function exhibits a high energy peak. For which ECR zone gets shifted according to the relation [2], known as Doppler shift.

ISBN 978-3-95450-186-1

$\omega_{rf} \pm k(z)v_{res\|} = \omega_{ECR}(z) = \frac{B_{ECR}\, e}{m_e}$ .....(2)

$v_{res}\|$ is parallel component of electron velocity in resonance position, $k(z)$ relative dielectric constant. So here for 3 eV peak electron temperature v_{res} ~10^6 m/s[2 and 5] and k=0.514 cm^{-1}.As a result of Doppler shift, the corresponding resonant magnetic field gets higher or lowered. At the new position, electrons see different magnetic field gradient values parallel to magnetic field lines. Hence the resonance size is expanded by ±1.4 mm.and the resonant frequency is shifted by 2.5168-2.38 GHz.(0.0899-0.0715 T). For higher shifted resonant magnetic field (0.0899 T), gradient becomes lower(1.4 ×10^7 A/m^2) considering the following relation[2].

$\omega_{ce}(z') = \omega(1 + \alpha z')$, Where $z' = z - z_{res}$ and $\alpha = \frac{1}{\omega_{ce}}(\frac{\partial \omega_{ce}}{\partial z'})_{res}$.

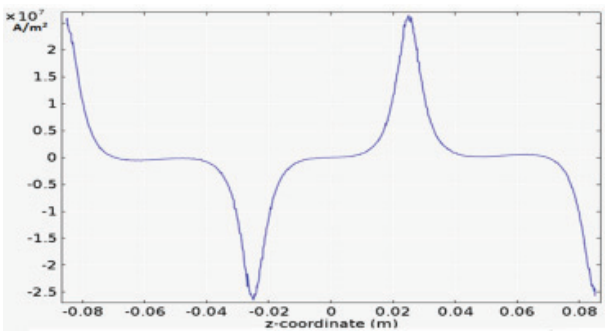

Figure 5: Magnetic Field Gradient parallel to microwave field line variations along z-axis of plasma chamber.

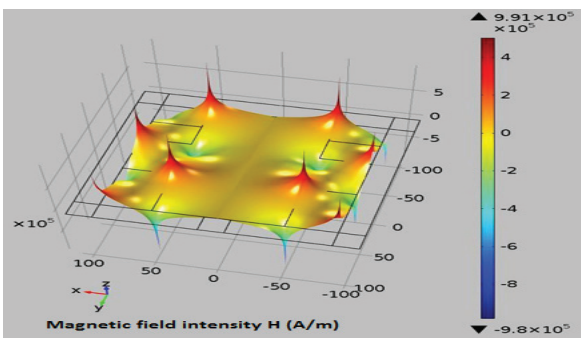

Figure 6: Total magnetic field gradient plot of the whole computational domain. (Mirror 2D taken of the half section of computational domain).

EXPERIMENTAL VALIDATION FOR B-FIELD

Two NdFeB based permanent ring magnets are used to generate the required magnetic field to create ECR zone inside the source volume. Each ring magnet is having OD=100 mm, ID=50 mm and thickness=10 mm. The axial spacing between two magnets was varied to get required field of 0.0875 Tesla. Field optimization has been carried out through simulation using the *B_ M Field* code. The required magnetic field profile is obtained at a spacing of 25mm between the two magnets. The axial and radial magnetic field is measured with the help of a Gauss meter (Lakeshore, Model 410), as shown in Fig. 7.

Axial simulated B-field (Fig. 8) is compared with the measured data. In B_*M Field* code simulation the magnetization value of each ring magnet was taken 8850. Axial and radial simulation results (Fig. 9) were taken always along the centre of the two magnets. Radially measured and simulated data were also taken along the centre of both the magnets.

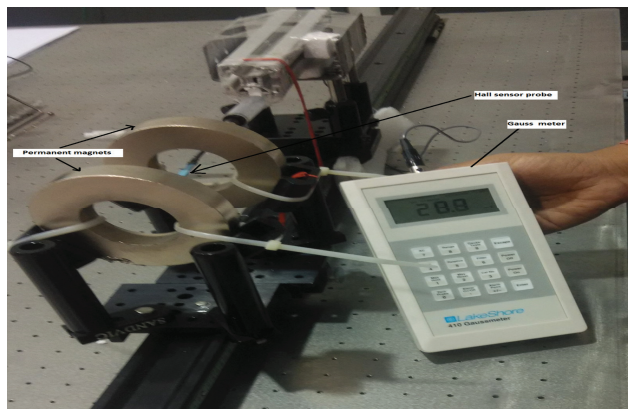

Figure 7: Experimental set up.

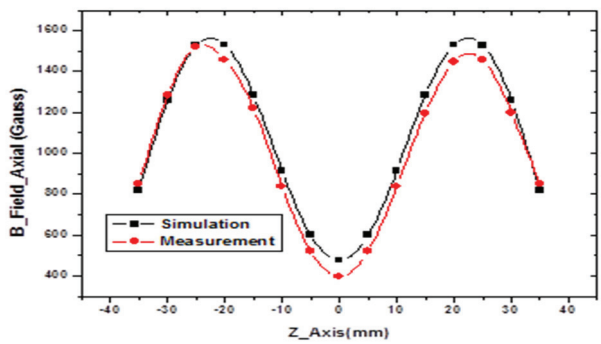

Figure 8: Axial measured and simulated B-field.

Finally, measured axial and radial field was benchmarked with B_ *M Field* code [6] and FEM model [7, 8 and 9] for NdFeB, GradeN48 four ring magnets simulation.

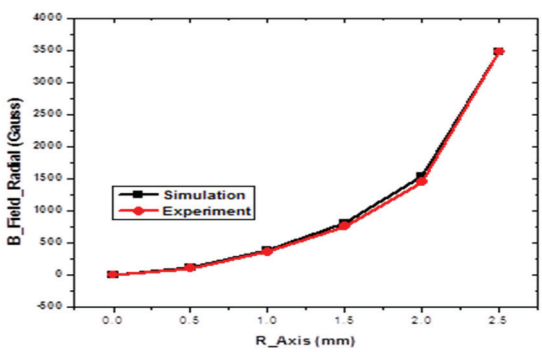

Figure 9: Radial measured and simulated B-field.

ISBN 978-3-95450-186-1

SUMMARY

Doppler shifted resonant zone depends on direction of electron's velocity w.r.t microwave propagation direction. Doppler effect broadens the resonance zone into region s of higher or lower magnetic field. Doppler broadening aids the power absorption capacity of plasma electron. Absorbed power depends on electric field, ECR surface area and more importantly on magnetic field gradient. Lower the gradient-higher the power absorbed by plasma. For shifted resonant field (0.0899 T) power absorption capability increased by 1.4 times.

REFERENCES

[1] Jianxiong Dai, Zhongjun Zhao, Gaoling Liang and Yixiang Duan, 'A Novel Microwave-Induced Plasma Ionization Source for Ion Mobility Spectrometry', Scientific Reports 44051(2017).
[2] M.A. Liberman , Allan J. Lichtenberg" Principles of plasma discharges and materials processing" ,John Wiley and Sons, New York,1994.
[3] Nasser, "Fundamentals of Gaseous Ionization and Plasma Electronics", John Wiley & Sons, 1971.
[4] Chapman, "Glow Discharge Processes", John Wiley & Sons, 1980.
[5] G J M Hagelaar , K Makasheva, L Garrigues, J-P Boeuf," J.Phys D:Appl. Phys. 42(194019),(2009).
[6] Donald Arnush., Phys. Plasmas 7, (3042) (2000).
[7] www.comsol.com .
[8] M. El Bojaddaini, H. Chatei, M. Atounti, M. El-Haim,I. Driouch and M. El Hammouti, Adv. Studies Theor. Phys.,7(22), 1071 – 1085 (2013).
[9] J.Y.Park, H. S. Lee, M. S. Won, B. S. Lee, J. P. Kim, J. H. Yoon, J. S. Bae ,J. K. Bang, J.K.Ahn., Journal of the Korean Physical Society 55(2), 409-414 (2009).

ISBN 978-3-95450-186-1

RECENT BEAM DYNAMICS STUDIES FOR THE SCL DEMO OF RISP

Hyunchang Jin*, Ji-Ho Jang, In-Seok Hong
Institute for Basic Science, Yuseong-daero 1689-gil, Yuseong-gu, Daejeon, Korea

Abstract

The rare isotope science project (RISP) has been developed the RAON accelerator to accelerate heavy ion and rare isotope beams for the various kinds of science programs. In the RAON accelerator, the beams created by a superconducting electron cyclotron resonance ion source (ECR-IS) will be accelerated by the radio-frequency quadrupole (RFQ) after passing through the low energy beam transport (LEBT) section. These accelerated beams will pass the medium energy beam transport (MEBT) section for the beam matching and be re-accelerated by the superconducting linac (SCL) for the higher beam energy. Prior to the construction of the RAON accelerator, the performance of each component of LEBT, RFQ, MEBT and SCL should be examined for the efficient mass production. Accordingly, we have been constructing the test facility, which is named SCL demo, since 2015. First beam test with an oxygen beam will be carried out at the end of 2016 and the next test with a bismuth beam will be performed in 2017. In this paper, we will present the beam dynamics studies with the recent lattice design of the SCL demo and describe the simulations results with the bismuth and oxygen beams.

INTRODUCTION

The RAON (Rare Isotope Accelerator of Newness) accelerator [1] being developed by the rare isotope science project (RISP) is designed to accelerate the stable ion beams from proton to uranium and transport these beams to the targets of experimental halls for a wide range of science programs with various rare isotopes created from the targets. An 28 GHz electron cyclotron resonance ion source (ECR-IS) creates various kinds of stable ion beams, and these beams are transported and accelerated through the low energy beam transport (LEBT) section [2], the radio-frequency quadrupole (RFQ), the medium energy beam transport (MEBT) section, and the superconducting linac (SCL) section. Here, the SCL section is divided into low and high energy sections: the low energy SCL (SCL1 and SCL3) section consists of two kinds of cavities, quarter-wave resonator (QWR) and half-wave resonator (HWR), depending on the beam velocity, and the high energy SCL (SCL2) section does two kinds of single-spoke cavities (SSR). The beam accelerated by the SCL1 or SCL3 are transported to the low energy experimental hall or can be accelerated again by the SCL2 after passing through the charge stripping section [3] for the high energy experiments. The schematic view of the RAON accelerator is shown in Fig. 1.

The lattice design of the RISP test facility started since 2014 as an injector test facility which did not include the SCL section [4], and then the lattice of this test facility was newly re-designed with the superconducting cavity and named SCL demo in 2015 [5]. Now the lattice of the SCL demo becomes more simplified and optimized within the limited space to test the front-end section of the RAON accelerator, and each equipment is being installed and tested individually for the beam commissioning at the end of 2016. Figure 2 shows the recent layout of the SCL demo, and one QWR cavity is located at the end of the SCL demo.

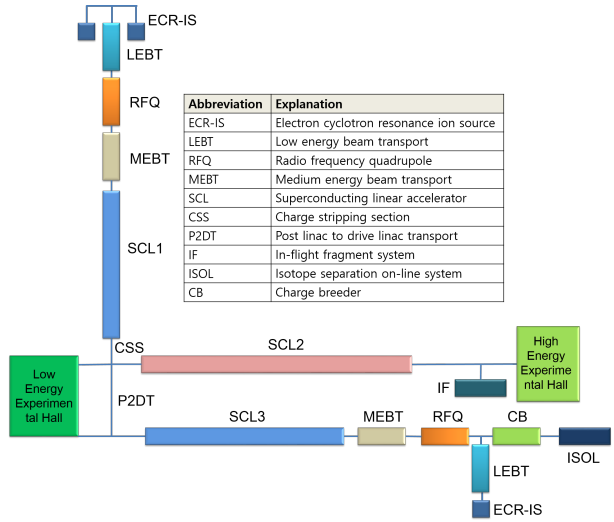

Abbreviation	Explanation
ECR-IS	Electron cyclotron resonance ion source
LEBT	Low energy beam transport
RFQ	Radio frequency quadrupole
MEBT	Medium energy beam transport
SCL	Superconducting linear accelerator
CSS	Charge stripping section
P2DT	Post linac to drive linac transport
IF	In-flight fragment system
ISOL	Isotope separation on-line system
CB	Charge breeder

Figure 1: Schematic view of the RAON accelerator.

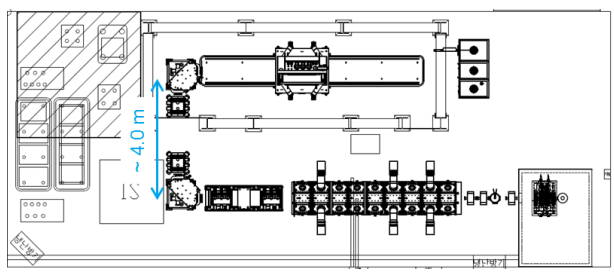

Figure 2: Layout of the SCLdemo.

In this paper, we will present the recent lattice design of the SCL demo and describe the results of the beam optics calculation and the particle tracking simulations with the bismuth beam and the oxygen beam. In the following beam dynamics simulations, the ELEGANT [6] and TRACK [7] codes were used.

DESIGN POINTS

For designing of the SCL demo lattice, several design points are considered as listed in Table 1. The bismuth and oxygen beams are selected as reference beams at the SCL

* hcjin@ibs.re.kr

ISBN 978-3-95450-186-1

demo. As satisfying these conditions, the lattice of the SCL demo is designed and optimized.

Table 1: Conditions for Lattice Design

Number	Conditions
1	Beam test from ECR-IS to SCL
2	Reference beams: ^{209}Bi, ^{16}O
3	Limited space: ~ 19m × 8m
4	Achromatic condition at bending section
5	Collimation for charge selection
6	Space for diagnostic equipments

SIMULATION RESULTS

Bismuth Beam

As reference beams in the SCL demo, the bismuth and oxygen beams are selected. The bismuth beam parameters used in the simulations are listed in Table 2. To match the (charge/mass) ratio of the bismuth beam to the reference uranium beam of the RAON accelerator, $^{238}U^{33.5+}$, a charge-state 29+ is selected.

Table 2: Bismuth Beam Information

Parameter	Value
Beam	$^{209}Bi^{29+}$
Energy	10 [keV/u]
Norm. rms. emittance	0.12 [μm]
Beam size	0.5 [cm]
Number of macro-particles	10,000
Beam distribution	4D water-bag

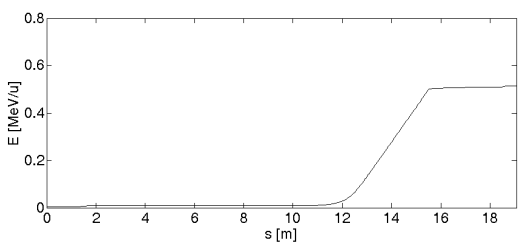

Figure 3: The energy of the bismuth beam along the SCL demo.

Figure 3 shows the beam energy along the SCL demo. After the RFQ, the beam energy becomes about 500 MeV/u which is the design value at the RAON accelerator, and then it reaches to about 515 MeV/u after the QWR cavity.

The transverse root-mean-square (rms.) beam size along the SCL demo is shown in Fig. 4. The beam size is kept much smaller than the beam pipe radii at each section (6.0 cm at the LEBT, 2.5 cm at the MEBT, 2.0 cm at the SCL) to keep the beam in stable along the SCL demo. Figure 5 shows the normalized transverse rms. emittance. Initial

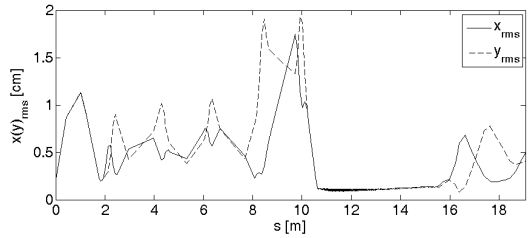

Figure 4: The transverse rms. beam size of the bismuth beam along the SCL demo.

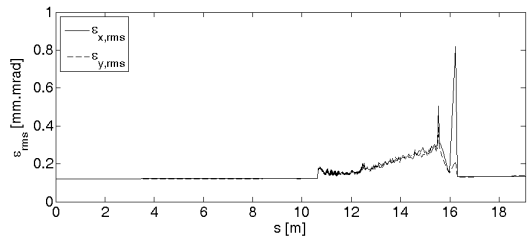

Figure 5: The normalized transverse rms. emittance of the bismuth beam along the SCL demo.

transverse rms. emittance is 0.12 [μm], and it is kept until the end of the QWR cavity. The increase of the transverse emittance at the RFQ is caused by the some particles which are not sufficiently accelerated, and those particles are clearly removed at the MEBT section.

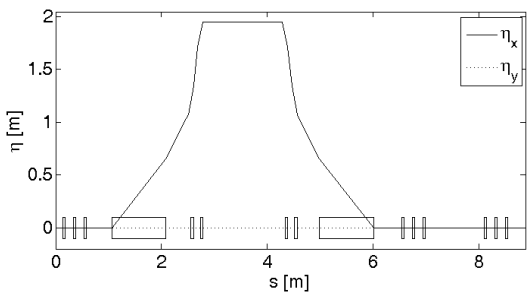

Figure 6: The dispersion function at the LEBT section of the SCL demo.

For the charge selection at the bending section of the SCL demo, the dispersion function is calculated to separate clearly the different charge-state bismuth beams as shown in Fig. 6. The achromatic condition is also satisfied. To select one-charge-state beam clearly among the multi-charge-state beams, two collimators are required. First collimator is located after first bending magnet and collimates the unwanted charge-state beams roughly. Also, second collimator is located at the middle of the bending section and selects a wanting charge-state beam. Figure 7 shows the horizontal beam distributions at the positions of first and second collimators, and we can select one-charge-state bismuth beam, $^{209}Bi^{29+}$, among multi-charge-state beams.

ISBN 978-3-95450-186-1

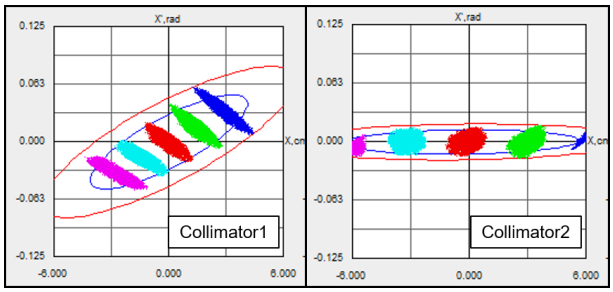

Figure 7: The horizontal distribution of bismuth beam, 27+ ~ 31+, at the collimators in the bending section.

Oxygen Beam

The oxygen beam, $^{16}O^{7+}$, will be tested at the SCL demo at the end of 2016, therefore this beam is also simulated for the successful beam commissioning. Except the (mass/charge) of the beam, the other parameters used in the simulations are same with the bismuth beam as shown in Table 2.

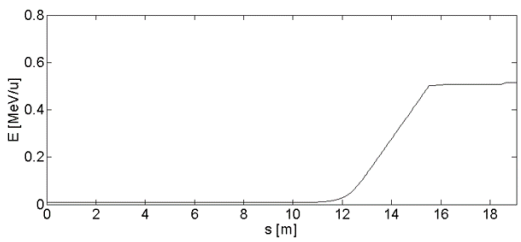

Figure 8: The energy of the oxygen beam along the SCL demo.

Figure 8 shows the oxygen beam energy along the SCL demo. The RF power of the RFQ is scaled to satisfy the target beam energy at the end of the RFQ, 500 MeV/u, and thus the beam energy becomes about 516 MeV/u at the end of the SCL demo.

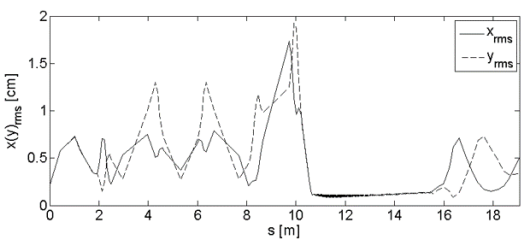

Figure 9: The transverse rms. beam size of the oxygen beam along the SCL demo.

The transverse rms. beam size of the oxygen beam is shown in Fig. 9. The beam size is much smaller than the beam pipe radii at each section like the bismuth beam. Figure 10 shows the normalized transverse rms. emittance along the SCL demo. The initial transverse rms. emittance is also kept until the end of the SCL demo.

Unlike the bismuth beam, the deviation of the (charge/mass) ratio of the multi-charge-state oxygen beams is larger. For that reason, one-charge-state oxygen beam, $^{16}O^{7+}$, only survives after first bending magnet, and thus the collimator is not necessary for the charge selection of the oxygen beam.

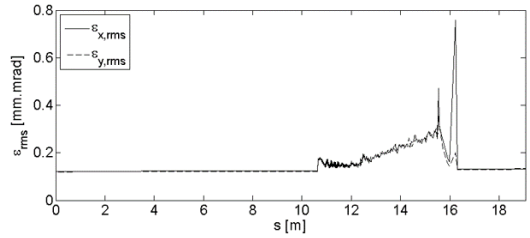

Figure 10: The normalized transverse rms. emittance of the oxygen beam along the SCL demo.

SUMMARY

We had presented the recent lattice design of the SCL demo and described the simulation results with the bismuth and oxygen beams. The first beam commissioning is scheduled at the end of 2016, and thus the beam dynamics simulations were carried out to prepare it. Transverse rms. beam sizes of both beams were kept much smaller than the beam pipe radii at each section, and the required matching conditions were also satisfied. In addition, the calculation for the charge selection at the bending section was successfully performed. These researches will be continued before the beam commissioning as accepting the changes of the equipments.

ACKNOWLEDGMENTS

This work was supported by the Rare Isotope Science Project of Institute for Basic Science funded by Ministry of Science, ICT and Future Planning and National Research Foundation of Korea (2013M7A1A1075764).

REFERENCES

[1] D. Jeon *et al.*, "Design of the RAON accelerator systems", *Journal of the Korean Physical Society* 65.7 (2014).

[2] H. Jin, J. Jang, "Beam dynamics at the main LEBT of RAON accelerator", *Journal of the Korean Physical Society* 67.8 (2015).

[3] H. Jin *et al.*, "Achromatic and isochronous lattice design of P2DT bending section in RAON accelerator", *Nuclear Instruments and Methods in Physics Research* A 795 (2015).

[4] RM. Bodenstein *et al.*, "Design status of the RISP test facility LEBT", in *Proc. of IPAC'14*, Dresden, Germany, TUPRO055 (2014).

[5] H. Jin *et al.*, "Start-to-end simulation for the RISP test facility", *Nuclear Instruments and Methods in Physics Research* A 799 (2015).

[6] M. Boland, "Elegant: A flexible SDDS-compliant code for accelerator simulation", Argonne National Lab., IL, USA (2000).

[7] VN. Aseev *et al.*, "TRACK: The new beam dynamics code", in *Proc. of PA'C05*, Knoxville, Tenessee, USA (2005).

ISBN 978-3-95450-186-1

FOUR-DIMENSIONAL TRANSVERSE PHASE-SPACE DISTRIBUTION MEASURED BY A PEPPER-POT EMITTANCE METER

T. Nagatomo*, V. Tzoganis[1], M. Kase, O. Kamigaito, and T. Nakagawa,
RIKEN Nishina Center, Wako, Japan
[1]Kockkroft Institute, Warrington, United Kingdom

Abstract

In this study, we observed variations in the four-dimensional transverse emittance, ϵ_{4D}, of argon beams having several charge states with respect to the amount of residual gas in the low-energy beam transport (LEBT) of a 18-GHz superconducting electron cyclotron resonance ion source (18-GHz SC-ECRIS) at RIKEN, as measured by a pepper-pot emittance meter. Natural krypton gas was injected into the LEBT to control the amount of residual gases. Collisions between the beams and the residual gaseous atoms generated electrons that were expected to cancel out the positive electric potential inside the beam, or, in other words, achieve space-charge compensation. Reductions in the emittance of $^{40}Ar^{8+}$, $^{9+}$ and $^{11+}$ beams were observed by the injection of krypton gas into the LEBT. The reductions in projected emittances such as ϵ_x and ϵ_y were different for each charge state; however, the reduction in ϵ_{4D} of these charge states were similar to each other. The degree of reduction in ϵ_{4D} was about 50% when the residual gas pressure of the LEBT was changed from 1.9×10^{-7} mbar to 1.3×10^{-5} mbar. The mechanism of the reduction in emittance is not clarified in this paper because there is a possibility that the reduction was caused by the change in electron cyclotron resonance plasma, which is induced by the penetration of the injected krypton gas into the plasma chamber.

INTRODUCTION

Recently, the importance of the emittance of four-dimensional (4-D) phase space, ϵ_{4D}, has received much attention, and it has been discussed with the aim of improving beam quality [1–3]. ϵ_{4D} is an invariant under linear 4-D symplectic transformation, such as beam transport using linear optical components including solenoid and skew-quadrupole lenses. On the other hand, the two-dimensional (2-D) emittances, ϵ_x and ϵ_y, are not invariant when a solenoid lens or a skew-quadruple lens are used because both types of lenses can couple these quantities. If there is no acceleration/deceleration, no beam loss, and no non-linear effects, ϵ_{4D} should remain constant during beam transport. Thus, measurement of ϵ_{4D} provides quantitative and essential information that can be used to improve beam quality in the real sense of the term.

As is well known, attention must be paid to any aberrations in the beam optics components and the space-charge effect when the ion-beam current is high, as these degrade the beam quality through the enhancement of the beam emittance. The possibility of space-charge compensation by a deliberate injection of a neutral gas into the LEBT was discussed by Toivanen et al. [4]. Based on that report, we have developed an on-line pepper-pot emittance meter that is suitable for obtaining ϵ_{4D} [5], and studied how the ϵ_{4D} of multiply charged argon beams evolves with respect to the amount of neutral krypton gas injected in the LEBT. We report some preliminary, but interesting, trends in these emittances.

EXPERIMENTAL SETUP

Pepper-pot Emittance Meter

The pepper-pot emittance meter consists of a thin metallic plate (50 μm thick) with a 25 × 25-pinhole array and an imaging screen to detect transverse deviation of the beamlets. The diameter of each pinhole is 0.1 mm, and the pitch of the pinholes is 2.0 mm in both the horizontal and vertical directions. An imaging screen (P46) was placed behind a microchannel plate (MCP) that was employed to convert the heavy ions into electrons in order to prolong the lifetime of the screen. The pinhole plate was translated along the beam axis using a stepper motor to find the optimum distance between the pinhole plate and the MCP. The distance could be varied from 23 mm to 56 mm, and was calibrated with respect to the number of electric pulses driving the stepper motor. The beamlet image reflected by a mirror angled at 45 degrees was detected through a viewport by a CMOS camera. An electrical beam chopper placed in front of the emittance meter was synchronized with the CMOS camera to stop the beam when images were not being acquired. For more details of the mechanical design, please refer to [5].

We also developed image-capture and emittance-analysis programs using LabVIEW (National Instruments Co.). We programmed a process that automatically identifies the correspondence between each of the beam spots and the pinhole through which the beamlet passed. It is possible to obtain the particle distribution in 4-D transverse phase-space from this analysis. Therefore, from the distribution in the 4-D phase space, (x, x', y, y'), six types of two-dimensional projections can be generated, i.e. x-x', y-y', x-y, x'-y', x-y' and y-x' projections. The developed program displays all the projected distributions simultaneously, as shown in Fig. 1, immediately after the beamlet image is captured. In addition, the ϵ_{4D}, the transverse beam matrix C and the two-dimensional emittances, which are described in the following section, are also calculated and displayed. All of these processes, including the image-capture process, can be com-

* email nagatomo@riken.jp

ISBN 978-3-95450-186-1

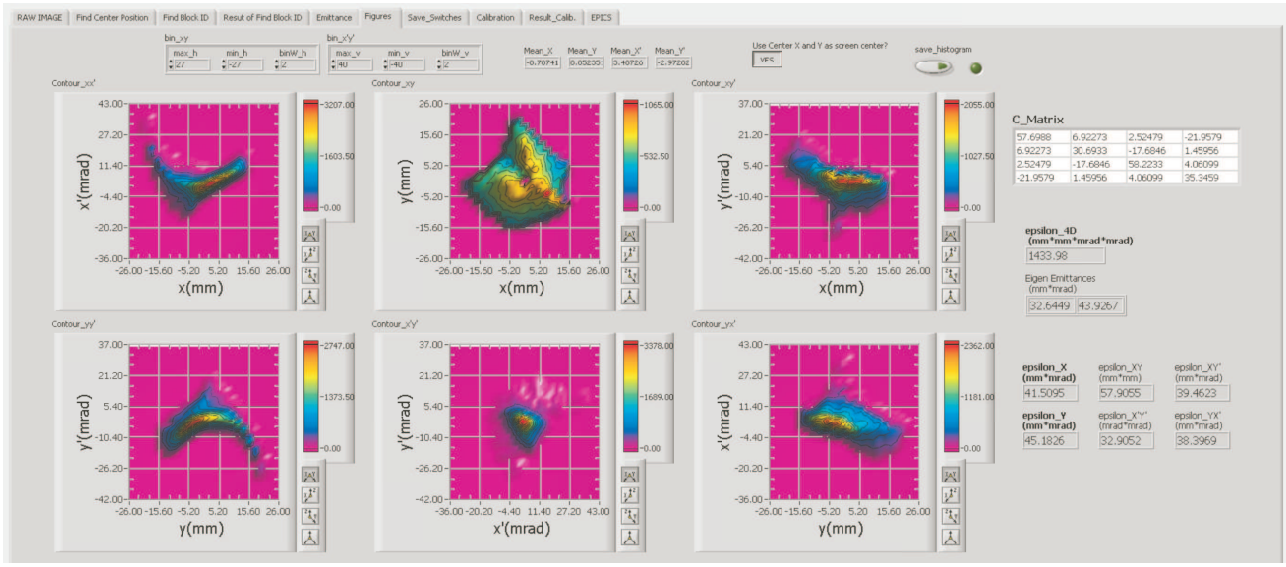

Figure 1: Typical screenshot of the developed on-line emittance monitor. This program displays six types of 2-D distributions together with the quantities of ϵ_{4D}, the 2-D emittances and the transverse beam matrix C.

pleted within one second, which is quick enough to enable this system to be used as an on-line emittance monitor.

RIKEN 18-GHz SC-ECR Ion Source and LEBT

The layout of the RIKEN 18-GHz Superconducting ECR Ion Source (18-GHz SC-ECRIS) together with the LEBT is shown in Fig. 2. The LEBT consists of an analyzing magnet, an electric beam chopper, a diagnostics chamber, a solenoid lens, and a pepper-pot emittance meter. An Einzel lens and two xy steering magnets are included in the setup; however, they were turned off during the measurements. A Faraday cup in a diagnostics chamber was used to measure the beam current with a set of horizontal and vertical slits (XY slits) fully opened as ±20 mm. The emittance meter described in the previous section was installed behind the solenoid lens.

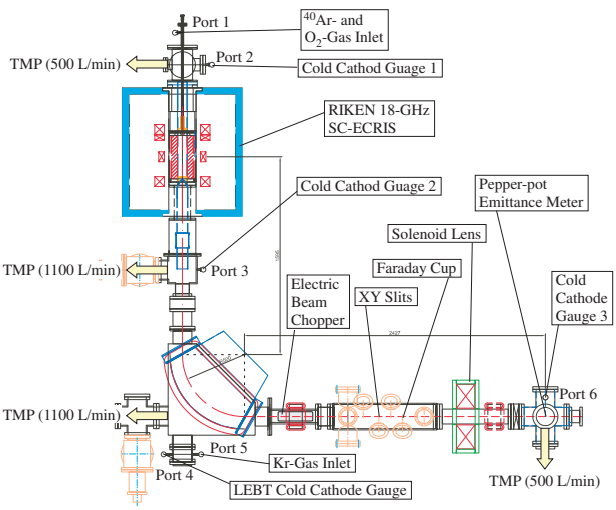

Figure 2: Schematic layout of the 18-GHz SC-ECRIS and LEBT.

The multiply charged argon beams were generated by the 18-GHz SC-ECRIS. A mixture of argon and oxygen gases was fed into a plasma chamber through Port 1 in Fig. 2, and the oxygen gas was employed as a support gas to optimize the argon beam by the gas mixing method. The flow rate of each gas was controlled using a precision variable leak valve. The ion-extraction voltage was set to 10.0 kV for all charge states. The parameters of the ECRIS, such as the microwave power of 680 W, the argon and oxygen flow rates, the mirror field, the position of a biased disk inside the plasma chamber, the voltage applied on the biased disk were adjusted in order to optimize the current of the $^{40}Ar^{11+}$ beam at the Faraday cap after the analyzing magnet, prior to the injection of krypton gas mentioned below. The ion-source parameters were kept constant during all measurements.

Natural krypton gas was injected through a precision variable leak valve attached to Port 5 in Fig. 2, which is located behind the analyzing magnet. Krypton was selected because the first ionization is slightly smaller than that of argon and nitrogen atoms, and is comparable to that of oxygen. The residual gas pressure of the LEBT was monitored using a cold cathode gauge (CCG) attached to Port 4, which is adjacent to Port 5 used for gas injection. In addition, CCGs 1–3 were attached to Ports 2, 3 and 6, respectively, to monitor the diffusion of the injected krypton gas. The LEBT residual gas pressure was controlled from 1.9×10^{-7} mbar to 1.3×10^{-5} mbar using the leak rate of the krypton gas.

We chose the $^{40}Ar^{8+,9+}$ and $^{11+}$ beams for the emittance measurements, and the magnetic fields of the analyzer magnet and the solenoid lens were tuned to the $B\rho$ for each beam. By measuring the beam current and 4-D phase-space distribution using the Faraday cup and the pepper-pot emittance meter, respectively, we studied how beam intensity and not only the projected emittances ϵ_x and ϵ_y, but also ϵ_{4D} varied along with the LEBT gas pressure.

ISBN 978-3-95450-186-1

RESULTS AND DISCUSSIONS

Definition of Emittance

As described in Refs. [1–3], the 4-D (rms) emittance ϵ_{4D} is determined by the transverse beam matrix C as:

$$\epsilon_{4D} = \sqrt{detC}, \tag{1}$$

where

$$C = \begin{pmatrix} \langle xx \rangle & \langle xx' \rangle & \langle xy \rangle & \langle xy' \rangle \\ \langle x'x \rangle & \langle x'x' \rangle & \langle x'y \rangle & \langle x'y' \rangle \\ \langle yx \rangle & \langle yx' \rangle & \langle yy \rangle & \langle yy' \rangle \\ \langle y'x \rangle & \langle y'x' \rangle & \langle y'y \rangle & \langle y'y' \rangle \end{pmatrix}. \tag{2}$$

The (rms) emittance projected into a 2-D phase space is determined as the square root of the determinant of a submatrix of C, for example:

$$\epsilon_x = \sqrt{detC_{xx'}} \text{ with } C_{xx'} = \begin{pmatrix} \langle xx \rangle & \langle xx' \rangle \\ \langle x'x \rangle & \langle x'x' \rangle \end{pmatrix}. \tag{3}$$

In the 2-D phase space, the area surrounded by the rms ellipse, S, is described as the product of its emittance value and π, for example, $S_x = \pi \times \epsilon_x$.

The following expression between ϵ_x, ϵ_y and ϵ_{4D} is established:

$$\epsilon_{4D} \leq \epsilon_x \epsilon_y, \tag{4}$$

with equality if there is no inter-plane correlation.

Changes in Beam Current and Mmittance

The beam currents, the 2-D emittances, ϵ_x and ϵ_y, and the 4-D emittance ϵ_{4D} are obtained with respect to the residual gas pressure of LEBT, as shown in Fig. 3. The $^{40}Ar^{9+}$- and $^{40}Ar^{11+}$-beam currents begin to decrease at an LEBT pressure of $\sim 2.5 \times 10^{-6}$ mbar. On the other hand, the $^{40}Ar^{8+}$-beam current begins to increase rapidly around 1.0×10^{-6} mbar. These decreases (increases) in beam current for higher (lower) charge states are caused by a charge exchange between the argon beam and neutral krypton gas occurring during beam transport, and/or the charge distribution of the ECR plasma being changed, as discussed in the following section.

Focusing on the 2-D emittance, both ϵ_x and ϵ_y gradually decrease as the LEBT gas pressure increases; however, the degree of the reduction of $^{40}Ar^{11+}$ is quite different from that of the others, as shown in Fig. 3. In Fig. 3, each emittance is normalized by a value obtained in a case where there is no krypton-gas injection, and these values are listed in the figure. Compared to the value obtained in the case where there is no gas injection, $\epsilon_x(\epsilon_y)$ of $^{40}Ar^{11+}$ decreases by 9%(14%) at 1.3×10^{-5} mbar. On the other hand, in the case of $^{40}Ar^{9+}$, ϵ_x (ϵ_y) decreases by 32% (33%), and in the $^{40}Ar^{8+}$ case, ϵ_x (ϵ_y) decreases by 26% (44%). Note that in the case of a charge state of 8+, despite the fact that the beam current increases by a factor of about two, both ϵ_x and ϵ_y decrease by about one third, and this indicates that the beam brightness of $^{40}Ar^{8+}$ is improved by the injection of krypton gas.

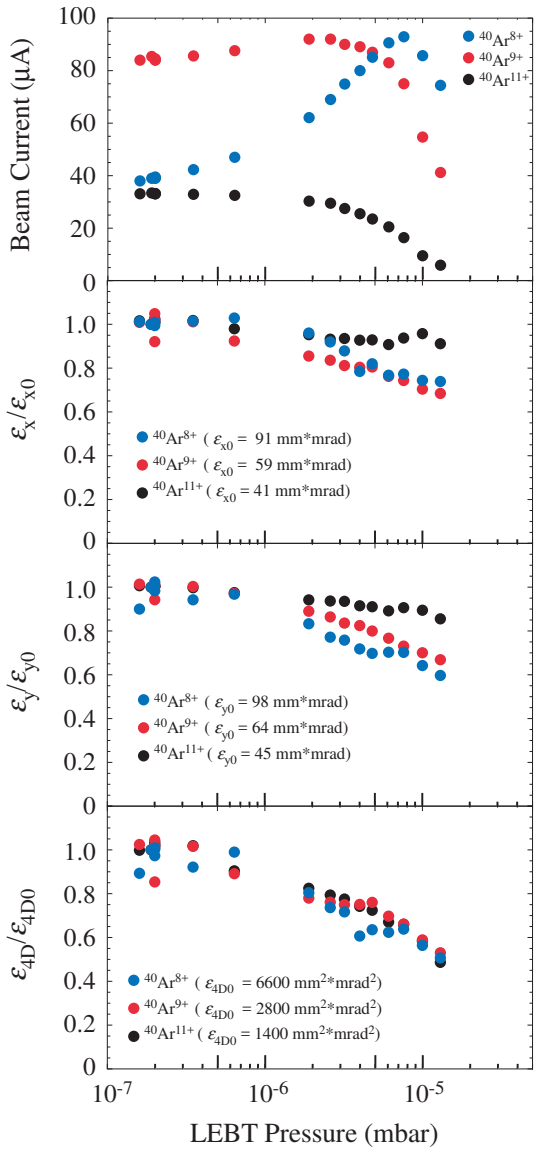

Figure 3: Obtained beam currents and rms emittances ϵ_x, ϵ_y and ϵ_{4D} of $^{40}Ar^{8+,9+}$ and $^{10+}$ with respect to the LEBT residual gas pressure. For each charge state, these emittances were normalized by the values obtained under the condition of no Kr-gas injection, ϵ_{x0}, ϵ_{y_0} and ϵ_{4D0}, respectively.

Furthermore, focusing on the 4-D emittance, the ϵ_{4D} of $^{40}Ar^{8+,9+}$ and $^{11+}$ seem to decrease similar to each other, despite the fact that its projections in the 2-D phase space, ϵ_x and ϵ_y, are different from each charge state. Compared to the value for the no-gas injection case, the amount of the reduction is about 50 % at 1.3×10^{-5} mbar for each charge state.

At present, we cannot clearly describe the mechanism that causes these emittance reductions, because we cannot distinguish the effects of the LEBT, e.g., the reduction of the beam-optics aberrations and reduction of the space-charge, from the effect caused by the changes in the electron cy-

ISBN 978-3-95450-186-1

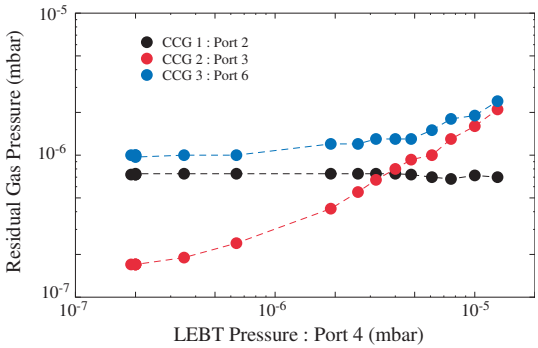

Figure 4: Residual gas pressure measured by cold cathode gauges CCGs 1–3 attached to Ports 2, 3 and 6, respectively, in Fig. 2. The residual gas pressure was expressed as a function of the LEBT residual gas pressure measured at Port 4 adjacent to the site of Kr-gas injection.

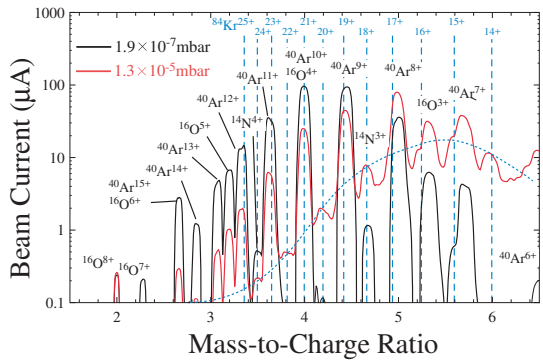

Figure 5: Charge distributions obtained at a residual LEBT gas pressure of 1.9×10^{-7} and 1.3×10^{-5} mbar, shown as black and red lines, respectively. Blue dashed lines indicate the mass-to-charge ratios of ^{84}Kr beams. The peaks of ^{84}Kr located between ^{40}Ar and ^{16}O peaks are smoothly connected, as shown using a blue dotted line to guide the eye.

clotron resonance (ECR) plasma as discussed in the following section. A complementary experiment to distinguish these effects is therefore required to clarify the emittance-reduction mechanism.

Possible Change in ECR Plasma

It is easily seen from Fig. 2 that the injected krypton gas was diffused into not only all areas of the LEBT but also the plasma chamber in which the ion beams are generated. Thus, we have to pay attention to the possibility of a change in the ECR plasma conditions caused by the penetrating krypton gas. Figure 4 shows the change in residual gas pressure measured by the CCGs installed at several points, as shown in Fig. 2. Two vacuum chambers, an upstream chamber and downstream chamber, the pressures of which are monitored by CCG1 and CCG2, respectively, sandwich the plasma chamber, and these chambers are connected to each other. The injected krypton gas penetrates from downstream into these chambers. As shown in Fig. 4, at an LEBT pressure of around 3.0×10^{-6} mbar, the vacuum levels of the upstream and downstream chambers are identical. Furthermore, at an LEBT pressure greater than 3.0×10^{-6} mbar, the magnitude relation of the vacuum levels of these chambers is reversed, which means that the amount of krypton gas that penetrated into the plasma chamber is not negligible.

Figure 5 shows the charge distributions of the extracted ion beams at an LEBT pressure of 1.9×10^{-7} mbar (no-krypton injection) and 1.3×10^{-5} mbar by a solid black line and a solid red line, respectively, together with the positions of mass-to-charge ratio of ^{84}Kr ions. We can clearly see several ^{84}Kr peaks between ^{40}Ar and/or ^{16}O peaks at 1.3×10^{-5} mbar, which vanish at 1.9×10^{-7} mbar. We can roughly estimate that the amount of Kr is about one order of magnitude smaller than that of Ar for each of the charge states of 8+, 9+ and 11+, taking the height of these clear ^{84}Kr peaks and the difference in the mass-to-charge ratio into account. However, the ECR plasma should be affected by the gas-mixing effect induced by the penetrating krypton.

In addition, note that the charge distribution shown in Fig. 5 was obtained after the analyzing magnet, which means that the obtained charge distribution includes both the effects of the change in ECR-plasma and the charge exchange effects during beam transport. Thus, further studies are required.

In a future study, we plan to inject krypton gas into Port 1 in Fig. 2, which is used for the injection of the argon and oxygen gases. After reconstruction of the charge distribution shown in Fig. 5, we will reinvestigate how the $\epsilon_{x,y}$ and ϵ_{4D} depends on the LEBT residual gas pressure or the extracted beam currents to distinguish the effects caused by the residual gas in the LEBT from the state of the ECR plasma.

REFERENCES

[1] L. Groening, "Concept for controlled transverse emittance transfer within a linac ion beam," *Phys. Rev. ST Accel. Beams*, Vol. 14, pp. 064201, Jun. 2011.

[2] C. Xiao *et al.*, "Single-knob beam line for transverse emittance partitioning," *Phys. Rev. ST Accel. Beams*, Vol. 16, pp. 044201, Apr. 2013.

[3] C. Xiao *et al.*, "Rotating system for four-dimensional transverse rms-emittance measurements," *Phys. Rev. ST Accel. Beams*, Vol. 19, pp. 072802, Jul. 2016.

[4] V. Toivanen *et al.*, "The effects of beam line pressure on the beam quality of an electron cyclotron resonance ion source," *Nucl. Instr. Meth. B*, Vol. 268, pp. 1508–1516, 2010.

[5] V. Tzoganis *et al.*, in *Proc. 7st Int. Particle Accelerator Conf. (IPAC'16)*, Busan, Koria, May 2016, paper MOPMR048, pp. 361–363.

ISBN 978-3-95450-186-1

FAST SPUTTERING MEASUREMENT STUDIES USING URANIUM WITH THE NSCL ECR ION SOURCES*

Derek Neben†, Jesse Fogleman, Daniela Leitner[1], Guillaume Machicoane, Guy Parsey, Alfonse Pham, Shane Renteria, Jeffry Stetson, Larry Tobos, and John Verboncoeur
National Superconducting Cyclotron Laboratory, Michigan State University, East Lansing, MI, USA
[1] Lawrence Berkeley National Laboratory, Berkeley, CA, USA

Abstract

Existing heavy ion facilities such as the National Superconducting Cyclotron Laboratory (NSCL) at Michigan State University rely on Electron Cyclotron Resonance (ECR) ion sources as injectors of highly charged ion beams. Long ion confinement times are necessary to produce dense populations of highly charged ions because of steadily decreasing ionization cross sections with increasing charge state. To further understand ion extraction and confinement we are using a fast sputtering technique first developed at Argonne National Laboratory [1] to introduce a small amount of uranium metal into the plasma at a well-defined time. In addition we utilize an axial x-ray apparatus [2] to characterize the hot electron plasma population via its bremsstrahlung emission.

INTRODUCTION

The Coupled Cyclotron Facility (CCF) at the NSCL [5] can accelerate ion beams up to 160 MeV/u with a corresponding beam power on target ranging from a few hundred watts to up to a kilowatt. Heavy ions from oxygen to uranium are injected from two ECR ion sources: a 14.5 GHz normal conducting Advanced Room TEMperature Ion Source (ARTEMIS) and the Superconducting Source for Ions (SuSI) operating at 18 and 24 GHz [8,9]. Typically a Mass to Charge (M/Q) range between 8 and 5 is injected for CCF operations, and some typical beams are: $^{48}Ca^{8+}$, $^{76}Ge^{12+}$, $^{238}U^{30+}$, and $^{16}O^{3+}$. The medium charge state is necessary because the final magnetic rigidity needs to be reduced approximately by half to inject properly into the K1200 after charge stripping inside the cyclotron.

We aim to probe ion confinement time by introducing a plasma contaminant and measuring its breeding and decay time. The fast sputtering technique, pioneered by ANL [1], was employed on ARTEMIS and SuSI with an uranium sample. Sputtering is a process where plasma ions are pulled onto a cathode, typically negatively charged to a few hundred to a few thousand volts, and cathode material is ejected [10]. Because ionization is an endothermic process cathode material cools the plasma and supplies cold electrons that perturb the plasma energy balance, therefore the smallest measurable contaminant currents are used. The high negative voltage applied to the sputter probe might perturb the electron losses and therefore plasma confinement [3]. Fast sputtering using an axial and radial geometry was investigated on ARTEMIS. On SuSI only the axial method was available.

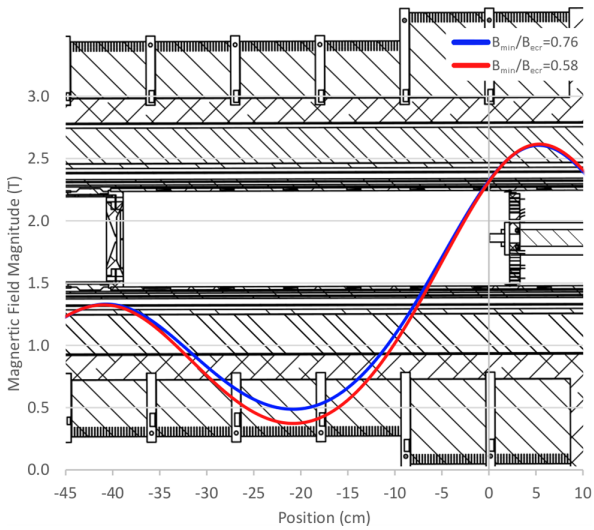

Figure 1: SuSI Magnetic field as simulated with Poisson Superfish overlaid with axial sputtering injection. The sputter probe was 55 mm forward of the peak at injection, and 10 mm forward of the bias ring.

EXPERIMENTAL SET-UP

The extracted beam current was measured on a Faraday cup after the analyzing magnet the current was sampled using an oscilloscope as a voltage across a 100 kΩ resistor. A low-pass circuit with cutoff frequency at 109 kHz was attached in series to suppress noise in the MHz range, and oscilloscope waveforms were converted to real currents in post-processing. The sputter probe voltage was pulsed using a PVX-4140 high voltage switch and a DC high voltage supply. We could operate in DC mode by driving the switch to a constant on or off state. The timing and width of the high voltage pulse was controlled by a TTL signal sent to the high voltage switch from a signal generator located at ground through a TTL-to-fiber converter. The output voltage was monitored at the high voltage switch through a port allowing us to measure the rise and fall times of voltage applied to the probe. The microwave power was measured at the forward coupler on the klystron for both ARTEMIS and SuSI.

On SuSI an axial High Purity Germanium (HPGe) x-ray detector and collimation system was used similar to [2] for observation of the high energy electron tail. The HPGe detection efficiency was measured offline using a ^{152}Eu source

* Work supported by Michigan State University and the National Science Foundation: NSF Award Number PHY-1415462
† neben@nscl.msu.edu

ISBN 978-3-95450-186-1

of known activity and allowed us to correct our spectra for efficiency. Collimation provides a maximum angle of about 10 minutes of arc as calculated using geometric optics, this angle when projected onto the extraction electrode produced a circle of 6.7 mm in diameter. Because the extraction electrode on SuSI was 8 mm we are detecting the plasma x-ray emission and backscattering from the sputter sample.

The axial sputtering apparatus on SuSI utilizes an electrically isolated probe that may be translated axially several centimeters relative to the injection baffle on axis. Our uranium slug was a cylinder 10 mm in diameter and was located 55 mm forward of the magnetic field peak at injection as shown in Fig. 1. The axial sputter probe passes through an isolated aluminum ring that can be independently tuned to preserve some bias disk function. The magnetic field at the sputter probe location on SuSI changed by 88 Gauss between the two different magnetic field configurations. Originally three different magnetic field configurations were chosen on SuSI but we found a $B_{min}/B_{ecr} = 0.9$ to be unstable. The sputter probe depth was chosen to achieve hundreds of nanoamperes of DC uranium current at modest neutral gas flows, and oxygen was used as a support gas.

On ARTEMIS the sputter depth was chosen with similar goals. However, the face of the axial uranium sample was protruding 6 mm outside of the iron plug at injection and places it at 5 mm behind the magnetic field peak as simulated using Poisson Superfish. The same axial sample was used on both sources, and we found there to be minimal surface degradation. The ARTEMIS radial uranium sample was made of a thin uranium strip 9 mm wide pressed into an aluminum holder. The face of the radial sample was protruding 2 mm into the plasma chamber inner diameter to ensure adequate DC uranium current.

AXIAL FAST SPUTTERING ON SUSI

The extracted uranium was peaked on U^{38+} shown in Fig. 3. The summed DC uranium spectra on SuSI when compared against the summed oxygen was 0.48% for the $B_{min}/B_{ecr} = 0.58$. The sputter pulse width was chosen by balancing the shortest pulse length possible while clearly being able to observe the waveform on the scope. Each current in Fig. 4 is averaged over 16 consecutive events. The averaging was necessary to produce a clear waveform. Two magnetic field configurations were probed in this measurement while keeping a constant injection pressure and microwave power. The plasma parameters used for the measurement are summarized in Table 1.

The sputter probe was driven at -500 V with a pulse width of 3.2 ms and repetition rate of 105 ms. For a $B_{min}/B_{ecr} = 0.58$ the bremsstrahlung spectra were sampled and fitted with an exponential function between 121 keV and 263 keV with a temperature of 39.7 keV and a highest measured energy of 271 keV. Similarly, with a $B_{min}/B_{ecr} = 0.76$ the temperature was 63.9 keV and a highest measured energy of 426 keV. The measurement angle is small, due to good collimation, so we were clearly able to observe in Fig. 2 the K edge,

Table 1: Key SuSI Parameters for Two Different Magnetic Field Configurations

Parameter	$B_{min}/B_{ecr} = 0.58$	$B_{min}/B_{ecr} = 0.76$
Injection Pressure	$7 * 10^{-8}$ mbar	$7 * 10^{-8}$ mbar
Extraction Pressure	$5 * 10^{-9}$ mbar	$7 * 10^{-9}$ mbar
Total Current	729 eμA	885 eμA
Microwave Power	700 W	700 W
Sputter Voltage	-500 V	-500 V
Bias Ring	-10 V	-50 V

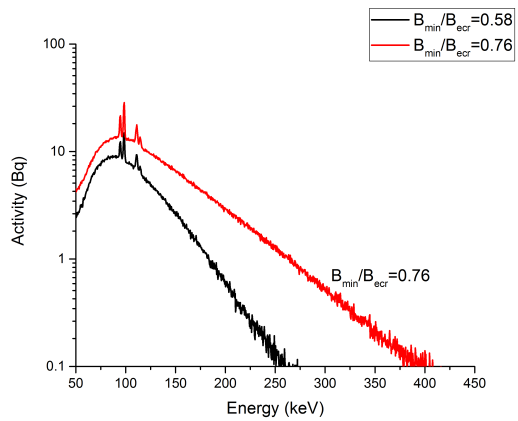

Figure 2: Axial bremsstrahlung spectra measured through the extraction electrode. With the magnetic field minimum closer to the ECR resonant field, the electron heating is more efficient for the same gas pressure and microwave power.

$K_{\beta 1}$, $K_{\alpha 1}$, and $K_{\alpha 2}$ in descending order from highest energy in both spectra with uranium. We observe a shift to higher charge states in Fig. 3 with a higher B_{min}/B_{ecr} ratio. We also observe a larger total xray emission and an emission at higher energies for a higher B_{min}/B_{ecr} ratio in Fig. 2.

As an example of the waveforms observed, U^{32+}, U^{35+}, and U^{38+} are shown in Fig. 4 for $B_{min}/B_{ecr} = 0.58$. The beam current decay after the high voltage pulse was fitted with an exponential function between 97% of the peak current and when the current returns to its prepulse value. The decay times from the fitting of U^{32+}, U^{35+}, and U^{38+} waveforms were 2.4 ms, 2.9 ms, and 2.4 ms respectively. We found that increasing the B_{min}/B_{ecr} ratio to 0.76 did not change significantly the observed waveform or decay time.

ISBN 978-3-95450-186-1

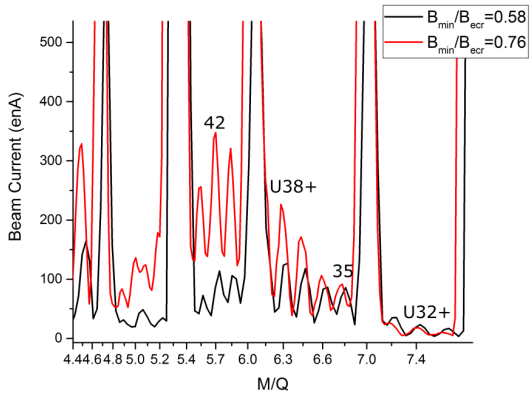

Figure 3: Beam current and mass to charge ratio on SuSI with two different magnetic fields characterized by their B_{min}/B_{ecr} ratios.

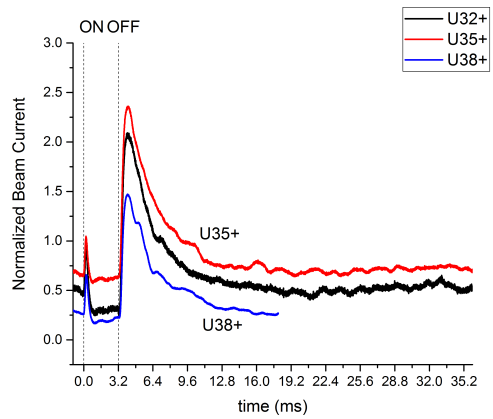

Figure 4: Beam current during and after a high voltage pulse event using an axial sputter probe on SuSI, the pulse began at time zero and was applied for 3.2 ms. The beam current has been normalized to the steady state sputtering value.

The plasma seems to collapse during the sputter pulse, but material is sputtered into the source as clearly observed in the decay after the sputter pulse. The decay time does not correlate with the confinement time or ionization time reported elsewhere and was surprisingly short for the measurements on SuSI.

The placement of the injection baffle with respect to the magnetic field in conjunction with the constant beam current DC offset at low repetition rates, may indicate the uranium was direct feeding into the plasma for this experiment. It is probable that the beam current waveforms represent the effect of high voltage modulation on the plasma. The afterglow-like waveform preceding the high voltage pulse that rose up to twice the DC beam current and the invariance in decay times across U^{32+} and U^{38+} support this idea. More studies will follow on the SuSI source to further investigate these experimental results.

Table 2: Key ARTEMIS Parameters Used for Both the Axial and Radial Sputtering Methods

Parameter	Axial Method	Radial Method
Injection Pressure	$1.3 * 10^{-7}$ mbar	$1.2 * 10^{-7}$ mbar
Extraction Pressure	$1.2 * 10^{-7}$ mbar	$1.3 * 10^{-7}$ mbar
Total Current	2.03 emA	2.09 emA
Microwave Power	200 W	200 W
Sputter Voltage	-400 V	-600 V

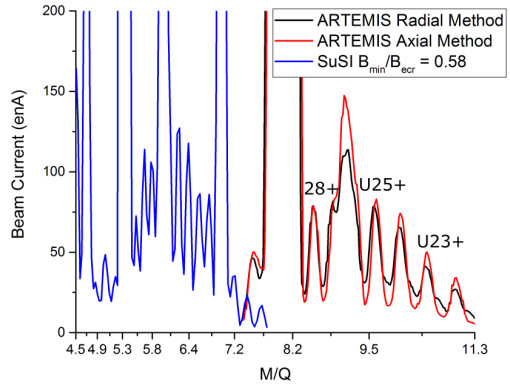

Figure 5: Charge state distribution of uranium on ARTEMIS and SuSI with an oxygen support gas.

AXIAL AND RADIAL FAST SPUTTERING ON ARTEMIS

In order to investigate the difference between radial and axial sputtering a series of measurements were done on ARTEMIS which allows for radial access as well as axial access to the plasma chamber. Similarly to SuSI, the ARTEMIS axial sputter probe was mounted directly on axis but in this case no bias disk or ring were used. The extracted uranium was peaked on U^{27+} shown in Fig. 5. The sum of measured uranium currents was 0.41% of the extracted beam when compared to the sum of oxygen and nitrogen peaks. Some important parameters are presented in Table 2 that compares axial and radial methods. For both methods nitrogen on ARTEMIS was 26% of the extracted oxygen beam was caused by a small vacuum leak. For Fig. 6 A duty cycle of 20% was used for 118.9 ms and 248.6 ms pulse widths because the use of a different signal generator was required. At lower microwave powers no averaging of the oscilloscope

ISBN 978-3-95450-186-1

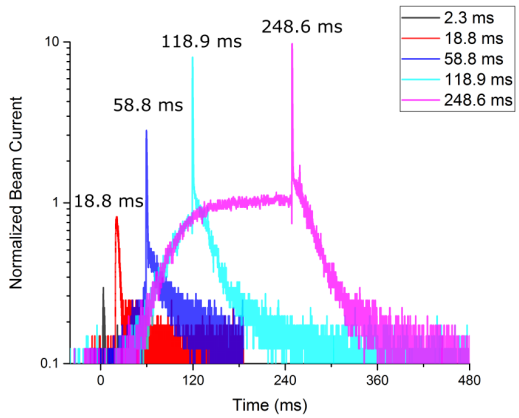

Figure 6: U^{25+} beam current for different high voltage pulse widths all starting at time zero using an axial sputter probe on ARTEMIS charged to a -400 V potential.

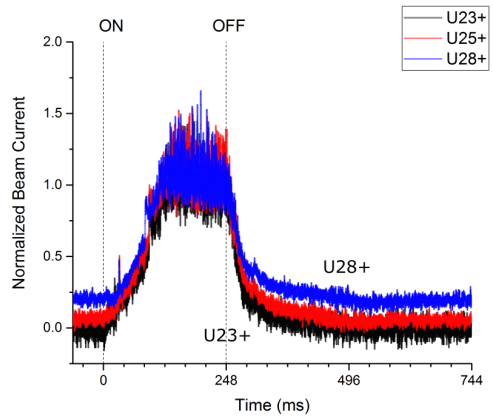

Figure 8: Beam current normalized to the steady state for three different charge states of uranium using a radial sputter probe on ARTEMIS. The pulse began at time zero and was applied for 248 ms at -600V potential.

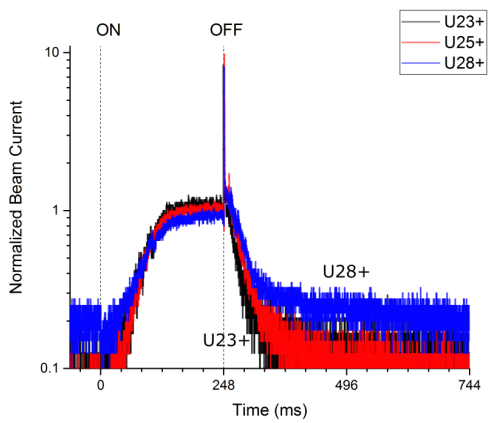

Figure 7: Beam current normalized to the DC value for three different charge states of uranium using an axial sputter probe on ARTEMIS. The pulse began at time zero and was applied for 248 ms at -400 V potential.

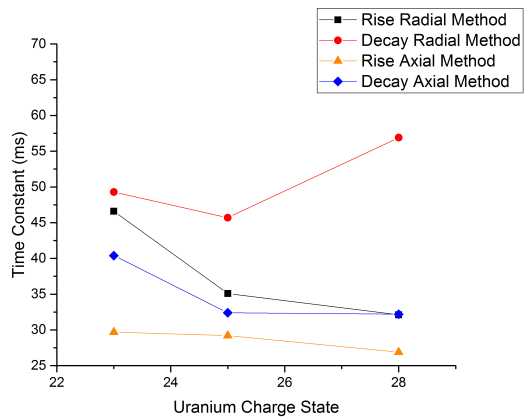

Figure 9: Time constants extracted from exponential fitting of beam current waveforms on ARTEMIS.

waveforms were necessary for all measurements conducted on ARTEMIS because the plasma was very stable.

The beam current waveforms in Figs. 7, 8 were fitted with an exponential function and the results of the fits are plotted in Fig. 9 for similar plasma conditions. For the decay fit all data was masked proceeding the 266 ms time mark, similarly for the rise time, data was masked after the 100 ms time mark. In all cases time zero marked the start of the high voltage pulse. Absolute times were used for fitting on ARTEMIS because the beam current waveform did not undershoot the prepulse value like it did on SuSI in Fig. 4. The steady state uranium currents for both axial and radial methods may be found in Fig. 5 and the charge state distributions were similar between methods. The fitting in Fig. 9 shows no clear trend with charge state and may have been caused by an unstable plasma with large variation between shots.

On ARTEMIS we found pulse widths of 2.3 ms were practically undetectable in either radial or axial geometries and led us to 248 ms pulses that produced clear waveforms including the saturation curve to the steady state current values. In order to probe the build up time of the steady state plasma containing uranium we increased the pulse lengths and found a time constant of about 120 ms to reach steady state. The time constants were bounded between 26.9 ms and 56.9 ms which is consistent with timescales observed in [1] for gold. However, in order to observe waveforms on ARTEMIS with uranium we needed to drive our high voltage pulses for in excess of 20 ms which is a factor of 40 longer than what was applied in [1].

SUMMARY AND DISCUSSION

On SuSI we observe a net shift to higher charge states when increasing the B_{min}/B_{ecr} ratio. The measured axial bremsstrahlung spectra increases in the high energy component and temperature when increasing the magnetic field B_{min}/B_{ecr} ratio while maintaining the injection and extraction magnetic field constant. We investigated axial fast sput-

ISBN 978-3-95450-186-1

tering with a uranium sample and found that the high voltage probe needed to be driven on the order of milliseconds to clearly observe a beam current response on the Faraday cup. The waveform would exceed the steady state uranium current by up to 2.5 times for a short time after the high voltage pulse ended indicating that we were driving a plasma instability. The decay times when fitted with an exponential function were on average 2.6 ms and exhibited no scaling with charge state or B_{min}/B_{ecr} ratio.

For the fast sputtering data on ARTEMIS with a radial uranium probe, we found the need to drive the high voltage for 250 ms to observe the beam current saturation at the DC value. The rise and decay across three charge states of uranium was on average 37.9 ms and 50.6 ms respectively when fit with an exponential function. In addition, using the fast axial sputtering method with a uranium sputter probe there was an afterglow-like pulse that could reach amplitudes between 5 and 10 times the steady state current for 1 ms. The afterglow amplitude increases with pulse width approximately linearly (or a weak higher order function) until saturation is reached. We are planning to investigate both methods further to gain a better understanding of the observed time constants in the plasma. We are also planning to investigate the role of plasma instabilities in effecting the sampled beam current waveforms resulting from a high voltage pulse event.

REFERENCES

[1] R. Vondrasek *et al.*, *Rev. Sci. Instrum.* **73**, 548-551 (2002).

[2] T. Ropponen *et al.*, "Bremsstrahlung and Ion Beam Current Measurements With SuSI ECR Ion Source", in *Proc. ECRIS'10*, Grenoble, France, paper WECOAK04, (2010).

[3] V. Mirinov *et al.*, *Rev. Sci. Instrum.* **73**, 623-625 (2002).

[4] G. Shirkov, *Plasma Sources Sci. Technol.* **2** 250-257 (1993).

[5] R. C. York *et al.*, "The NSCL Coupled Cyclotron Project–Overview and Status", in *Proc. Cyclotrons'98*, Caen, France, 14 - 19 Jun 1998, paper K-01, pp.687-691 (1998).

[6] G. Douysset *et al.*, *Phys. Rev. E* **61** 3015-3022 (2000).

[7] D. H. Edgell *et al.*, "Modeling of Electron Cyclotron Resonance Ion Source Plasmas", in *Proc. PAC'01*, Chicago, USA, paper WPAH026 (2001).

[8] G. Machicoane *et al.*, "First Results at 24 GHz with the Superconducting Source for Ions (SuSI)", in *Proc. ECRIS'14*, Nizhny Novgorod, paper MOOMMH03, Russia (2014).

[9] G. Machicoane *et al.*, *Rev. Sci. Instrum.* **77**, 03A322 (2006).

[10] R. Behrisch *et al.*, "Sputtering by Particle Bombardment", ISBN 987-3-540-44500-5, Springer (2006).

ISBN 978-3-95450-186-1

MEASUREMENT OF MICROWAVE FREQUENCIES EMITTED BY INSTABILITIES OF ECRIS PLASMA WITH WAVEGUIDE FILTERS AND MICROWAVE SENSITIVE DIODES*

J. Orpana†, O. Tarvainen, T. Kalvas, H. Koivisto, R. Kronholm, J. Laulainen
University of Jyväskylä, Jyväskylä, Finland
I. Izotov[1], D. Mansfeld, V. Skalyga[1]
Institute of Applied Physics, RAS, 46 Ul'yanova St., 603950, Nizhny Novgorod, Russian Federation
[1]also at Lobachevsky State University of Nizhny Novgorod (UNN), 23 Gagarina St., 603950 Nizhny Novgorod, Russian Federation

Abstract

Periodic emission of strong microwave bursts at certain frequencies is a characteristic feature of kinetic instabilities in ECRIS plasmas. Precise measurement of the temporally evolving microwave frequency spectra requires a high bandwidth oscilloscope, which can make the experiments prohibitively expensive to conduct. An alternative low-cost method to study the microwave emission in narrow frequency bands is to apply band-pass waveguide filters and microwave sensitive diodes. The microwave emission from the plasma of the JYFL 14 GHz ECRIS has been studied with both methods. The results of the experiments are compared and their interpretation is discussed. It is demonstrated that the method based on filters and diodes can provide useful information about the microwave emission spectra induced by electron cyclotron instabilities.

INTRODUCTION

The electron velocity distribution in electron cyclotron resonance ion source (ECRIS) plasmas is non-Maxwellian and strongly anisotropic i.e. $v_{e,\perp} \gg v_{e,\parallel}$ [1, 2]. Magnetized non-equlibrium plasmas are prone to cyclotron instabilities emitting microwaves due to resonant amplification of plasma waves by hot electrons [3]. The Doppler shifted emission frequency (see e.g. Ref. [4]) can be expressed as

$$\omega = \frac{\omega_{ce}}{\gamma} \pm |k_\parallel v_{e,\parallel}|, \quad (1)$$

where $\omega_{ce} = eB/m_e$ is the cold electron gyrofrequency, $\gamma = 1 + E_k/E_0$ the relativistic Lorentz factor expressed here with the electron kinetic (E_k) and rest ($E_0 = 511$ keV) energies, $k_\parallel$ the longitudinal wave number of the plasma wave and $v_{e,\parallel}$ the longitudinal (hot) electron velocity. The measurement of the emission frequency serves as an indirect plasma diagnostics method, which can be used e.g. to determine the excited wave mode [5]. Since ω is a function of magnetic field strength B and electron kinetic energy E_k, measuring the emitted microwave frequencies together with the energies of the electrons escaping the magnetic confinement as a result of the interaction with the plasma wave, would also allow determining the range of magnetic field values where the instability is triggered.

The purpose of this paper is to demonstrate the feasibility of low-cost bandpass filters and Schottky diodes for the measurement of the microwave emission frequencies related to kinetic instabilites of ECRIS plasmas.

EXPERIMENTAL SETUP

In earlier experiments two techniques have been used for the detection and diagnostics of the instability-related microwave emission of the A-ECR-U type JYFL 14 GHz ECRIS [6]:

- a Schottky diode, sensitive to frequencies of 0.01–50 GHz [7] and
- a high-bandwidth (25 GHz / 100 Gs/s) oscilloscope [5].

In both experiments the microwave emission was detected by connecting the diagnostics system to the ECRIS through an off-axis WR-75 waveguide port (cut-off frequency of 7.9 GHz) normally used for injection of microwave power at secondary frequency. Appropriate adapters and attenuators were used to transport the signal and protect the equipment. The Schottky diode alone is sufficient for measuring the duration of the microwave bursts while the oscilloscope can be used for measuring the dynamic spectrum of the microwave emission i.e. the frequencies emitted by the instabilities as illustrated in Fig. 1.

The dynamic spectrum yields all the necessary information on the microwave emission, i.e. temporal evolution of the emission frequencies and their intensities. However, the measurement technique requires purchasing or renting a high-bandwidth oscilloscope, preferably having a sampling rate ≥ 100 Gs/s to allow collecting sufficient number of data points per microwave cycle for a Fourier transform. Unfortunately, such devices are prohibitively expensive in most cases. Thus, development of an alternative method for detecting the emission frequencies on daily basis is desirable. This work benefits from the fact that the microwave emission has been shown [5] to exhibit certain characteristic features that are also visible in Fig. 1. The emission

* Work supported by the EU 7th framework programme 'Integrating Activities — Transnational Access', project number: 262010 (ENSAR), the Academy of Finland under the Finnish Centre of Excellence Programme 2012–2017 (Nuclear and Accelerator Based Physics Research at JYFL).
† joose.j.orpana@student.jyu.fi

ISBN 978-3-95450-186-1

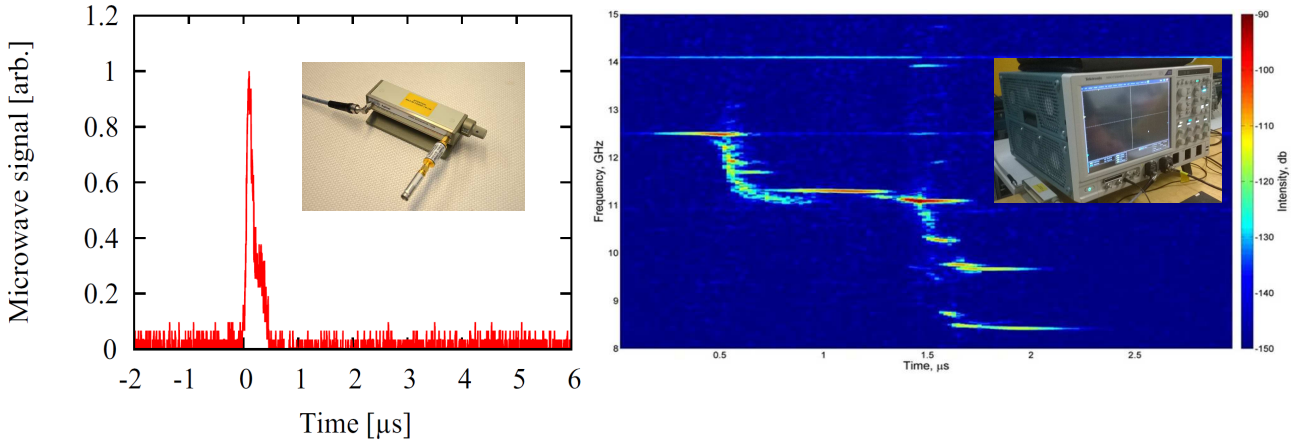

Figure 1: The voltage signal of the microwave sensitive Schottky diode (left) and dynamic spectrum obtained with the high-bandwidth oscilloscope (right).

related to an onset of the instability occurs in bursts, each of them lasting for some hundreds of nanoseconds. Moreover, the frequencies of the microwave emission within each of these intense bursts are limited to a narrow range of about 0.1 GHz and have a descending tone from 'packet-to-packet' as explained thoroughly in Ref. [5]. In the case of the JYFL 14 GHz ECRIS the dominant emission frequencies in temporal sequence are 12.5–12.6, 11.1–11.2 and 9.4–9.6 GHz. The separation of these emission bands makes it possible to study the microwave emission by applying a combination of waveguide filters.

The diagnostics setup used in this feasibility study is shown in Fig. 2. Similar to the experiments described in Refs. [5, 7] the microwave emission was studied by connecting the diagnostics setup to the WR-75 waveguide port of the JYFL 14 GHz ECRIS. A low pass filter (later referred as filter A) with a cut-off frequency of 13.2 GHz was used in order to suppress the signal of the 14 GHz primary frequency. Thus, the frequency range that can be detected, namely 7.9–13.2 GHz, is defined by the waveguide and low pass filter cut-off frequencies. Following the signal path, the subsequent component is a hybrid coupler known as a 'magic tee', which splits the microwave signal of the H-arm (port 3) equally between the two E-arms (ports 1 and 2) ideally attenuating both signals by -3 dB. The remaining H-arm (port 4) of the 'magic tee' is connected to a matched load. The signal from port 1 is adapted to a coaxial line and attenuated by a combination of attenuators by -40 dB before it is detected by a Schottky diode. The signal from port 2 first passes through a high-pass filter (B,C or D), is then adapted to a coaxial line of equal length and attenuated before being detected by another identical Schottky diode. The signals from the Schottky diodes are compared with an oscilloscope which is also connected to an X-ray detector sensitive to burst of bremsstrahlung generated by the electrons expelled from the magnetic trap by the plasma wave [7].

The described setup allows identifying the range of microwave emission frequencies through a comparison of the signals measured from ports 1 (unfiltered) and 2 (filtered). The 'resolution' of the method depends on the number of available high-pass filters. Three different high-pass filters with cut-off frequencies of 9.4 GHz (B), 10.2 GHz (C) and 11.8 GHz (D) were designed and constructed in-house for this feasibility study. Combined with the low-pass filter (A) they form a set of interchangeable band-pass filters limiting the detectable frequency ranges to 9.4–13.2 GHz (A+B), 10.2–13.2 GHz (A+C) and 11.8–13.2 GHz (A+D). The transmission curves of these filter combinations, measured with a 15 GHz network analyzer, are shown in Fig. 3. The frequency ranges were chosen to cover/exclude the afore-mentioned emission bands of the JYFL 14 GHz ECRIS plasma.

RESULTS AND DISCUSSION

An example of the diagnostics signals, measured with an oxygen plasma (400 W / $2.8{\cdot}10^{-7}$ mbar / $B_{\min}/B_{\mathrm{ECR}}$=0.77) through different filter combinations is shown in Fig. 4 together with a typical dynamic spectrum recorded earlier [5].

The following interpretations can be made:

- It can be seen from the upper right subfigure that only the first microwave 'packet' is detected by both diodes of the diagnostics setup with the filter D attached to the output of port 2. The subsequent emission signals can be seen only in port 1. This implies that the first emission burst (f_1) emits microwaves in the frequency range of 11.8 GHz $< f_1 <$ 13.2 GHz while the following bursts (f_2 and f_3) emit at frequencies $f_2, f_3 <$ 11.8 GHz.
- The lower left subfigure shows that the first two microwave 'packets' are detected by both diodes with the filter C attached to the output of port 2. This implies that 10.2 GHz $< f_2 <$ 11.8 GHz and restricts f_3 further down to $f_3 <$10.2 GHz.
- Finally, the lower right subfigure shows that all microwave 'packets' are detected by both diodes with the filter B attached to the output of port 2. Hence, 9.4 GHz $< f_3 <$ 10.2 GHz.

ISBN 978-3-95450-186-1

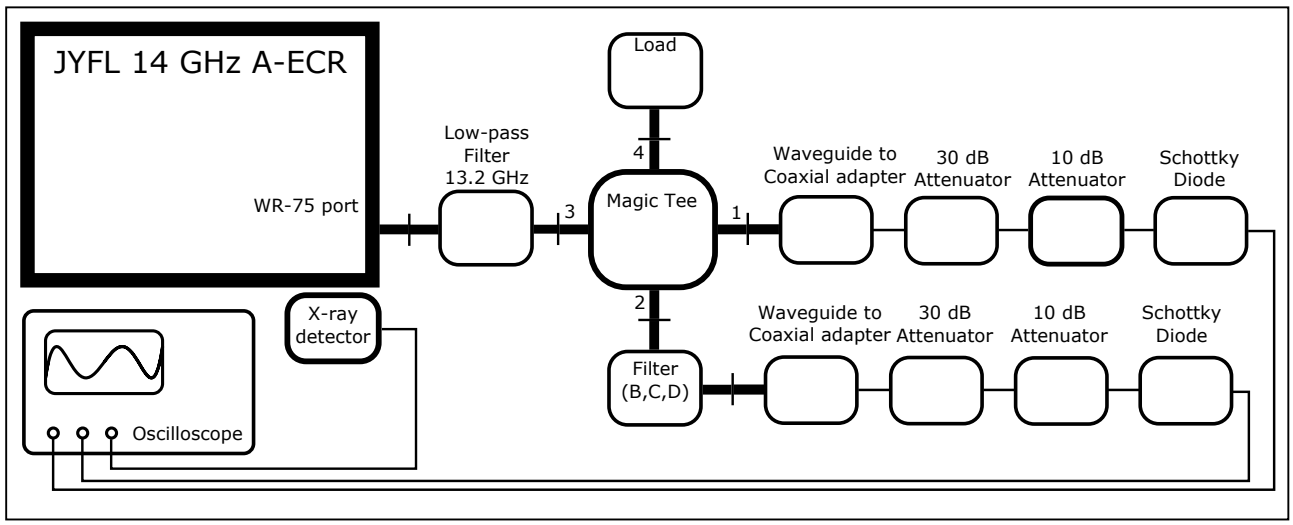

Figure 2: Schematic presentation of the diagnostics setup.

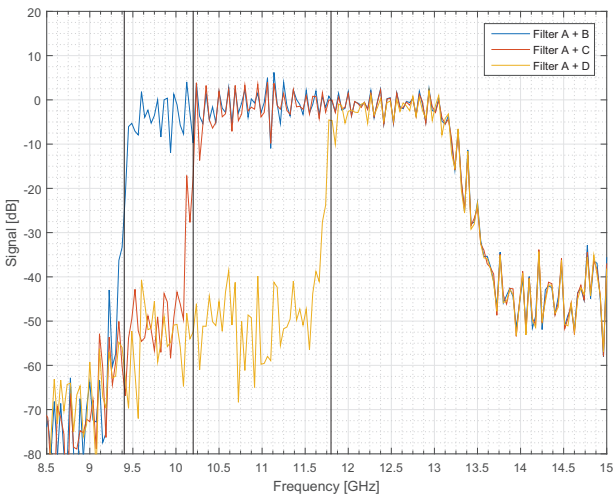

Figure 3: The transmission curves of the filter combinations.

The diagnostics signals presented in Fig. 4 are snapshots of the vast amount of data collected during the experiments. However, they are representative examples that match the microsecond-level temporal sequence and intensity of the dynamic spectrum (recorded earlier) remarkably well. It must be emphasized that the diagnostics signals are highly repeatable from pulse-to-pulse.

The summary of the results is presented in Table 1 comparing the two diagnostics methods in terms of cost and obtained microwave emission frequency information.

The content of this work can be summarized as follows: it has been demonstrated that low-cost bandpass filters and Schottky diodes can be applied for the measurement of the microwave emission frequencies related to kinetic instabilites of ECRIS plasmas. The 'frequency resolution' of the method depends on the mechanical design and number of available high-pass filters. In principle with the demonstrated design, featuring a cut-off edge of approximately -20dB/100 MHz, the resolution could be as good as ±0.1 GHz.

Table 1: Comparison of the ECRIS Plasma Microwave Emission Frequency Detection Methods

Method	100 Gs/s oscilloscope	Filters & diodes
f_1 [GHz]	12.5–12.6	11.8–13.2
f_2 [GHz]	11.1–11.2	10.2–11.8
f_2 [GHz]	9.4–9.6	9.4–10.2
Cost	Buy ~ 250 k€ Rent ~10 k€	2–3 k€

Thus, the presented method can be considered as an attractive alternative for the high-bandwidth oscilloscope especially if the research budget is scarce, which is often the case. The selection of filters should be designed individually for each ECRIS as their instability-related emission frequencies cannot be expected to be identical to the JYFL 14 GHz ECRIS.

REFERENCES

[1] C. Barue, M. Lamoreux, P. Briand, A. Girard, and G. Melin, *J. Appl. Phys.* **76**, 5, (1994).

[2] G. Douysset, H. Khodja, A. Girard, and J.P. Briand, *Phys. Rev.* E **61**, 3, (2000).

[3] S.V. Golubev and A.G. Shalashov, *Phys. Rev. Lett.* **99**, 205002, (2007).

[4] D. Mansfeld, I. Izotov, V. Skalyga, O. Tarvainen, T. Kalvas, H. Koivisto, J. Komppula, R. Kronholm, and J. Laulainen, *Plasma Phys. Contr.* F. **58**, 045019, (2016).

[5] I. Izotov, O. Tarvainen, D. Mansfeld, V. Skalyga, H. Koivisto, T. Kalvas, J. Komppula, R. Kronholm, and J. Laulainen, *Plasma Sources Sci. Technol.* **24** 045017, (2015).

[6] H. Koivisto, P. Heikkinen, V. Hänninen, A. Lassila, H. Leinonen, V. Nieminen, J. Pakarinen, K. Ranttila, J. Ärje, and E. Liukkonen, *Nucl. Instrum. Methods* B 174, (2001), p. 379.

[7] O. Tarvainen *et al.*, *Plasma Sources Sci. Technol.* **23**, (2014), 025020.

ISBN 978-3-95450-186-1

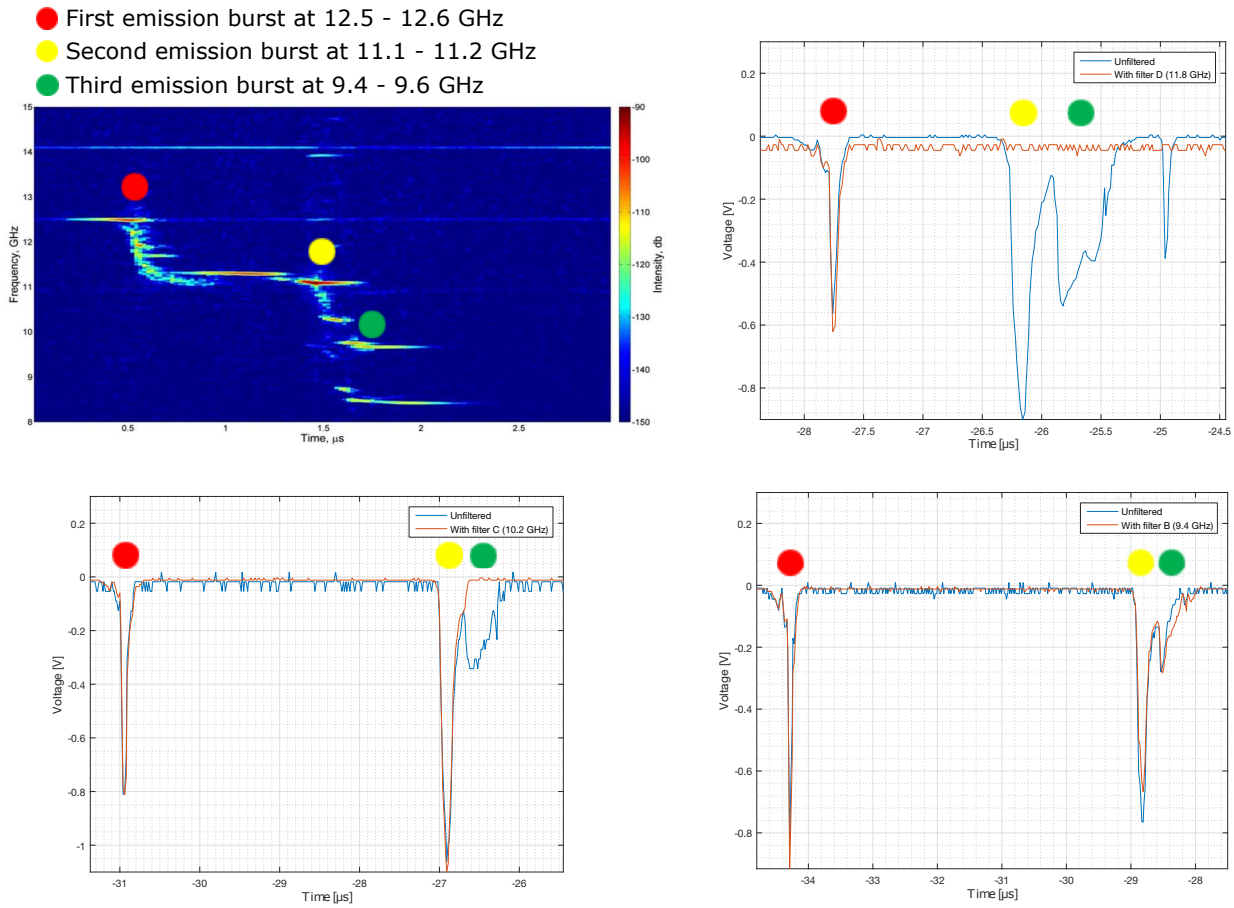

Figure 4: Typical dynamic spectrum of the microwave emission (upper left) and examples of diode signals in frequency ranges of 7.9–13.2 GHz (unfiltered) and 11.8–13.2 GHz (upper right), 7.9–13.2 GHz and 10.2–13.2 GHz (lower left) and 7.9–13.2 GHz and 9.4–13.2 GHz (lower right). Different emission 'packets' are identified in each figure with corresponding color symbols.

ISBN 978-3-95450-186-1

INVESTIGATION OF 2.45 GHz MICROWAVE RADIATED ARGON PLASMA UNDER MAGNETIZED CONDITION

Chinmoy Mallick†, Somesh V. Tewari, Rajesh Kumar, Mainak Bandyopadhyay
Institute for Plasma Research, HBNI, Gandhinagar-382428, Gujarat, India

Abstract

Permanent magnet based ECR ion source (PMECRIS) is a compact microwave discharged ECR ion source. This work models microwave plasma coupling in 2D axis symmetric configuration to investigates plasma parameters and corresponding influence of electric field in plasma environment. A microwave field of the order of 1.3 x10^5 V/m is obtained at the Centre of the plasma chamber cavity for an input microwave power of 500 W. Present microwave coupled plasma has a maximum density of 9.04×10^{16} / m^3. The steady state peak electron temperature is around 3 eV under various pressure (1mbar-10^{-3} mbar) conditions of argon gas. Most of power deposition takes place on the ECR surface zone which corresponds to 0.0875 T contour. Steady state argon plasma results show that beyond a critical plasma density of 7.4×10^{16} /m^3 most of the microwave power is deposited at the plasma edge.

INTRODUCTION

Since last few decades, dipolar and multipolar based microwave plasma based ECR ion source have been studied[1 and 2]. Hagelaar et.al [3and 4] and J Pelletier group [5] obtained a uniform high density plasma up to gas pressures 10^{-2} mbar.

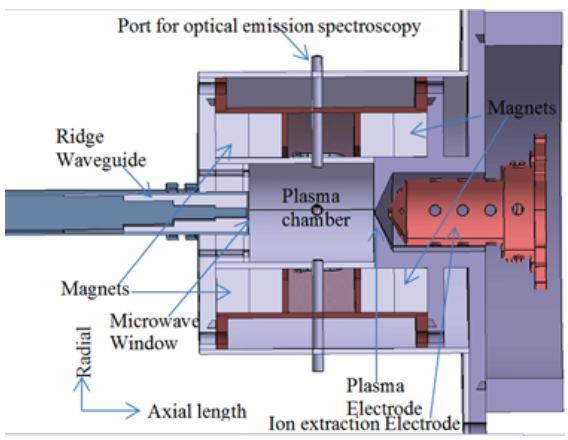

Figure 1: Cut section of negative hydrogen PMECRIS.

A detailed insight on microwave fed ion source physics is discussed for different absorbed power conditions by Hagelaar. Microwave heated ECR plasma is growing its interest in numerous number of applications under low pressure conditions, in plasma electron heating and power deposition by microwave electric field infusion plasma. A recent trend in the ion source technology aims at decreasing the gas pressure in the 10^{-3}mbar range using the same resonance heating by creating MW plasma.

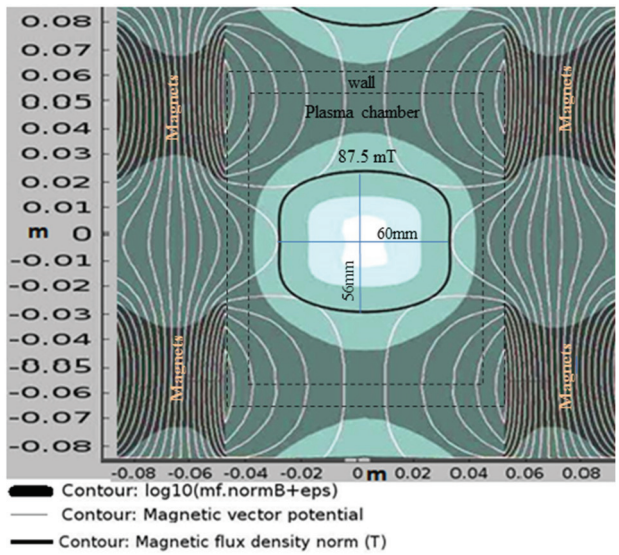

Figure 2: ECR contour for 2.45 GHz frequency.

At high pressures, ohmic heating (collision based) occurs in which gyrating electron motion is randomized by collisions with background gas molecules[6, 7 and 8]. With spatially varying electric fields in resonance zone, phase randomization can also happen due to thermal electrons motions even in the absence of collisions. This collision less heating dominates under low pressures. Under low pressure conditions plasma can be maintained uniformly and parameters can be well controlled [4-9]. However, in low pressure (10^{-3} mbar range), sufficient database is not available for negative ion source in R&D sectors.

This paper investigates a microwave coupled PMECRIS plasma under low gas pressure (≤10^{-2}mbar), which finally will be used as a negative hydrogen ion source for an RFQ accelerator. Effect of time scale dependent microwave propagation into the plasma is also discussed. A further study on how the power deposition is taking place with time into the plasma volume has been done. A detailed picture of time varying electric field distribution in plasma environment has been demonstrated clearly.

MICROWAVE PLASMA MODEL

This model is based on the finite element method (FEM) considering fluid approach with drift diffusion approximation. Ion motion is negligible w.r.t the electron motion in microwave timescale (ns). Electron density is

†chinmoy.mallick@ipr.res.in

ISBN 978-3-95450-186-1

constant in space in ECR zone. Electric field throughout the plasma is solved by following equations [3, 4 and 9].

$$\nabla \times \mu_0^{-1}(\nabla \times E) - \kappa_0^2(\epsilon_r - \frac{\iota\sigma}{\omega\epsilon_0})\nabla.E = 0 \quad \ldots\ldots\ldots (1)$$

σ is full tensor plasma conductivity. Perfect electric conductor boundary conditions are chosen on plasma chamber wall. All three components of electric field are computed despite the fact that only excitation occurs in the r-z plane from the coaxial port. Electron velocities, parallel to magnetic field, obtained from local momentum equation as follows [3, 4 and 9].

$$\frac{\partial \tilde{v}_e}{\partial t} = -\frac{q}{m_e}\tilde{E} + \nu_m \tilde{v}_e \quad \ldots\ldots\ldots\ldots (2)$$

The above equation is linearized by neglecting permanent magnetic force so that we can take a fourier transform of equation(2). In microwave plasma interaction time scale (time-scale:10^{-8}s, $10^{-7.4}$s, $10^{-6.8}$s, $10^{-6.2}$s, $10^{-5.6}$s, 10^{-5}s, $10^{-4.4}$s, $10^{-3.8}$s, $10^{-3.2}$s, $10^{-2.6}$s, 10^{-2}s), gyrating electrons do not travel appreciable distance, so space derivative components are not included in equation (2), assuming uniform pressure within the plasma volume. However, before coming to steady state, microwave plasma interaction ontinues over many microwave periods and electron's velocity is established after many periods.That's why electrons encounter appreciable electric field variations while passing through the ECR resonant surface zone in a very short time interval with their thermal motion along magnetic field lines. This is non-local kinetic effects which does not obey the above momentum equation (2). As a consequence, phase coherence between electron velocity and E-field oscillations is destroyed and electron faces spatial field variations. During stay at resonant surface electrons is accelerated in very short time and at next pass electron is accelerated from zero again. One of the methods to include this non-local kinetic effects is to add one component (doppler shift component) to the momentum collision frequency.

$$\nu_{eff} = \nu_m + \frac{\omega}{\delta} \quad \ldots\ldots\ldots (3)$$

$\boldsymbol{\delta}$ is doppler broadening parameter [4 and 9], ν_{eff} is effective collision frequency. ν_m is the normal electron momentum collision frequency. From Fig. 2,width of resonant surface is obtained as ~1 mm and for λ=122.2 mm. For 3 eV electron temperature , the thermal velocity of electron is ~10^6 m/sec. For k=0.5 cm^{-1},we get an effective collision frequency in resonance zone as $\frac{v_T\omega}{\delta}$~10^9per second[4]. v_T is electron's thermal velocity. The normal electron collision frequency (ν_m) with the background gas (pressure~mbar) obtained from simulation is 4.25×10^6 Hz which is three times smaller than the effective collision frequency.The effective collision frequency makes the E-field smooth over ECR surface thus keeping the total absorbed power intact.

E-FIELD DISTRIBUTION WITHOUT PLASMA

Microwave E-field is optimized using four-step ridge waveguide at an input port power of 500W. At 2.45GHz microwave frequency, E-field is maximum at the centre having value 1.29×10^5 V/m. The WR 284 ridge waveguide at the mouth of the plasma chamber injection side has a width of 48mm and height of 9.8 mm.The length of the total waveguide is 220 mm. Ridge lengths are 35.1 mm, 37.4 mm, 45.1 mm and 102.4 mm respectively, as shown in Fig.3.

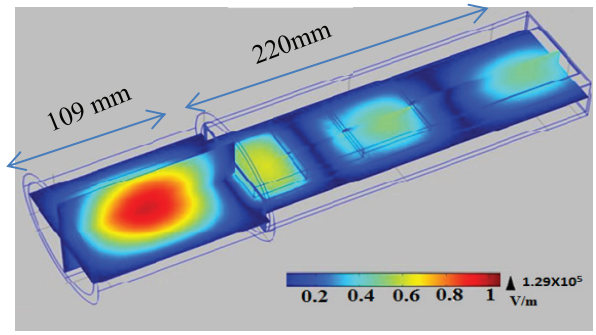

Figure 3: E-field under empty plasma chamber cavity of dimension 109 mm.

E-FIELD DISTRIBUTION IN PLASMA

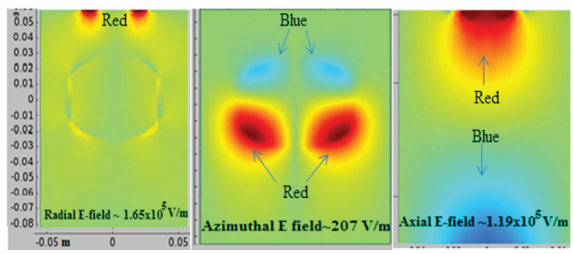

Figure 4: E-field distribution in plasma for 50W total absorbed power and 10^{-2}mbar pressure.

Peak values are shown on the graphs. Scales are linear. Axial field ranges from -0.4×10^5 V/m to 1.19×10^5V/m, azimuthal field ranges from -597 V/m to 207 V/m and radial field from -1.55×10^5 V/m to 1.65×10^5 V/m are shown. Blue colour denotes positive maximum and red colour negative maximum (colour online). Axial and radial e-field is discontinuous on ECR surface due to high microwave conduction current (high plasma conductivity).

RESULTS AND DISCUSSIONS

For 2.45 GHz microwave frequency, critical density of plasma is $7.4\times10^{16}/m^3$, beyond which MW power is not absorbed and gets reflected Figure 4 and 5 shows the results simulated in 2D-axis-symmetric domain under three different low gas pressure conditions and at a fixed plasma absorbed power of 50 W. Microwave is launched through coaxial port to the plasma chamber in TEM mode.

Two axial and radial electric fields are mainly responsible for the plasma generation. The azimuthal electric field is two orders less than the axial and radial electric field. Electrons absorb microwave power mainly

ISBN 978-3-95450-186-1

on ECR surface area. Fig. 6 shows power absorption is peaked along the resonant surface. Peak electron temperature is ~3 eV which is almost constant along the magnetic flux density lines. Plasma potential of 18.7 V has almost flat profile from the ionization region to the pre-sheath region which is five times more than the peak electron temperature.

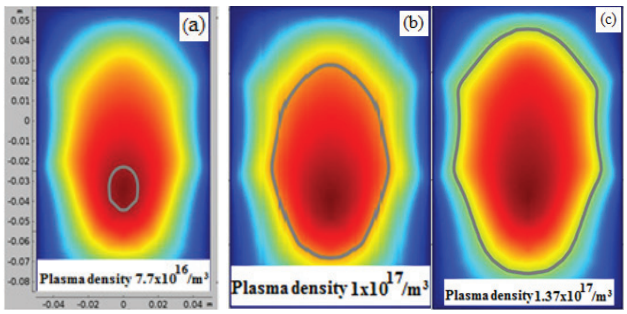

Figure 5: Plasma density contours at different pressures (a) 2×10^{-3} mbar, (b) 3×10^{-3}mbar, (c) 5×10^{-3} mbar. Thick grey line represents critical plasma density of 7.4×10^{16} /m^3. Total plasma absorbed power is fixed at 50 W.

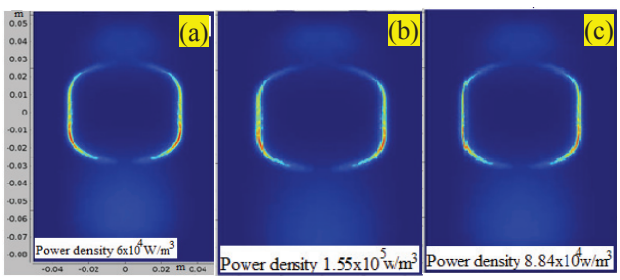

Figure.6: Spatial distribution of Power density at various pressures (a) 2×10^{-3} mbar**,** (b) 3×10^{-3} mbar and (c) 5×10^{-3} mbar and at constant absorbed power of 50 W.

At low pressure, magnetized electrons have high axial mobility and very low radial component across the magnetic field line. So, electrons gyrating around the pre-sheath region, assumed to be isolated from the ionization region. Argon ions have mobility, which is almost equally distributed along the radial and axial direction, so that quasi-neutrality is lost around the sheath region. To attenuate the radial ion velocity, potential becomes nearly flat profile.

From Fig. 5, it is observed that plasma density increases from 7.7×10^{16}/m^3 to 1×10^{17}/m^3 for increase in pressure from 2×10^{-3} mbar to 3×10^{-3} mbar. From Fig. 5 and Fig. 6, it is visible that an increase of the plasma density from 7.7×10^{16}/m^3 to 1×10^{17}/m^3 is observed as power density is increased from 6×10^{4}W/m^3 to 1.55×10^{5}W/m^3. From these data, we can deduce a significant increase in plasma density with increasing the power density. Increase in the microwave power density actually increases the gas temperature also.

It is noted that plasma density increases with pressure and reaches beyond a critical density. Power density profile coincides with the critical density contour shown (grey colour). Similar trends happen while increasing absorbed power at constant pressure also.

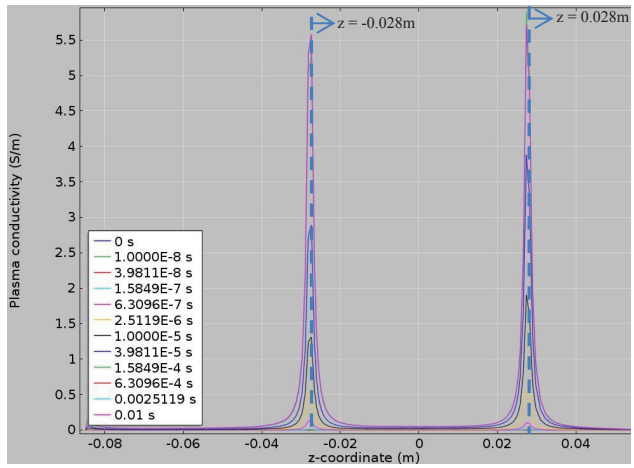

Figure 7: Plasma conductivity near resonant surface locations due to the permanent magnet.

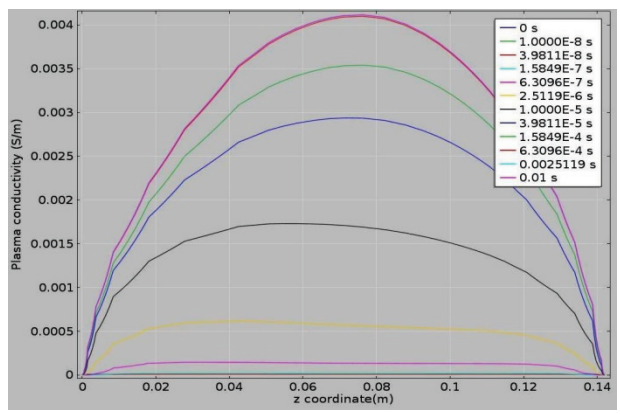

Figure 8: Variation of plasma conductivity with axial distance for different time, without magnets.

At the resonant flux density (0.0875T) the plasma conductivity is 2×10^{3} times higher than the case where no static magnetic field is present, as shown in Fig. 7 and Fig. 8.

TIME EVOLUTION OF PLASMA WITH POWER DEPOSITION

Microwave can't penetrate the critical density into the plasma. In Fig. 9, it is clear that microwave imparts very less amount of energy to the electrons from time = 2.5 µS onwards on the ECR surface zone, because during that time plasma started evolving. As a result, Microwave power deposition is shifted from ECR zone to the plasma edge (from ns to µs).

Initially, during 1550 microwave periods electrons are gaining energy continuously on resonant surface at an ionization rate ~ 2.66×10^{22}/m^{3}sec (From simulation results).

ISBN 978-3-95450-186-1

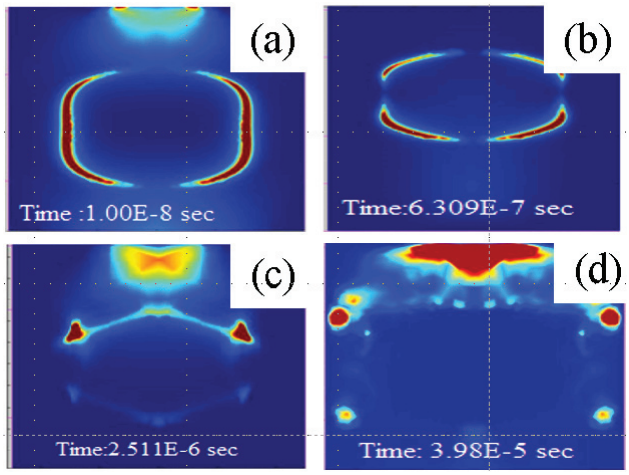

Figure 9: Maximum Power density at different time instants. (a) 6.6×10^{4} W/m^3, (b) 1.43×10^{7} W/m^3, (c) 3.12×10^{6} W/m^3 and (d)1.67×10^{7} W/m^3 at pressure 10^{-2} mbar, 50 W power.

Up to time 6.31×10^{-7}-s density is increased by 1.17×10^{15}/m^3.At instant 2.511×10^{-6}s, density becomes 6.65×10^{16}/m^3 which is close to critical density and correspondingly resonant power deposition area is least. At 0.01s power deposition no longer takes place on ECR surface but shifted towards wall because of the peak density~1.16×10^{18}/m^3 near resonant zone which is beyond critical density. This plasma creation near the edge replenishes the plasma loss in the core and maintains steady state. The power density variation on the resonance surfaces during the microwave discharge process gives an estimation of the total time required for the plasma come to steady state. The results shows plasma obtains steady state condition within 100-200µs which is in good agreement with the experimental data given in Ref.10.

SUMMARY

The purpose of this paper is to describe the effects of gas pressures and power density on the microwave argon plasma characteristics under low pressure. A FEM model in a cylindrical 2D axis-symmetric environment is simulated. Comparatively at higher pressure, more molecules are available to collide with electrons and generate electron-ion pair. So, with increasing pressure plasma density increases but collisional mean free path of electron decreases. If electrons get less time before collision, it will gain less energy. Hence, electron impact ionization will be less and there will be decrease in electron-ion pair. So these two effects are contradictory to each other. Power density is decreased from 1.55×10^{5} W/m^3 to 8.84×10^{4} W/m^3 for pressure from $3\text{x}10^{-3}$ mbar to 5×10^{-3} mbar. Analytically it can be deduced that at this higher pressure (5×10^{-3}mbar) collision frequency becomes more than the resonant frequency, so the power density in the resonance zone decreases.

REFERENCES

[1] Hussein M and Emmert G J. Vac. Sci. Technol.A 82913(1990).
[2] Morito Matsuoka, Kenichi Ono Journal of Vacuum Science & Technology A 6(25) (1988).
[3] G J M Hagelaar, K Makasheva, L Garrigues, J-P Boeuf," J.Phys D:Appl. Phys. 42(194019) ,(2009).
[4] G J M Hagelaar, N Oudini, Plasma Phys. Control. Fusion53(124032) (2011).
[5] A. Lacoste, T. Lagarde, S. Bechu, ,Y. Arnal and J. Pelletier ,Plasma Source Sci.Technol., 11 (407), (2002).
[6] M.A. Liberman, Allan J. Lichtenberg, "Principles of plasma discharges and materials processing", John Wiley and Sons, New York, 1994
[7] Nasser, "Fundamentals of Gaseous Ionization and Plasma Electronics", John Wiley & Sons, 1971
[8] Chapman, "Glow Discharge Processes", John Wiley & Sons, 1980
[9] www.comsol.com
[10] O. Daniel Cortázar et al., "Experimental Study of Breakdown Time in a Pulsed 2.45-ghz ECR Hydrogen Plasma Reactor", IEEE transactions on plasma science, vol. 40, no. 12, December 2012.

ISBN 978-3-95450-186-1

RECENT PRODUCTION OF INTENSE HIGH CHARGE ION BEAMS WITH VENUS

D. Z. Xie†, W. Lu[1], J. Y. Benitez, C. M. Lyneis, D. S. Todd
Lawrence Berkeley National Laboratory, Berkeley, CA 94720, USA
[1]also at Institute of Modern Physics, Lanzhou 730000, China

Abstract

Several modifications have been made to VENUS to enhance its performance at high microwave power and bring its beam production closer to the levels predicted by scaling laws for 28 GHz operation. Two of these modifications allowed for an increase of injected microwave power: the cooling scheme on the plasma chamber wall was improved to eliminate damage caused by localized electron heating, and the extraction electrode was redesigned to remove the thermal energy from incident hot electrons more effectively. A further modification was the reduction in the diameter of the waveguide which launches 28 GHz power into the plasma chamber. With these remedies, the source now operates stably up to 10 kW of injected power and allows for more favorable magnetic field configurations. The extraction of high charge state ion beams from VENUS has been substantially enhanced as demonstrated by the recent production of a number of intense CW beams: 4.75 emA of O^{6+}, 1.90 emA of O^{7+}, 1.06 emA of Ar^{12+}, 0.523 emA of Ar^{16+}, 0.115 emA of Ar^{17+}, 0.77 emA of Kr^{18+}, 0.355 emA of Kr^{26+} and 0.007 emA of Kr^{31+}. For the first time VENUS has been able to produce more than 1 emA of O^{7+} and Ar^{12+}, and enhance the intensity of the higher charge state ion beams by a factor of 2 and higher.

INTRODUCTION

VENUS is the first 3rd generation superconducting ECR ion source (ECRIS) operating at 28 GHz with magnetic field maxima of 4 T on axis and 2 T radial at the inner surfaces of the plasma chamber [1]. Beginning with its initial operation in 2002, VENUS produced a number of record CW beams from an ECR source and delivered a wide variety of highly-charged, heavy ion beams to enhance the capability of the 88-Inch Cyclotron [2]. However, VENUS was limited in its potential magnetic field configurations at higher input microwave power due to a thin-edged plasma electrode, shown in Fig. 1, which insufficiently transported away the heat load generated by hot electron bombardment. In order to avoid melting this electrode, higher extraction peak fields were required to reduce the flux of hot electrons to the plasma electrode by guiding them to the chamber radial walls. Consequently these higher extraction fields resulted in the lowest total magnetic fields on the chamber surface occurring in localized areas on the chamber radial walls, as shown in Fig. 2, leading to an intense heat transfer to these spots by the hot electrons. This localized heating severely deteriorated the plasma chamber walls over time and resulted in two burned out plasma chambers; even while operating with microwave power limited to 7 kW or lower [3, 4]. This very restrictive constraint on input heating power resulted in VENUS not reaching its full potential even after 15 years of operations.

This article presents and discusses the two recent modifications addressing insufficient chamber cooling, which now allow for more input microwave power. These improvements, coupled with the studies into the effects of reducing the exit diameter of the 28 GHz waveguide from 31.8 mm to 20.0 mm which are also discussed, have allowed for operating VENUS with more preferable magnetic field configurations, with more power, and have led to a stable plasma resulted in significant enhancements on the extracted beam current.

NEW PLASMA ELECTRODE

Figure 1 shows the previous plasma electrode having a slant taper of a minimum thickness of ~ 0.6 mm at the aperture edge of Ø10 mm and ~1.4 mm at Ø16 mm slant-step transition region. This electrode design is poor in transporting away the thermal load on the thin edge and thus not suitable for the hot ECR plasma operating at high microwave power. The high thermal heat load on the electrode thin edge could lead to microscopic and macroscopic surface melting in certain locations, and the presence of molten aluminium decreases plasma stability. Heat transport simulations indicate that for a circular region of radius of ~ 8 mm it takes ~ 950 W power, equivalent of 775 W/cm^2 in an area of $S = \pi(0.8^2\text{-}0.5^2)$ cm^2, for the thin edge temperature rising up to ~ 350 ^{0}C in which the aluminium recrystallization will occur.

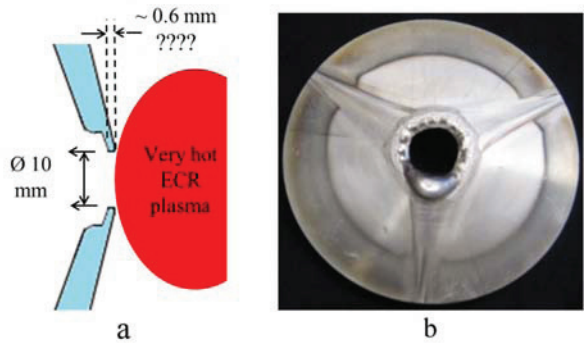

Figure 1: a). The previous plasma electrode with the aperture supported by a very thin slant backing resulted in poor power transportation; b). This thin aperture edge was melted for a few hours of operation at ~ 7.5 kW microwave power with extraction peak field lower than the minimum total field at the chamber walls.

† zqxie@lbl.gov

ISBN 978-3-95450-186-1

When VENUS was operated at total microwave power of 7.5 kW with the extraction field lower than the minimum total field at the chamber walls for about a few hours, the thin-edged extraction aperture melted, as shown in Fig. 1b, and resulted in an unstable plasma. A modification was then made to the extraction electrode by eliminating the slant-step transition which has led to a minimum thickness of ~ 3.8 mm at the aperture edge. This thickness increase improves thermal conduction from the primary heat load of electrons near the inner aperture edge to the outer radius of the electrode where it is thermally connected to the water-cooled chamber. Simulations have shown the revised plasma electrode with the 3.8 mm minimum thickness should withstand up 30% more power than the thin-edged electrode to reach recrystallization. Indeed, in operating for months with the modified electrode using low extraction magnetic fields, essentially no corrosion has been observed and the plasma remain stable even at microwave power of ~ 10 kW.

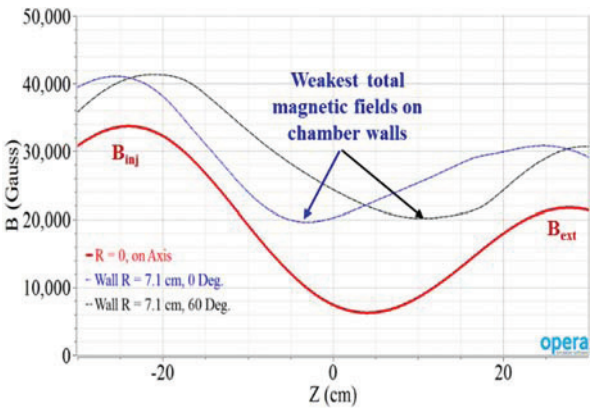

Figure 2: VENUS had been operating for many years with constrained magnetic field configurations like the one is shown. There were always magnetic holes on the plasma chamber walls due to the peak field at extraction is higher than the total fields at some locations of the walls.

NEW COOLING SCHEME FOR THE PLASAMA CHAMBER

The previous cooling scheme of the VENUS plasma chamber had a wide water channel right behind a ~ 2 mm thick aluminium wall that is in touch with each of the six plasma flutes, as shown in Fig. 3a. Though the overall cooling capacity of the chamber is sufficient to remove much more than 10 kW power, the chamber was burned out twice along a flute, shown in Fig. 3b, due to hot electrons reaching the chamber wall at the location of the magnetic weak point. Hot electron bombardment can easily result in power being deposited at these small magnetic holes in excess of the critical heat flux of 1 MW/m^2 [4]. When the temperature at these locations exceeds 150 ^{0}C, the cooling water immediately outside the hot spots is vaporized dramatically reducing cooling and the localized temperature can continue to rise to 350 ^{0}C. Above these temperatures the aluminium can recrystallize and lead to catastrophic failures.

To reduce the localized overheating on the chamber walls, we have rotated the existing plasma chamber 30^0 to align the plasma flute along a section of ~ 7-mm-thick aluminium situated between two adjacent water channels, as shown schematically in Fig. 3c. The two adjacent cooling channels are at ~ 5 mm azimuthally from the center of the plasma flute, therefore cooling the plasma flute contact area is through lateral thermal conduction instead of the direct back-cooling. VENUS has been operating with this new cooling scheme for about one year and although it has run frequently with a total microwave power of 10 kW for extended periods, no visible damage has been found in the chamber surfaces.

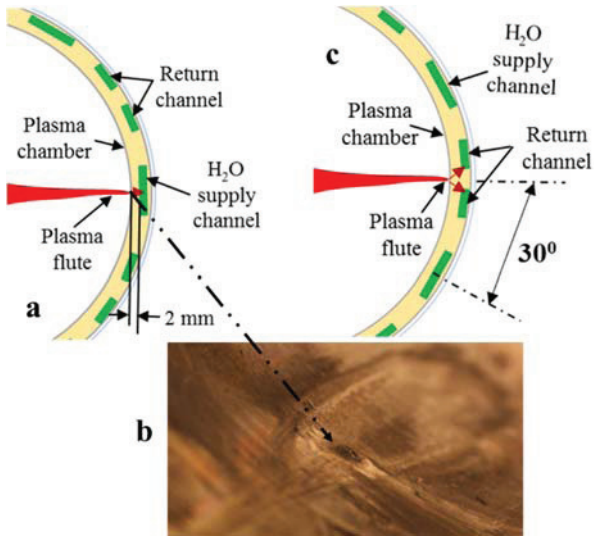

Figure 3: **a**. The previous plasma chamber cooling scheme aligned a water channel with ~ 2 mm thick wall right on a plasma flute (red colour); **b**. The resulted burned out at a location where the total magnetic field is the weakest; **c**. New scheme by rotating 30^0 of the chamber to align a plasma flute onto a section of ~ 7 mm thick solid aluminium that is cooled laterally (indicated by the two green arrows) by two adjacent water channels.

MAGNETIC FIELD CONFIGURATIONS

With sufficient cooling to the plasma chamber, VENUS can operate with a wider range of magnetic field configurations; most importantly it can operate using lower peak extraction fields. In comparison to the previous constrained field configuration shown in Fig. 2, the field strength at extraction is now typically run about 10% lower when $B_{min} \leq 0.5$ T, while the fields at injection and the chamber walls remain about the same. Having a low extraction field is expected to result in an increase of hot electrons lost to the plasma electrode, reducing some of the heat load to the hot spots along plasma flutes where chambers have been burned out previously. Improved cooling at the extraction electrode and along the flutes allows for higher input microwave power. These subtle changes and the ensuing results have demonstrated that with better plasma chamber cooling VENUS can operate with more preferable magnetic field configurations while

ISBN 978-3-95450-186-1

maintaining good plasma stability so that more microwave power can be injected into the ECR plasma resulting in better performance. It is important to note that the performance improvements with these modifications are with little operation time. Exploration into newly available magnetic field configurations, such as with higher B_{min} fields, will continue.

LAUNCHING 28 GHZ MICROWAVES WITH A 20 MM CIRCULAR TRANSITION

Following the first successful coupling of 28 GHz microwaves into SERSE [5], all subsequent 3rd generation ECRISs use oversized circular waveguides (Ø ~ 30-32 mm) to launch the 24-28 GHz TE_{01} circular microwaves into their ECR plasma and have substantially enhanced ECRIS performance. However, the question remains how to achieve the best coupling of higher frequency microwaves ($f \geq 20$ GHz) into an ECRIS. In other words, it is not clear how to maximize the forward power and minimize the reflection through microwave mode or launching scheme. For frequency $f > 20$ GHz, HE_{11} microwave was proposed for better heating ECR plasma because of its Gaussian energy concentration on axis [6], but so far two explorations have failed to demonstrate the expected enhancements [7, 8].

The merits of launching scheme with optimum size of the coupling waveguide had not been explored until recently by the ECR group of IMP [8]. In an over-simplified analysis, as schematically shown in Fig. 4a, a coupling waveguide of about the same diameter as the plasma chamber will not work very well as much of the input microwave power will easily escape the plasma cavity and stream back to the microwave generator causing substantial variation of the forward power level and possible damages to the microwave generator. On the other hand, limiting reflected power by employing a very small-diameter waveguide such as a quasi-zero one shown in Fig. 4b won't work either as little power is transported into the chamber. Based on this simple analysis, it should be expected that the optimum diameter for a coupling waveguide into an ECRIS should fall somewhere between zero and the chamber diameter, schematically illustrated in Fig. 4c.

Exploration of the different coupling waveguides is underway in VENUS and the first test has been carried out by tapering the straight circular waveguide of Ø31.8 mm down to Ø20 mm at the coupling exit into the plasma chamber. Preliminary tests with TE_{01} microwaves and different operating magnetic field configurations, combined with the better chamber cooling, demonstrated different operation characteristics. The plasma is now more stable at higher input power and shows no saturation for many high charge ion beams even at total power reaching ~ 10 kW. In these tests the source is operated with a low central field, B_{min} of 0.3 ~ 0.5 T (B_{ecr} = 1 T for 28 GHz microwaves) but with high microwave power. Such a low B_{min} was chosen in order to lower the electron spectral temperature, T_s, of bremsstrahlung radiation as this spectral temperature is proportional to B_{min} [9]. Operating with such field configurations with lower B_{min}, was suggested before, and when doing so the generated heat load to the VENUS cryostat is typically ≤ 1 W even at microwave power of 10 kW injected [10].

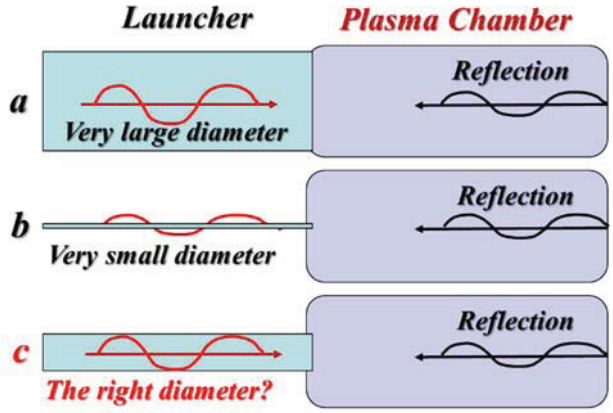

Figure 4: **a**. A launching waveguide of very large diameter enables high portion of microwave power escaping; **b**. Launching waveguide of very small diameter won't work due to that little power can be transported; **c**. There should be an optimum launching waveguide of the right diameter producing the best microwave coupling to an ECRIS.

NEW RESULTS AND COMPARISON

Table 1 lists the recent VENUS performance compared to previous VENUS production and that of some other sources for a few example heavy ion. It is clearly seen that for very highly charged ion beams, VENUS shows a factor of ~ 2 or greater improvement, and for lower charge states the results from VENUS are very comparable [8, 11]. This is the first time that VENUS has produced more than 1 emA of O^{7+} and Ar^{12+}, which had been strived for many years but never achieved until the improved cooling. The production of 0.5 emA of Ar^{16+}, 0.1 emA of Ar^{17+} and 0.007 emA of Kr^{31+} has also set new beam records from VENUS, demonstrating that the source potential has not yet been fully realized.

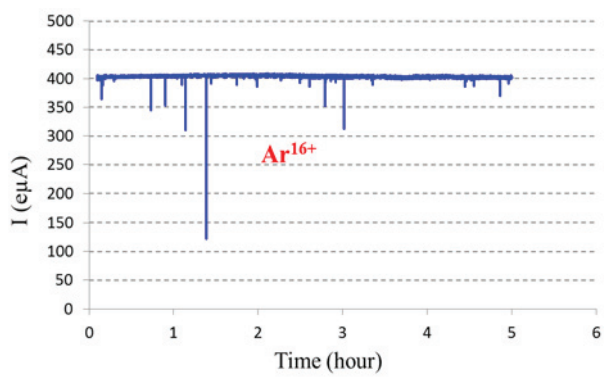

Figure 5: A measurement of 0.4 emA of Ar^{16+} produced with VENUS for 5 hours demonstrates the good beam stability at high microwave power of 8 kW, though with a few trips of unknown causes.

ISBN 978-3-95450-186-1

Figure 5 shows a measurement of the beam stability of 0.4 emA of Ar^{16+} produced with VENUS at microwave power of 8 kW. Excluding a few trips, this measurement has demonstrated with sufficient chamber cooling VENUS can stably produce intense high charge state ion beams even at high microwave power of 8 ~ 10 kW for hours, and it should work the same for days or weeks if all inputs kept stable.

Table 1: Recent Performance of VENUS and Comparison

	VENUS 28+18 GHz (≤ 2015)	VENUS 28+18 GHz (2016)	SECRAL 24+18 GHz	SuSI 24+18 GHz
$^{16}O^{6+}$	2.85	**4.75**	2.3	2.2
O^{7+}	0.85	**1.90**	0.81	1.4
$^{40}Ar^{12+}$	0.86	**1.06**	1.42	0.86
Ar^{14+}	0.514	**0.84**	0.846	0.53
Ar^{16+}	0.27	**0.523**	0.35	0.22
Ar^{17+}	0.037	**0.115**	0.05	
Ar^{18+}	0.001	**0.004**		
$^{78}Kr^{18+}$	^{84}Kr	**0.77**		
Kr^{23+}	0.088	**0.42**		
Kr^{28+}	0.025	**0.089**		
Kr^{31+}		**0.007**		

*: Quoted currents are in unit of emA.

DISCUSSIONS

The performance of VENUS has been substantially enhanced by a combination of the few presented, recent modifications, and exploration into the performance gains from these modifications will continue. The improvement of a factor of 2 or higher for very highly charged ions enables VENUS to further enhance the capability of the 88-Inch Cyclotron. Because this limited exploration was not done systematically in order to determine the contribution of each modification individually, the question arises as to which one of the modifications plays the most important role in VENUS new achievement?

Getting a clear answer to this question would require a long time and great effort. However, a very plausible scenario would be that the two cooling modifications to the plasma chamber have allowed VENUS to operate at higher microwave power with more preferable magnetic field configurations. In addition, the smaller 28 GHz launch waveguide of Ø20 mm reduces the reflected microwave power to minimize the interference with the 28 GHz microwave generator. Thus the combination of these changes enables VENUS to manifest its potential.

It is worth of pointing out the future generation of ECRIS will likely operate with microwave power much greater than 10 kW [12]. Based on Geller's scaling [13]: q_{opt} the optimum charge state is proportional to the angular frequency ω, power dependence on q_{opt} and ω:

$$q_{opt} \sim \log(\omega^{3.5}) \text{ and } P_{\mu} \sim \omega^{1/2} q^3 V$$

Using SECRAL's best bismuth results [8] and assuming the same chamber volume V, one would find that as we move toward 45 GHz sources:

@ 24 GHz Bi $q_{opt\,1} \sim 30+$ and $P_{\mu 1} \sim 8.5$ kW →

@45 GHz, Bi $q_{opt\,2} \sim 36+$ and $P_{\mu 2} \sim 20$ kW

With a power level of 20 – 30 kW launched into an ECR plasma chamber the cooling will definitely become much more challenging, thus the plasma chamber should be very well engineered.

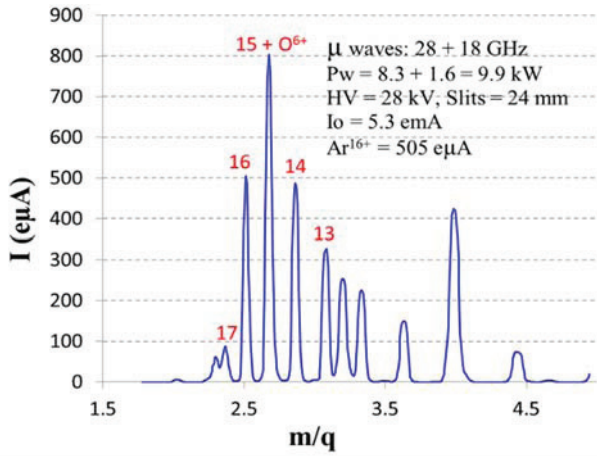

Figure 6: Argon charge state distribution produced recently with the VENUS which was optimized on Ar^{16+} and peaked at either 15+ or 16+ for the first time. Oxygen gas was used as the support gas with microwave power ~ 10 kW.

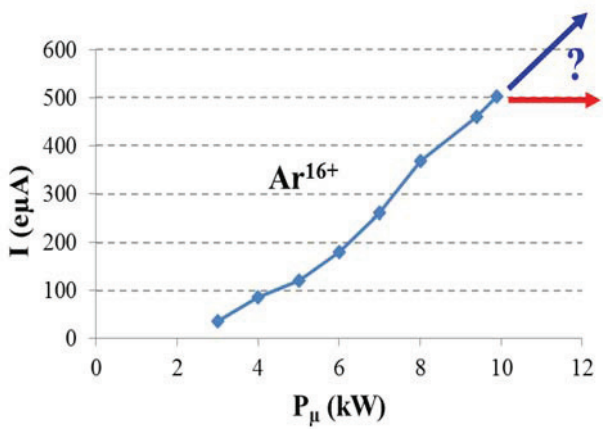

Figure 7: Intensity of Ar^{16+} versus injected microwave power up to 10 kW shows no sign of saturation indicating that higher intensity is possible with more microwave power.

Figure 6 shows a VENUS spectrum optimized for Ar^{16+} with oxygen as the support gas. It is the first ever charge state distribution of argon produced by VENUS peaking at either Ar^{15+} or Ar^{16+} with intensity of 0.5 emA. The curve of the intensity of Ar^{16+} versus the microwave power up to 10 kW in Fig. 7 shows no sign of saturation indicating higher yield of Ar^{16+} would be possible with more microwave power. This should also be the case for other

ISBN 978-3-95450-186-1

high charge state ions, such as O^{7+}, Ar^{17+}, Ar^{14+}, Kr^{28+} and Kr^{31+}, etc.

Tests of two different sizes, Ø15 and Ø25 mm, of the 28 GHz coupling waveguides have been planned to explore a better coupling of the 28 GHz microwaves to VENUS. Even though so far no any conclusive evidence supports the role of the microwave mode played in the ECRIS performance, investigation of the effects of TE_{01} and TE_{11} microwaves are planned for future developments.

Based on the discussed modifications that have led to the recent performance enhancements with VENUS, it is reasonable to arguably conclude that a well cooled ECRIS can stably operate at > 10 kW microwave power. The maximum operating power could likely to be determined by the combination of plasma chamber cooling and the magnetic field configurations.

REFERENCES

[1] C. M. Lyneis and Z. Q. Xie, "Concept for a third generation ECR source at LBL," Proceedings of the 12th International Workshop on ECR Ion Sources, RIKEN, Japan, 1995, p. 119, (unpublished).
[2] C. Lyneis, D. Leitner, M. Leitner, C. Taylor and S. Abbott, Rev. Sci. Instrum. **81**, 02A201 (2010).
[3] C. M. Lyneis, D. Leitner, O. Tarvainen, D. Todd, S. Virostek, T. Loew, and A. Heinen, Rev. Sci. Instrum. **77**, 03A342 (2006).
[4] T. Thuillier, J. Angot, J. Y. Benitez, A. Hodgkinson, C. M. Lyneis, D. S. Todd, and D. Z. Xie, Rev. Sci. Instrum. **87**, 02A736 (2016).
[5] S. Gammino, G. Ciavola, L. Celona, D. Hitz, A. Girard, and G. Melin, Rev. Sci. Instrum. **72**, 4090 (2001).
[6] D. Hitz, Adv. Imaging Electron Phys. 144, 1–164 (2006).
[7] C. Lyneis, J. Benitez, A. Hodgkinson, B. Plaum, M. Strohmeier, T. Thuillier, D. Todd, Rev. Sci. Instrum. **85**, 02A932 (2014).
[8] L. Sun *et al.*, Rev. Sci. Instrum. **87**, 02A707 (2016).
[9] J. Y. Benitez, C. M. Lyneis, L. Phair, D. S. Todd, and D. Z. Xie, "Recent bremsstrahlung measurements from the superconducting electron cyclotron resonance ion source VENUS," MOCO04, these proceedings.
[10] D. Leitner, C. M. Lyneis, H. Koivisto, T. Ropponen, J. Ropponen, D. S. Todd, J. Y. Benitez, S. Gammino, Rev. Sci. Instrum. **79**, 033302 (2008).
[11] G. Machicoane, D. Cole, K. Holland, D. Leitner, D. Morris, D. Neben, and L. Tobos, "First results at 24 GHz with the superconducting source for ions (SuSI)," Proceedings of 21st International Workshop on ECR Ion Sources, p. 1, Nizhny Novgorod, Russia, 24–28 August, 2014, http://www.JACoW.org
[12] C. Lyneis, P. Ferracin, S. Caspi, A. Hodgkinson and G. L. Sabbi, Rev. Sci. Instrum. **83**, 02A301 (2012).
[13] R. Geller *et al.*, "The Grenoble ECRIS Status 1987 and Proposals for ECRIS Scalings," Proc. of the 8th ECR Workshop, NSCL Report: MSUCP-47 (unpublished), E. Lansing, MI, USA, 1987, p1.

ISBN 978-3-95450-186-1

ISBN 978-3-95450-186-1

List of Authors

Bold papercodes indicate primary authors

ISBN 978-3-95450-186-1

ISBN 978-3-95450-186-1

ISBN 978-3-95450-186-1

Institutes List

AEC
Chiba, Japan
- Fukushima, K.
- Sasano, T.
- Suzuki, T.
- Takahashi, K.
- Takasugi, W.

ANL
Argonne, Illinois, USA
- Dickerson, C.
- Ostroumov, P.N.
- Pardo, R.C.
- Scott, R.H.
- Vondrasek, R.C.
- Zinkann, G.P.

ATOMKI
Debrecen, Hungary
- Biri, S.
- Rácz, R.

CEA/DRF/IRFU
Gif-sur-Yvette, France
- Bogard, D.
- Delferrière, O.
- Desmons, M.
- Gauthier, Y.
- Gobin, R.
- Harrault, F.
- Peauger, F.
- Perreu, G.
- Pottin, B.
- Sauce, Y.
- Schwindling, J.
- Senée, F.
- Tuske, O.
- Uriot, D.
- Vacher, T.V.

CEA/DSM/IRFU
France
- Harrault, F.
- Vacher, T.V.

CEA/IRFU
Gif-sur-Yvette, France
- Bolzon, B.
- Chancé, A.
- Chauvin, N.
- de Guiran, R.
- Delferrière, O.
- Gauthier, Y.
- Girardot, P.
- Gobin, R.
- Misiara, N.
- Sauce, Y.
- Senée, F.
- Simon, C.
- Tuske, O.

CERN
Geneva, Switzerland
- Bellodi, G.
- Fichera, C.
- Küchler, D.
- Lombardi, A.M.
- Maintrot, M.
- Michet, A.I.
- O'Neil, M.
- Sadovich, S.
- Somoza, J.A.F.
- Toivanen, V.
- Wenander, F.J.C.

Cockcroft Institute
Warrington, Cheshire, United Kingdom
- Tzoganis, V.

DREEBIT
Großröhrsdorf, Germany
- Baumgart, C.
- Kreller, M.
- Zschornack, G.

DU
Debrecen, Hungary
- Pálinkás, J.

F4E
Germany
- Beauvais, P.-Y.
- Dzitko, H.

FRIB
East Lansing, Michigan, USA
- Machicoane, G.

Fusion for Energy
Garching, Germany
- Cara, P.
- Heidinger, R.

GANIL
Caen, France
- Bajeat, O.
- Barthe-Dejean, C.
- Barue, C.
- Delahaye, P.

ISBN 978-3-95450-186-1

- Dubois, M.
- Flambard, J.L.
- Frigot, R.
- Jardin, P.
- Jeanne, A.
- Kamalou, O.
- Lechartier, N.
- Lecomte, P.
- Lemagnen, F.
- Maunoury, L.
- Metayer, V.
- Osmond, O.
- Peschard, G.
- Savalle, A.

Graduate University, Chinese Academy of Sciences
Beijing, People's Republic of China
- Chen, J.E.

GSI
Darmstadt, Germany
- Ameil, F.
- Berezov, R.
- Endermann, M.
- Fils, J.
- Hollinger, R.
- Lang, R.
- Mäder, J.
- Maimone, F.
- Patchakui, P.T.
- Spädtke, P.
- Tinschert, K.

IAP/RAS
Nizhny Novgorod, Russia
- Izotov, I.
- Mansfeld, D.
- Skalyga, V.

IBAM-CNR
Catania, Italy
- Romano, F.P.

IBS
Daejeon, Republic of Korea
- Hashimoto, T.
- Heo, J.
- Hong, I.S.
- Ishiyama, H.
- Jang, J.-H.
- Jin, H.
- Kim, Y.H.

IFK Berlin
Berlin, Germany
- Huke, A.
- Ruprecht, G.
- Weißbach, D.

IFMIF/EVEDA
Rokkasho, Japan
- Knaster, J.
- Marqueta, A.
- Nishiyama, K.
- Okumura, Y.
- Pruneri, G.
- Scantamburlo, F.

IMP/CAS
Lanzhou, People's Republic of China
- Fang, X.
- Feng, Y.C.
- Guo, J.W.
- Liu, Y.
- Lu, W.
- Ma, H.Y.
- Ma, L.Z.
- Ma, Y.M.
- Shen, Z.
- Sun, L.T.
- Wu, Q.
- Wu, W.
- Yang, T.
- Yang, Y.
- Yuan, Y.J.
- Zhang, W.H.
- Zhang, X.Z.
- Zhao, B.
- Zhao, H.W.

IN2P3 IPNL
Villeurbanne, France
- Peaucelle, C.

INFN/LNL
Legnaro (PD), Italy
- Bellan, L.
- Comunian, M.
- Fagotti, E.
- Galatà, A.
- Pisent, A.

INFN/LNS
Catania, Italy
- Allegra, L.
- Altana, C.
- Amato, A.
- Calabrese, G.
- Caliri, C.
- Caruso, A.C.
- Castro, G.
- Celona, L.
- Chines, F.
- Ciavola, G.
- Costa, G.
- Gallo, G.

ISBN 978-3-95450-186-1

- Gammino, S.
- Leonardi, O.
- Longhitano, A.
- Manno, G.
- Marletta, S.
- Mascali, D.
- Massara, A.
- Maugeri, A.
- Mazzaglia, M.
- Neri, L.
- Nicolosi, D.
- Noto, F.
- Passarello, S.
- Pastore, G.
- Reitano, R.
- Romano, F.P.
- Seminara, A.
- Sorbello, G.
- Spartà, A.
- Torrisi, G.
- Vinciguerra, S.

Institute for Plasma Research
Bhat, Gandhinagar, India
- Bandyopadhyay, M.
- Kumar, R.K.
- Mallick, C.
- Tewari, S.V.

IUAC
New Delhi, India
- Ahuja, R.
- Barua, P.
- Kanjilal, D.
- Kothari, A.
- Malyadri, A.
- Mandal, A.
- Mathur, Y.M.
- Rao, U.K.
- Rodrigues, G.O.
- Sharma, A.

JINR
Dubna, Moscow Region, Russia
- Bogomolov, S.L.
- Bondarchenko, A.E.
- Efremov, A.A.
- Loginov, V.N.
- Mironov, V.

JYFL
Jyväskylä, Finland
- Kalvas, T.
- Koivisto, H. A.
- Komppula, J.
- Kronholm, R.J.
- Laulainen, J.P.
- Orpana, J.
- Tarvainen, O.A.

KAERI
Daejon, Republic of Korea
- Kim, H.S.

KBSI
Deajeon, Republic of Korea
- Won, J.

Korea Atomic Energy Research Institute (KAERI)
Gyeongbuk, Republic of Korea
- Cho, Y.-S.
- Kim, D.I.
- Kwon, H.-J.
- Yun, S.P.

Korea Basic Science Institute
Busan, Republic of Korea
- Bahng, J.
- Choi, S.
- Hong, J.G.
- Kim, H.G.
- Kim, S.J.
- Lee, B.S.
- Ok, J.W.
- Park, J.Y.
- Won, M.
- Yoon, J.H.

Korea University
Seoul, Republic of Korea
- Kumwenda, M.J.

Kyoto ICR
Uji, Kyoto, Japan
- Fuwa, Y.
- Iwashita, Y.
- Tongu, H.

Kyungpook National University
Daegu, Republic of Korea
- Bahng, J.

LANL
Los Alamos, New Mexico, USA
- Valdez, J.A.

LBNL
Berkeley, California, USA
- Benitez, J.Y.
- Leitner, D.
- Lyneis, C.M.
- Phair, L.

ISBN 978-3-95450-186-1

- Sabbi, G.L.
- Todd, D.S.
- Xie, D.

LPSC
Grenoble Cedex, France
- Angot, J.
- Bonny, L.
- Jacob, J.
- Lamy, T.
- Sole, P.
- Thuillier, T.
- Villa, F.

Michigan State University
East Lansing, Michigan, USA
- Verboncoeur, J.P.

MSU
East Lansing, Michigan, USA
- Parsey, G.

National Institute of Radiological Sciences
Chiba, Japan
- Muramatsu, M.

NFRI
Daejon, Republic of Korea
- Choo, W.I.
- Jang, S.O.
- You, H.J.

NIRS
Chiba-shi, Japan
- Iwata, Y.
- Kitagawa, A.
- Muramatsu, M.
- Noda, E.
- Sekiguchi, M.

NSCL
East Lansing, Michigan, USA
- Fogleman, J.
- Neben, D.E.
- Pham, A.N.
- Renteria, S.
- Stetson, J.W.
- Tobos, L.

Osaka University, Graduate School of Engineering
Osaka, Japan
- Kato, Y.

PKU
Beijing, People's Republic of China
- Chen, J.E.
- Guo, Z.Y.
- Peng, S.X.
- Ren, H.T.
- Wen, J.M.
- Wu, W.B.
- Xu, Y.
- Zhang, A.L.
- Zhang, J.F.
- Zhang, T.

Polygon Physics
Grenoble, France
- Sortais, P.

QST/Takasaki
Takasaki, Japan
- Miyawaki, N.

QST
Tokai, Japan
- Ichikawa, M.
- Ichimiya, R.
- Ihara, A.
- Kasugai, A.
- Kitano, T.
- Komata, M.
- Kondo, K.
- Sakamoto, K.
- Shinya, T.
- Sugimoto, M.

RIKEN Nishina Center
Wako, Japan
- Haba, H.
- Higurashi, Y.
- Kamigaito, O.
- Kase, M.
- Kidera, M.
- Nagatomo, T.
- Nakagawa, T.
- Ohnishi, J.
- Ozeki, K.

SHI
Kanagawa, Japan
- Murata, H.
- Takahashi, T.

Si.A.Tel SRL
Catania, Italy
- Di Martino, S.
- Nicotra, P.

ISBN 978-3-95450-186-1

Technische Universität Dresden, Institut für Angewandte Physik
Dresden, Germany
- Zschornack, G.

Univ. degli Studi di Padova
Padova, Italy
- Bellan, L.

Universita Degli Studi Di Catania
Catania, Italy
- Mazzaglia, M.
- Reitano, R.

University of Catania
Catania, Italy
- Sorbello, G.

University of Chinese Academy of Sciences
Beijing, People's Republic of China
- Zhang, A.L.

University of Szczecin, Institute of Physics
Szczecin, Poland
- Czerski, K.
- Kaczmarski, M.
- Targosz-Ślęczka, N.

UNN
Nizhny Novgorod, Russia
- Izotov, I.
- Skalyga, V.

ISBN 978-3-95450-186-1

Participants List

Last Name	First Name	Country	Affiliation
Akuwuike	Darlington	Nigeria	Gombe State Polytechnic Faculty of Sciences
Angot	Julien	France	Laboratoire de Physique Subatomique et de Cosmologie
Asselineau	C?ric	Germany	Advanced Ferrite Technology
Barue	Christophe	France	Grand Acc?ateur Nat. d'Ions Lourds
Bashir	Abdul Hannan	Ghana	Minequip Ghana Limited Minequip Ghana Limited
Benitez	Janilee	United States of America	Lawrence Berkeley National Laboratory
Biri	Sandor	Hungary	Hungarian Academy of Sciences Institute of Nuclear Research
Bolzon	Benoit	France	Commissariat l'Energie Atomique Institut de recherche sur les lois fondamentales de l'Univers (IRFU)
Castro	Giuseppe	Italy	Istituto Nazionale di Fisica Nucleare Laboratori Nazionali del Sud
Celona	Luigi	Italy	Centro Siciliano di Fisica Nucleare e Struttura della Materia
Chang	Doo-Hee	Republic of Korea	Korea Atomic Energy Research Institute
Cho	Yong-Sub	Republic of Korea	Korea Atomic Energy Research Institute
Choi	Bong Hyuk	Republic of Korea	Institute for Basic Science
Choi	Seyong	Republic of Korea	Korea Basic Science Institute
Choo	Wonil	Republic of Korea	National Fusion Research Institute
de Guiran	Remi	France	Commissariat a l'Energie Atomique Institute of Research into the Fundamental Laws of the Universe
Delferriere	Olivier	France	Commissariat a l'Energie Atomique Institute of Research into the Fundamental Laws of the Universe
Dominguez Canizares	Guillermo	The Netherlands	High Voltage Engineering Europa B.V.
Efremov	Andrey	Russia	Joint Institute for Nuclear Research
Galata	Alessio	Italy	Istituto Nazionale di Fisica Nucleare Laboratori Nazionali di Legnaro
Gobin	Raphael	France	Commissariat a l'Energie Atomique Direction des Sciences de la Matiere
Heo	Jeong Il	Republic of Korea	Institute for Basic Science
Higurashi	Yoshihide	Japan	RIKEN Nishina Center
Hong	In-Seok	Republic of Korea	Institute for Basic Science
Hong	Jonggi	Republic of Korea	Korea Basic Science Institute
Huh	Sung-Ryul	Republic of Korea	Korea Atomic Energy Research Institute
Izotov	Ivan	Russia	Institute of Applied Physics Russian Academy of Sciences
Jang	Soouk	Republic of Korea	National Fusion Research Institute
Jeong	Sunchan	Republic of Korea	Institute for Basic Science
Jin	Hyunchang	Republic of Korea	Institute for Basic Science
Keens	Simon	Switzerland	Ampegon AG
Kim	Do Yoon	Republic of Korea	Vitzrotech Co., Ltd.
Kim	Hye-Jin	Republic of Korea	Institute for Basic Science
Kim	Kye-Ryung	Republic of Korea	Korea Atomic Energy Research Institute
Kim	Seongjun	Republic of Korea	Institute for Basic Science
Kim	Yonghwan	Republic of Korea	Institute for Basic Science
Kitagawa	Atsushi	Japan	National Institute of Radiological Science
Koivisto	Hannu	Finland	University of Jyvaskyla
Kondrashev	Sergey	Republic of Korea	Institute for Basic Science
Kreller	Martin	Germany	Dreebit GmbH

ISBN 978-3-95450-186-1

Last Name	First Name	Country	Affiliation
Kuchler	Detlef	Switzerland	European Organization for Nuclear Research
Kumar	Rajesh	India	Institute for Plasma Research
Kurokawa	Shin-ichi	Japan	Cosylab, Inc.
Lee	Byoung Seob	Republic of Korea	Korea Basic Science Institute
Leitner	Daniela	United States of America	Lawrence Berkeley National Laboratory
Maimone	Fabio	Germany	GSI Helmholtzzentrum f? Schwerionenforschung GmbH
Mascali	David	Italy	Istituto Nazionale di Fisica Nucleare Laboratori Nazionali del Sud
Maunoury	Laurent	France	Grand Accelerateur Nat. d'Ions Lourds
Mironov	Vladimir	Russia	Joint Institute for Nuclear Research
Muramatsu	Masayuki	Japan	National Institute of Radiological Science
Nagatomo	Takashi	Japan	RIKEN Nishina Center
Nakagawa	Takahide	Japan	RIKEN Nishina Center
Ok	Jung-Woo	Republic of Korea	Korea Basic Science Institute
Okebe	Ogba	Nigeria	Gombe State Polytechnic Faculty of Sciences
Pardo	Richard	United States of America	Argonne National Laboratory
Park	Bum-Sik	Republic of Korea	Institute for Basic Science
Park	Jin Yong	Republic of Korea	Korea Basic Science Institute
Peng	ShiXiang	People's Republic of China	Peking University
R?z	Rich?d	Hungary	Hungarian Academy of Sciences Institute of Nuclear Research
Rodrigues	Dr. Gerard	India	Inter University Accelerator Centre
Salou	Pierre	France	PANTECHNIK
Skalyga	Vadim	Russia	Institute of Applied Physics Russian Academy of Sciences
Spaedtke	Peter	Germany	GSI Helmholtzzentrum fur Schwerionenforschung GmbH
Sun	Liangting	People's Republic of China	Institute of Modern Physics, Chinese Academy of Sciences
Tarvainen	Olli	Finland	University of Jyvaskyla
Tewari	Somesh	India	Institute for Plasma Research
Thuillier	Thomas	France	Laboratoire de Physique Subatomique et de Cosmologie
Tinschert	Klaus	Germany	GSI Helmholtzzentrum fur Schwerionenforschung GmbH
Toivanen	Ville	Switzerland	European Organization for Nuclear Research
Tuske	Olivier	France	Commissariat ?l'Energie Atomique Direction des Sciences de la Mati?e
Vala	Sudhirsinh	India	Institute for Plasma Research
Vondrasek	Richard	United States of America	Argonne National Laboratory
Won	Mi-Sook	Republic of Korea	Korea Basic Science Institute
Wu	Qi	People's Republic of China	Institute of Modern Physics, Chinese Academy of Sciences
Xie	Daniel	United States of America	Lawrence Berkeley National Laboratory
Yang	Yao	People's Republic of China	Institute of Modern Physics, Chinese Academy of Sciences
Yoon	Jang-Hee	Republic of Korea	Korea Basic Science Institute
You	Hyun-Jong	Republic of Korea	National Fusion Research Institute
Zhang	Xuezhen	People's Republic of China	Institute of Modern Physics, Chinese Academy of Sciences
Zhao	Hongwei	People's Republic of China	Institute of Modern Physics, Chinese Academy of Sciences

ISBN 978-3-95450-186-1